



## City Research Online

### City, University of London Institutional Repository

---

**Citation:** Zhang, X. (2018). Multi-model method for simulating 2D Surface-Piercing Wave-Structure Interactions. (Unpublished Doctoral thesis, City, University of London)

This is the accepted version of the paper.

This version of the publication may differ from the final published version.

---

**Permanent repository link:** <https://openaccess.city.ac.uk/id/eprint/19772/>

**Link to published version:**

**Copyright:** City Research Online aims to make research outputs of City, University of London available to a wider audience. Copyright and Moral Rights remain with the author(s) and/or copyright holders. URLs from City Research Online may be freely distributed and linked to.

**Reuse:** Copies of full items can be used for personal research or study, educational, or not-for-profit purposes without prior permission or charge. Provided that the authors, title and full bibliographic details are credited, a hyperlink and/or URL is given for the original metadata page and the content is not changed in any way.



# **Multi-model method for simulating 2D Surface-Piercing Wave-Structure Interactions**

Xi Zhang

Supervisors

Prof. Qingwei Ma

A thesis submitted for the degree of Doctor of Philosophy

School of Mathematics, Computer Science and Engineering

City, University of London

April, 2018

# Contents

Acknowledgement.....	7
Declaration .....	8
List of Figures .....	9
List of tables .....	13
Notation.....	14
Abstract .....	18
Chapter 1 Introduction .....	20
1.1 Background .....	20
1.2 Aim and Objectives of the study .....	23
1.3 Structure of the paper .....	23
1.4 Originalities in the research.....	24
Chapter 2 Literature review and discussions on previous works .....	25
2.1 literature review of traditional numerical models .....	25
2.1.1 The potential model.....	25
2.1.2 The viscous model.....	26
2.2 Literature review of hybrid numerical models .....	27
2.2.1 Hybrid numerical models based on domain-decomposition method.....	28
2.2.2 Hybrid Numerical models based on the function-decomposition method.....	32
2.3 Literature review of OpenFOAM for wave-structure interactions.....	37
Chapter 3 An Euler-viscous hybrid model for interaction of a surface-piercing fixed structure with waves.....	39
3.1 The mathematical formulations.....	39
3.1.1 The governing equations of the two-phase Euler solver .....	39
3.1.2 The governing equations of the two-phase complementary RANS solver .....	40
3.2 The numerical method.....	42
3.3 The computational domain for the Euler-viscous hybrid solver .....	44
3.4 The boundary conditions .....	44
3.4.1 The boundary condition in the Euler domain.....	44

3.4.2 The boundary condition in the viscous domain .....	45
3.5 The relaxing zone and the transition zone.....	46
3.5.1 The transition zone in the viscous domain.....	47
3.5.2 The relaxation method in the transition zone .....	47
3.6 The interpolation technique.....	48
3.7 The solution procedure of the Euler-viscous hybrid solver .....	49
Chapter 4 Convergence study of the Euler-viscous hybrid solver for interaction of a surface-piercing fixed structure with waves .....	52
4.1 The numerical configuration .....	52
4.2 The effects of the mesh resolution .....	53
4.2.1 The mesh for the Euler-viscous hybrid solver and the conventional RANS solver	53
4.2.2 The convergence study of the conventional RANS solver and the Euler solver ....	54
4.2.3 The simulation results based on the Euler-viscous hybrid solver .....	59
4.2.4 The effects of mesh resolution for the Euler-viscous hybrid solver .....	61
4.3 The effects of the length ( $L_V$ ) of the viscous domain.....	65
4.3.1 The effects of $L_V$ on wave loads .....	65
4.3.2 The effects of $L_V$ on wave elevation .....	67
4.3.3 The effects of $L_V$ on velocity .....	69
4.3.4 The effects of $L_V$ on computational efficiency .....	70
4.4 The effects of the width ( $H_V$ ) of the viscous domain .....	71
4.4.1 The effects of $H_V$ on wave loads .....	71
4.4.2 The effects of $H_V$ on CPU time .....	73
4.5 The effects of the length ( $L_{tr}$ ) of the transition zone in the viscous domain .....	74
4.5.1 The effects of the length ( $L_{tr}$ ) of the transition zone on wave loads .....	74
4.5.2 The effects of the length ( $L_{tr}$ ) of the transition zone on computational efficiency .	76
4.6 The validation of the Euler-viscous hybrid solver .....	77
4.7 Summary .....	80
Chapter 5 Investigation of wave interaction with surface-piercing fixed structure subjected to complex seabed topography .....	81
5.1 Introduction .....	81



5.2 Problem description .....	81
5.3 The numerical methods .....	82
5.3.1 The computational domain and mesh .....	82
5.3.2 The validation of the numerical methods .....	83
5.3.3 The CPU time consumed in the simulation.....	86
5.4 Results and discussion.....	86
5.4.1 The effects of the water depth ( $d_2$ ) on wave loads .....	86
5.4.2 The effects of the top width ( $B_2$ ) on the wave loads .....	90
5.5 Summary .....	92
Chapter 6 Euler-viscous hybrid model for interaction of a surface-piercing moving structure .....	94
6.1 The mathematical model .....	94
6.1.1 Governing equations of the two-phase Euler solver with dynamic mesh .....	94
6.1.2 Governing equations of the two-phase complementary RANS solver with dynamic mesh .....	95
6.2 The numerical methods .....	96
6.3 Computational domain configuration for the Euler-viscous hybrid solver with dynamic mesh .....	97
6.4 Boundary conditions .....	97
6.4.1 Structure-surface boundary condition in the Euler domain .....	97
6.4.2 Structure surface boundary condition in the viscous domain .....	98
6.5 Numerical techniques in the Euler-viscous hybrid solver with dynamic mesh .....	98
6.6 The solution procedure of the Euler-viscous hybrid solver with dynamic mesh .....	99
6.6.1 Solution procedure for interaction between waves and a floating structure undergoing forced motion .....	99
6.6.2 The solution procedure for interaction between waves and floating structure undergoing freely motion .....	101
Chapter 7 Convergence study of the Euler-viscous hybrid solver for moving surface-piercing structures in waves .....	105
7.1 Description of the physical model.....	105

7.2 Convergence study .....	106
7.2.1 Computational mesh.....	106
7.2.2 Convergence properties of the conventional RANS solver and the Euler solver ..	107
7.2.3 Convergent property of the Euler-viscous hybrid solver .....	112
7.3 Performance of the Euler-Viscous Hybrid solver a forced rolling floating structure in water .....	114
7.3.1 The effects of the length of the viscous domain ( $L_v$ ).....	114
7.3.2 The effects of the width of the viscous domain ( $H_v$ ) .....	115
7.3.3 The effects of the length of the transition zone ( $L_{tr}$ ) .....	117
7.3.4 The effects of the motion frequency .....	118
7.4 Performance of the Euler-Viscous hybrid solver for simulating roll damping of a floating structure .....	120
7.4.1 The effects of the length of the viscous domain ( $L_v$ ).....	120
7.4.2 The effects of the width of the viscous domain ( $H_v$ ) .....	121
7.4.3 The effects of the length of the transition zone in the viscous domain ( $L_{tr}$ ) .....	122
7.5 Summary .....	123
Chapter 8 Hybrid Model Incorporating Domain-decomposition and Function-decomposition Methods for Wave-Structure Interaction .....	125
8.1 Extended Euler-viscous hybrid solver .....	126
8.2 Computational domain .....	127
8.3 Convergence study of the Extended Euler-viscous hybrid solver for interactions between wave and fixed structures.....	128
8.3.1 Physical model .....	129
8.3.2 Mesh resolution .....	130
8.3.3 The effects of the distance $L_p$ before reaching the inlet boundary of the Euler domain.....	130
8.4 Convergence study of the extended Euler-viscous hybrid solver for modelling rolling structures in waves .....	134
8.4.1 Physical model .....	134
8.4.2 Convergence study .....	134

8.4.3 Effects of the length of the viscous domain ( $L_v$ ) .....	139
8.4.4 Effects of the width of the viscous domain ( $H_v$ ).....	141
8.4.5 Effects of the length of the transition zone ( $L_{tr}$ ).....	142
8.4.6 Effects of distance $L_P$ before reaching the inlet boundary of the Euler domain ...	143
8.5 Validation of the extended Euler-viscous hybrid solver .....	144
8.6 Summary .....	146
Chapter 9 Investigation of wave interaction with surface-piercing moving structure subjected to complex seabed topography .....	148
9.1 Introduction .....	148
9.2 Physical model .....	149
9.3 The numerical methods .....	149
9.3.1 The computational domain and mesh .....	150
9.3.2 The validation of the numerical methods .....	151
9.4 Systematic Investigation .....	152
9.4.1 Effects of $d_2$ on wave-excited roll motions .....	152
9.4.2 Effects of the top width ( $B_2$ ) .....	154
9.5 Summary .....	155
Chapter 10 Conclusions and recommendations .....	156
10.1 Numerical techniques .....	156
10.2 Computational robustness of hybrid solvers .....	157
10.3 Application to wave interactions with a floating structure subjected to complex seabed topography.....	158
10.4 Contributions .....	158
10.5 Recommendations .....	158
References .....	160

**THE FOLLOWING PART OF THIS THESIS HAS BEEN REDACTED  
FOR COPYRIGHT REASONS:**

Fig. 1.1.2 the ship disaster due to complex topography ..... 21

## **Acknowledgement**

Firstly, I would like to give my sincere gratitude to my supervisor Professor Qingwei Ma for his tutoring, patience, inspiration, and motivation. Professor Ma helps me in all the time of the research and the writing of my Ph.D. thesis. During this period, Professor Ma gives me too much useful advice and encouragement, which are not only in the research, but also in the personal life. Due to his effort, I could not have imagined making better progress.

I would also like to thank Dr. Shiqiang Yan and Dr. Jinghua Wang for their comments and suggestions on my Ph.D. thesis.

I gratefully acknowledge the financial support of my three years' study provided by the University Ph.D. Studentship and Lloyd's Register.

Finally, I also thank my parents for their invaluable support.

## **Declaration**

“I hereby certify that the work embodied in this Thesis is the result of original research and has not been submitted for a higher degree to any other University or Institute”

---

Xi Zhang

## List of Figures

Fig. 1.1.1 Wave-structure interactions .....	20
Fig. 1.1.2 the ship disaster due to complex topography .....	21
Fig. 1.1.3 A rolling floating structure under incident waves.....	22
Fig. 2.2.1 The hybrid numerical models .....	28
Fig. 3.3.1 The computational domain for the Euler-viscous hybrid model .....	43
Fig. 3.5.1 The transition zone in the viscous domain.....	47
Fig. 3.5.2 The transition zone in the viscous domain.....	48
Fig. 3.6.1 The interpolation method.....	49
Fig. 3.7.1 The interpolation procedure.....	50
Fig. 4.1.1 the physical model .....	52
Fig. 4.2.1 Mesh used in the hybrid model and conventional RANS model.....	53
Fig. 4.2.2 Time history of moment .....	55
Fig. 4.2.3 The convergence study ( $nB_C$ and $nB_E$ ) of conventional RANS solver and Euler solver .....	56
Fig. 4.2.4 The convergence study ( $nH_C$ and $nH_E$ ) of conventional RANS solver and Euler solver .....	56
Fig. 4.2.5 The convergence study ( $nL_C$ and $nL_E$ ) of conventional RANS solver and Euler solver .....	58
Fig. 4.2.6 The comparison of wave loads between the Euler-viscous hybrid solver and the conventional RANS solver.....	60
Fig. 4.2.7 The comparison of wave loads by using different mesh resolution in the Euler-viscous hybrid solver and the conventional RANS solver .....	63
Fig. 4.2.8 The average error against cases with different mesh configuration .....	63
Fig. 4.2.9 The average error under different mesh resolution.....	64
Fig. 4.3.1 The comparison of wave loads at different $L_V$ .....	66
Fig. 4.3.2 The average error of wave loads at different $L_V$ .....	67
Fig. 4.3.3 The comparison of wave elevation in one wave period at different $L_V$ .....	68
Fig. 4.3.4 The average error of wave elevation and velocity in the horizontal direction.....	69
Fig. 4.3.5 The comparison of the horizontal velocity over one wave period.....	70
Fig. 4.3.6 The CPU time ratio against length ( $L_V$ ) of the viscous domain.....	70
Fig. 4.4.1 The comparison of wave loads at different $H_V$ .....	72
Fig. 4.4.2 The average error of wave loads at different $H_V$ .....	73
Fig. 4.4.3 The CPU time ratio against width ( $H_V$ ) of the viscous domain .....	73
Fig. 4.5.1 The comparison of wave loads at different $L_{tr}$ .....	75

Fig. 4.5.2 The average error of wave loads at different $L_{tr}$ .....	76
Fig. 4.5.3 The CPU time ratio at different $L_{tr}$ .....	76
Fig. 4.6.1 The comparison of wave loads with different incident waves.....	78
Fig. 4.6.2 The CPU time ratio against frequency of incident waves.....	79
Fig. 5.2.1 The sketch of the wave-fixed structure over the complex topography .....	82
Fig. 5.3.1 The computational domain and mesh used in the simulation .....	83
Fig. 5.3.2 Comparison of the time histories of the moment acting on the floating structure subjected to water waves propagating over submerged structure ( $d_2=0.2\lambda$ , $\lambda=2.1\text{m}$ , $H_w=0.07\text{m}$ ) .....	84
Fig. 5.3.3 The comparison of wave loads in one wave period for wave-structure interaction under the effects of the submerged structure ( $d_2=0.2\lambda$ , $\lambda=2.1\text{m}$ , $A=0.035\text{m}$ ).....	85
Fig. 5.3.4 The CPU time ratio at different $d_2$ for wave interactions with the floating structure subject to a submerged structure .....	85
Fig. 5.4.1 The comparison of wave loads under submerged structure with different $d_2$ .....	88
Fig. 5.4.2 The comparison of 1 <sup>st</sup> order wave loads under effects of submerged structures at different $d_2$ .....	89
Fig. 5.4.3 the comparison of the amplification factor of linear vertical force component under different incident waves at different $d_2$ .....	90
Fig. 5.4.4 The comparison of 1 <sup>st</sup> order of wave loads under submerged structure at different $B_2$ .....	91
Fig. 5.4.5 The comparison of relative increase ratio under different incident waves at different $B_2$ .....	92
Fig. 6.3.1 the computational domain for the Euler-viscous hybrid model.....	97
Fig. 6.6.1 The flow chart of the simulation of the floating structure with forced motion by the Euler-viscous hybrid solver under dynamic mesh .....	100
Fig. 6.6.2 The flow chart of the simulation of the floating structure with free motion by Euler- viscous hybrid solver under dynamic mesh .....	103
Fig. 7.1.1 the physical model .....	105
Fig. 7.2.1 mesh with feature parameters .....	106
Fig. 7.2.2 The comparison of moment at different time step .....	108
Fig. 7.2.3 The comparison of moment ( $nL_C$ and $nL_E$ ) between the conventional RANS solver and the Euler solver .....	109
Fig. 7.2.4 The comparison of moment ( $nB_C$ and $nB_E$ ) between the conventional RANS solver and the Euler solver .....	110
Fig. 7.2.5 The comparison of moment ( $nH_C$ and $nH_E$ ) between the conventional RANS solver and the Euler solver .....	111



Fig. 7.2.6 The comparison of time history of moment between the Euler-viscous hybrid solver and the conventional RANS solver .....	113
Fig. 7.3.1 The comparison of moment at different $L_V$ by the Euler-viscous hybrid solver ...	115
Fig. 7.3.2 The average error and CPU time ratio at different $L_V$ .....	115
Fig. 7.3.3 The comparison of moment at different $H_V$ by the Euler-viscous hybrid solver...	116
Fig. 7.3.4 The average error and CPU time ratio at different $H_V$ .....	116
Fig. 7.3.5 The comparison of moment at different $L_{tr}$ by the Euler-viscous hybrid solver ...	118
Fig. 7.3.6 The average error and CPU time ratio at different $L_{tr}$ .....	118
Fig. 7.3.7 The comparison of 1 <sup>st</sup> order amplitude of moment between the Euler-viscous hybrid solver and the conventional RANS solver at different motion frequency .....	119
Fig. 7.3.8 The average error and CPU time ratio at motion frequency .....	119
Fig. 7.4.1 The comparison of time history of roll angle at different $L_V$ .....	121
Fig. 7.4.2 The average error and CPU time ratio at different $L_V$ .....	121
Fig. 7.4.3 The comparison of time history of roll angle at different $H_V$ .....	121
Fig. 7.4.4 The average error and CPU time ratio at different $H_V$ .....	122
Fig. 7.4.5 The comparison of time history of roll angle at different $L_{tr}$ .....	123
Fig. 7.4.6 average error and CPU time ratio at different $L_{tr}$ .....	123
Fig. 8.1.1 The extending of the Euler-viscous hybrid solver with a fully nonlinear potential solver .....	126
Fig. 8.1.2 Data flow in the extended Euler-viscous hybrid solver .....	127
Fig. 8.2.1 Surface-piercing potential-Euler-viscous hybrid domains.....	128
Fig. 8.3.1 Mesh in hybrid domains .....	130
Fig. 8.3.2 The comparison of wave loads at different $L_P$ .....	132
Fig. 8.3.3 average error of wave loads under different $L_P$ .....	132
Fig. 8.3.4 CPU time ratio at different $L_P$ $F$ .....	133
Fig. 8.3.5 CPU time ratio for different solvers .....	133
Fig. 8.4.1 The time history of roll angle .....	135
Fig. 8.4.2 The comparison of the roll ( $nH_C$ and $nH_E$ ) between the conventional RANS solver and the Euler solver.....	136
Fig. 8.4.3 The comparison of the roll ( $nL_C$ and $nL_E$ ) between the conventional RANS solver and the Euler solver.....	137
Fig. 8.4.4 Time histories of the roll angles in the cases with different values of $nB_C$ and $nB_E$ for the conventional RANS solver and the Euler solver, respectively.....	138
Fig. 8.4.5 The time histories of the roll angle obtained by the conventional RANS solver and the extended Euler-viscous hybrid solver .....	139
Fig. 8.4.6 The comparison of roll angle at different $L_V$ .....	140
Fig. 8.4.7 Average error and CPU time ratio at different $L_V$ .....	140

Fig. 8.4.8 The comparison of roll angle at different $H_v$ .....	141
Fig. 8.4.9 The time histories of roll angle in the cases with different $L_{tr}$ .....	142
Fig. 8.4.10 Average error and CPU time ratio at different $L_{tr}$ .....	142
Fig. 8.4.11 The comparison of roll angle at different $L_p$ .....	144
Fig. 8.4.12 Average error and CPU time ratio at different $L_p$ .....	144
Fig. 8.5.1 The comparison of the first order ( $\psi$ ) of roll angle for incident waves .....	145
Fig. 8.5.2 The comparison of CPU time ratio for different incident waves .....	146
Fig. 9.2.1 The physical model .....	149
Fig. 9.3.1 The computational mesh used in the simulation.....	150
Fig. 9.3.2 The time histories of the roll angle in the cases with different $d_2$ using different numerical solvers .....	151
Fig. 9.3.3 CPU time ratio in the cases with different $d_2$ .....	151
Fig. 9.4.1 The time histories of the roll angle of a free rolling structure subjected to a submerged structure with different $d_2$ .....	152
Fig. 9.4.2 First order harmonics of roll motion $\psi$ at different wave condition and different $d_2$ .....	153
Fig. 9.4.3 The relationship between $\psi_d/\psi_f$ and $\lambda/d_2$ in the cases with different $d_2$ .....	153
Fig. 9.4.4 The time histories of the roll angle of a free rolling structure subjected to a submerged structures with different $B_2$ .....	154
Fig. 9.4.5 The effects of $B_2$ on 1 <sup>st</sup> order roll amplitude under different incident waves at different $B_2$ .....	155
Fig. 9.4.6 The relationship between $\phi_d/\phi_f$ and $\lambda/d_2 \cdot B_2/B$ .....	155

## List of tables

Table 2.2.1 The Category of the literatures about domain-decomposition method.....	31
Table 2.2.2 The category of the literatures about velocity decomposition method .....	36
Table 4.2.1 The mesh resolution and computational domain for the conventional RANS solver and the Euler-viscous hybrid solver .....	61
Table 4.3.1 The mesh for study the effects of $L_V$ .....	65
Table 4.4.1 The mesh for study the effects of $H_V$ .....	71
Table 4.5.1 The mesh for study the effects of $L_{tr}$ .....	71
Table 4.6.1 Non-dimensional parameters of incident waves .....	77
Table 5.3.1 The mesh resolution for conventional RANS solver and Euler-viscous hybrid solver .....	83
Table 5.4.1 The incident waves.....	86
Table 7.2.1 Parameters for features of mesh.....	107
Table 7.2.2 The mesh for the study of convergent property .....	113
Table 7.3.1 The mesh for the study of effects of $L_V$ .....	114
Table 7.3.2 The mesh for the study of effects of $H_V$ .....	116
Table 7.3.3 The mesh for the study of effects of $L_{tr}$ .....	116
Table 8.3.1 Parameters related with mesh features .....	129
Table 8.4.1 The mesh for the study of effects of length ( $L_V$ ) of the viscous domain .....	139
Table 8.4.2 The mesh for the study of effects of the width ( $H_V$ ) of the viscous domain .....	141
Table 8.4.3 The mesh for the study of effects of the length ( $L_{tr}$ ) of transition zone .....	142
Table 8.4.4 The mesh for the study of effects of $L_P$ of the viscous domain .....	143
Table 8.5.1 Non-dimensional parameters of incident waves and the computational domain .....	145
Table 9.3.1 The mesh for conventional RANS solver and Euler-viscous hybrid solver .....	150
Table 9.4.1 The incident waves and domain sizes .....	152

## Notation

### Roman Letters:

$U$  the velocity in the conventional RANS domain

$U^I$  the velocity in the Euler domain

$p^I$  the pressure in the Euler domain

$g$  the acceleration induced by gravity

$U^D$  the complementary velocity in the viscous domain

$U^D_t$  the final relaxed velocity in the transition zone of the viscous domain

$U^D_{Target}$  the target velocity in the transition zone of the viscous domain

$p^D$  the complementary pressure in the viscous domain

$t$  time

$k$  turbulent energy

$U^I_{in}$  the velocity induced by incident waves

$\mathbf{t}$  the vector

$\mathbf{n}$  the vector

$w$  the relaxation coefficient

$x_{point}$  the x coordinate of points in the transition zone

$x_{boundary}$  the x coordinate in boundary 1 or boundary 2

$L_{tr}$  the length of the transition zone

$B$  the width of the structure

$l$  the height of the structure

$L$  the length of the structure

$d$  the initial draft of the structure

$h$  the water depth of the structure

$H_w$  wave height

$k$  wave number

$A$  wave amplitude, half of wave height

$F_s$  the wave load in the horizontal direction

$F_h$  the wave load in the vertical direction

$M$  moment induced by waves

$T$  wave period

$f_B$  non dimensional wave frequency

$Re$  Reynolds Number

$L_C$  the length of the conventional RANS domain

$H_C$  the width of the conventional RANS domain

$L_E$  the length of the Euler domain

$H_E$  the width of the Euler domain

$L_V$  the length of the viscous domain

$H_V$  the width of the viscous domain

$n_{L_C}$  the number of division per wave length far away from the structure in the horizontal direction in the conventional RANS domain

$n_{L_E}$  the number of division per wave length far away from the structure in the horizontal direction in the Euler domain

$n_{L_V}$  the number of division per wave length far away from the structure in the horizontal direction in the viscous domain

$n_{B_C}$  the number of division per width of the structure in the horizontal direction in the conventional RANS domain

$n_{B_E}$  the number of division per width of the structure in the horizontal direction in the Euler domain

$nB_V$  the number of division per width of the structure in the horizontal direction in the viscous domain

$nH_C$  the number of division per wave height in the vertical direction in the conventional RANS domain

$nH_E$  the number of division per wave height in the vertical direction in the Euler domain

$nH_V$  the number of division per wave height in the vertical direction in the viscous domain

$\Delta t$  the time step

REM the relative average error

Err the average error over ten wave periods

$B_2$  the top width of the submerged bottom-standing structure

$B_3$  the bottom width of the submerged bottom-standing structure

$d_2$  the water depth of the submerged bottom-standing structure

$f_a$  1<sup>st</sup> order amplitudes of wave loads

$u_b$  the velocity of the mesh motion

$U_m^I$  the velocity of the moving structure

$U_n^I$  the velocity in the neighbour cell of the moving structure

$T_0$  the ceasing time in forced rolling

$f$  the wave frequency

$L_P$  the length of the wave propagation before the Euler domain

$L_{EH}$  the head part of the Euler domain

$L_{ER}$  the rear part of the Euler domain

$f_N$  the natural frequency of the structure

### **Greek Letters:**

$\rho'$  the density of the fluid in the Euler domain

$\rho_{\text{water}}$  the density of water

$\rho_{\text{air}}$  the density of air

$\gamma'$  the volume fraction of fluid in the Euler domain

$\gamma$  the volume fraction of fluid in the viscous domain

$\gamma_{\text{in}}^{\text{I}}$  the fraction volume induced by incident waves

$\gamma_{\text{t}}$  the final relaxed volume fraction of fluid in the transition zone of the viscous domain

$\gamma_{\text{Target}}$  the target volume fraction of fluid in the transition zone of the viscous domain

$\mu_{\text{t}}$  the total viscosity

$\mu_{\text{f}}$  the fluid viscosity

$\mu_{\text{a}}$  the turbulence viscosity

$\mu_{\text{f}}^{\text{water}}$  the viscosity of water

$\mu_{\text{f}}^{\text{air}}$  the viscosity of air

$\varepsilon$  turbulent dissipate rate

$\sigma$  the parameter related with the coordinates of the points in the transition zone

$\lambda$  wave length

$\Gamma_{\text{b}}$  the diffusion coefficient in mesh motion

$\alpha_0$  the roll amplitude of forced rolling

$\alpha$  the roll angle

$\psi(\text{M})$  1<sup>st</sup> order of moment due to forced rolling

$\psi$  1<sup>st</sup> order of roll amplitude

## Abstract

Wave-structure interactions play an important role on the design and maintenance of coastal and offshore constructions. Computational Fluid Dynamics (CFD) is a convenient tool for analyzing wave-structure interactions in coastal and offshore engineering. The potential model and the viscous model are traditional mathematical models for wave-structure interactions, which have disadvantages in computational robustness, when they are applied individually. Therefore, recently, more and more multi-model methods are used for coupling the viscous model and the potential model together. So far, in the existing multi-model methods, the surface-piercing structure only exists in the viscous domain so that the viscous domain should be large enough. In order to improve the computational efficiency, some multi-model methods are developed, where the structure is considered in both viscous domain and Euler domain.

Firstly, by function-decomposition method, an Euler-viscous hybrid model is proposed. Comparing with the other function-decomposition hybrid models, a surface-piercing structure exists in both a large Euler domain and a small viscous domain. By this, the reflection, diffraction, and radiation waves from the structure can be considered in both two computational domains. Therefore, the computational efficiency can be enhanced remarkably. To couple the Euler model and the viscous model, complementary RANS equations are deduced, with complementary turbulence models. Corresponding boundary conditions are also developed for coupling. A relaxed scheme is proposed for damping the viscous effects and keeping free surface consistent. For wave interactions with moving structures, the transition of total forces acting on the structure from the viscous domain to the Euler domain is used to guarantee the same motion of structures in two domains.

Secondly, the function-decomposition Euler-viscous hybrid model is extended by domain-decomposition method. Then, function-decomposition method and domain-decomposition method are coupled together. The wave generation and propagation is solved in a potential domain. By this, the computational efficiency for wave-structure interactions in a large real wave tank can be improved.

Computational robustness of Euler-viscous hybrid model for surface-piercing wave-structure interactions are studied by some cases. It is found that the size of the viscous domain, the length of transition zone, and mesh resolution can affect computational precision. Computational efficiency is mainly affected by the size of the viscous domain. For extended Euler-viscous hybrid model, the distance before reaching the inlet boundary of the Euler domain plays a crucial role on computational accuracy and efficiency. Validations are done



by comparing numerical results based on hybrid models, conventional RANS model and experimental results. It is shown that hybrid models own the same computational accuracy as the conventional RANS model. Furthermore, the computational accuracy can be improved remarkably. In some cases, more than 85% CPU time can be saved.

The hybrid models are applied to simulate wave interactions with a structure subjected to seabed effects. By comparing with numerical simulations based on the conventional RANS model, it is indicated that hybrid models can be also used on complex computational domain. Some properties of wave interactions with a floating structure subjected to a submerged structure are found by numerical simulations.

# Chapter 1 Introduction

## 1.1 Background

Waves are one of the most common features of the ocean and can be generated by many factors, e.g., wind, earth quake, and heat-transfer. Thus, marine engineering structures such as bridges, ships, and oil platforms are unavoidably subjected to ocean waves, especially the floating structures. As a matter of fact, wave-structure interactions play a crucial role in the design, manufacture and operation of floating structures in the ocean.



(a) A fixed structure interacts with waves

(<http://www.cnblogs.com/ovspianist/archive/2010/10/31/1865438.html>)



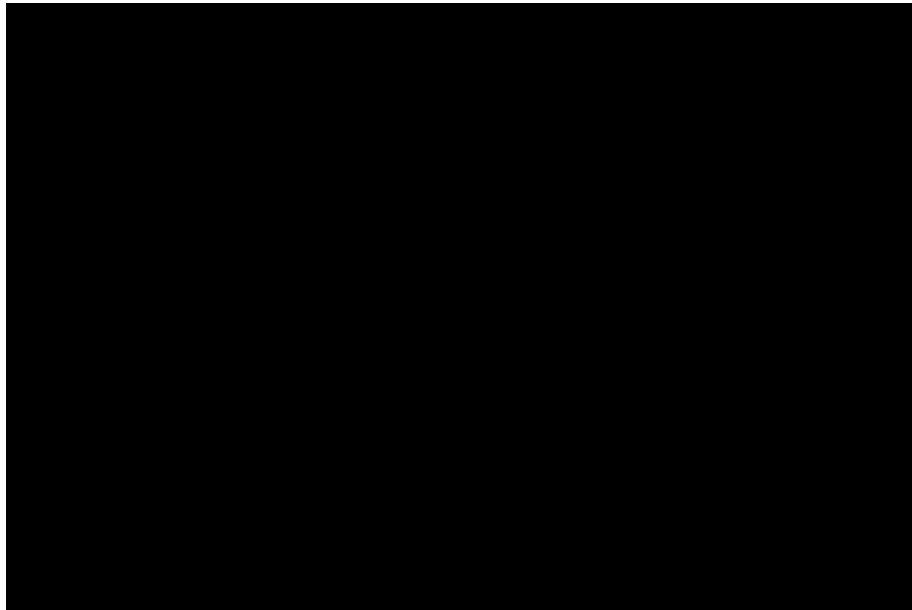
(b) A moving structure interacts with waves

(<http://shipsbusiness.com/parametric.html>)

Fig. 1.1.1 Wave-structure interactions

Due to that, the wave-structure interaction problems have attracted extensive attentions. Since the fixed cylinder structures, such as supporting pillars of bridges or jack-up rigs are widely adopted in the ocean engineering practices, on which the wave loads must be considered. One approach to calculate the wave loads is to use empirical formulas, e.g., the Morison's equations (Morison, 1950). These empirical formulas are based on linear or weakly non-linear wave-structure interaction theories and are only accurate when the nonlinear effects are neglectable. (MacCamy and Fuchs, 1954; Newman, 1996) However, they become less

accurate and cannot be applied when the non-linear effects are significant. Whereas, the fact that ocean waves in reality consist infinite wave components with different periods and amplitudes, renders the problem to be highly non-linear as wave-wave interactions cannot be neglected. In addition, the non-linear effects of the reflection and diffraction waves induced by the cylinders further increase the degrees of the complexity of such a problem (Faltinsen, 1993). Therefore, the empirical formulas can only be used in very limited situations.



([http://www.nola.com/business/index.ssf/2012/01/cruise\\_bookings\\_in\\_new\\_orleans.html](http://www.nola.com/business/index.ssf/2012/01/cruise_bookings_in_new_orleans.html))

Fig. 1.1.2 the ship disaster due to complex topography

Apart from the fixed structures, the moving structures, such as buoys, floating oil platforms, and ships are more desired in ocean engineering, and their safety against waves needs to be accessed. For instance, during the design of the naval architecture, the resonance should be avoided by examining the frequency of the incident waves over the natural frequency of the floating structure. If the two frequencies are very close, the resonance will occur and the motions of the structure will be enhanced, which can cause damages to the ship. Another aspect to be examined is the roll motion, which is the rotation of a vessel about its longitudinal axis. A rolling floating structure under incident waves is shown in Fig. 1.1.1(b). In some harsh sea state, the excessive roll motion can be induced, especially when resonant behaviour happens. Sometimes, the roll angle can reach more than 20 degrees (Na et al., 2002). Thus, wave interactions with moving structures have also received great attentions.

However, waves interacting with moving structures are more complex comparing with those in the fixed condition, mainly due to the non-linear interactions between incident waves and structures with six degrees of freedom, and the non-linear interactions between incident

waves with radiation, reflection and diffraction waves. Furthermore, it is recorded that the ship disaster can happen under the complex topography, shown in Fig. 1.1.2. The effects of bottom topography on propagation of the incident waves cannot be neglected (Fochesato, et al. 2003), thus the motions of floating structures will also be affected (Grilli, et al. 2001). Therefore, the dynamic motions of the moving structures are difficult to be predicted.

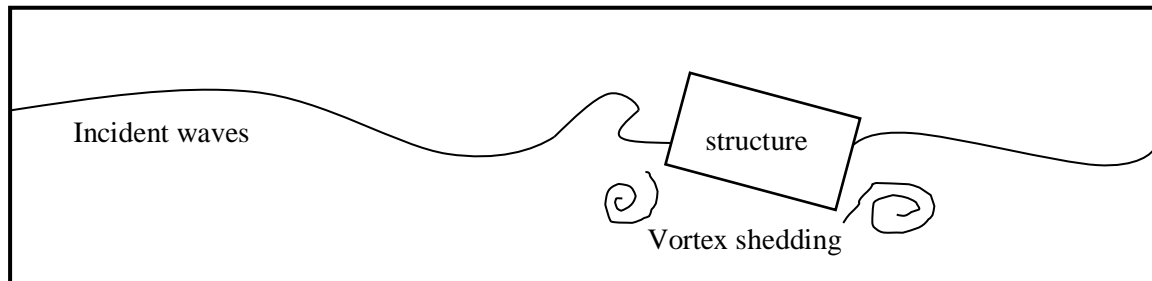


Fig. 1.1.3 A rolling floating structure under incident waves

In order to study the structure-wave interactions, laboratory experiments and Computational Fluid Dynamics (CFD) are adopted as two main methods. The former requires a big wave basin and is very time consuming, e.g., the work done by Chaplin, et al. (1997). Besides, the bottom topography is difficult to be made in the experiments, while the cost is high. Thanks to the recent development of computer science, CFD software has been widely used in the study of wave-structure interactions. Two mathematical models are often used in the numerical simulations including the potential model and the viscous model. In the potential model, due to simple control equations and less independent unknowns, the computational efficiency is high. However, the viscous effects are neglected in the potential model, which is important in the study of wave-structure interactions because the local viscous effects cannot be overlooked, especially in this research, where cases of Reynolds Number  $Re > 10000$  are considered. Unlike the potential model, the viscous model takes the viscous effects into account by solving the Reynolds Averaged Navier-Stokes (RANS) equations. Nevertheless, more computational resources are required due to complex control equations, independent unknowns, and large number of computational nodes.

To overcome drawbacks of each individual model, some hybrid numerical models are developed. In the hybrid models, the viscous effects are only considered in the local area close to the floating structure, while the potential model is applied in a larger computational domain far away from the floating structure. Hence, both the computational efficiency and the computational precision can be guaranteed.

Researchers have proposed many different hybrid numerical models. Specifically, those hybrid models can be classified into domain-decomposition models and function-decomposition models. Each model has its own advantages and disadvantages and one cannot

simply justify which model is superior. In this thesis, a new function-decomposition model is proposed. Finally, the function-decomposition model is hybrid with a domain-decomposition model.

## **1.2 Aim and Objectives of the study**

The study aims to develop new hybrid numerical models based on open-source CFD toolbox OpenFOAM. In the new function-decomposition model, the corresponding complementary RANS equations, boundary conditions, transition zones, and new computing procedure are proposed. The structure can be considered in both the Euler domain and the viscous domain. By doing so, the computational efficiency can be enhanced. In addition to that, the function-decomposition model can be extended to couple with a potential model by the domain-decomposition method. Then, the computational efficiency can be future improved.

The main tasks are,

1. Derive the complementary RANS equations by function-decomposition method for calculating complementary velocity and pressure in the viscous domain.
2. Propose boundary conditions for complementary RANS equations to keep the total velocity and total pressure the same as those by conventional RANS equations.
3. Develop transition zones for dissipating the viscous effects to cancel the complementary velocity and make sure the free surface consistent on the boundaries.
4. Design the computing procedures for the function-decomposition model to solve the complementary RANS equations and the Euler equations.
5. To further improve the computational efficiency, the function-decomposition model is extended to couple with the potential model by using the domain-decomposition method.
6. Apply these hybrid models to simulate two-dimensional surface-piercing fixed and floating structures interacting with incident waves over complex topography.

## **1.3 Structure of the paper**

Hybrid numerical models are reviewed and the corresponding discussion is carried out in Chapter 2. In Chapter 3, a new function-decomposition based Euler-viscous hybrid model is developed for simulating wave interacting with fixed a surface-piercing structure. More, specifically, formulas of complementary RANS equations are proposed, as well as the new boundary conditions, transition zone techniques, and computing procedures. Then, the new Euler-viscous hybrid model is validated by simulating waves acting on a two-dimensional fixed surface-piercing structure. In Chapter 4, the convergence property of the Euler-viscous hybrid solver are investigated by simulating wave-fixed structure interactions. Chapter 5 studies effects of variable bottom topography on the interaction between waves and fixed surface-piercing structure by the new Euler-viscous hybrid model. In Chapter 6, the dynamic

mesh is introduced to the new function-decomposition based Euler-viscous hybrid model for simulating waves interacting with moving structures. Then, in Chapter 7, the convergence properties of the new Euler-viscous hybrid model with dynamic mesh is studied by simulating the forced rolling and roll damping of a floating structure. Chapter 8 presents the extension of the new function-decomposition based Euler-viscous hybrid model hybrid with a potential model by the domain-decomposition method, of which the convergence properties are investigated and validated. Chapter 9 presents the applications of the extended Euler-viscous hybrid model to study the effects of complex topography on wave-induced roll motion of a floating structure. Finally, the conclusion is drawn and the recommendations are given in Chapter 10.

## **1.4 Originalities in the research**

The research contains two originalities. Firstly, new function-decomposition hybrid methods are developed for surface-piercing wave-structure interactions. Secondly, multi-model methods including potential, Euler, and viscous models are developed by function-decomposition method and domain-decomposition method together.

## **Chapter 2 Literature review and discussions on previous works**

Potential models and viscous models are traditional numerical models for simulating wave-structure interactions, and each category has its own advantages and disadvantages. The most significant feature of the potential model is that it's more efficient and precise for simulating wave propagation in a large physical domain. However, the viscosity is neglected, which plays a crucial part in the wave-structure interactions (used by Chen, et al. 2014). On the other hand, the viscosity, vorticity, and wave breaking can be simulated in the viscous model. However, large mesh resolution is required leading to low computational efficiency. Therefore, in recent years, hybrid numerical models are proposed. In the hybrid model, the potential model often covers a large computing domain for wave generation and propagation, while viscous model is just applied in a small domain surrounding the floating structure. By doing so, both the computational efficiency and accuracy can be guaranteed (e.g., Vukčević, et al. 2016). For more details, a literature review about potential models, viscous models, and hybrid models is given below.

### **2.1 literature review of traditional numerical models**

#### **2.1.1 The potential model**

For the potential model, the velocity potential and free surface elevation are the only unknown variables. The Laplace equation about the velocity potential can be discretized and solved by numerical methods such as Boundary Element Method (BEM) (used by Grilli, et al. 1989), Finite Element Method (FEM) (Wu, Ma, and Eatock, 1998), and Finite Difference Method (FDM) (Engsig-Karup, et al. 2012). According to the free surface and body surface boundary conditions, the potential model can be classified into linear/high-order models and fully nonlinear models. The linear/high-order models (Newman, 1977) have been widely used for engineering and research purposes. However, they are only accurate in limited conditions, e.g., small incident waves and small body motions.

To overcome those limitations, Fully Nonlinear Potential Theory (FNPT) models are suggested and many researchers have done valuable works on developing the FNPT models for simulating wave-structure interactions. For example, a time marching procedure proposed by Longuet-Higgins, and Cokelet (1976) is used to update the wave elevation and the velocity potential. The free surface is tracked by a mesh moving controlled method based on mixed-Euler-Lagrange scheme. By using FNPT models, Markiewicz, et al. (2003) and Koo (2007) investigate wave interactions with fixed structures. For waves interacting with moving

structures, relevant works have been done by Yan and Ma (2007) for simulating steep waves interacting with a two-dimensional floating structure, Bai and Eatock (2009) for simulating waves interacting with fixed and floating flared structures, Wang et al.(2011) for simulating the resonant motion of two two-dimensional floating structures.

From these works, it is found that FNPT models are accurate and efficient, supposed that the boundary of the structure is smooth and the viscous effects are insignificant. Nevertheless, the FNPT models have several drawbacks. Firstly, the viscosity cannot be directly considered in FNPT models, although artificial viscosity may be imposed on the free surface (Chen and Lu, 2009) or the body surface condition (Yan and Ma, 2010). Therefore, both the hull friction and vortex force related with viscous effects cannot be well estimated by the potential model unless benchmarking experimental studies are carried out to identify the above-mention artificial coefficients (Kharif, et al. 2008). Secondly, the roll motion induced flow separation increases the effects of vortices. (Yi, et al. 2005) To predict the vortex forces, discrete vortex methods (Seah and Ronald, 2003) are used in FNPT models. In their numerical model, the vorticity field is assumed to be a collection of discrete vortices of finite core size and the position of the separation point must be known in advance. Nevertheless, this assumption is not suitable for complex geometry. Thirdly, FNPT models cannot simulate wave breaking, which is often observed near the structure in reality. However, the viscosity, vorticity, and wave breaking are important in modelling wave-structure interactions. Therefore, the potential model is not sufficient.

### 2.1.2 The viscous model

For viscous models, the viscosity is considered in Navier Stokes (NS) equations. The NS equations and continuity equations can be numerically solved by two methods including the mesh-based method and the meshless method. The former discretizes and solves NS equations and the continuity equation by FDM (Chorin, 1965), FVM (Patankar, 1980), and FEM (Girault, 2012) methods. The free surface can be captured by a convective equation such as Marker and Cell method (MAC) (Harlow and Welch, 1965), Volume Of Fluid (VOF) method (Hirt and Billy, 1981), Level Set method (Sussman et al. 1994). By using the surface capturing method, the wave breaking can be considered in modelling wave-structure interactions. Park, et al. (2001) investigated waves and currents acting on a fixed vertical truncated cylinder. Yang, et al. (2006) simulated motions of floating LNG carrier with fully or partially filled tanks with effects of waves. Carrica, et al. (2007) studied the interaction between ship and head waves, where wave breaking and extreme motions of the ship could be simulated. The green water on the deck and the sloshing in the tank can be simulated simultaneously. Panahi, et al. (2006) studied the cylinder entry problem. More works by using

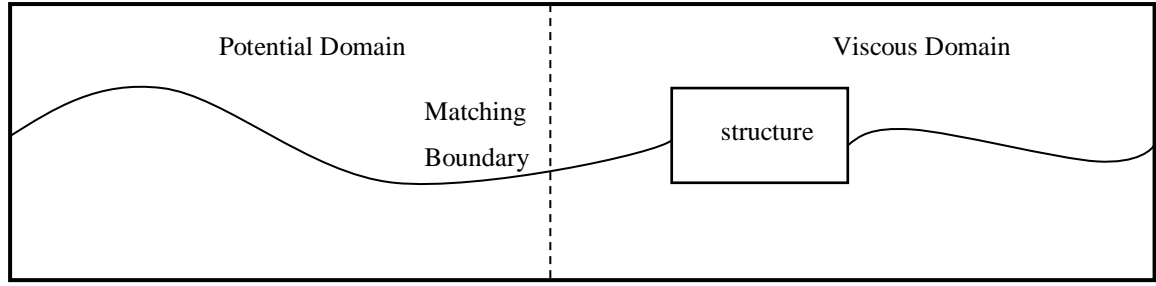


the free surface tracking method to study the ship hydrodynamics can be found in Alessandrini and Delhommeau, (1999) and Garcia and Oñate, (2003). In the family of meshless methods, SPH (Omidvar, et al. 2012), MPS (Sueyoshi, et al. 2008) and MLPG (Ma, 2005) have been attempted. Detailed review can be found from the cited papers above and will not be given here. However, due to the pressure evaluation (Molteni and Colagrossi, 2009), meshless method can only be used for some simple wave-structure interactions. Thus the meshless method will not be employed in the research.

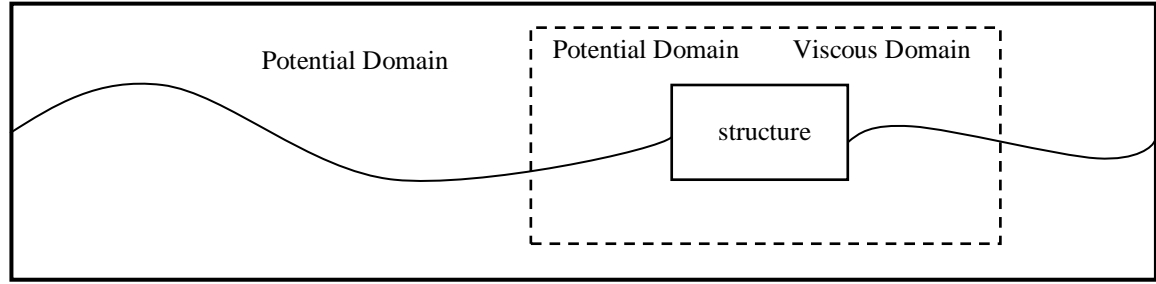
Even though the viscous effects can be considered, the efficiency of the viscous model is often lower than the potential model, especially for modelling interactions between waves and moving structures. The reasons are: firstly, at least three independent unknowns including two velocity components and pressure should be solved in two-dimensional NS equations, comparing with potential model which only requires finding velocity potential and free surface elevation. Besides, the turbulence model should be used in the viscous model so that some more control equations must be considered. Furthermore, the disadvantage about efficiency is more obvious for wave-structure interactions in a large computing domain, especially when the dynamic mesh based method is used. Last but not least, to capture vortex shedding, the mesh surrounding the structure must be refined, which makes the computation more time consuming. For example, Veer and Fathi (2011) used the commercial CFD software StarCCM+ to simulate the roll damping of a FPSO with bilge keels. In their research, the Volume of fluid (VOF) method was used to capture the free surface. The mesh was refined around the free surface and bilge keels. Even though the coarse mesh was used away from the hull, 2.7 million cells grid was used, which was very computing resource consuming.

## **2.2 Literature review of hybrid numerical models**

From the review about the conventional numerical models used in the simulation of wave-structure interactions, it can be seen that the potential model and the viscous model have their own advantages and disadvantages. By using the potential model, both efficiency and accuracy are high in the large-scale domain for wave generation and propagation. However, it is difficult to take viscous effects and vortex shedding into account. While by using the viscous model, the viscous effects can be considered in the vicinity of the floating structure. Nevertheless, the efficiency is low for the large computing domain. In recent years, to combine advantages of the potential model and the viscous model together, some potential viscous hybrid numerical models are established. In these hybrid models, the potential model is used in a large-scale domain for wave generation and propagation. The viscous model is only applied in a small-scale domain surrounding the floating structure. By using those hybrid models, both the computational precision and the computational efficiency can be guaranteed.



(a) The computational domain for the domain-decomposition model



(b) The computational domain for the function-decomposition model

Fig. 2.2.1 The hybrid numerical models

The potential viscous hybrid models can be classified into two groups depending on the coupling method. One is called domain-decomposition method (or zonal method), and the other is called function-decomposition method (or velocity-decomposition method) (Rosemurgy et al. 2012). In the domain-decomposition method, the potential model and the viscous model are applied separately in two domains including the potential domain and the viscous domain, respectively, described in Fig. 2.2.1 (a). Hence, a matching boundary exists between the potential domain and the viscous domain. Sometimes, for data exchange, an overlapped area can be used to replace the matching boundary. In the function-decomposition method, the potential solution covers the whole domain and the viscous model is only used in a small domain surrounding the floating structure. Thus, in the function-decomposition method, the viscous domain is often overlapped by the potential domain, shown in Fig. 2.2.1 (b). In the viscous domain, by decomposing velocity (sometimes also pressure) into the viscous part and the potential part, the viscous components are solved by the viscous model with potential components explicitly from the potential solution.

### 2.2.1 Hybrid numerical models based on domain-decomposition method

The domain-decomposition model came up from the Prandtl's boundary layer theory (Schlichting, 1968). In the boundary layer theory, the domain can be divided into two parts. Specifically, one is a thin viscous layer around the body where the viscous effects play the key role, and the other is away from the boundary layer where the flow is potential. In the

boundary layer, NS equations are simplified into the boundary layer equations. The method can be used to calculate the displacement thickness around the body in order to correct the potential solution outside the boundary layer. The boundary layer theory is widely used in aeronautics since 1960 (Dolling, 2001) as well as ship hydrodynamics. However, the boundary layer theory is not suitable if the boundary layer thickness is large, especially when the vorticity separation exists. When it happens, the NS equations cannot be simplified. To overcome this issue, the NS equations or RANS equations with the turbulence model are often used in the viscous sub domain, which not only contains the body, but also the wake area including vortices separation. That whether the feedback of the viscous solution is considered in the potential domain, classifies domain-decomposition models into the weak hybrid model and the strong hybrid model.

#### 2.2.1.1 The weak domain-decomposition hybrid models

For the weak domain-decomposition hybrid model, the potential solution is used to initiate and supply the boundary condition of the viscous domain. The data transfer is just one direction from the potential domain to the viscous domain. Thus, the weak hybrid model is also called one-way hybrid model. The influence of the viscous solution on the potential solution is not considered.

The waves shoaling and breaking near shore has been studied by using weak hybrid domain-decomposition models. For example, Guignard, et al. (1999) and Lachaume, et al. (2003) developed a weak FNPT NS-VOF hybrid model. In the domain-decomposition hybrid model, the wave generation and propagation was done in the FNPT domain. Then, close to wave breaking, the NS-VOF model was initiated by the FNPT solution. After that, the velocity on the lateral matching boundary in the NS-VOF domain was supplied by the FNPT solution. Later, the hybrid model was extended by Biaisser, et al. (2003, 2004) for modelling a three-dimensional solitary waves breaking on a slope. In this case, the FNPT solution was just used to initiate the NS-VOF domain. The no flow boundary condition was applied so that the matching boundary was far away from the sea shore. However, a large computing domain was used. Gilbert, et al. (2007) studied nonlinear-wave-forced sediment transport by coupling FNPT and NS-LES model. In the hybrid model, a numerical wave tank was established based on the FNPT model. The NS-LES domain was wrapped by the FNPT domain below the free surface. The FNPT solution provided the gradient of the dynamic pressure for the NS-LES solver, which was just regarded as a source term in momentum equations. Yan and Ma (2010) studied the interaction between the wind and the freak wave by using a model coupling QALE-FEM (a FNPT model) and StarCD (a NS-VOF model). The inlet boundary of the NS-VOF model was transiently specified by the simulation results of QALE-FEM. In the

simulation, the NS-VOF domain should be long enough to avoid the effects of reflection waves on the FNPT domain.

The weak hybrid domain-decomposition model is also employed to model wave-structure interactions. Corte and Grilli (2006) studied the extreme wave slamming on a fixed cylinder. In the research, the extreme waves were generated by a FNPT model. Then the NS-VOF domain was initiated and the boundary conditions in the NS-VOF model were specified by the FNPS solution. Finally, the cylinder slammed by extreme waves was simulated in the NS-VOF domain. However, to minimize the effects of the reflection waves on the FNPT model, the simulation in the NS\_VOF domain cannot last long.

As mentioned above, it indicates that the weak hybrid model is very effective if the viscous domain has little effect on the potential domain. However, such effect can be significant. For example, the reflection waves from the floating structure and the radiation wave due to the motion of the floating structure in the viscous domain will affect the incident waves in the potential domain. To achieve sufficient accuracy, one must use a damping zone near the interface between two domains to remove the reflection and radiation waves caused by the structures. Otherwise, simulation time in the viscous domain must be short (Guignard, 1999; Lachaume et al. 2003; Biaisser et al. 2003, 2004; Corte and Grilli 2006; Gilbert et al. 2007), or long computational viscous domain should be applied so that the simulation terminates before those waves reach the interface (Yan and Ma, 2010 ).

#### 2.2.1.2 The strong domain-decomposition hybrid models

To improve the weak hybrid domain-decomposition models, some strong domain-decomposition hybrid models are proposed and the floating body induced reflection and radiation waves in the viscous domain can be considered in the potential domain. The data transfer exists in two directions between the viscous domain and the potential domain. Thus, the strong domain-decomposition hybrid model is also called two-way hybrid model. The effects of the viscous solution on the potential solution are gain on the velocity potential or the normal derivative of it on the boundary condition of the potential solver. To achieve that, the overlap zones are used for data transfer between the potential domain and the viscous domain, which can be classified into the fixed mode (Sitanggang, et al. 2008; Kim, et al. 2010; and Guo et al. 2012) and the moving mode (Sriram, et al., 2014). In the overlap zone, one domain's boundary exists in the other domain's interior. By doing so, the boundary conditions are easily updated by the interpolation of corresponding values in the overlap zone.

The strong domain-decomposition hybrid model has been used for the simulation of offshore-to-coastline wave propagation. Sitanggang (2008) developed a Boussinesq and RANS-VOF

hybrid model, where the solitary waves or tsunami was generated by the Boussinesq model. Then, those waves propagated into RANS-VOF domain. Finally, wave breaking and shoaling happens in RANS-VOF domain. Kim, et al. (2010) proposed a strong FNPT and NS-VOF hybrid domain-decomposition model for simulations of random waves and similar strong domain-decomposition model was used by Guo et al. (2012). To simulate the wave breaking in seashore, Sriram, et al. (2014) developed a strong domain-decomposition model coupling a FNPT solver and a viscous solver called Improved Meshless Local Petrov Galerkin method with Rankine source solution (IMLPG\_R).

Strong domain-decomposition models are also used for the simulation of wave-structure interactions. Campana and Lalli (1992) simulated a submerged foil moving forward under free surface, where the free surface was simulated in the FNPT domain, while the foil and its wake were simulated in the RANS domain. A matching surface between two domains existed for data transfer on the boundary and an iterative procedure was required at every time step. Then, the same problem was studied by Iafrati and Campana (2003), where an overlapped zone was used to couple the potential domain and the viscous domain, based on Schwarz method (Widlund and Toselli, 2005). It was found that the iteration can be reduced, comparing with the matching surface used by Campana and Lalli, (1992).

Table 2.2.1 The category of the literatures about domain-decomposition method

Domain-decomposition models	Without a structure	With a structure
Weak domain- decomposition hybrid model	Guignard et al. (1999), Lachaume et al. (2003) Yan and Ma (2010) Biausser et al. (2003, 2004) Gilbert et al. (2007)	Corte and Grilli (2006)
Strong domain-decomposition hybrid model	Campana and Lalli (1992) Iafrati and Campana (2003) Kim et al. (2010) Guo et al. (2012) Sitanggang (2008) Sriram et al. (2014)	Zhang et al. (2013, 2014, 2015) Colicchio et al. (2006, 2010). Greco et al. (2007)

In addition, the strong domain-decomposition hybrid models are also used to simulate interactions between waves and surface piercing floating structures. For example, Colicchio et al. (2006, 2010) and Greco, et al. (2005) developed a FNPT and NS-Level Set domain-decomposition hybrid model to study green water on the deck of a ship. Zhang et al. (2013,

2014, 2015) developed a FNPT and RANS domain-decomposition hybrid model to study solitary waves impacting on a fixed cylinder.

From the above, it is found that by using the overlap zone, the two solvers can provide the boundary conditions for each other more conveniently. However, in strong domain-decomposition hybrid methods, the iteration between the potential domain and the viscous domain is often required, which affects the computational efficiency.

In summary, the mentioned literatures related with domain-decomposition models can be divided into two groups. One is with the floating structure, and the other is without the floating structure, described in Table 2.2.1. It can be seen that only a few works contain the floating structure. In these works, the surface-piercing structure is fixed. Even though strong coupling models can be used so that the effects of the viscous domain on the potential domain can be considered, the iteration is needed, which will reduce the computational efficiency. Thus, the function-decomposition model is proposed in order to avoid those drawbacks

### 2.2.2 Hybrid Numerical models based on the function-decomposition method

The function-decomposition method (also called velocity-decomposition method) is based on velocity decomposition, by which velocity is decomposed into different parts. Different mathematical models are used for solving different parts of velocity. The function-decomposition model is firstly used in the computing acoustics (Morino, et al. 1999 and Hafez, et al. 2007). In recent years, the function-decomposition method is also used in CFD. For wave-structure interactions, potential-viscous function-decomposition method is often used in the simulation.

In the potential-viscous function-decomposition model, the total velocity  $\mathbf{U}_{\text{total}}$  can be decomposed into two parts including the potential part  $\mathbf{U}_{\text{pot}}$  related with the gradient of the velocity potential  $\nabla\phi$  and the viscous part  $\mathbf{U}_{\text{vis}}$ , described as

$$\mathbf{U}_{\text{total}} = \mathbf{U}_{\text{pot}} + \mathbf{U}_{\text{vis}} = \nabla\phi + \mathbf{U}_{\text{vis}} \quad (2.2.1)$$

In the computing domain of the potential-viscous function-decomposition method, the potential model is used in the potential domain for  $\mathbf{U}_{\text{pot}}$ . In the viscous domain, the potential solution is used as the potential part explicitly. Meanwhile, the viscous parts including  $\mathbf{U}_{\text{vis}}$  are the only unknowns, which are solved by the viscous model. The viscous domain is often wrapped by the potential domain. The overlapped area is the whole viscous domain, where is also the final solution.

In order to study wave-induced sediment transport, some researchers (Grilli, et al. 2008; Harris and Grilli, 2010, 2012) developed a complementary NS-LES model by decomposing both the velocity  $U_i$  and the pressure  $p$  into an incident part ( $U_i^I$  for incident velocity and  $p^I$  for incident pressure) and a perturbation part ( $U_i^P$  for perturbation velocity and  $p^P$  for perturbation pressure) as  $U_i = U_i^I + U_i^P$  and  $p = p^I + p^P$ . And the original NS-LES equations are changed into the complementary NS-LES equations, i.e.,

$$\frac{\partial U_i^P}{\partial x_i} = 0 \quad (2.2.2)$$

$$\begin{aligned} \frac{\partial U_i^P}{\partial t} + \left( U_j^I + U_j^P - \frac{\partial v_T}{\partial x_j} \right) \frac{\partial U_i^P}{\partial x_j} + \frac{1}{\rho} \frac{\partial p^P}{\partial x_i} = & -U_j^P \frac{\partial U_i^I}{\partial x_j} + (v + v_T) \frac{\partial^2 U_i^P}{\partial x_j \partial x_j} + \frac{\partial v_T}{\partial x_j} \left( \frac{\partial U_i^I}{\partial x_j} + \frac{\partial U_j^I}{\partial x_i} + \right. \\ & \left. \frac{\partial U_j^P}{\partial x_i} \right) \end{aligned} \quad (2.2.3)$$

In (2.2.3), the incident part including  $U_i^I$  and  $p^I$  is explicitly provided by the FNPT solver. In the complementary NS-LES equations, the independent unknown variables are  $U_i^P$  and  $U_j^P$ . It was concluded by Grilli, et al. (2008) that the hybrid FNPT complementary NS-LES model can avoid the numerical instability that existed in the domain-decomposition method. Later, Janssen, et al. (2010) hybrid an FNPT model and a complementary NS model for the simulation of wave breaking, where the complementary NS equations were solved by using a particle based Lattice Boltzmann model.

Kim, et al. (2005) developed a complementary RANS model based on the function-decomposition method. By decomposing the total velocity and the total pressure, the original RANS equations were changed into the complementary RANS equations, which were similar as those proposed by Grilli, (2008). By the complementary RANS model, the uniform flow passing a wing section was studied. The velocity potential was obtained from a potential model with the domain covering the wing section. However, it was found that the complementary RANS model cannot provide computing savings. Besides that, it was indicated that the computing domain could be reduced, if viscous effects were involved in the potential solution. Rosemurgy, et al. (2012) applied the similar coupling numerical method for predicting the resistance of the ship. A free surface Green function (FSGF) was used to calculate the potential velocity. The RANS equations with  $k - \omega$  SST turbulence model were used for the viscous domain. The boundary condition of velocity was determined by the FSGF model. In the coupling model, only a linear free surface condition was used on the free surface. Subsequently, Edmund, et al. (2013) used viscous potential velocity instead of the potential velocity, while traditional RANS equations were used in the computing domain. Even though the function-decomposition method was not used directly in control equations,

the boundary condition on the inlet and far-field boundary can be considered to satisfy the velocity decomposition method by  $\mathbf{u} = \nabla\phi + \mathbf{w}$  and  $\mathbf{w} = \mathbf{0}$  ( $\mathbf{w}$  is the viscous part of the velocity).

Some researchers (Ferrant, et al. 2008, 2013; Luquest, et al. 2003, 2004, 2005, 2007; Monroy, et al. 2009, 2011; Gentaz, 2004) developed a complementary RANS solver for free surface piercing problems. The corresponding complementary RANS equations were similar as those developed by Grilli, et al. (2008). The difference was that the free surface piercing was considered in the simulation. Thus, the free surface tracking method should be considered. In this model, the free surface is tracked by moving mesh under the kinematic free surface boundary condition and the dynamic free surface boundary condition is described as

$$\frac{\partial h}{\partial t} + u_1 \frac{\partial h}{\partial x_1} + u_2 \frac{\partial h}{\partial x_2} = u_3 \quad (2.2.4)$$

$$P - \rho gh + 2\rho(v + v_t) \frac{\partial u_i}{\partial x_j} n_i n_j = 0 \quad (2.2.5)$$

$$\begin{cases} (n_j t_{1i} + n_i t_{1j}) \frac{\partial u_i}{\partial x_j} = 0 \\ (n_j t_{2i} + n_i t_{2j}) \frac{\partial u_i}{\partial x_j} = 0 \end{cases} \quad (2.2.6)$$

In the above equations,  $n_i$  are components of the normal vector  $\mathbf{n}$  pointing outside of the free surface.  $t_{1i}$  and  $t_{2i}$  are components of the two tangential vectors  $\mathbf{t}_1$  and  $\mathbf{t}_2$ . The wave elevation  $h$  is along  $x_3$ . By decomposing the velocity  $u_i$ , the pressure  $P$ , and the wave elevation  $h$  as  $u_i = u_i^I + u_i^D$ ,  $P = P_I + P_D$ , and,  $h = h_I + h_D$ , the complementary kinematic free surface boundary condition is described as

$$\frac{\partial h_D}{\partial t} + u_1^D \left( \frac{\partial h_D}{\partial x_1} + \frac{\partial h_I}{\partial x_1} \right) + u_2^D \left( \frac{\partial h_D}{\partial x_2} + \frac{\partial h_I}{\partial x_2} \right) - u_3^D = u_3^I - \frac{\partial h_I}{\partial t} - u_1^I \left( \frac{\partial h_D}{\partial x_1} + \frac{\partial h_I}{\partial x_1} \right) - u_2^I \left( \frac{\partial h_D}{\partial x_2} + \frac{\partial h_I}{\partial x_2} \right) \quad (2.2.7)$$

The complementary free surface dynamic condition in the normal direction is obtained as

$$P_D - \rho gh_D = \rho gh_I - P_I - 2\rho(v + v_t) \left( \frac{\partial u_i^I}{\partial x_j} + \frac{\partial u_i^D}{\partial x_j} \right) n_i n_j \quad (2.2.8)$$

The complementary surface dynamic conditions in the tangential directions are gain as

$$\begin{cases} (n_j t_{1i} + n_i t_{1j}) \frac{\partial u_i^D}{\partial x_j} = -(n_j t_{1i} + n_i t_{1j}) \frac{\partial u_i^I}{\partial x_j} \\ (n_j t_{2i} + n_i t_{2j}) \frac{\partial u_i^D}{\partial x_j} = -(n_j t_{2i} + n_i t_{2j}) \frac{\partial u_i^I}{\partial x_j} \end{cases} \quad (2.2.9)$$



In the function-decomposition model, the potential parts including the potential velocity  $u_i^I$ , the potential pressure  $P_I$ , and the potential wave elevation  $h_I$  are provided from the potential wave propagation model. Two kinds of potential models are used in the function-decomposition method including the stream function wave model and the high order spectral model. It should be noted that the two potential models are just about waves without the floating structure, which means the reflected wave is not considered in the potential solution. On the far field boundary, the diffracted velocity  $u_i^D$  is set as  $u_i^D = 0$  with a stretching of the grid. By this, the wave reflections can be prevented and the diffracted wave field decays to zero far from the structure. Nevertheless, the domain cannot be reduced efficiently, because the reflected waves by the floating structure are not contained in the potential solution.

Alternatively, Kenton, et al. (2003) and Huijsmans, et al. (2005) developed a potential viscous function-decomposition hybrid model to study the roll motion of a floating structure. In their method, the total velocity  $\mathbf{u}$  can be decomposed into two parts including the gradient of the velocity potential  $\nabla\phi$  and the viscous velocity  $\mathbf{u}_R$ , described as

$$\mathbf{u} = \nabla\phi + \mathbf{u}_R \quad (2.2.10)$$

The conventional NS equations can be changed from

$$\nabla \cdot \mathbf{u} = 0 \quad (2.2.11)$$

$$\frac{\partial \mathbf{u}}{\partial t} + (\mathbf{u} \cdot \nabla)\mathbf{u} = -\frac{\nabla P}{\rho} + \nu \nabla^2 \mathbf{u} + \mathbf{g} \quad (2.2.12)$$

into

$$\nabla \cdot \mathbf{u}_R = 0 \quad (2.2.13)$$

$$\frac{\partial \mathbf{u}_R}{\partial t} + ((\nabla\phi + \mathbf{u}_R) \cdot \nabla)\mathbf{u}_R + (\mathbf{u}_R \cdot \nabla)\nabla\phi = -\frac{\nabla P_R}{\rho} + \nu \nabla^2 \mathbf{u}_R \quad (2.2.14)$$

$$P_R = P + \rho \frac{\partial \phi}{\partial t} + \frac{1}{2} \rho (\nabla\phi \cdot \nabla\phi) - \rho g z \quad (2.2.15)$$

In equations (2.2.12) and (2.2.14),  $\nu$  is the viscosity of fluid. From above, it can be seen that in Kenton's model, only the velocity is decomposed. Unlike Grilli, et al. (2008), Kim, et al. (2005), and Ferrant, et al. (2013), the pressure  $P$  is not decomposed. Nevertheless, a new pressure  $P_R$  is used here containing the effects of the potential solution. In the hybrid model,  $\nabla\phi$  is obtained from the strip method, which is based on the 2D potential theory. Thus, the viscous part is just solved in several 2D domains. However, the mean free surface obtained in the strip method is used in the complementary NS domain. Therefore, only linear free surface boundary condition is applied. Due to the viscous effects, the hydrodynamic forces on the

ship section are different in two solvers, which means that the feedback of the viscous solution should be considered. Therefore, in every time step, an iterative process is required to obtain the final motion and hydrodynamic forces.

In summary, based on that whether the floating structure is considered in both the potential and the viscous domains, the works related with the function-decomposition model can be classified in Table 2.2.2.

From Table 2.2.2, it can be seen that most works are related with submerged structures. Even though some researchers (Ferrant, et al. 2008, 2013; Luquest, et al. 2003, 2004, 2005, 2007; Monroy, et al. 2009, 2011, Gentaz, L. et al. 2004) did simulations about the surface piercing floating structures, the floating structures were not considered in the potential domain. Thus, the reflection waves and radiation waves induced by the floating structures did not exist in the potential domain. So, the viscous domain must be large enough to contain the reflection and the radiation waves. Only Kenton, et al. (2003), Huijsmans, et al. (2005) and Rosemurgy, et al. (2012) considered the floating structure in both the potential domain and the viscous domain. Nevertheless, only linear free surface boundary condition was used.

Table 2.2.2 The category of the literatures about velocity decomposition method

			Potential model	
			With the structure	Without the structure
Viscous model with the structure	With the free surface piercing	Linear Incident waves	Kenton et al. (2003) Huijsmans et al. (2005) Rosemurgy et al. (2012)	None
		Non linear incident waves	None	Ferrant et al. (2008, 2013) Luquest et al. (2003, 2004, 2005, 2007) Monroy et al. (2009, 2011) Gentaz et al. (2004)
	Without the free surface piercing		Kim et al. (2005) Edmund et al. (2013)	Grilli et al. (2008) Harris and Grilli (2010, 2012) Janssen et al. (2010)

Moreover, so far as the author knows, domain-decomposition models and function-decomposition models are used independently in numerical simulations. By those hybrid numerical models, high computational efficiency and high computational precision are obtained. As a matter of fact, it can be imaged that if the domain-decomposition model and the function-decomposition model were combined, the computational efficiency could be further enhanced.

Thus, in this research, an Euler-viscous function-decomposition hybrid model is proposed, which is used to model interaction between waves and surface-piercing structure. The difference between the new function-decomposition hybrid model and the other existing models lies in that the floating structure exists in both the Euler domain and the viscous domain. So, the diffraction and reflection velocity due to the floating structure can be considered not only in the viscous domain, but also in the Euler domain. By doing so, the computational efficiency can be significantly improved. Furthermore, the function-decomposition Euler-viscous hybrid model is extended to be hybrid with a potential model by using the domain-decomposition method. The wave generation and propagation is modelled in the potential domain. By combining the function-decomposition method and the domain-decomposition method, the computational efficiency of the proposed model can be further enhanced.

### **2.3 Literature review of OpenFOAM for wave-structure interactions**

OpenFOAM is a powerful tool for the simulation of wave structure interactions. Many validations have been done for wave structure interactions by the comparison between the simulation results and hydrodynamic experiments. Gatin et al. (2018) validated the green sea simulations. Chen's study (2014) indicated that OpenFOAM can be used for simulating non-linear waves and structure interactions accurately to 4<sup>th</sup> order harmonic capture. Besides wave fixed-structure interactions, Chen (2016) also simulated free rolling of a floating structure in regular waves. Chen's research (2018) showed that OpenFOAM is capable to tackle wave induced fluid-structure interactions. Bruinsma et al. (2016) indicated that 6DOF motion of a floating structure under waves can be predicted accurately by OpenFOAM. Hu et al. (2016) simulated extreme waves and wave-structure interaction by OpenFOAM and the simulation results matched well with the experimental results. Higuera et al. (2013) implemented specific boundary condition for piston-like wave generation module and active absorbing wave module, which are validated by theoretical results and experimental results.

OpenFOAM has been used for the simulation of wave structure interaction in ocean engineering and ship engineering. In ocean engineering, some researchers studied Wave Energy Converters (WEC) by OpenFOAM. Palm et al. (2016) computed the motion of a

floating WEC coupled with mooring analysis. Sjökvist et al. (2017) simulated point-absorbing WEC in extreme waves. Iturrioz et al. (2015) simulated an Oscillating Water Column (OWC) and validated the numerical results with laboratory experiments. Vyzikas et al. (2016) investigated the behaviour and the performance of OWCs in different alternative design concepts. Schmitt et al. (2015) used studied OWC in significant wave. Ransley et al. (2017) simulated a WEC device called Wave star in extreme seas and shows good quality of numerical results comparing with the experimental results. In ship engineering, Jiang et al. (2018) studied wave resonance in the narrow gap between two non-identical boxes. Moradi et al. (2016) studied the effects of water depth on the resonance of trapped water between two bodies. Liu et al. (2017) did an accurate numerical study of a floating offshore wind turbine system. A numerical simulation of a flexible barge (Seng et al., 2014) is done and validated by corresponding experiments. Sigmund et al. (2018) investigated the added resistance of different ship types in short and long waves by numerical simulations (OpenFOAM), which matched well with the experiment results. Lavrov et al. (2017) investigated viscous unsteady properties of three different sections of a container ship.

For simulating wave structure interactions, wave generation and absorption are two important aspects, which can be achieved by two techniques including free surface capturing method and free surface tracking method. In OpenFOAM, free surface capturing method is often used for wave generation and absorption, in which the phase of fluid is represented by a scalar called phase volume ranging from 0 to 1. Specifically, the phase volume of water is 1 and the phase volume of air is 0. For wave generation, the phase volume and velocity can be prescribed in the boundary, based on wave theories. Many modules have been developed for prescribing the incident waves, among which waves2Foam (Jacobsen, 2012) is a popular third-party module that have been validated by many researchers for wave-structure interaction (Jose, 2017; Sjökvist, 2017; Palm, 2016; Hu, 2016; Chen, 2018; Teng, 2017; Bruinsma, 2016; Sun, 2016; Moradi, 2016; Vyzikas, 2016; Ransley, 2017). Besides prescribing incident waves on boundary, dynamic mesh is often used to simulate the real wave maker (Martínez-Ferrer, 2018; Sigmund, 2018). Similar as wave generation, waves2Foam can also supply wave relaxation zone for wave absorption. By simulating real wave makers, dynamic mesh is also used for absorbing waves actively (Higuera, 2013). Although dynamic mesh can be used for wave generation and absorbing, numerical instability is often induced. Thus, incident waves prescribing and wave relaxation zone is chosen for wave generation and absorbing. Finally, waves2Foam is used in the research for wave generation and absorption.

## **Chapter 3 An Euler-viscous hybrid model for interaction of a surface-piercing fixed structure with waves**

In this section, an Euler-Viscous hybrid solver is developed by the function-decomposition method for the simulation of wave-fixed structure interactions. The Euler-viscous hybrid solver contains two parts. One part is a two-phase Euler solver, where the viscous effects are neglected. The other part is a so called complementary RANS solver (two-phase), in which viscous effects and turbulence are considered. In fact, the complementary RANS solver is derived from the conventional RANS solver, by functionally decomposing both velocity and pressure into the Euler components and complementary components. In the complementary RANS model, the Euler components are explicit from the Euler solution. The complementary components are unknown independent variables. Correspondingly, complementary turbulence models are proposed by the function-decomposition method. For the Euler-viscous hybrid model, an interpolation process is required for the data transition from the Euler domain into the viscous domain. Besides that, special boundary conditions should be proposed in the viscous domain for the complementary RANS solver. In addition, a transition zone scheme is used for dissipating the viscous effects at the boundaries of the viscous domain. Furthermore, the transition zone is also applied to keep the free surface consistent. Finally, a solution procedure is established for the Euler-viscous hybrid model.

### **3.1 The mathematical formulations**

Two kinds of solvers are described in detail. Firstly, the conventional two-phase Euler solver is given. Secondly, the complementary two-phase RANS solver is derived from the conventional RANS solver. The corresponding complementary turbulence model used in the RANS solver is also discussed.

#### **3.1.1 The governing equations of the two-phase Euler solver**

The two-phase Euler solver is used in the Euler domain. Both viscous effects and turbulent effects are neglected in the model. The governing equations of the Euler solver is described as below

$$\nabla \cdot (\mathbf{U}^I) = 0 \quad (3.1.1)$$

$$\frac{\partial(\rho' \mathbf{U}^I)}{\partial t} + (\mathbf{U}^I \cdot \nabla)(\rho' \mathbf{U}^I) = -\nabla(p^I) + \rho' \mathbf{g} \quad (3.1.2)$$

In these equations,  $\mathbf{U}^I$  is the velocity and  $p^I$  is the pressure.  $\rho'$  is the density of the fluid in the Euler computing domain, which is calculated by  $\rho' = \gamma' \cdot \rho_{\text{water}} + (1 - \gamma') \cdot \rho_{\text{air}}$ .  $\rho_{\text{water}}$  and  $\rho_{\text{air}}$  are density of water ( $1000 \text{ kg/m}^3$ ) and air ( $1 \text{ kg/m}^3$ ).  $\gamma'$  represents the volume fraction of the fluid in

the Euler domain, which is 1 and 0 for water and air respectively.  $\mathbf{g}$  is the acceleration induced by gravity.

The free surface is captured by VOF (Volume of Fraction) model (Weller, H. G. 2002), where the volume fraction of fluid is the only unknown variable as  $\gamma'$ . The governing equation of the VOF model is shown as below

$$\frac{\partial \gamma'}{\partial t} + \nabla \cdot (\gamma' \mathbf{U}^I) = 0 \quad (3.1.3)$$

### 3.1.2 The governing equations of the two-phase complementary RANS solver

In the viscous domain, the complementary RANS equations are derived from the conventional RANS equations, where both viscosity and turbulence are considered.

The basic idea of the complementary RANS equations stems from decomposing of the unknown variables in the conventional RANS equations. By the function-decomposition method, both the velocity and the pressure can be divided into two components including the Euler component and the complementary component, which is described below

$$\mathbf{U} = \mathbf{U}^I + \mathbf{U}^D \quad (3.1.4)$$

$$p = p^I + p^D \quad (3.1.5)$$

In equation (3.1.4) and equation (3.1.5),  $\mathbf{U}^I$  and  $p^I$  is the solution of the Euler solver described before. Both  $\mathbf{U}^D$  and  $p^D$  are the unknown variables in the complementary RANS equations.

By decomposing the velocity  $\mathbf{U}$  into the Euler part  $\mathbf{U}^I$  and the complementary part  $\mathbf{U}^D$ , the continuity equation is changed from  $\nabla \cdot (\mathbf{U}) = 0$  into

$$\nabla \cdot (\mathbf{U}^I) + \nabla \cdot (\mathbf{U}^D) = 0 \quad (3.1.6)$$

Then, similarly, by decomposing of velocity and pressure, the conventional momentum equation is changed from

$$\frac{\partial(\rho \mathbf{U})}{\partial t} + (\mathbf{U} \cdot \nabla)(\rho \mathbf{U}) = -\nabla(p) + \rho \mathbf{g} + \nabla \cdot (\mu_t \nabla \mathbf{U})$$

into

$$\begin{aligned} \frac{\partial(\rho \mathbf{U}^D)}{\partial t} + [(\mathbf{U}^I \cdot \nabla) + (\mathbf{U}^D \cdot \nabla)](\rho \mathbf{U}^D) - \nabla \cdot (\mu_t \nabla \mathbf{U}^D) + \frac{\partial(\rho \mathbf{U}^I)}{\partial t} + [(\mathbf{U}^I \cdot \nabla) + (\mathbf{U}^D \cdot \nabla)](\rho \mathbf{U}^I) - \nabla \cdot (\mu_t \nabla \mathbf{U}^I) = -\nabla(p^I) - \nabla(p^D) + \rho \mathbf{g} \end{aligned} \quad (3.1.7)$$

In the complementary momentum equations,  $\mu_t$  is the total viscosity, which is described as  $\mu_t = \mu_f + \mu_a$ .  $\mu_f$  is the fluid viscosity, calculated by  $\mu_f = \gamma \cdot \mu_f^{\text{water}} + (1 - \gamma) \cdot \mu_f^{\text{air}}$ .  $\mu_f^{\text{water}}$  and  $\mu_f^{\text{air}}$  are viscosity of water and air.  $\mu_a$  is the turbulence viscosity, determined by the turbulence model.  $\gamma$  represents the volume fraction of fluid in the viscous domain, which is 1 and 0 for water and air respectively.  $\rho$  is the density of the fluid, which is gain by  $\rho = \gamma \cdot \rho_{\text{water}} + (1 - \gamma) \cdot \rho_{\text{air}}$ .

Even though  $\frac{\partial(\rho \mathbf{U}^I)}{\partial t} + (\mathbf{U}^I \cdot \nabla)(\rho \mathbf{U}^I) = -\nabla(p^I) + \rho' \mathbf{g}$  can be found in Equation (3.1.1), those terms including  $\frac{\partial \rho \mathbf{U}^I}{\partial t}$ ,  $(\mathbf{U}^I \cdot \nabla)(\rho \mathbf{U}^I)$ ,  $-\nabla(p^I)$ , and  $\rho \mathbf{g}$  cannot be cancelled. That's because the free surface is different in the Euler domain and in the viscous domain, especially around the floating structure. In the two-phase model, the density is determined by the free surface. Thus, the density in the Euler domain is different from that in the viscous domain.

The free surface in the viscous domain is also tracked by the VOF model, which is described as below

$$\frac{\partial \gamma}{\partial t} + \nabla \cdot [\gamma(\mathbf{U}^I + \mathbf{U}^D)] = 0 \quad (3.1.8)$$

In equation (3.1.7), the turbulence viscosity  $\mu_a$  is determined by the turbulence model. In the complementary RANS model, the turbulence model is also derived from the conventional turbulence model by decomposing the velocity. Taking Re Normalisation Group (RNG) k epsilon model for instance, by dividing the velocity  $\mathbf{U}$  into  $\mathbf{U}^I$  and  $\mathbf{U}^D$ , the conventional RNG k epsilon turbulence model (Yakhot, V., 1992) for the incompressible flow can be changed from

$$\frac{\partial k}{\partial t} + \nabla \cdot (\mathbf{U}k) = \nabla \cdot \left[ \left( \mu + \frac{\mu_t}{\sigma_k} \right) \nabla k \right] + G - \varepsilon$$

$$\frac{\partial \varepsilon}{\partial t} + \nabla \cdot (\mathbf{U}\varepsilon) = \nabla \cdot \left[ \left( \mu + \frac{\mu_t}{\sigma_\varepsilon} \right) \nabla \varepsilon \right] + (C_{1\varepsilon} - R) \cdot G \cdot \frac{\varepsilon}{k} - C_{1\varepsilon} \cdot \frac{\varepsilon^2}{k}$$

into

$$\frac{\partial k}{\partial t} + \nabla \cdot [(\mathbf{U}^I + \mathbf{U}^D) \cdot k] = \nabla \cdot \left[ \left( \mu + \frac{\mu_t}{\sigma_k} \right) \nabla k \right] + G - \varepsilon \quad (3.1.9)$$

$$\frac{\partial \varepsilon}{\partial t} + \nabla \cdot [(\mathbf{U}^I + \mathbf{U}^D) \cdot \varepsilon] = \nabla \cdot \left[ \left( \mu + \frac{\mu_t}{\sigma_\varepsilon} \right) \nabla \varepsilon \right] + (C_{1\varepsilon} - R) \cdot G \cdot \frac{\varepsilon}{k} - C_{2\varepsilon} \cdot \frac{\varepsilon^2}{k} \quad (3.1.10)$$

In the complementary RNG k epsilon model, some constants are described as below  $\sigma_k = 0.7194$ ,  $\sigma_\varepsilon = 0.7194$ ,  $C_{1\varepsilon} = 1.42$ ,  $C_{2\varepsilon} = 1.49$ .  $G$  is defined as  $G = \frac{1}{2} \mu_t \cdot |\nabla(\mathbf{U}^I + \mathbf{U}^D)| +$

$[\nabla(\mathbf{U}^I + \mathbf{U}^D)]^T]^2$ . R is determined by  $R = \frac{\eta(1-\eta/\eta_0)}{1+\beta\eta^3}$ ,  $\eta = \frac{\nabla(\mathbf{U}^I + \mathbf{U}^D) + [\nabla(\mathbf{U}^I + \mathbf{U}^D)]^T}{\varepsilon} \mathbf{k}$ ,  $\eta_0=4.38$ , and  $\beta=0.012$ .

### 3.2 The numerical method

In the research, the open-source computational fluid dynamics software OpenFOAM is used. In OpenFOAM, the finite volume method is used for the space domain discretization. The governing equations are discretized in space domain over the control volume. The unstructured mesh (Jasak, H. et al. 2007) is used in OpenFOAM. Furthermore, the control volume can be arbitrary polygon volume, which cannot be overlapped with neighbour control volumes.

Momentum equations including (3.1.1) and (3.1.7) can be multiplied on both sides over a small control volume. Then, by Gauss's theorem, the integration over a control volume can be changed into the integration over surfaces of the control volume (Gauss scheme). After that, temporal terms including  $\frac{\partial(\rho\mathbf{U}^D)}{\partial t}$ ,  $\frac{\partial(\rho\mathbf{U}^I)}{\partial t}$ , and  $\frac{\partial(\rho'\mathbf{U}^I)}{\partial t}$  are discretized by fully implicit scheme (Euler scheme). Convective terms including  $[(\mathbf{U}^I \cdot \nabla) + (\mathbf{U}^D \cdot \nabla)](\rho\mathbf{U}^D)$ ,  $[(\mathbf{U}^I \cdot \nabla) + (\mathbf{U}^D \cdot \nabla)](\rho\mathbf{U}^I)$ , and  $(\mathbf{U}^I \cdot \nabla)(\rho'\mathbf{U}^I)$  are discretized by high order upwind scheme (limitedLinearV scheme). Diffusive terms including  $\nabla \cdot (\mu_t \nabla \mathbf{U}^D)$  and  $\nabla \cdot (\mu_t \nabla \mathbf{U}^I)$  are discretized by central scheme (linear scheme). Finally, momentum equations are transformed into linear equations as

$$A_c^U \mathbf{U}_c + \sum_n A_n^U \mathbf{U}_n = \mathbf{S}_c^U \quad (3.2.1)$$

In linear equations (3.2.1),  $\mathbf{U}_c$  is the unknown velocity ( $\mathbf{U}^I$  for the Euler solver and  $\mathbf{U}^D$  for the complementary RANS solver) at the control volume  $c$ .  $\mathbf{U}_n$  is the unknown velocity at neighbour volumes of the control volume  $c$ .  $A_c^U$  and  $A_n^U$  are coefficients related with flux terms, convective terms on the faces of the control volume  $c$  and temporal terms.  $\mathbf{S}_c^U$  is the source term, which is related with the known velocity terms, pressure terms, and temporal terms. Then, by solving a series of linear equations on all of control volumes, momentum equations are solved and unknown velocity can be obtained.

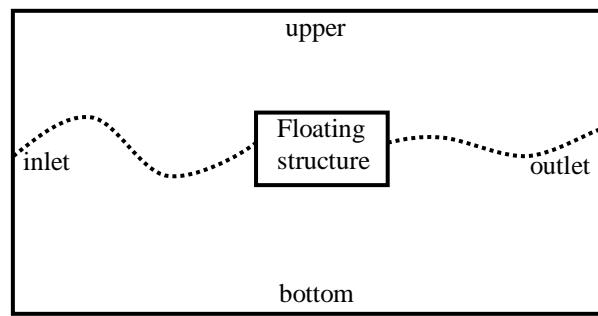
By using half-discretized momentum equations, the flux on the faces of a control volume can be represented by an equation with the divergence of pressure. Then, the equation of pressure is constructed by the continuity equation, in which the total flux is zero. By using the central scheme (linear scheme), the divergence of pressure is discretized. Finally, the linear equation related with pressure is obtained as

$$A_c^p p_c + \sum_n A_n^p p_n = S_c^p \quad (3.2.2)$$

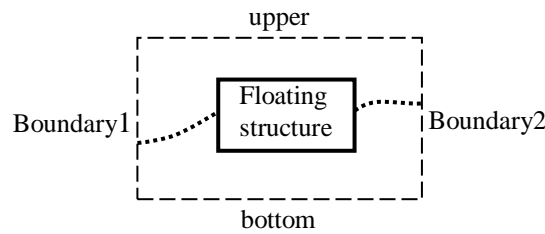


In equation (3.2.2), the unknown independent variable is  $p^I$  for the Euler solver and  $p^D$  for the Euler-viscous hybrid solver. The linear equation can be formed by  $p_c$  at the control volume with  $p_n$  at the neighbours of the control volume.  $A^p_c$  and  $A^p_n$  are coefficients for  $p^D_c$  and  $p^D_n$ , respectively. In OpenFOAM, pressure is collocated with velocity, at the centre of the control volume. The problem induced by the collocated pressure (Vuorinen, et al. 2014) and velocity can be solved by Rhie-Chow method (Kärholm, 2006).

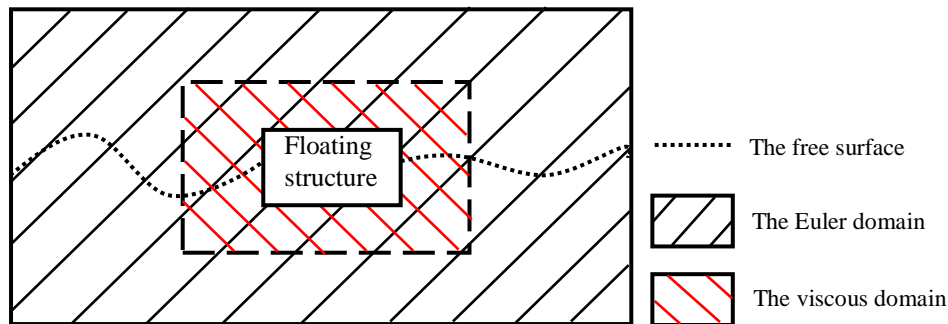
The PISO algorithm (Morgan and Zang, 2011) is used for solving the hybrid equation of momentum equations (3.2.1) and pressure equation (3.2.2). More details can be found in Morgan and Zang (2011), which is omitted here for brevity.



(a) The Euler computing domain



(b) The viscous computing domain



(c) The overlap of the Euler computing domain and the viscous computing domain

Fig. 3.3.1 The computational domain for the Euler-viscous hybrid model

### 3.3 The computational domain for the Euler-viscous hybrid solver

The mathematical formulations are described in section 3.1. Comparing with the conventional RANS solver, the Euler-viscous hybrid solver contains two models including the two-phase Euler model and the two-phase complementary RANS model. Correspondingly, an Euler domain and a viscous domain are used for the Euler model and the complementary RANS model, respectively. The Euler model is solved in a large computing domain, which is shown in Fig. 3.3.1 (a). Comparing with the Euler domain, the viscous domain is smaller for the complementary RANS model, which is shown in Fig. 3.3.1 (b). Free surface is captured in both two domains. Besides that, a fixed structure exists in both the Euler domain and the viscous domain.

It is shown in Fig. 3.3.1 (c) that the Euler domain and the viscous domain are overlapped. During the simulation, the solution of the two-phase Euler model can be transmitted into the viscous domain. Furthermore, the overlapped zone is the whole viscous domain. It should be noted that the floating structure exists in both domains, which is different from the other function-decomposition methods proposed so far. By doing this, the reflection and diffraction waves induced by the floating structure can be considered in the Euler domain, hereafter be transmitted into the viscous domain. Therefore, the size of the viscous domain can be reduced remarkably.

### 3.4 The boundary conditions

The boundary conditions play a crucial role in the numerical simulation. By using the suitable boundary conditions, the reasonable simulation results can be obtained. Because two computational domains are used for the Euler-viscous hybrid solver, the boundary conditions are more complex than those for the conventional RANS solver. Especially in the viscous domain, the boundary conditions should be treated appropriately.

#### 3.4.1 The boundary condition in the Euler domain

In the Euler domain, the boundary conditions of the velocity  $\mathbf{U}^I$  and volume fraction  $\alpha'$  are described on different boundaries as below.

On the inlet boundary,  $\mathbf{U}^I$  and  $\gamma'$  should be set by incident waves, which is described as

$$\mathbf{U}^I = \mathbf{U}_{in}^I, \text{ and } \gamma' = \gamma_{in}^I \quad (3.4.1)$$

$\mathbf{U}_{in}^I$  and  $\gamma_{in}^I$  are velocity and volume fraction provided by analytical wave solutions depending on incident wave conditions, e.g., the first order stokes wave solution for modelling small steepness waves or the fifth order stokes wave solution for moderate steepness waves.

On the rigid boundaries such as bottom and structure, the wall boundary condition should be satisfied, i.e., the slip wall boundary where the fluid particle cannot go through the wall. Specifically, the velocity  $\mathbf{U}^I$  can be divided into the tangential part  $(\mathbf{U}^I \cdot \mathbf{t})\mathbf{t}$  and the normal part  $(\mathbf{U}^I \cdot \mathbf{n})\mathbf{n}$  on the boundary and the normal part  $(\mathbf{U}^I \cdot \mathbf{n})$  should be zero on the rigid boundaries. In addition, the normal gradient of the tangential part  $(\mathbf{U}^I \cdot \mathbf{t})\mathbf{t}$  should be zero, as well as the gradient of volume fraction  $\gamma'$ . Finally, the boundary condition on the bottom, structure and wall boundary is described as

$$\mathbf{U}^I = (\mathbf{U}_{nbr}^I \cdot \mathbf{t})\mathbf{t} \text{ and } \frac{\partial \gamma'}{\partial \mathbf{n}} = 0 \quad (3.4.2)$$

where  $\mathbf{U}_{nbr}^I$  is the velocity on the neighbour volume of the boundary. Thus,  $\mathbf{U}^I$  is set by the tangential part of  $\mathbf{U}_{nbr}^I$ .

On the upper boundary,  $\mathbf{U}^I$  and  $\gamma'$  are determined by the direction of the flux, which is described as below

$$\left\{ \begin{array}{l} \frac{\partial \mathbf{U}^I}{\partial \mathbf{n}} = 0 \text{ } (\mathbf{U}^I \cdot \mathbf{S}_f > 0) \\ \mathbf{U}^I = (\mathbf{n} \otimes \mathbf{n}) \cdot \mathbf{U}_{nbr}^I \text{ } (\mathbf{U}^I \cdot \mathbf{S}_f < 0) \end{array} \right. \text{ and } \left\{ \begin{array}{l} \frac{\partial \gamma'}{\partial \mathbf{n}} = 0 \text{ } (\mathbf{U}^I \cdot \mathbf{S}_f > 0) \\ \gamma' = 0 \text{ } (\mathbf{U}^I \cdot \mathbf{S}_f < 0) \end{array} \right. \quad (3.4.3)$$

In (3.4.3), the flux on the boundary is  $\mathbf{U}^I \cdot \mathbf{S}_f$ , where  $\mathbf{S}_f$  is the area vector with the magnitude of area and normal direction. As flux flows into the upper boundary ( $\mathbf{U}^I \cdot \mathbf{S}_f < 0$ ), the velocity is equal to the normal part of the velocity in the neighbour volume of the boundary, while only air can flow into the neighbour volume ( $\gamma' = 0$ ). On the contrary ( $\mathbf{U}^I \cdot \mathbf{S}_f > 0$ ), the normal zero gradient should be satisfied for both the velocity  $\mathbf{U}^I$  and volume fraction  $\gamma'$ .

On the outlet boundary, the wall boundary condition should be satisfied with the help of the relaxation zone, which is often used in the numerical wave tank. The relaxation zone is used for absorbing the diffraction waves by damping the velocity and volume fraction, which is achieved in waves2Foam.

### 3.4.2 The boundary condition in the viscous domain

In the viscous domain, the boundary conditions are related with those in the Euler domain. The complementary velocity  $\mathbf{U}^D$ , and volume fraction  $\gamma$  should also be defined. Besides, since the turbulence is considered in the viscous domain, the boundary conditions of turbulence should also be considered.

On the boundaries far away from the floating structure such as boundary 1, boundary 2, upper, and bottom, the viscous effects must be zero, due to the dissipation of the viscous effects.

Therefore, the complementary velocity  $\mathbf{U}^D$  should be set as zero. Apart from that, to keep the free surface consistent in two computational domains, the volume fraction  $\gamma$  is the same as that ( $\gamma'$ ) in the Euler domain. Finally, the boundary condition can be described as

$$\mathbf{U}^D = \mathbf{0} \text{ and } \gamma = \gamma' \quad (3.4.4)$$

For the turbulence model, taking k- $\epsilon$  two-equation model for instance, due to the dissipation of the viscous effects, the turbulence should be small and fully developed. Therefore, far away from the floating structure, zero normal gradient boundary condition is applied, which can be described as

$$\frac{\partial k}{\partial \mathbf{n}} = 0 \text{ and } \frac{\partial \epsilon}{\partial \mathbf{n}} = 0 \quad (3.4.5)$$

On the fixed structure, the total velocity should be zero, which satisfies the no slip boundary condition in the viscous domain. Therefore,  $\mathbf{U} = \mathbf{U}^I + \mathbf{U}^D = \mathbf{0}$  should be guaranteed. Meanwhile, the volume fraction should also fulfil zero normal gradient condition. Thus, the boundary condition is described as

$$\mathbf{U}^D = -\mathbf{U}^I \text{ and } \frac{\partial \gamma}{\partial \mathbf{n}} = 0 \quad (3.4.6)$$

For the turbulence model, the wall function is used on the fixed structure, which can be the same with that used for the conventional RANS solver.

### 3.5 The relaxing zone and the transition zone

For the simulation of wave-structure interactions, the relaxing zone is always employed by using the conventional RANS mode, which is mainly used to, firstly, damp the reflection waves from the structure, and, secondly, absorb waves at the end of the wave basin. Similarly, the relaxing zone is also required by the Euler solver for such purposes, i.e., to generate incident waves and damp the reflection waves close to the inlet boundary, meanwhile, absorb waves close to outlet boundary. Details about the relaxing zone are omitted here for brevity, since it is not the focus of this study.

In the viscous domain, in order to dissipate the viscous effects, the transition zone is applied far away from the floating structure. With the transition zone, the viscous effects can be diminished to zero, while the free surface in the Euler domain and in the viscous domain can remain consistent. The details of the transition zone are described in the subsections below.

### 3.5.1 The transition zone in the viscous domain

Two transitional zones are distributed in two zones close to two ends of the numerical wave tank including boundary 1 and boundary 2, as shown in Fig. 3.5.1. In the transition zone, both complementary velocity  $\mathbf{U}^D$  and volume fraction  $\gamma$  are relaxed by blending the simulation values with target values, which is described as

$$\begin{cases} \mathbf{U}^D_t = \mathbf{U}^D_{Target} * (1 - w) + \mathbf{U}^D_0 * w \\ \gamma_t = \gamma_{Target} * (1 - w) + \gamma_0 * w \end{cases} \quad (3.5.1)$$

In the formula (3.5.1),  $\mathbf{U}^D_t$  and  $\gamma_t$  are the final relaxing results at the current step  $t$ ;  $\mathbf{U}^D_0$  and  $\gamma_0$  are simulation values before transition;  $\mathbf{U}^D_{Target}$  and  $\gamma_{Target}$  are target values.  $\mathbf{U}^D_{Target}$  is set as  $\mathbf{U}^D_{Target} = \mathbf{0}$  so that the complementary velocity  $\mathbf{U}^D_t$  is damped to  $\mathbf{U}^D_t = \mathbf{0}$  on both boundary 1 and boundary 2.  $\gamma_{Target}$  is set by the volume fraction in the Euler domain  $\gamma'$ . By doing so, the volume fraction  $\gamma$  on both boundary 1 and boundary 2 in the viscous domain is set as the same value as the volume fraction  $\gamma'$  in the Euler domain, for keeping the free surface consistent in the Euler domain and viscous domain.  $w$  is the relaxation coefficient, which will be discussed in the following subsection.

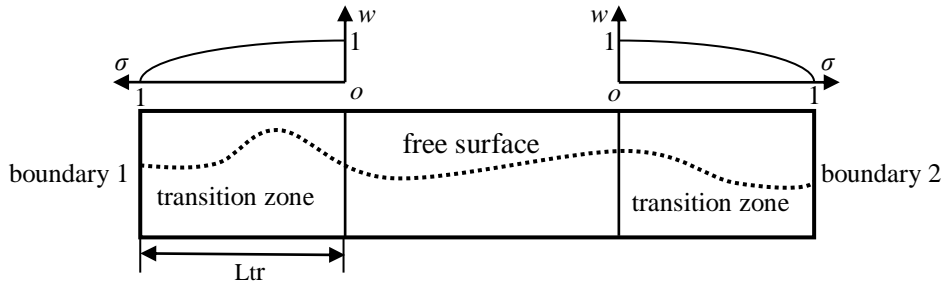


Fig. 3.5.1 The transition zone in the viscous domain

### 3.5.2 The relaxation method in the transition zone

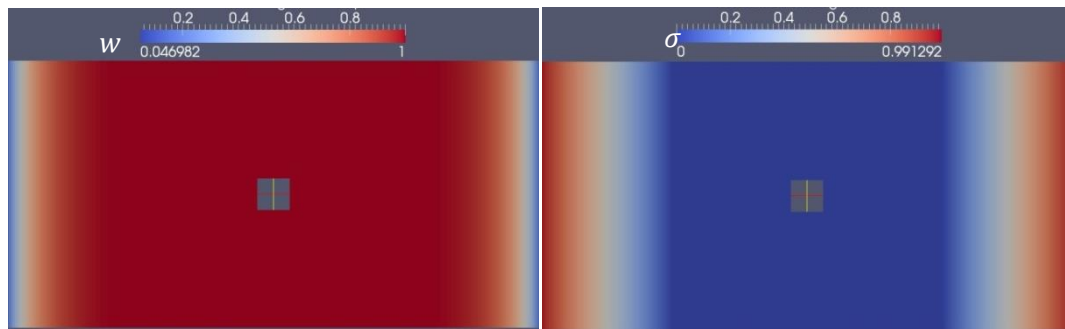
The relaxation coefficients  $w$  is defined as

$$w = 1 - \frac{e^{(\sigma^p)} - 1}{e - 1} \quad (3.5.2)$$

In the formula (3.5.2),  $p$  is a constant, which is 3.5 by numerical tests.  $\sigma$  is a parameter related with the coordinates of the points in the transition zone, which is given by

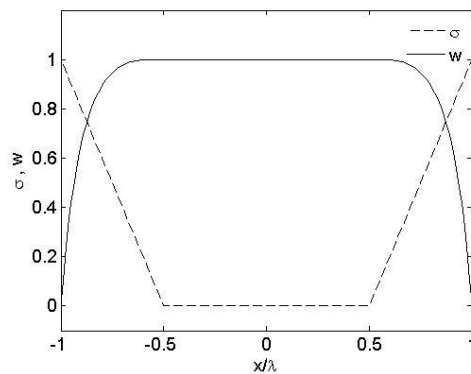
$$\sigma = \frac{|x_{point} - x_{boundary}|}{L_{tr}} \quad (3.5.3)$$

where  $x_{point}$  is x coordinate of the point in the transition zone.  $x_{boundary}$  is x coordinate of boundary 1 or boundary 2 depending on the location of  $x_{point}$ ,  $L_{tr}$  is the length of the transition zone. It is noticed that  $w$  is 0 on both boundary 1 and boundary 2 and it ranges from  $w=0$  to  $w=1$  smoothly along the transition zone. Correspondingly, in the viscous domain, on both boundary 1 and boundary 2,  $U_t^D$  can be set as  $U_t^D=0$  and  $\gamma$  can be set as  $\gamma=\gamma'$ . The transition of  $U^D$  and  $\gamma$  also depends on the variation of  $w$  and  $\sigma$ , which is described below.



(a)  $w$

(b)  $\sigma$



(c)  $w$  and  $\sigma$  change along the horizontal direction

Fig. 3.5.2 The transition zone in the viscous domain

Taking  $L_{tr} = \lambda/2$ ,  $x_{boundary1} = -\lambda$ , and  $x_{boundary2} = \lambda$  ( $\lambda$  is the wave length.) for instance,  $w$  and  $\sigma$  are distributed in a viscous domain ranging from 0 to 1 given that  $x \in [-\lambda, \lambda]$ , which are shown in Fig. 3.5.2 (a) and Fig. 3.5.2(b), respectively. Meanwhile, the relationship between  $w$  and  $\sigma$  is demonstrated in Fig. 3.5.2(c). It is noted that both  $w$  and  $\sigma$  change only along the horizontal direction, and, the values of  $w$  and  $\sigma$  are inversely distributed. By using this technique, it can guarantee that  $U_t^D=0$  and  $\gamma_t=\gamma'_t$  on both boundary 1 and boundary 2, while  $U_t^D=U_0^D$  and  $\gamma_t=\gamma'_0$  outside the transition zone as  $w=1$  and  $\sigma=0$ .

### 3.6 The interpolation technique

Due to different mesh used in the Euler domain and the viscous domain, an interpolation process is applied for transiting the data from the Euler domain to the viscous domain. Three

steps must be taken. Firstly, the target position in the viscous domain is found in the Euler domain. By the first step, the projection between the target cells in the viscous domain and the source cells in the Euler domain is established. Taking Fig. 3.6.1 for instance, the source position cell  $E_0$  that contains the target cell  $V_0$ 's centre is found. Secondly, search the Euler domain to find all the neighbour cells of the source cell, e.g., as shown in Fig. 3.6.1, cell  $E_1$ , cell  $E_2$ , cell  $E_3$ , and cell  $E_4$  are neighbour cells of cell  $E_0$ . In the final step, by using the values at the centres of the source cell and neighbour cells, the interpolation result on the target cell centre can be obtained.

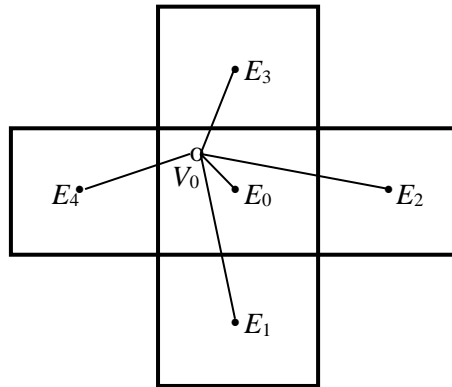


Fig. 3.6.1 The interpolation method

The interpolation formula can be described as

$$V_0 = \sum_{i=1}^n w_{0i} \cdot V_i \quad (3.6.1)$$

In the equation,  $V_0$  is the interpolation value on the target cell centre in the viscous domain.  $V_i$  ( $i=0 \dots n$ ) is the corresponding values on the source cell's centre and neighbour cells' centres in the Euler domain.  $w_{0i}$  is the weight coefficients for interpolation, which are given by

$$w_{0i} = \frac{1/l_{0i}}{\sum_{m=0}^n (1/l_{0m})} \quad (3.6.2)$$

where  $l_{0i}$  ( $i=0, \dots, n$ ) is the distance between the centres of the target cell centre in the viscous domain and the source cell in the Euler domain. It indicates that the weight coefficient varies inversely as the distance, which means that the contribution of the source cell goes down with the increasing of the distance.

### 3.7 The solution procedure of the Euler-viscous hybrid solver

In the Euler-viscous hybrid solver, the inlet boundary of the Euler domain is updated firstly, which can be supplied by a prescribed wave theory such as 1<sup>st</sup> order and 5<sup>th</sup> order Stokes waves etc. Then, the Euler equations and complementary RANS equations are solved subsequently. Meanwhile, the free surface is updated in the Euler domain and viscous domain,

respectively. During that, the interpolation process described in section 3.6 is required. The flow chart of the Euler-viscous hybrid solver is shown in the Fig. 3.7.1, which can be demonstrated as below:

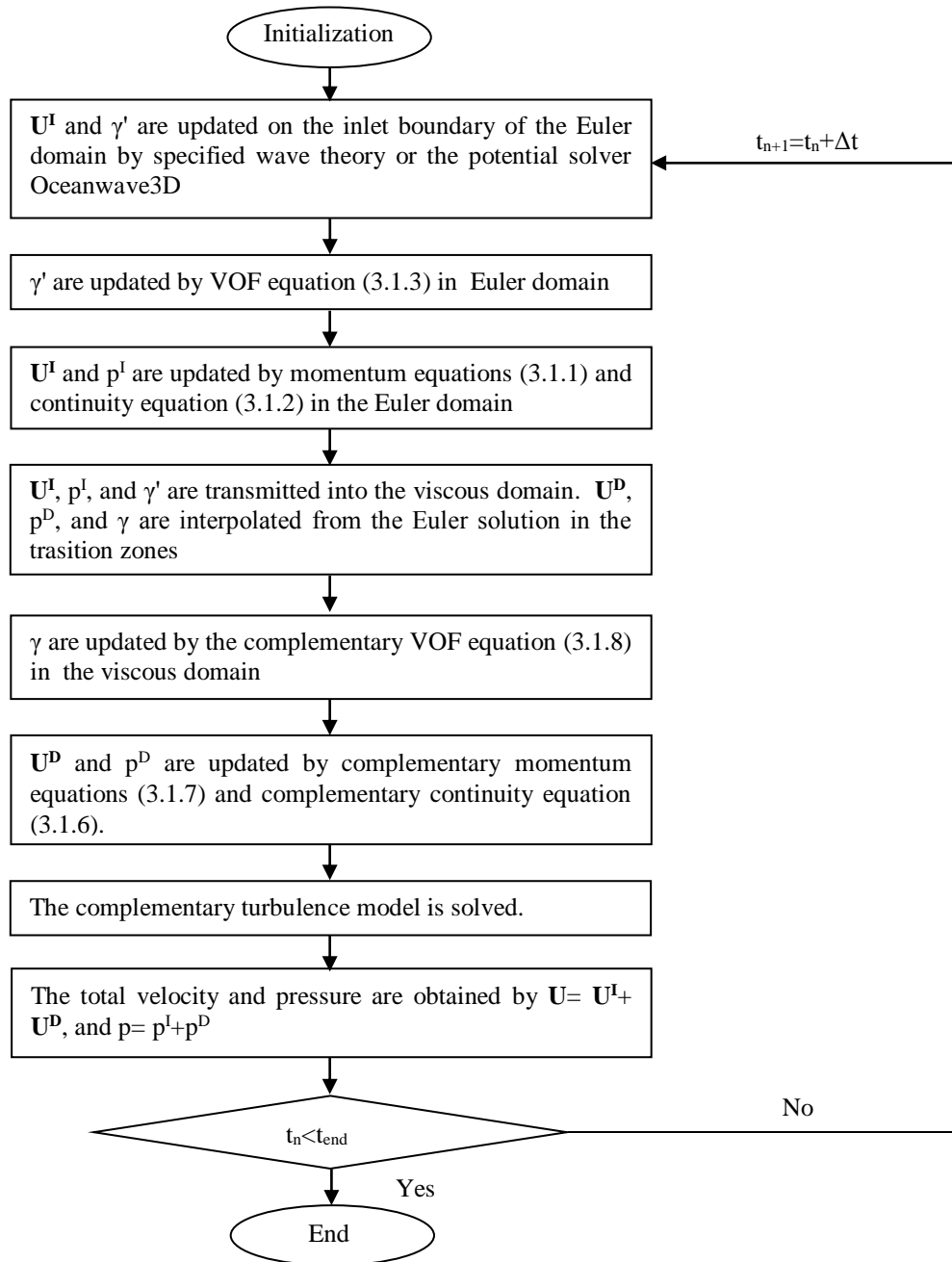


Fig. 3.7.1 The interpolation procedure

Step1 Initialise the unknown variables including  $\mathbf{U}^I$ ,  $p^I$ , and  $\gamma'$  in the Euler domain and establish the projection relationship between the Euler domain and the viscous domain for interpolation.

Step2 By using the prescribed linear or non-linear wave theory,  $\mathbf{U}_{in}^I$  and  $\gamma_{in}^I$  on the inlet boundary of the Euler domain is obtained.



Step3 In the Euler domain, the free surface is updated by using equation (3.1.3). Then,  $\mathbf{U}^I$  and  $p^I$  are updated for the next time step by solving the momentum equations and the pressure equation obtained from (3.1.1) and (3.1.2)

Step4 The Euler solutions including  $\mathbf{U}^I$ ,  $p^I$ , and  $\gamma'$  are interpolated into the viscous domain, which are regarded as known variables.

Step5 In the viscous domain,  $\mathbf{U}^D$  and  $p^D$  is updated in the next time step by solving the complementary momentum equations and the corresponding pressure equation obtained from (3.1.6) and (3.1.7) by using the PISO algorithm. Meanwhile, the complementary turbulence model is solved by using the obtained values of  $\mathbf{U}^I$  and  $\mathbf{U}^D$  in the current time step. The volume fraction  $\gamma$  is updated by using (3.1.8). A transitional zone technique described in section 2.3 is used to keep volume fraction consistent and smooth between the Euler domain and the viscous domain.

Step6 Finally, the total velocity and the total pressure in the next time step are obtained by  $\mathbf{U} = \mathbf{U}^I + \mathbf{U}^D$  and  $p = p^I + p^D$  respectively.

The simulation advances into the next time step and the program returns to Step2 until the final time step is reached.

## Chapter 4 Convergence study of the Euler-viscous hybrid solver for interaction of a surface-piercing fixed structure with waves

In this chapter, based on the convergence study of the newly developed Euler-viscous hybrid solver introduced in Chapter 3, for simulating wave interacting with fixed surface-piercing structure will be explored. The effects of the mesh resolution, the size of the viscous domain, the length of the transition zone, and the incident waves on the numerical results are studied. The computational accuracy and efficiency are discussed. Finally, the validation of the Euler-viscous hybrid solver is done.

### 4.1 The numerical configuration

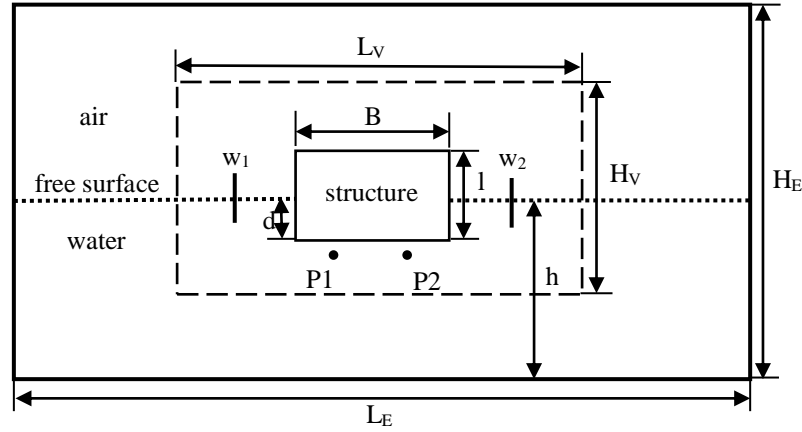


Fig. 4.1.1 the physical model

A two-dimensional case of fixed surface-piercing structure interacting with regular waves is selected which has been studied by many researchers (Tanizawa, and Minami, 1998; Koo, and Kim, 2007; Li, and Lin, 2012). It is sufficient to investigate the convergence of the Euler-viscous hybrid solver, which will further be used to study the effects of complex topography on wave interacting with fixed surface-piercing structure (Chapter 5). Note that the same case has been used by Koo and Kim (2007) to validate the in-house code, and Li and Lin, (2010) to validate a numerical wave tank based on OpenFOAM.

As shown in Fig. 4.1.1, the fixed structure is a two-dimensional rectangular barge with width ( $B$ ) of 0.5m and height ( $l$ ) of 0.5m. The initial draft ( $d$ ) of the floating structure is 0.25m. The water depth  $h$  is taken as the same as the incident wave length  $h=\lambda$ . Non-dimensional wave forces are used, e.g., the horizontal force  $F_s$  is non-dimensionalized by dividing  $\rho g L d A$ , where  $L$  is the length of the floating structure and  $A$  is half of the wave height  $H_w$ . Similarly, the vertical force  $F_h$  and the moment force  $M$  are also non-dimensionalized by dividing

$\rho gLBA$  and  $\rho gLBdA$  respectively. Due to the sharp corner of the floating structure and high Reynolds number ( $Re > 10000$ ), the potential model is insufficient (Koo, 2004), thus the viscous model should be used for simulations. In this research, the case is simulated by both the conventional RANS solver and the Euler-viscous hybrid solver. Finally, the computational accuracy and the efficiency of the Euler-viscous hybrid solver is discussed.

## 4.2 The effects of the mesh resolution

### 4.2.1 The mesh for the Euler-viscous hybrid solver and the conventional RANS solver

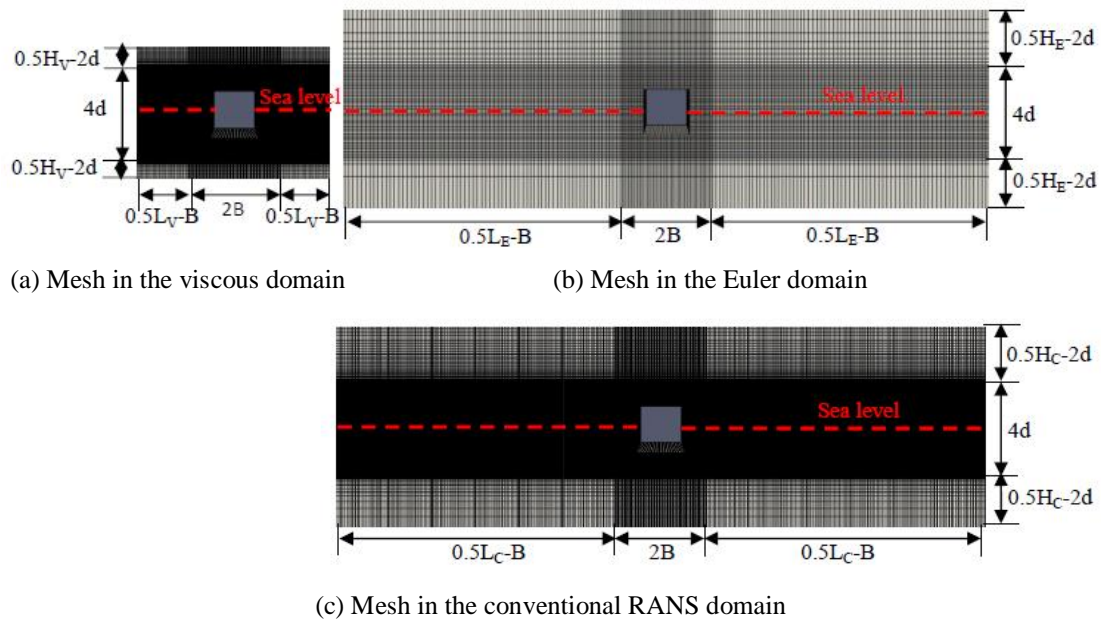


Fig. 4.2.1 Mesh used in the hybrid model and conventional RANS model

Both the Euler domain and the viscous domain are rectangular with the floating structures being placed in the centre, shown in Fig. 4.1.1. The length and the width of the Euler domain are  $L_E = 8\lambda$  and  $H_E = 2\lambda$ , respectively. Some researchers used smaller computational domains for simulations of the same case (Tanizawa and Minami, 1998; Koo and Kim, 2007; Li and Lin, 2012). The viscous domain is much smaller than the Euler domain. Meanwhile, the mesh in the viscous domain is denser than that in the Euler domain. The mesh uses hexahedral cells and is refined around the structure and free surface, which is generated by the mesh generating program blockMesh built in OpenFOAM. The scale of conventional RANS domain is the same as that of the Euler domain for comparison. In order to capture the vortex around the floating structure and free surface, the mesh surrounding the structure must be refined. Apart from that, the mesh close to that must be refined. i.e., the mesh is refined along the horizontal direction with the length of  $2B$ , and refined along the vertical direction with the length of  $4d$ . Finally, an example of the mesh is shown in Fig. 4.2.1, which it is found that along the vertical direction, the mesh is refined and uniformed, close to the sea level, but is

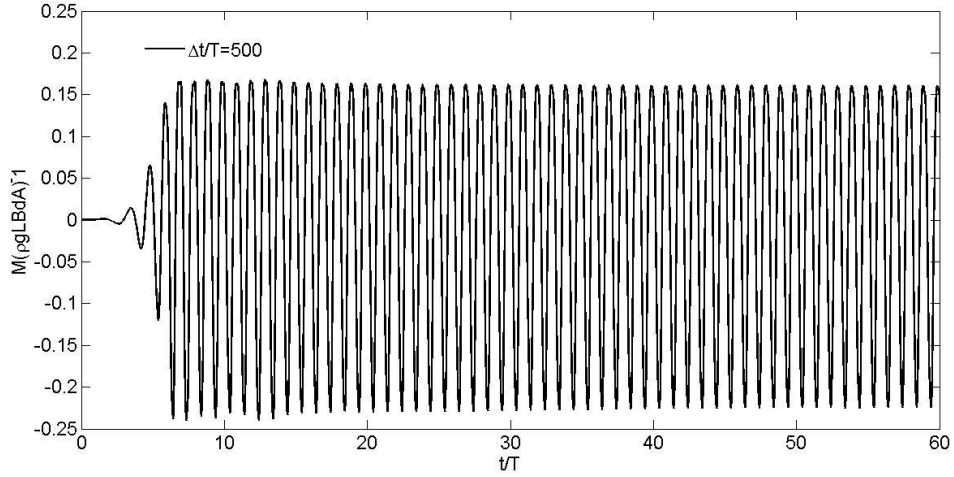
coarser and non-uniform (with the ratio of 1/30) far away from the floating structure. While on the horizontal direction, the mesh is uniformed and denser surrounding the floating structure.

Some parameters are used to describe the effects of the mesh. Firstly, the number of division per wave length is used for the mesh far away from the structure in the horizontal direction. Specifically,  $nL_E$  divisions in the length of  $0.5L_E-B$  in the Euler domain and  $nL_V$  divisions in the length of  $0.5L_V-B$  in the viscous domain are applied for the Euler-viscous hybrid solver. Similarly,  $nL_C$  divisions in the length of  $0.5L_C-B$  in the conventional RANS domain are applied for the conventional RANS solver. Secondly, the number of division per width of the structure is used to describe the mesh close to the structure in the horizontal direction along the length of  $2B$ , i.e.,  $nB_E$  divisions in the Euler domain and  $nB_V$  divisions in the viscous domain are used for the Euler-viscous hybrid solver, while  $nB_C$  is used for the conventional RANS solver. Thirdly, to describe the mesh close to the structure in the vertical direction along the length of  $4d$ ,  $nH_E$ ,  $nH_V$ , and  $nH_C$  are used in the Euler domain, the viscous domain and conventional RANS domain, respectively. In the simulation based on the Euler-viscous hybrid solver, the mesh in the viscous domain is finer than that in the Euler domain, which means that  $nL_V > nL_E$ ,  $nB_V > nB_E$ , and  $nH_V > nH_E$ . That's because finer mesh is required by the viscous solver for convergence.

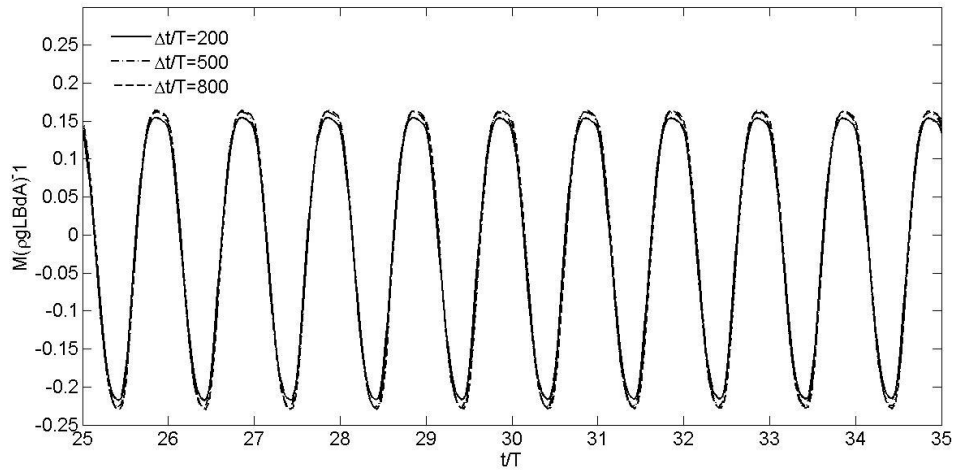
Linear wave theory is used for generating incident regular waves at inlet boundary with the wave height  $H_w=0.07\text{m}$  and the incident wave length  $\lambda=2.1\text{m}$ . It should be noted that all parameters in length are non dimensionalized by dividing the draft  $d$ , i.e.,  $B/d=2$ ,  $l/d=2$ ,  $h/d=8.4$ ,  $\lambda/d=8.4$ , and  $H_w/d=0.28$ . In the next subsections, the effects of mesh resolution are explored.

#### 4.2.2 The convergence study of the conventional RANS solver and the Euler solver

Firstly, the convergence study of the time step is carried out by using the conventional RANS solver, where  $nL_C=200$ ,  $nB_C=80$ , and  $nH_C=30$ . Cases with the same incident waves  $h/d=8.4$ ,  $\lambda/d=8.4$ , and  $H_w/d=0.28$  are simulated by using different time step size, i.e.,  $\Delta t/T=200$ ,  $\Delta t/T=500$ , and  $\Delta t/T=800$ . Wave loads acting on the structure are recorded for evaluating the convergence, as the main concern of the ship design is the environmental force and the resulted ship motion. The time history of the dimensionless moment is recorded and shown in Fig. 4.2.2.



(a) Time history of moment at  $\Delta t/T=500$



(b) The comparison of moment at different time step

Fig. 4.2.2 Time history of moment

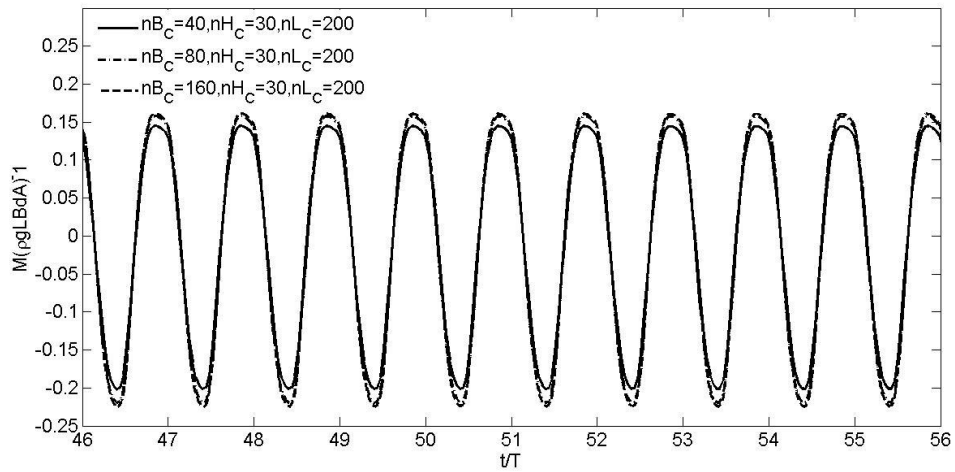
It shows that the moment changes periodically and a quasi-steady state can be found after 10 wave periods, which also validated the stability of the numerical method. In fact, not only moment, but also the horizontal force and the vertical force vary periodically after  $t/T=10$  (not showing here for brevity). However, in the quasi-steady state, the amplitudes of wave loads are not stable. Hence, the average moment in continuous ten wave periods is considered. A relative average error of moment is defined as

$$REM(1, 2) = \sum_{i=1}^{10} \left[ \frac{\text{Max}(|M_1^i - M_2^i|)}{\text{Max}(M_1^{\text{max}} - M_1^{\text{min}}, M_2^{\text{max}} - M_2^{\text{min}})} \right]_i / 10 \quad (4.2.1)$$

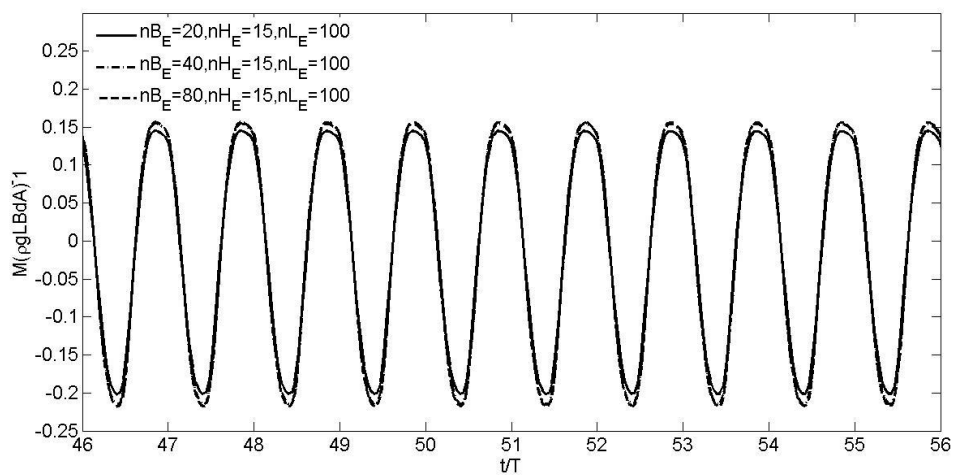
In (4.2.1),  $\text{Max}(|M_1^i - M_2^i|)$  is the maximum discrepancy in one wave period between moments in solution1 and solution 2.  $\text{Max}(M_1^{\text{max}} - M_1^{\text{min}}, M_2^{\text{max}} - M_2^{\text{min}})$  is the maximum discrepancy in the same solution. By using that, the effects of time step in Fig. 4.2.2 (a) is investigated.

$REM(\Delta t/T=200, \Delta t/T=500)=7.2\%$  is larger than  $REM(\Delta t/T=500, \Delta t/T=800)=1.6\%$ , which means that  $\Delta t/T=500$  is sufficient and can be chosen as the time step for both the conventional RANS solver and the Euler solver.

In addition to the time step, the mesh resolution plays a crucial role on the convergence of a solver. Both the horizontal and vertical grid sizes affect the convergence of the numerical simulation. Therefore, the convergence study of mesh resolution is done based on the conventional RANS solver and the Euler solver with the same domain size. Specifically, the effects of  $nB_C$ ,  $nH_C$ , and  $nL_C$  on the wave loads are studied based on the conventional RANS solver. Apart from that, the effects of  $nB_E$ ,  $nH_E$ , and  $nL_E$  on the wave loads are also studied based on the Euler solver.



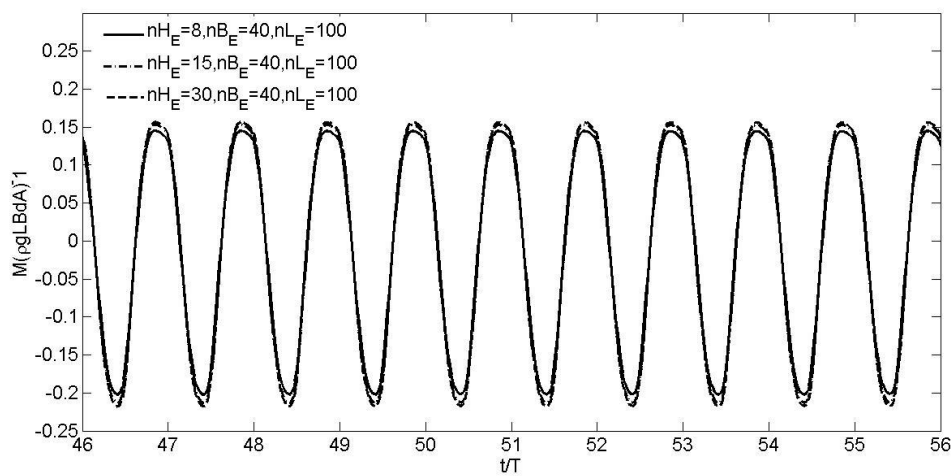
(a) The convergence study of  $nB_C$  based on the conventional RANS solver



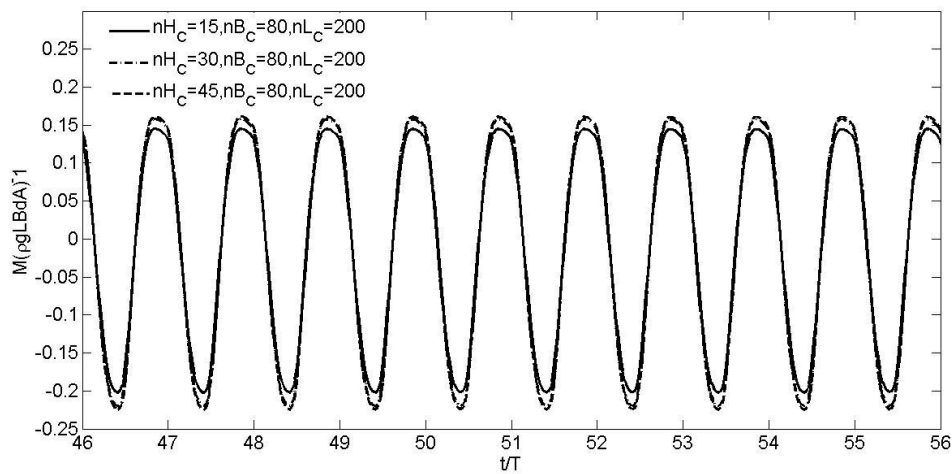
(b) The convergence study of  $nB_E$  based on the Euler solver

Fig. 4.2.3 The convergence study ( $nB_C$  and  $nB_E$ ) of conventional RANS solver and Euler solver

In order to study the horizontal mesh resolution surrounding the floating structure based on the conventional RANS solver, different mesh resolution is used with  $nB_C=40, 80, \text{ and } 160$ . The convergence study of  $nB_C$  is shown in Fig. 4.2.3 (a), from which it can be seen that the maximum discrepancy between  $nB_C=80$  and  $nB_C=160$  is much smaller than that between  $nB_C=40$  and  $nB_C=80$ , e.g.,  $(\text{REM}(nB_C=80, nB_C=160)=0.7\%) < (\text{REM}(nB_C=40, nB_C=80)=15\%)$ . Thus,  $nB_C=80$  is selected for the conventional RANS solver. Similar study of  $nB_E$  is also done based on the Euler solver. Where  $nB_E=20, 40, \text{ and } 80$  are tested. It is found that  $nB_E=40$  is sufficient for the Euler solver, as  $\text{REM}(nB_E=40, nB_E=80)=1.1\%$  is much smaller than  $\text{REM}(nB_E=20, nB_E=40)=17\%$ .



(a) The convergence study of  $nH_C$  based on the conventional RANS solver



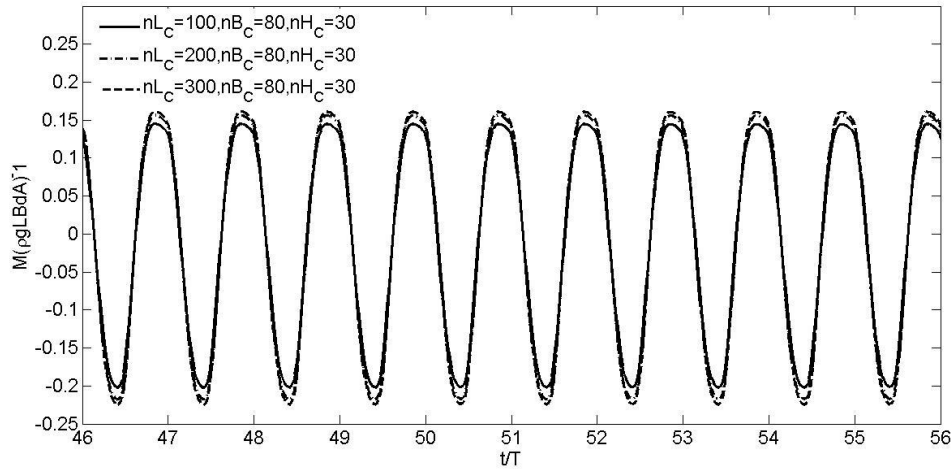
(b) The convergence study of  $nH_E$  based on the Euler solver

Fig. 4.2.4 The convergence study ( $nH_C$  and  $nH_E$ ) of conventional RANS solver and Euler solver

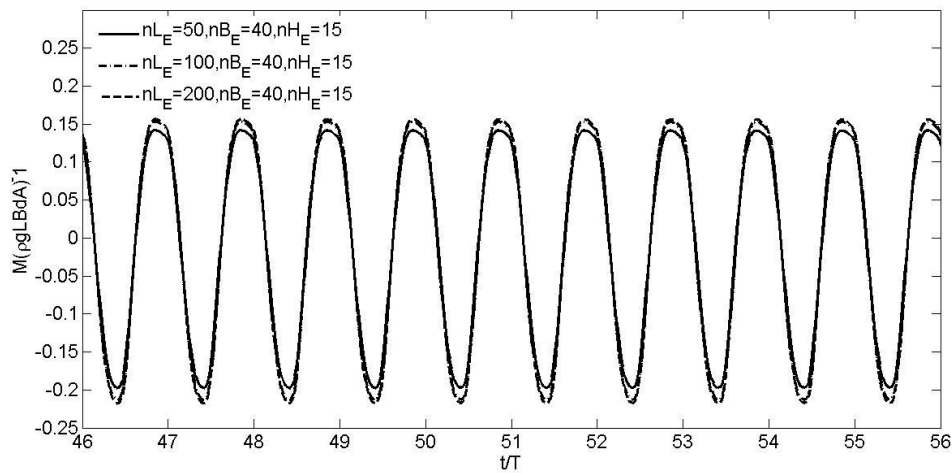
The vertical mesh resolution close to free surface is also investigated, which can be seen in Fig. 4.2.4. For the conventional RANS solver, different vertical mesh resolution with  $nH_C=15, 30, \text{ and } 45$  are tested. It is found that  $nH_C=30$  is sufficient as  $\text{REM}(nH_C=30, nH_C=45)=0.4\%$  is

much smaller than  $REM(nH_C=15, nH_C=30)=10.6\%$ . Meanwhile, the convergence study of vertical mesh resolution is also done based on the Euler solver with  $nH_E=8, 15$ , and  $30$ . It is shown in Fig. 4.2.4 (b) that the gap between  $nH_E=15$  and  $nH_E=30$  is much smaller than that between  $nH_E=8$  and  $nH_E=15$ , which is also supported by  $REM(nH_E=15, nH_E=30)=1.3\% < REM(nH_E=8, nH_E=15)=14.5\%$ . Therefore,  $nH_E=15$  should be used for the Euler solver.

Finally, the horizontal mesh resolution far away from the structure is studied. Cases with  $nL_C=100, 200$ , and  $300$  are simulated based on the conventional RANS solver. Since  $REM(nL_C=100, nL_C=200)=16.2\%$  is larger than  $REM(nL_C=200, nL_C=300)=0.85\%$ ,  $nL_C=200$  is sufficient for the conventional RANS solver, which can be also seen from Fig. 4.2.5 (a). Similarly,  $nL_E=50, 100$ , and  $200$  are tested based on the Euler solver. It is found that  $nL_E=100$  should be used for the Euler solver, where it is observed that  $REM(nL_E=50, nL_E=100)=12.7\%$  is significantly smaller than  $REM(nL_E=100, nL_E=200)=1.4\%$ .



(a) The convergence study of  $nL_C$  based on the conventional RANS solver



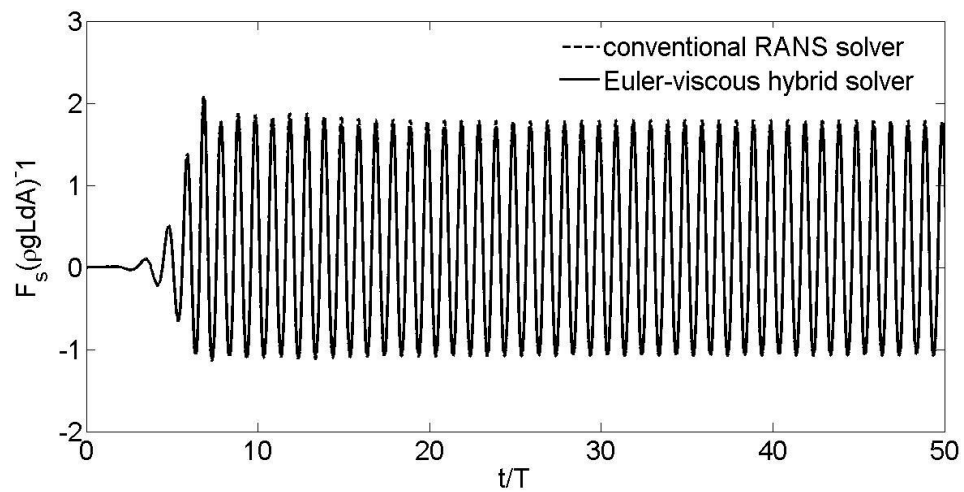
(b) The convergence study of  $nL_E$  based on the Euler solver

Fig. 4.2.5 The convergence study ( $nL_C$  and  $nL_E$ ) of conventional RANS solver and Euler solver

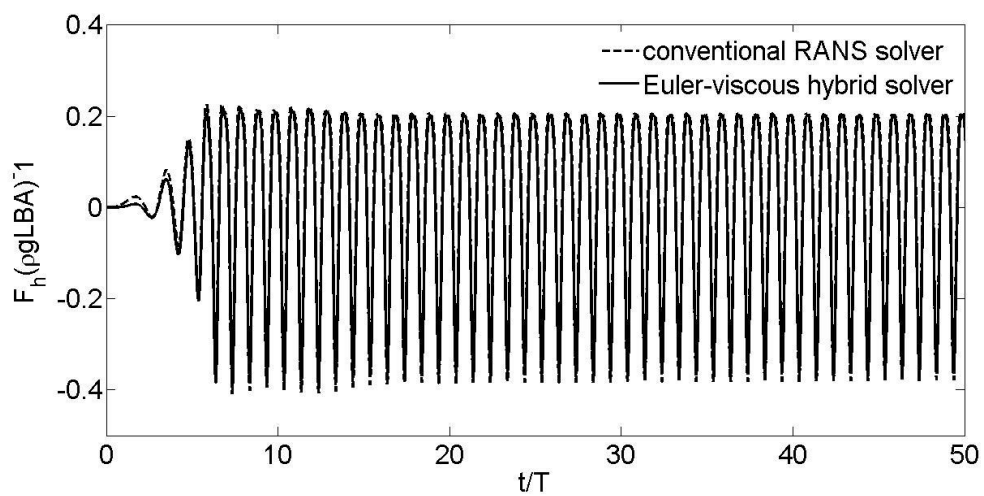


In summary, the time step  $\Delta t=T/500$  should be used for both the conventional RANS solver and the Euler solver. Furthermore, the suitable mesh resolution for the conventional RANS solver is  $n_{B_C}=80$ ,  $n_{L_C}=200$ , and  $n_{H_C}=30$ , which is finer than that for the Euler solver with  $n_{B_E}=40$ ,  $n_{L_E}=100$ , and  $n_{H_E}=15$ . Note that due to coarser mesh used by the Euler solver, it requires less CPU time comparing with the conventional RANS solver in a large computing domain. Meanwhile, in the Euler-viscous hybrid model, the complementary RANS solver just covers a small domain surrounding the floating structure, which improves the accuracy of the solution by using the Euler solver along while does not cost significant computation time. By doing so, the CPU time can be saved by the Euler-viscous hybrid solver, while keeping the same accuracy with the conventional RANS solver.

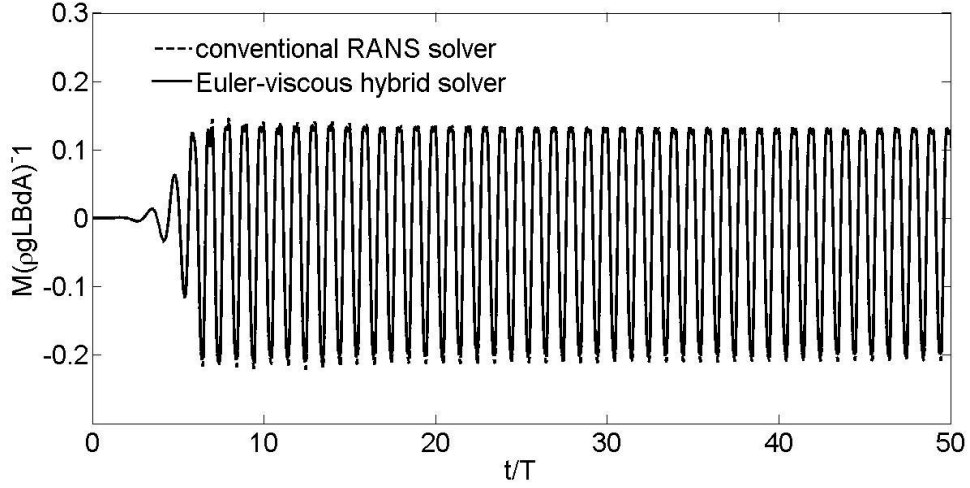
#### 4.2.3 The simulation results based on the Euler-viscous hybrid solver



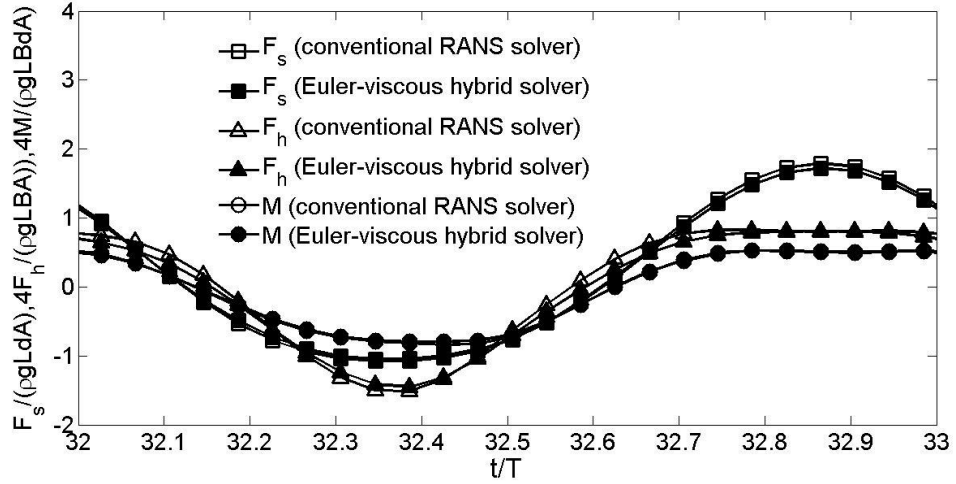
(a) The time history of horizontal force ( $F_s$ )



(b) The time history of vertical force ( $F_h$ )



(c) The time history of moment (M)



(d) The comparison of wave loads over one wave period

Fig. 4.2.6 The comparison of wave loads between the Euler-viscous hybrid solver and the conventional RANS solver

A numerical simulation based on the Euler-viscous hybrid solver is carried out. The incident wave is the same as that in section 4.2.2. In the Euler domain, the length  $L_E=8\lambda$  and the width  $H_E=2\lambda$  is used with the mesh resolution  $nB_E=40$ ,  $nL_E=100$ , and  $nH_E=15$  obtained previously. In the viscous domain, the length  $L_V=2\lambda$  and the width  $H_V=2\lambda$  is used with the mesh resolution  $nB_V=80$ ,  $nL_V=200$ , and  $nH_V=30$  same to the conventional RANS solver. Simulations are also carried out by the conventional RANS solver for comparison. The corresponding computational domain is described by the length  $L_C=8\lambda$  and the width  $H_C=2\lambda$  with  $nB_C=80$ ,  $nL_C=200$ , and  $nH_C=30$ . The simulation results are shown in Fig. 4.2.6.

From Fig. 4.2.6 (a)~(c), it can be seen that the time history of wave loads of the Euler-viscous hybrid solver agrees very well with the conventional RANS solver. A closer look at the wave

loads in one wave period from  $t/T=32$  to  $t/T=33$  is shown in Fig. 4.2.6 (d), where the discrepancy of wave loads between the conventional RANS solver and the Euler-viscous hybrid solver is quite small. Although the quasi-steady state is reached after  $t/T=10$ , amplitudes of wave load vary with time. Therefore, the average error over 10 wave periods is adopted and defined as

$$\text{err}(V) = \sum_{j=1}^{10} \left\{ \sum_{i=1}^n \frac{|V_c^i - V_o^i|}{[\text{Max}(V_o) - \text{Min}(V_o)]n} \right\} / 10 \quad (4.2.2)$$

where  $V_c^i$  and  $V_o^i$  are solutions obtained by the Euler-viscous hybrid solver and the conventional RANS solver at the  $i^{\text{th}}$  time step  $\Delta t_i$ .  $\text{Max}(V_o)$  and  $\text{Min}(V_o)$  are the maximum and minimum values of  $V_o$  by the conventional RANS solver. This formula will be used in the following subsection to represent the error by using the Euler-viscous hybrid solver.

#### 4.2.4 The effects of mesh resolution for the Euler-viscous hybrid solver

Two sets of mesh are used for the Euler-viscous hybrid solver. Furthermore, the mesh resolution is different between the Euler domain and the viscous domain. Therefore, it is necessary to study the effects of mesh resolution on its accuracy for the Euler-viscous hybrid solver.

In this section, different combinations of mesh resolution in the Euler domain and the viscous hybrid domain are applied. 5 cases are studied and the mesh resolution is described in Table 4.2.1 (b). Wave loads by the Euler-viscous hybrid solver are compared with those by the conventional RANS solver. The mesh resolution for the conventional RANS solver is described in Table 4.2.1 (a). The incident wave parameters are the same as that used in section 4.2.3.

From Table 4.2.1 (b), it can be seen that the mesh resolution of case 1 is the same as that in section 4.2.3, which is obtained by the convergence study for the Euler solver and the conventional RANS solver, respectively. For case 2, the mesh in the Euler domain is finer than that of case 1, by increasing from  $nH_E=15$  to  $nH_E=30$ , whereas the mesh in the viscous domain is still the same. For case 3, the mesh in the Euler domain is the same as that in the viscous domain by doubling  $nL_E$ ,  $nB_E$  and  $nH_E$  of that in case 1. For case 4 and case 5, the mesh in the viscous domain is finer than that in case 1, whereas the mesh in the Euler domain is the same as that in case 1.

Table 4.2.1 The mesh resolution and computational domain for the conventional RANS solver and the Euler-viscous hybrid solver

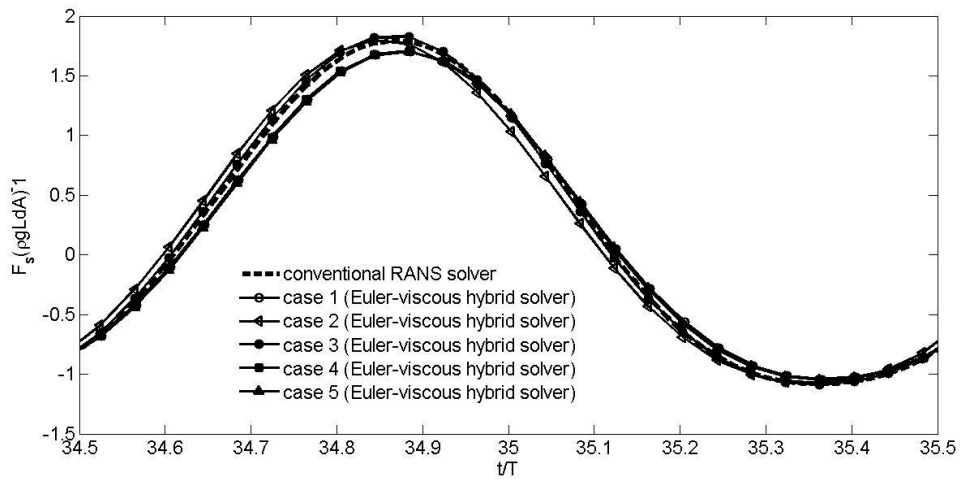
(a) The mesh resolution and computational domain for the conventional RANS solver

Conventional RANS domain				
$L_C$	$H_C$	$nL_C$	$nB_C$	$nH_C$
$8\lambda$	$2\lambda$	200	80	30

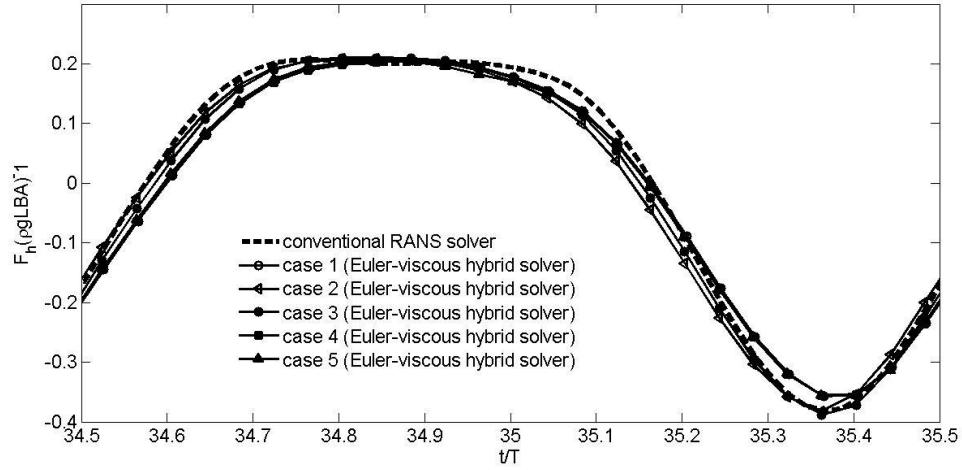
(b) The mesh resolution and computational domain for the Euler-viscous hybrid solver

No.	Euler domain					Viscous domain					
	$L_E$	$H_E$	$nL_E$	$nB_E$	$nH_E$	$L_V$	$H_V$	$L_{tr}$	$nL_V$	$nB_V$	$nH_V$
1	$8\lambda$	$2\lambda$	100	40	15	$2\lambda$	$2\lambda$	$0.5\lambda$	200	80	30
2	$8\lambda$	$2\lambda$	100	40	30	$2\lambda$	$2\lambda$	$0.5\lambda$	200	80	30
3	$8\lambda$	$2\lambda$	200	80	30	$2\lambda$	$2\lambda$	$0.5\lambda$	200	80	30
4	$8\lambda$	$2\lambda$	100	40	15	$2\lambda$	$2\lambda$	$0.5\lambda$	200	80	45
5	$8\lambda$	$2\lambda$	100	40	15	$2\lambda$	$2\lambda$	$0.5\lambda$	200	160	30

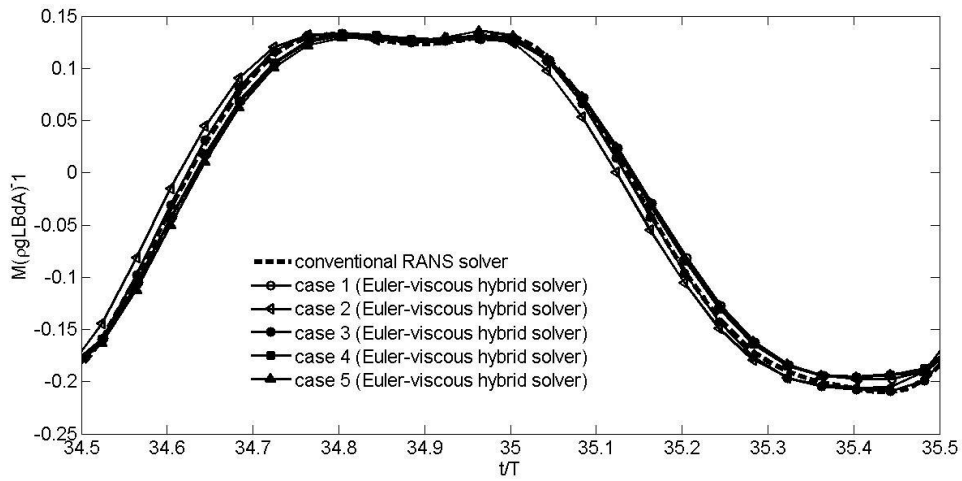
Firstly, wave loads by the Euler-viscous hybrid solver at different mesh resolution are compared with those by the conventional RANS solver. The comparison of wave loads in one wave period is shown in Fig. 4.2.7. It is obvious that the variation of wave loads with time is the same. However, the discrepancy of wave loads exists between the Euler-viscous solver and the conventional RANS solver. Furthermore, the degree of discrepancy is different with different mesh resolution. It can be found that the wave load at case 3 is closer to the numerical results by the conventional RANS solver. To be more specific, the average errors are estimated and plotted in Fig. 4.2.8. It indicates that the average error of case 3 is the smallest. Thus, when the mesh resolution in the Euler domain is the same as that in the viscous domain, the best computational precision can be obtained. It further implies that the different mesh resolution in the Euler and the viscous domain is an important factor, which leads to the numerical error between the Euler-viscous hybrid solver and the conventional RANS solver.



(a) The comparison of the horizontal force ( $F_s$ )



(b) The comparison of the vertical force ( $F_h$ )



(c) The comparison of the moment ( $M$ )

Fig. 4.2.7 The comparison of wave loads by using different mesh resolution in the Euler-viscous hybrid solver and the conventional RANS solver

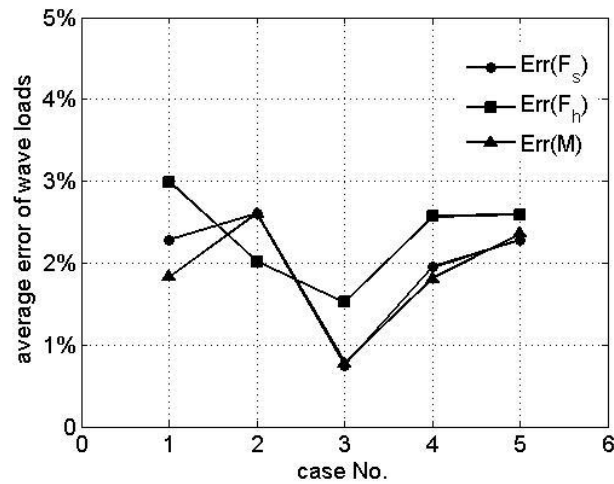


Fig. 4.2.8 The average error against cases with different mesh configuration

In addition, the computational efficiency is also discussed as the aim of the study is to reduce the CPU time while maintaining high accuracy. Numerical simulations are carried out based on OpenFOAM-2.2.0, on a workstation with the XEON E5-2692 V2 and 64GB RAM. All of simulations are carried out by using single thread computation. In the simulation, the CPU time (wall time) is recorded. Then, the ratio by dividing the CPU time of the Euler-viscous hybrid solver over that of the conventional RANS solver is used to evaluate the computational efficiency of the Euler-viscous hybrid solver.

In Fig. 4.2.9, the computational efficiency under different mesh resolution is shown. It indicates that the CPU time ratio is less than 1 for all of 5 cases, which means that the CPU time can be saved by the Euler-viscous hybrid solver. Furthermore, the computational efficiency varies largely with different mesh resolution. Specifically, the computational efficiency of case 3 is the lowest (91.2%), because the largest mesh resolution in the Euler domain is used. On the other hand, the highest computational efficiency is achieved for case 1, where almost 70% CPU time can be saved, comparing with that consumed by the conventional RANS solver. Although the mesh in the viscous domain is finer in case 4 and case 5, the corresponding computational efficiency is higher than both case 2 and case 3. Because the size of the viscous domain is much smaller than that of the Euler domain, the effects of it is less significant.

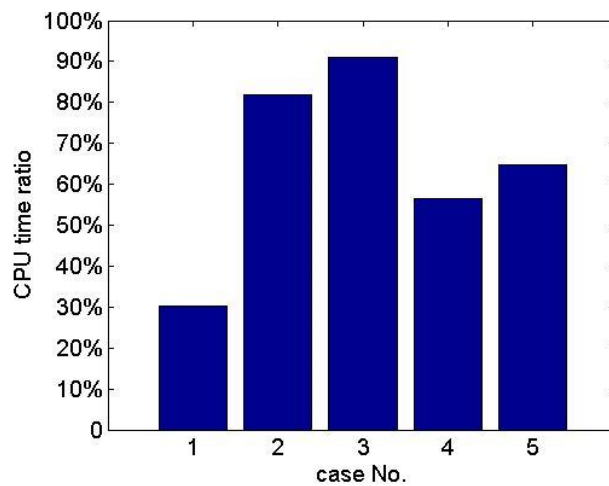


Fig. 4.2.9 The average error under different mesh resolution

Considering both the computational accuracy and efficiency, it is found that the highest accuracy corresponds to the lowest efficiency as shown in case 3. If considering the error less than 3% can be accepted, the mesh resolution of case 1 can be used for Euler-viscous hybrid solver, which corresponds to the highest efficiency. Thus, in the investigation below, the mesh resolution of case 1 is used.

### 4.3 The effects of the length ( $L_V$ ) of the viscous domain

In the simulation based on the Euler-viscous hybrid solver, the viscous domain is just surrounding the floating structure, which is much smaller than the Euler domain. By this, the computational efficiency can be improved. Nevertheless, the viscous domain cannot be arbitrarily small. That's because the viscous effects are assumed to be insignificant at the boundary of the viscous domain, which is true if the boundary is sufficiently far away from the structure. To guarantee the computational accuracy for the Euler-viscous hybrid solver, it is important to study the effects of the size of the viscous domain on numerical simulations based on the Euler-viscous hybrid solver.

Table 4.3.1 The mesh for study the effects of  $L_V$

(a) The mesh configuration for the Euler-viscous hybrid solver

No.	Euler domain					Viscous domain					
	$L_E$	$H_E$	$nL_E$	$nB_E$	$nH_E$	$L_V$	$H_V$	$L_{tr}$	$nL_V$	$nB_V$	$nH_V$
1	$8\lambda$	$2\lambda$	100	40	15	$\lambda$	$2\lambda$	$0.25\lambda$	200	80	30
2	$8\lambda$	$2\lambda$	100	40	15	$2\lambda$	$2\lambda$	$0.5\lambda$	200	80	30
3	$8\lambda$	$2\lambda$	100	40	15	$3\lambda$	$2\lambda$	$0.5\lambda$	200	80	30
4	$8\lambda$	$2\lambda$	100	40	15	$4\lambda$	$2\lambda$	$0.5\lambda$	200	80	30

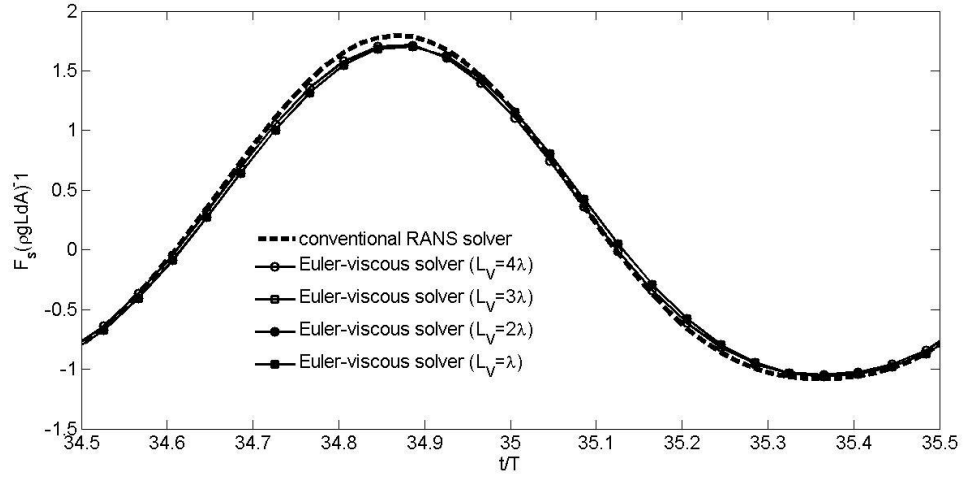
(b) The mesh configuration for the conventional RANS solver

Conventional RANS domain				
$L_C$	$H_C$	$nL_C$	$nB_C$	$nH_C$
$8\lambda$	$2\lambda$	200	80	30

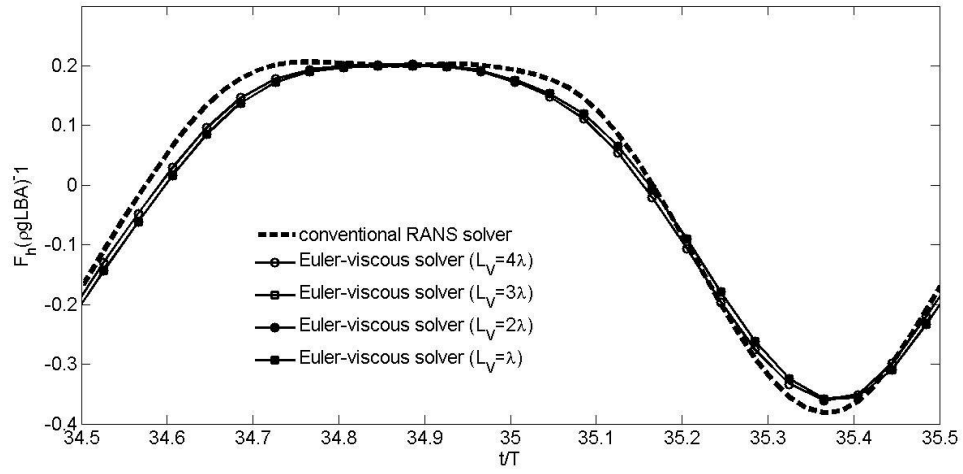
In this section, cases with different length ( $L_V$ ) of the viscous domain are simulated based on the Euler-viscous hybrid solver. In these cases, the size of the Euler domain is kept the same as  $L_E=8\lambda$  and  $H_E=2\lambda$ , while the width of the viscous domain is the same as  $H_V=2\lambda$ . The length ( $L_V$ ) of the viscous domain varies with  $L_V=\lambda$ ,  $L_V=2\lambda$ ,  $L_V=3\lambda$ , and  $L_V=4\lambda$  in 4 cases. The length ( $L_{tr}$ ) of the transition zone is one fourth of  $L_V$ . The same mesh resolution of case 1 in section 4.2.4 is used, which is described in Table 4.3.1 (a). Incident waves with  $h/d=8.4$ ,  $\lambda/d=8.4$ , and  $H_w/d=0.28$  are simulated based on the Euler-viscous hybrid solver. Numerical results are compared with those based on the conventional RANS solver under mesh resolution described in Table 4.3.1 (b). Finally, the influence of  $L_V$  on computational precision and efficiency is discussed.

#### 4.3.1 The effects of $L_V$ on wave loads

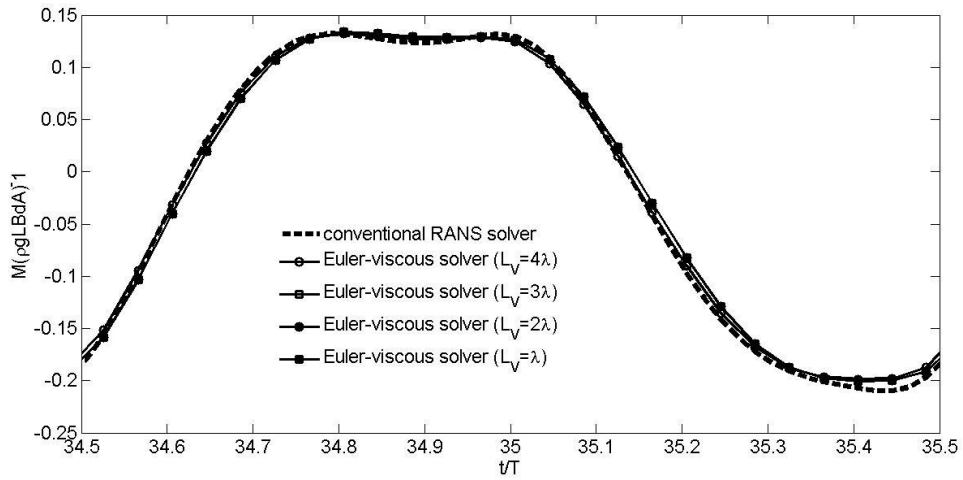
From section 4.2.3, it is found that by looking at the time history of the wave loads, a quasi-steady state can be achieved. Thus, the wave loads in one incident wave period from  $t/T=34.5$  to  $t/T=35.5$  is chosen for comparison, which is shown in Fig. 4.3.1.



(a) The comparison of the horizontal force ( $F_s$ )



(b) The comparison of the vertical force ( $F_h$ )



(c) The comparison of the moment ( $M$ )

Fig. 4.3.1 The comparison of wave loads at different  $L_v$



The Figure shows that the discrepancy of numerical results between the conventional RANS solver and the Euler-viscous hybrid solver is small. Hence, the wave-fixed structure interaction can be simulated based on the Euler-viscous hybrid solver at different  $L_V$ . Furthermore, it is found that the effects of  $L_V$  on the horizontal force ( $F_h$ ) are more obvious. Specifically, from Fig. 4.3.1 (b), it indicates that with the increase of  $L_V$ , the numerical result based on the Euler-viscous hybrid solver is closer to that based on the conventional RANS solver.

The average errors of wave loads over 10 incident wave periods are shown in Fig. 4.3.2. It indicates that the average errors of wave loads increase as the length of the viscous domain are reduced. Nevertheless, the average error is less than 3%, when the length of the viscous domain is larger than  $L_V = \lambda$ .

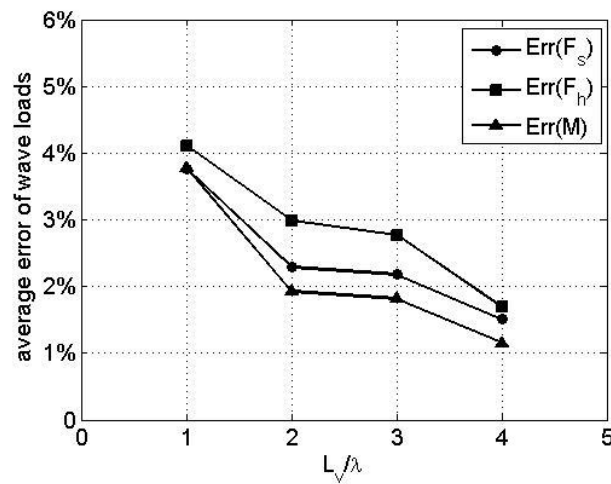


Fig. 4.3.2 The average error of wave loads at different  $L_V$

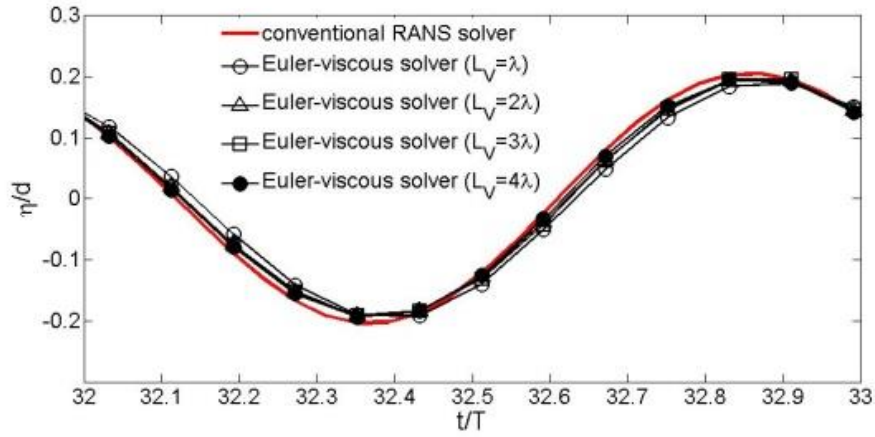
As a matter of fact, the average error of wave loads is induced by the cut-off of the viscous domain. Although the viscous effects dissipate far away from the floating structure, the numerical error can be induced by the cancelling of the viscosity at the ends of the viscous domain. With the decrease of  $L_V$ , the numerical error is amplified.

Wave loads are hydrodynamics integrated on the floating structure, which is related with wave elevation and velocity. Hence, besides wave loads, in order to study the computational accuracy of wave loads, effects of the length ( $L_V$ ) of the viscous domain on wave elevation and velocity should be also studied.

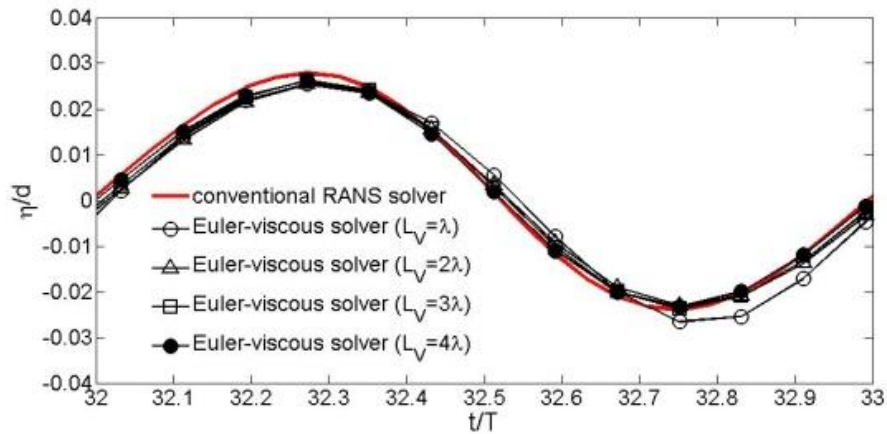
#### 4.3.2 The effects of $L_V$ on wave elevation

In order to study the effects of  $L_V$  on wave elevation, two wave gauges  $w_1$  and  $w_2$  are placed at the distance of 0.25m away from the structure at the front side and Lee side, respectively.

Wave elevation is recorded at two wave gauges. Wave elevation at different  $L_V$  over one wave period is shown in Fig. 4.3.3, which is also compared with results by the conventional RANS solver.



(a) Wave elevation at wave gauge w1



(b) Wave elevation at wave gauge w2

Fig. 4.3.3 The comparison of wave elevation in one wave period at different  $L_V$

From Fig. 4.3.3, it can be seen that the wave elevation by the Euler-viscous hybrid solver match well with that by the conventional RANS solver. Nevertheless, small discrepancy of wave elevation exists between the Euler-viscous hybrid solver and the conventional RANS solver. However, in Fig. 4.3.3 (b), it is obvious that the discrepancy is much larger at  $L_V = \lambda$ . Hence, the wave elevation is affected by  $L_V$ . The average error of wave elevation is shown in Fig. 4.3.4, which indicates that with the increase of  $L_V$ , the average error  $\text{Err}(\eta)$  decreases.

The difference of wave elevation induces the discrepancy of velocity of water particles in the flow field. Hence, it is necessary to study the effects of  $L_V$  on velocity.

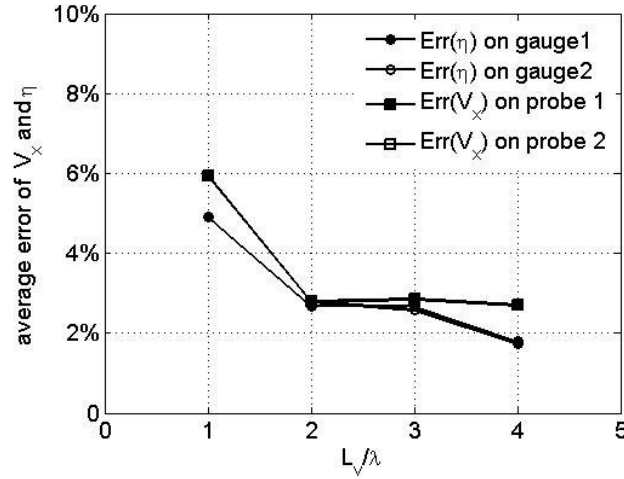
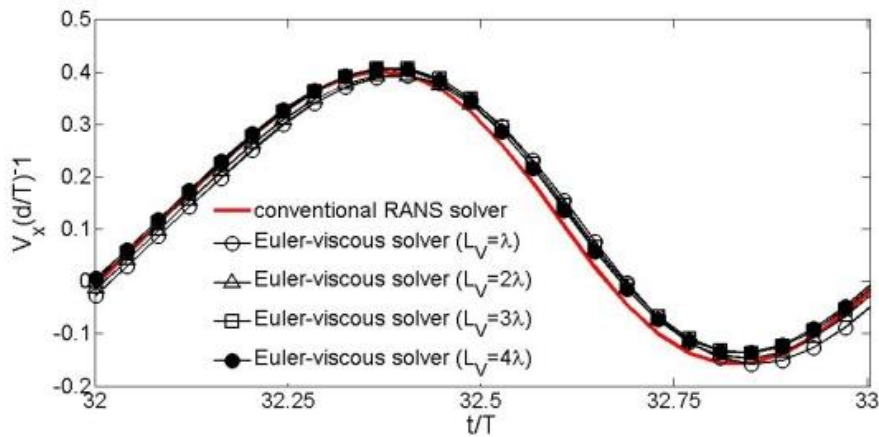


Fig. 4.3.4 The average error of wave elevation and velocity in the horizontal direction

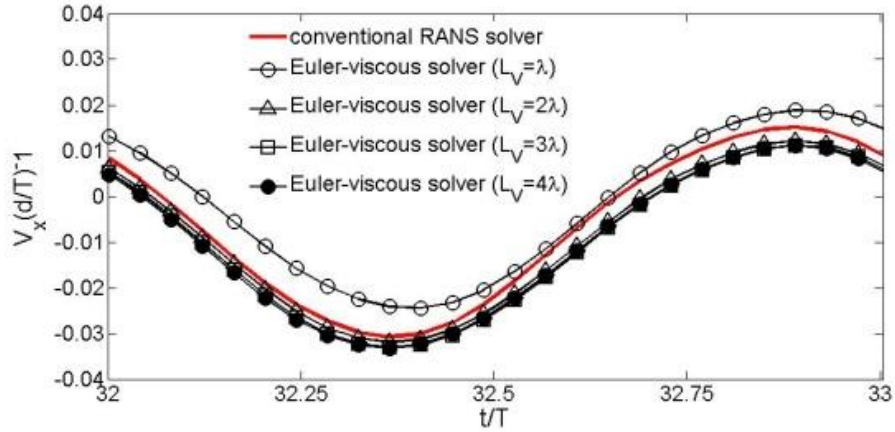
#### 4.3.3 The effects of $L_v$ on velocity

In order to study the effects of  $L_v$  on the velocity, two probe points are set below the floating structure for recording the velocity. These two points are set at a distance of 0.03m below the bottom. One probe point is located at 0.2m from the left wall. The other one is located at 0.2m from the right wall. The location of probe points is shown in Fig. 4.1.1. Because the magnitude of the vertical velocity is very small, only the horizontal velocity  $V_x$  is recorded. The comparison of the horizontal velocity between the Euler-viscous solution and the conventional RANS solution is shown in the Fig. 4.3.5.

It shows that the numerical result by the Euler-viscous hybrid solver agrees well with that by the conventional RANS solver, except for  $L_v = \lambda$ . By looking at the average error of the horizontal velocity shown in Fig. 4.3.4, it can be also observed that  $\text{Err}(V_x)$  is the highest at  $L_v = \lambda$ , which is close to 6%. Furthermore, with the increase of  $L_v$ , the average error is reduced. It shows that the average error of the horizontal velocity is below 3%, when  $L_v > \lambda$  is satisfied.



(a) The horizontal velocity at probe P1



(b) The horizontal velocity at probe P2

Fig. 4.3.5 The comparison of the horizontal velocity over one wave period

In summary, it can be concluded that numerical error can be induced by cut-off of the viscous domain. Due to the cut-off, the discrepancy of wave loads, wave elevation, and velocity is induced between the Euler-viscous hybrid solver and the conventional RANS solver. Nevertheless, the discrepancy is small if  $L_v > \lambda$ . In these cases described in table 4.3.1, the average error can be smaller than 3%, when  $L_v$  is larger than  $L_v = \lambda$ .

#### 4.3.4 The effects of $L_v$ on computational efficiency

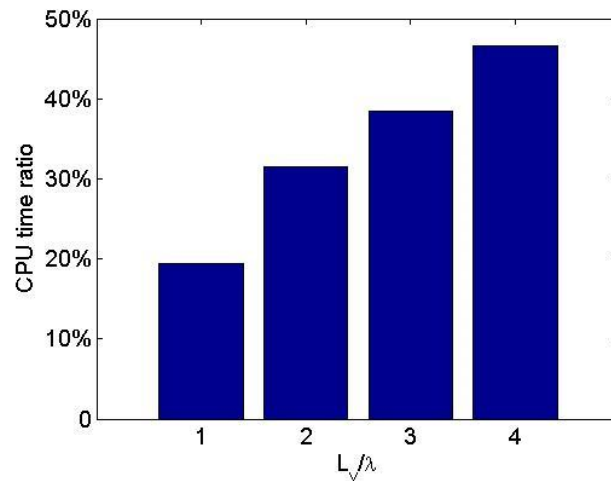


Fig. 4.3.6 The CPU time ratio against length ( $L_v$ ) of the viscous domain

The computational efficiency is shown in Fig. 4.3.6, where the CPU time ratio at different length ( $L_v$ ) of the viscous domain is presented. It indicates that with the decrease of the length ( $L_v$ ) of the viscous domain, the CPU time ratio is reduced. At  $L_v = \lambda$ , more than 80% CPU time can be saved by the Euler-viscous hybrid solver, comparing with the conventional RANS solver. It means that by reducing the length of the viscous domain, the computational efficiency can be enhanced remarkably. However, considering the computational precision

discussed from section 4.3.1 to section 4.3.3, the average error is too large at  $L_v=\lambda$ . Generally speaking,  $L_v=2\lambda$  can be chosen for the Euler-viscous hybrid solver. That's because at the condition of  $L_v=2\lambda$ , almost 70% CPU time can be saved by the Euler-viscous hybrid solver, while a good computational accuracy can be also achieved, which is below 3%.

#### 4.4 The effects of the width ( $H_v$ ) of the viscous domain

The size of the viscous domain is determined not only by the length ( $L_v$ ), but also by the width ( $H_v$ ). Numerical errors must be induced by the cut-off of the width of the viscous domain. Hence, it is necessary to study the effects of width ( $H_v$ ) of the viscous domain on numerical simulations based on the Euler-viscous hybrid solver.

Table 4.4.1 The mesh for study the effects of  $H_v$

(a) The mesh for the conventional RANS solver

Conventional RANS domain				
$L_c$	$H_c$	$L_c$	$nB_c$	$nH_c$
$8\lambda$	$2\lambda$	200	80	30

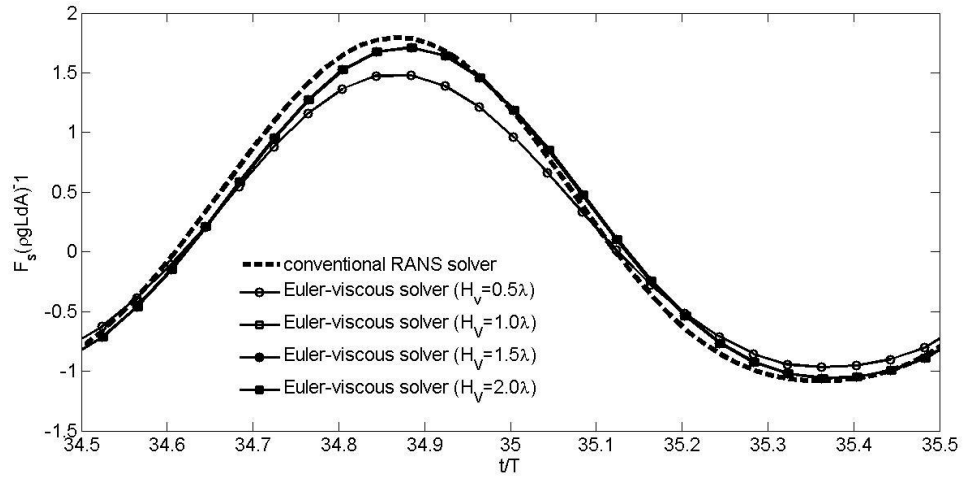
(b) The mesh for the Euler-viscous hybrid solver

No.	Euler domain					Viscous domain					
	$L_E$	$H_E$	$nL_E$	$nB_E$	$nH_E$	$L_v$	$H_v$	$L_w$	$nL_v$	$nB_v$	$nH_v$
1	$8\lambda$	$2\lambda$	100	40	15	$2\lambda$	$0.5\lambda$	$0.5\lambda$	200	80	30
2	$8\lambda$	$2\lambda$	100	40	15	$2\lambda$	$\lambda$	$0.5\lambda$	200	80	30
3	$8\lambda$	$2\lambda$	100	40	15	$2\lambda$	$1.5\lambda$	$0.5\lambda$	200	80	30
4	$8\lambda$	$2\lambda$	100	40	15	$2\lambda$	$2\lambda$	$0.5\lambda$	200	80	30

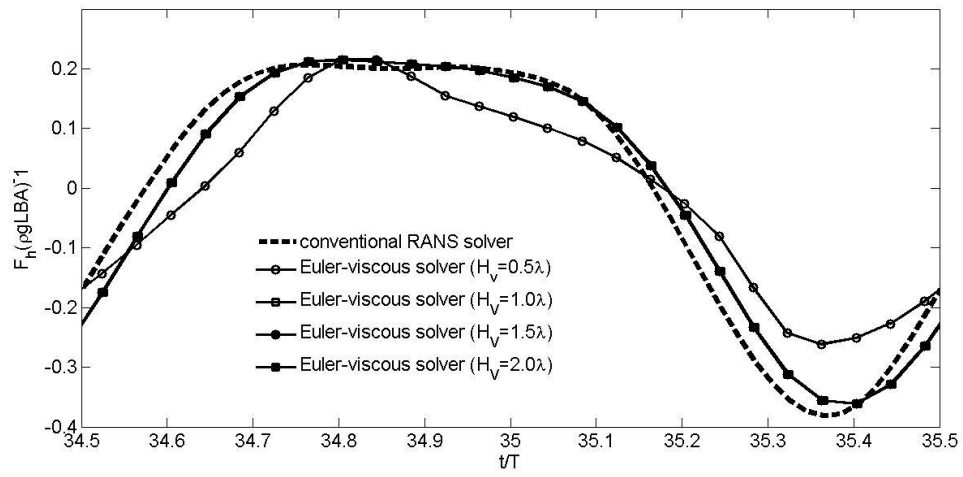
Some cases are simulated at different  $H_v$ , based on the Euler-viscous hybrid solver. The mesh configuration is described in Table 4.4.1 (b), where the Euler domain is not changed for cases, which is the same as that of case 1 in section 4.2.3. The length of the viscous domain  $L_v=2\lambda$  is used, which corresponds to good computational efficiency and accuracy. The mesh resolution in viscous domain is the same as that of case 1 in section 4.2.3. Different width ( $H_v$ ) of viscous domain is used, i.e.,  $H_v=0.5\lambda$ ,  $H_v=\lambda$ ,  $H_v=1.5\lambda$ , and  $H_v=2\lambda$ . The numerical results based on the Euler-viscous hybrid solver are then compared with those by the conventional RANS solver, of which mesh configuration is described in Table 4.4.1 (a). Both computational accuracy and efficiency are discussed below.

##### 4.4.1 The effects of $H_v$ on wave loads

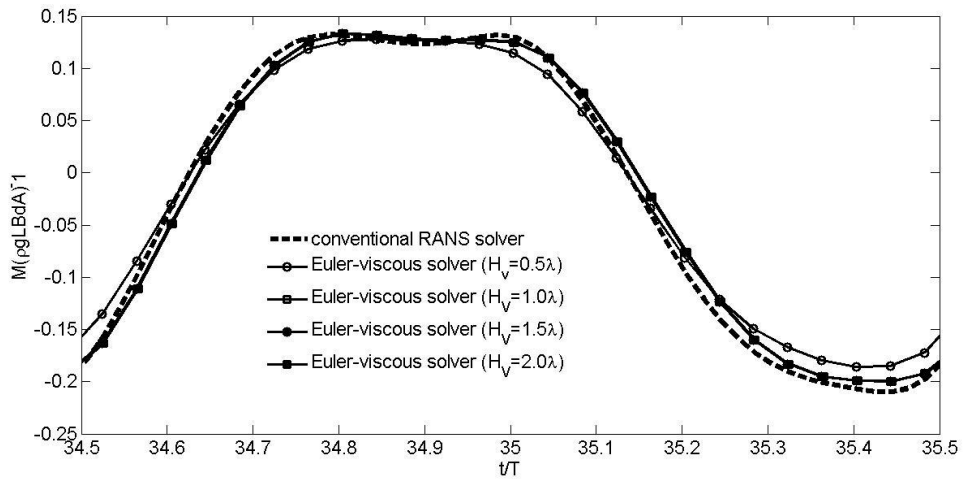
In order to study the effects of  $H_v$  on wave loads, wave loads over one wave period in quasi-steady state are shown in Fig. 4.4.1, which are also compared with those by the conventional RANS solver.



(a) The comparison of the horizontal force ( $F_s$ )



(b) The comparison of the vertical force ( $F_h$ )



(c) The comparison of moment ( $M$ )

Fig. 4.4.1 The comparison of wave loads at different  $H_v$

From Fig. 4.4.1, it is shown that the numerical results by the Euler-viscous hybrid solver can match well with those by the conventional RANS solver. However, the width ( $H_V$ ) of the viscous domain cannot be reduced arbitrarily. From Fig. 4.4.1 (b), it is obvious that at  $H_V=0.5\lambda$ , the discrepancy of  $F_h$  between the Euler-viscous hybrid solver and the conventional RANS solver is largest. To further show the discrepancy of wave loads, the average error of wave loads under different  $H_V$  is presented in Fig. 4.4.2.

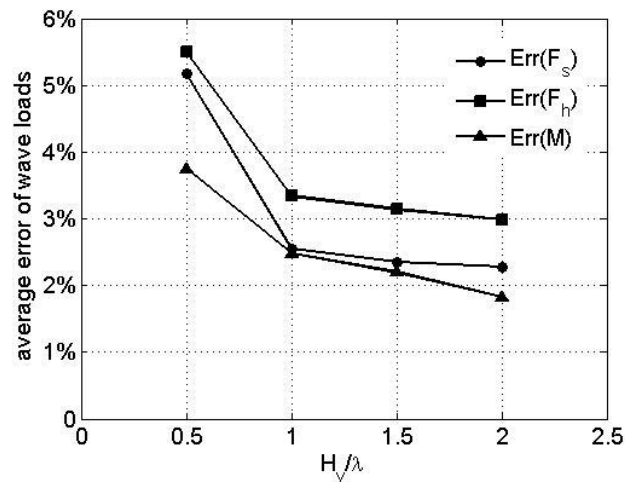


Fig. 4.4.2 The average error of wave loads at different  $H_V$

In Fig. 4.4.2, it is found that with the increase of  $H_V$ , the average error decreases. It indicates that the numerical errors can be induced by neglecting the viscosity, due to cut-off of the width of the viscous domain. The average error is very large if  $H_V$  is smaller than  $\lambda$ . Otherwise, when  $H_V$  is larger than  $\lambda$ , the average error reduces slowly with the increase of  $H_V$ . In addition, it is noted that the error of  $F_h$  is more sensitive to the width of the viscous domain, which is always above 3%.

#### 4.4.2 The effects of $H_V$ on CPU time

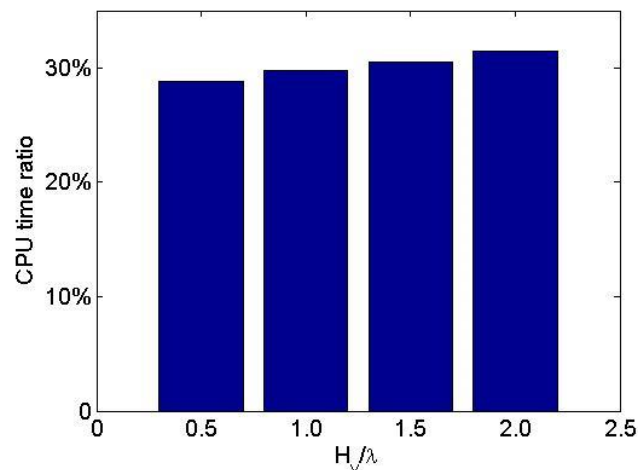


Fig. 4.4.3 The CPU time ratio against width ( $H_V$ ) of the viscous domain

The CPU time ratio at different height  $H_v$  of the viscous domain is shown in Fig. 4.4.3, which shows that the influence of  $H_v$  on computational efficiency is less significant, comparing with that of  $L_v$ . Because the mesh in the vertical direction is coarse far away from the free surface, the CPU time is reduced slightly with the decrease of  $H_v$ . Considering both the computational accuracy and efficiency,  $H_v=1.5\lambda$  is chosen for the Euler-viscous hybrid solver, which can save almost 70% CPU time while the average error is below 3%.

## 4.5 The effects of the length ( $L_{tr}$ ) of the transition zone in the viscous domain

Table 4.5.1 The mesh for study the effects of  $L_{tr}$

(a) The mesh for the conventional RANS solver

Conventional RANS domain				
$L_c$	$H_c$	$n_{Lc}$	$n_{Bc}$	$n_{Hc}$
$8\lambda$	$2\lambda$	200	80	30

(b) The mesh for the Euler-viscous hybrid solver

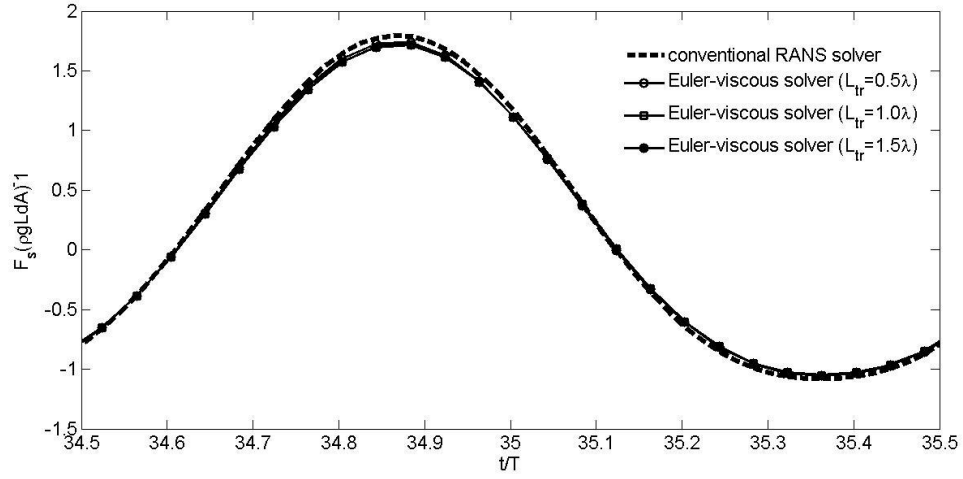
No.	Euler domain					Viscous domain					
	$L_E$	$H_E$	$n_{L_E}$	$n_{B_E}$	$n_{H_E}$	$L_v$	$H_v$	$L_{tr}$	$n_{L_v}$	$n_{B_v}$	$n_{H_v}$
1	$8\lambda$	$2\lambda$	100	40	15	$4\lambda$	$2\lambda$	$0.5\lambda$	200	80	30
2	$8\lambda$	$2\lambda$	100	40	15	$4\lambda$	$2\lambda$	$1\lambda$	200	80	30
3	$8\lambda$	$2\lambda$	100	40	15	$4\lambda$	$2\lambda$	$1.5\lambda$	200	80	30

The length of the transition zone plays an important role on the numerical simulations based on the Euler-viscous hybrid solver, which is used to dissipate the viscous effects in the transition zone. The length of the transition zone must affect the computational accuracy. In order to study its effects, some cases are simulated with different  $L_{tr}$ , i.e.,  $L_{tr}=0.5\lambda$ ,  $L_{tr}=\lambda$ , and  $L_{tr}=1.5\lambda$ . The mesh used for the Euler-viscous hybrid solver is described in Table 4.5.1 (b). The computational results by the Euler-viscous hybrid solver are compared with those by the conventional RANS solver as well. The mesh for the conventional RANS solver is shown in Table 4.5.1 (a). The effects of  $L_{tr}$  on computational precision and efficiency are discussed.

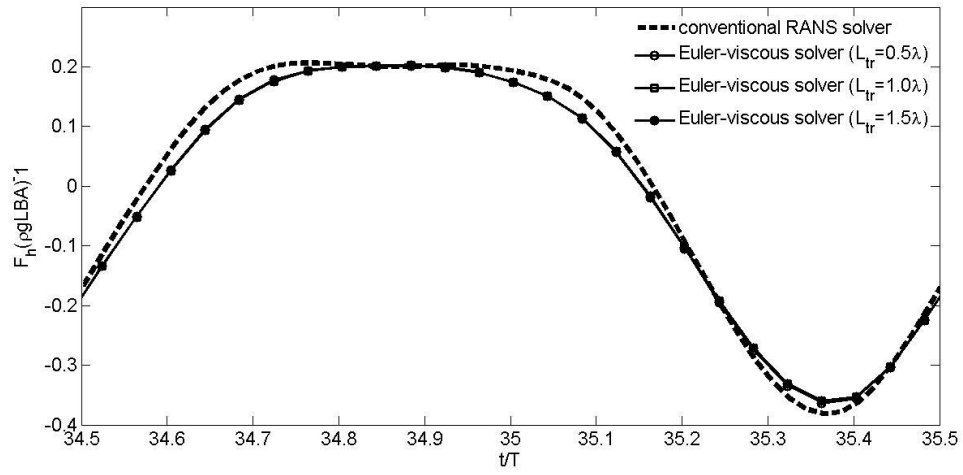
### 4.5.1 The effects of the length ( $L_{tr}$ ) of the transition zone on wave loads

Wave loads at different  $L_{tr}$  over one wave period from  $t/T=34.5$  to  $t/T=35.5$  are shown in Fig. 4.5.1, where the numerical results by the Euler-viscous hybrid solver agree very well with those by the conventional RANS solver. The discrepancy between the Euler-viscous hybrid solver and the conventional RANS solver is small. Furthermore, at different  $L_{tr}$ , numerical results based on the Euler-viscous hybrid solver change a little. Thus, it can be concluded that wave loads are not sensitive to the length of the transition zone.

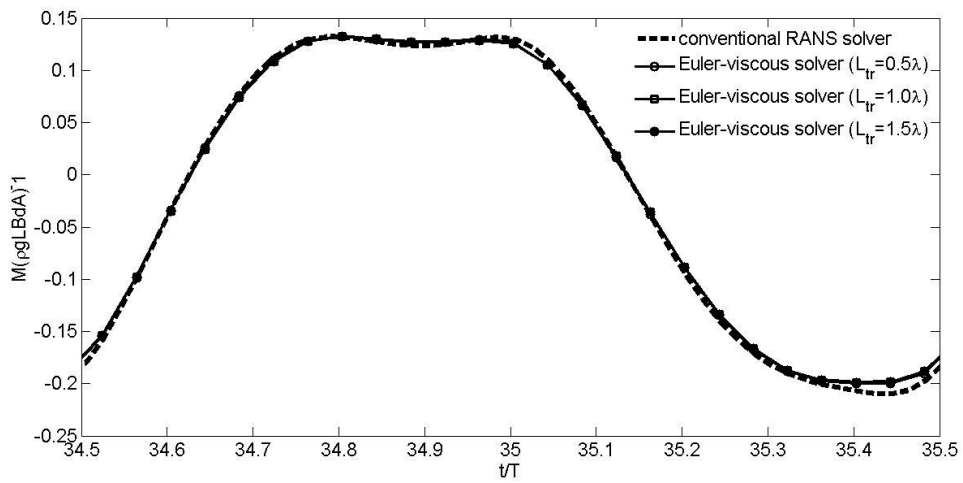




(a) The comparison of the horizontal force ( $F_s$ )



(b) The comparison of the vertical force ( $F_h$ )



(c) The comparison of the moment ( $M$ )

Fig. 4.5.1 The comparison of wave loads at different  $L_{tr}$

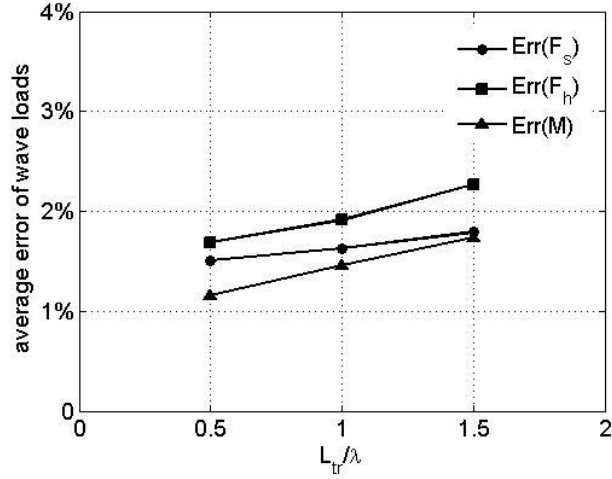


Fig. 4.5.2 The average error of wave loads at different  $L_{tr}$

Then, the average error of wave loads at different  $L_{tr}$  is shown in Fig. 4.5.2. It can be seen that with the increase of  $L_{tr}$ , the average error increases. The numerical error can be explained in two aspects. Firstly, the numerical error can be induced by the difference of wave elevation between the Euler domain and the viscous domain, due to the viscous effects. Specifically, in the transition zone, the free surface is relaxed according to the wave elevations in the Euler domain, which is blending of free surface in the Euler domain and the viscous domain. Nevertheless, the blending result cannot fully reflect the difference of the free surface between the Euler domain and the viscous domain. Secondly, the transition zone may be too long so that viscous effects close to the structure are cancelled.

#### 4.5.2 The effects of the length ( $L_{tr}$ ) of the transition zone on computational efficiency

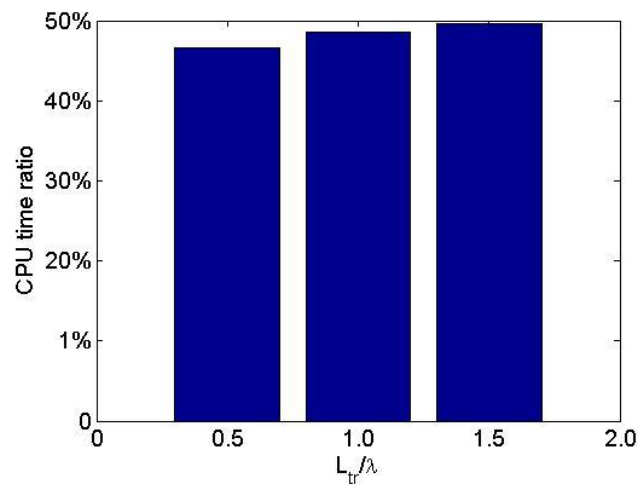


Fig. 4.5.3 The CPU time ratio at different  $L_{tr}$

The comparison of CPU time ratio is shown in Fig. 4.5.3. It indicates that the influence of the length ( $L_{tr}$ ) of transition zone on consumed CPU time is small. With the increase of  $L_{tr}$ , the

CPU time increases a little. Considering both computational accuracy and efficiency,  $L_{tr}=0.5\lambda$  is selected for the Euler-viscous hybrid solver.

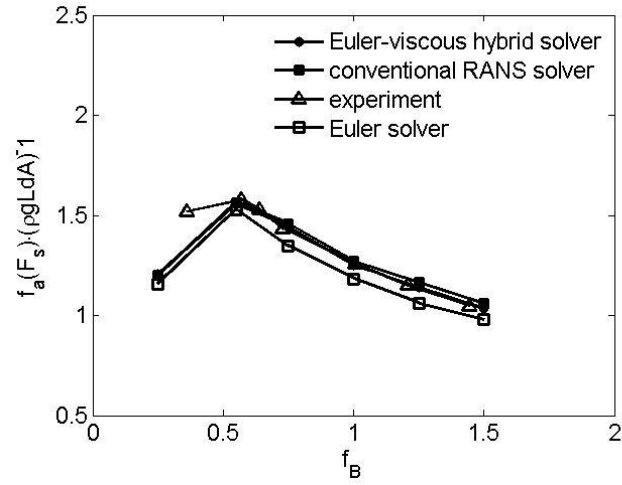
#### 4.6 The validation of the Euler-viscous hybrid solver

Based on the study from section 4.2 to section 4.5, the time step  $\Delta t=T/500$  is selected for both the Euler solver and the viscous solver. It can be found that the mesh resolution can be different in the Euler domain and the viscous domain, due to the different convergence property of the Euler solver and the viscous solver. However, the data transition under different mesh resolution can induce numerical error, which can affect the computational precision. Besides computational accuracy, the computational efficiency is also affected by the mesh resolution. Based on previous results, the mesh resolution with  $nB_E=40$ ,  $nL_E=100$ ,  $nH_E=15$ ,  $nB_V=80$ ,  $nL_V=200$ , and  $nH_V=30$  is efficient to be applied for wave-fixed structure interactions by using the Euler-viscous hybrid solver. The computational efficiency can be increased remarkably by reducing the size of the viscous domain. Considering both accuracy and efficiency, the viscous domain size with  $L_V=2\lambda$  and  $H_V=1.5\lambda$  should be used, corresponding to the average error below 3%. Meanwhile, the length of the transition zone  $L_{tr}=0.5\lambda$  in the viscous domain is used. The above computational configuration is applied for the validation of the Euler-viscous hybrid solver below.

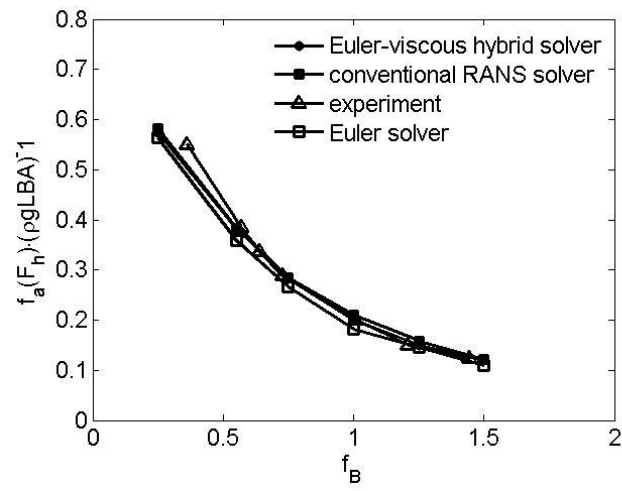
In order to validate the Euler-viscous hybrid model for interaction of a surface-piercing fixed structure with waves, a series of numerical simulations are carried out. The sketch of interaction of a surface-piercing fixed structure ( $B=0.5\text{m}$  and  $l=0.5\text{m}$ ) with waves has been shown in Fig. 4.1.1. Different incident waves are generated in the numerical simulations, where wave lengths  $\lambda=6.28\text{m}$ ,  $\lambda=2.86\text{m}$ ,  $\lambda=2.1\text{m}$ ,  $\lambda=1.58\text{m}$ ,  $\lambda=1.25\text{m}$ , and  $\lambda=1.05\text{m}$  with the same wave height  $H_w=0.07\text{m}$ . The initial water draft is  $d=0.25\text{m}$ . The water depth  $h$  is equal to the wave length  $\lambda$ . A non-dimensional wave frequency  $f_B$  is defined as  $f_B=0.5\cdot(2\pi/T)^2\cdot B/g$ . The corresponding non-dimensional parameters are described in Table 4.6.1. For the validation, the time step is kept constant as  $\Delta t=T/500$  for the Euler solver, the conventional RANS solver and the Euler-viscous hybrid solver.

Table 4.6.1 Non-dimensional parameters of incident waves

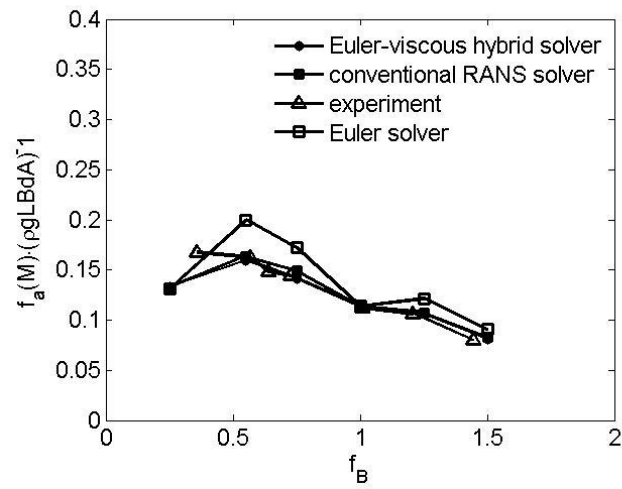
No.	$f_B$	$\lambda/d$	$h/d$	$H_w/d$
1	0.25	25.12	25.12	0.28
2	0.55	11.44	11.44	0.28
3	0.75	8.40	8.40	0.28
4	1.0	6.32	6.32	0.28
5	1.25	5	5	0.28
6	1.5	4.2	4.2	0.28



(a) The comparison of the horizontal force ( $F_s$ ) with different incident waves



(b) The comparison of the vertical force ( $F_h$ ) with different incident waves



(c) The comparison of the moment ( $M$ ) with different incident waves

Fig. 4.6.1 The comparison of wave loads with different incident waves

In order to study both computational accuracy and efficiency, numerical results based on the Euler-viscous hybrid solver with the efficient computational configuration are compared with the experimental results (Tanizawa, K., and Minami, M., 1998), the numerical results based on the conventional RANS solver, and the numerical results based on the Euler solver.

For comparing with the experimental result, the first-harmonic of the horizontal force, the vertical force and the moment is obtained by Fast Fourier Transform (FFT). Wave loads in 10 continuous wave periods are used for FFT after the quasi-steady state is achieved. The comparison of the 1<sup>st</sup> order horizontal force, vertical force and moment is shown in Fig. 4.6.1 (a)~(c). It can be seen that both the Euler-viscous hybrid results and the conventional RANS results agree well with the experimental results. The discrepancy between the conventional RANS results and the experimental results is due to some unknown physical properties such as friction coefficients of the structure. Besides that, the discrepancy between the Euler-viscous hybrid results and the conventional RANS results is very small. On the other hand, the Euler results cannot match well with the experimental results and the conventional RANS results. That's because due to the neglect of the viscous effects, the Euler model is insufficient, which is also mentioned in some author's work (Li and Lin, 2010). Hence, only the conventional RANS solver and the Euler-viscous hybrid solver can be used for interaction of a surface-piercing structure with waves.

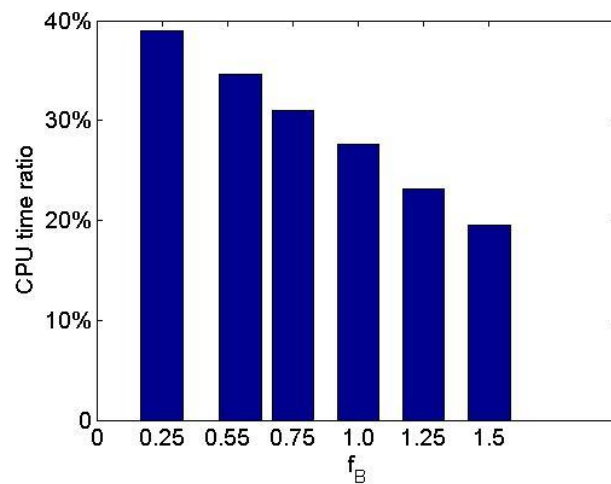


Fig. 4.6.2 The CPU time ratio against frequency of incident waves

Besides the comparison of wave loads, the computational efficiency is also compared with different incident waves. The ratio of CPU time between the Euler-viscous hybrid solver and the conventional RANS solver is shown in Fig. 4.6.2. It indicates that with the increase of the wave frequency  $f_B$ , the computational efficiency increases. Considering the same wave height  $H_w$  is applied, the wave steepness increases, when the wave length  $\lambda$  is reduced. It means that with larger steepness, as  $f_B$  changes from  $f_B=0.25$  to  $f_B=1.25$ , the computational efficiency is

higher. Furthermore, it can be seen that more than 80% CPU time can be saved by the Euler-viscous hybrid solver at  $f_B=1.5$ .

## 4.7 Summary

From this chapter, the convenient mesh resolution and suitable configuration can be obtained by a series of numerical tests. Firstly, the convergence study is carried out based on the Euler solver and the conventional RANS solver separately. The sufficient mesh resolution for the Euler solver and the conventional RANS solver can also be used for the Euler solver and the complementary RANS solver. Then, by the study of computational robustness, the convenient configuration including the size of the viscous domain and the length of the transition zone can be found.

According to convergence study of the Euler-viscous hybrid solver, it indicates that the numerical robustness of the hybrid solver can be affected by mesh resolution, the length of the viscous domain, the width of the viscous domain, and the length of the transition zone.

Specifically, different mesh resolution in the Euler domain and the viscous domain increases the computational efficiency, however reduces the computational accuracy. The length of the viscous domain influences the computational robustness remarkably. With the decrease of the length of the viscous domain, the computational efficiency increases, while the computational accuracy decreases. For the width of the viscous domain, it affects the computational efficiency insignificantly. However, with the decrease of the width of the viscous domain, the accuracy goes down as well. For the length of the transition zone, it affects a little on the computational efficiency. With the increase of the length of the transition zone, the computational accuracy decreases a little.

In summary, the computational efficiency of the Euler-viscous hybrid solver is increased significantly. Meanwhile, the computational accuracy can be kept the same as that of the conventional RANS solver. In some cases, more than 85% CPU time can be saved.

# **Chapter 5 Investigation of wave interaction with surface-piercing fixed structure subjected to complex seabed topography**

## **5.1 Introduction**

Water wave propagation over complex seabed topography is an attractive and practical problem. When ocean waves propagate towards the coastal zone, near the sea shore, the seabed topography is generally not even and the water depth changes from the deep water to shallow water condition. Consequently, the water wave property changes significantly. The wave propagation with seabed effects has been studied by many researchers. The wave field is influenced remarkably by the reflection and diffraction from seabed, as shoaling on the shore (e.g., Mei and Liu, 1993). The non-linearity of the waves can be enhanced by the complex topography, which is observed by experiments (e.g., Beji and Battjes, 1993) and numerical simulations (e.g., Kirby, 1996).

In most work (Mei, 1985; Liu and Yue, 1998; Porter and Porter, 2003; Heathershaw, 1982; Davies and Heathershaw, 1984), the seabed topography is specified by some simple functions such as a sinusoidal function or a slope function, which can be seen in the ocean environment. Nevertheless, in the coastal area, the topography is often more complex. Some bottom-mounded submerged structures often exist, such as breakwaters. Submerged bottom-mounded structures have many advantages in coastal engineering compared to surface-piercing structures as mentioned by Hur et al., 2011. e.g., more convenient for ship navigation and lower construction cost. Submerged structures can affect the propagation of water waves (Chang and Liu, 2007; Rahman and Al Womera, 2013; Koley et al., 2015; Liu and Li, 2017). Generally speaking, such submerged structures may be considered to alter the seabed topography.

In this study, wave-structure interaction subjected to complex seabed topography is numerically studied. As sketched in Fig. 5.2.1, a submerged breakwater is mounted on a flat seabed. The seabed effects on the wave diffraction by a fixed structure are carefully examined.

## **5.2 Problem description**

The sketch of the problem to be considered is shown in Fig. 5.2.1, in which a surface-piercing floating structure is fixed and interacts with incoming waves propagating over submerged bottom-mounted structure. The breadth, height and draft of the surface-piercing structure are  $B$ ,  $l$  and  $d$ , respectively. The bottom-mounted structure is trapezium. The breadth of its top and bottom surface and its submerged depth are  $B_2$ ,  $B_3$  and  $d_2$ , respectively. The water depth far

away from the bottom-mounted submerged structure is equal to the incident wave length  $\lambda$ . In this investigation,  $B=0.5\text{m}$ ,  $l=0.5\text{m}$  and  $d=0.25\text{m}$ .

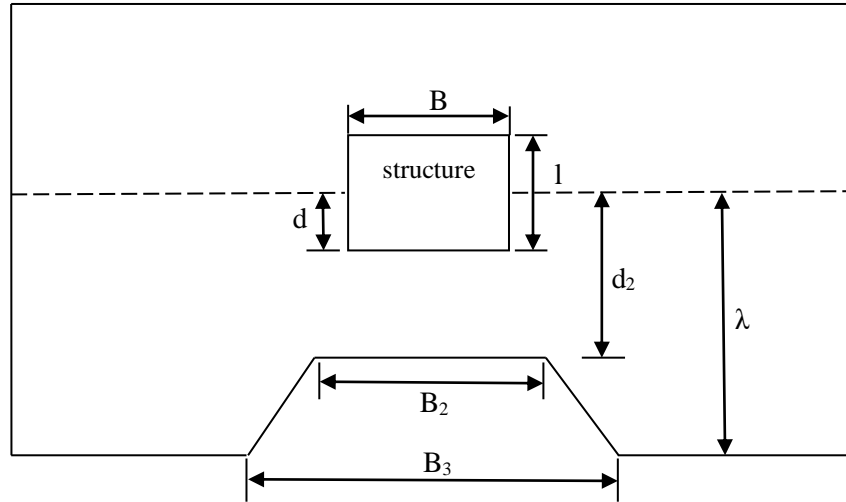


Fig. 5.2.1 The sketch of the wave-fixed structure over the complex topography

### 5.3 The numerical methods

It is understood that when the gap between the floating structure and the submerged structure becomes small, vortex shedding may become more significant. Consequently, the potential theory based solver or the Euler equation may not be applicable to deal with this problem and a Navier-Stokes solver may be necessary. However, in the area far away from structures, the Euler's equation or fully nonlinear potential theory are sufficient in the case without wave breaking. For this reason, the present Euler-viscous hybrid solver is used here for maximising the computational robustness. In the Euler domain, the viscosity is set as zero. In the viscous domain, the complementary RANS solver and the complementary RNG k-epsilon model are considered. The detail of the numerical model is described in Chapter 3. The computational domain and mesh are introduced below. The validation is conducted firstly before a systematic numerical investigation. The computational efficiency is discussed finally.

#### 5.3.1 The computational domain and mesh

The configuration of the computational domain adopted here is similar to that used in section 3.3. In this investigation, the computational mesh around the submerged structure and the floating structure are refined in order to well capture the reflection of the waves by the structures and the turbulent flow in the gap between two structures. The computational domain and mesh are illustrated in Fig. 5.3.1.

The length and the width of the Euler domain are  $L_E=8\lambda$  and  $B_E=2\lambda$  respectively. The length of the viscous domain is set as  $L_V=2\lambda$ , which is one fourth of the Euler domain and the width  $B_V=B_E$  is applied. Both the fixed structure and the submerged structure are included in the



Euler domain and the viscous domain. The parameters related with the mesh resolution are described in the Table 5.3.1 (b), according to the convergence study presented in Chapter 3.

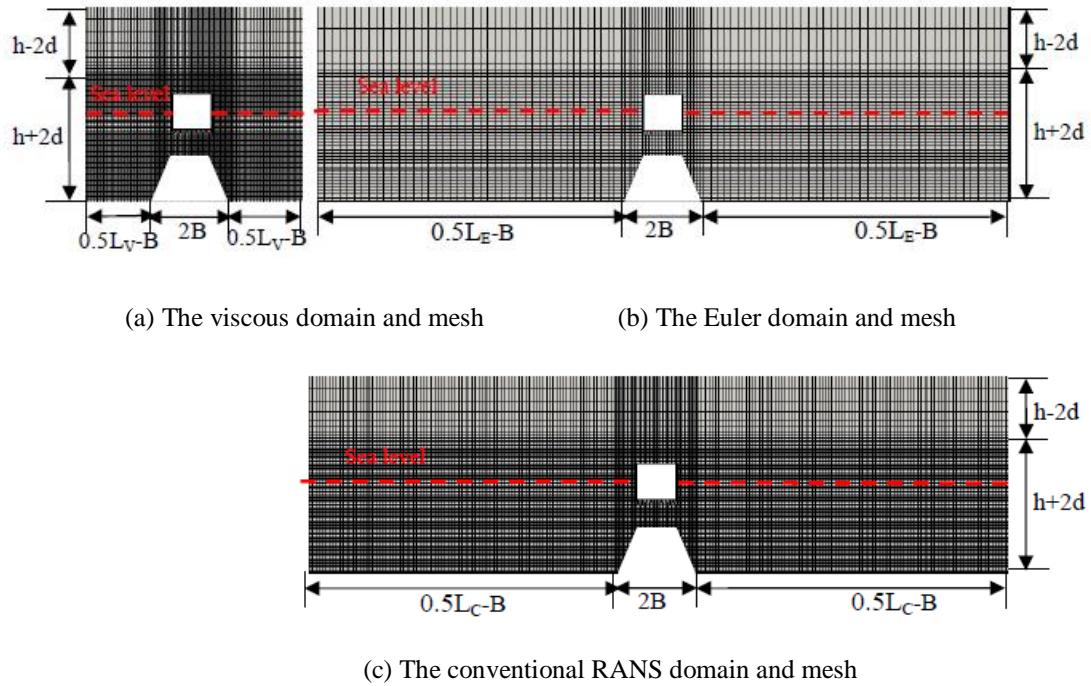


Fig. 5.3.1 The computational domain and mesh used in the simulation

Table 5.3.1 The mesh resolution for conventional RANS solver and Euler-viscous hybrid solver

(a) The mesh for conventional RANS solver

Conventional RANS domain				
$L_C$	$H_C$	$nL_C$	$nB_C$	$nH_C$
$8\lambda$	$2\lambda$	200	80	30

(b) The mesh for Euler-viscous hybrid solver

Euler domain					Viscous domain					
L <sub>E</sub>	H <sub>E</sub>	nL <sub>E</sub>	nB <sub>E</sub>	nH <sub>E</sub>	L <sub>V</sub>	H <sub>V</sub>	L <sub>tr</sub>	nL <sub>V</sub>	nB <sub>V</sub>	nH <sub>V</sub>
8λ	2λ	100	40	15	2λ	2λ	0.5λ	200	80	30

### 5.3.2 The validation of the numerical methods

In order to validate the hybrid solver for wave interacting with the floating structure subjected to complex seabed topography, the results of some cases are compared with corresponding results obtained by the conventional RANS solver. In these cases,  $B_2=B$  and  $B_3=3B$ .  $d_2$  varies from  $0.2\lambda$  to  $0.5\lambda$ . The wave length of the incident wave  $\lambda=2.1\text{m}$  and the wave height is  $H_w=0.07\text{m}$ .

The time histories of non-dimensional moment at  $d_2=0.2\lambda$  by both the Euler-viscous hybrid solver and the conventional RANS solver respectively are shown in Fig. 5.3.2. It can be seen

that the moment varies periodically. The quasi-steady state can be obtained after 15 wave periods. Most importantly, the moment predicted by the Euler-viscous hybrid solver agrees well with that by the conventional RANS solver. Furthermore, wave loads over one wave period in the quasi-steady state are also considered in the comparison. Some results are shown in Fig. 5.3.3. Once again, the wave loads estimated by the present solver agree with those by the conventional RANS solver. The average error for the horizontal, vertical force and the moment between two solvers are 1.2%, 1.4% and 0.7%, respectively. Although no experimental data are used in the validation study, the agreement between the present solver and the conventional RANS solver may conclude that the present solver has a similar accuracy as the conventional RANS solver for the problems concerned in this Chapter.

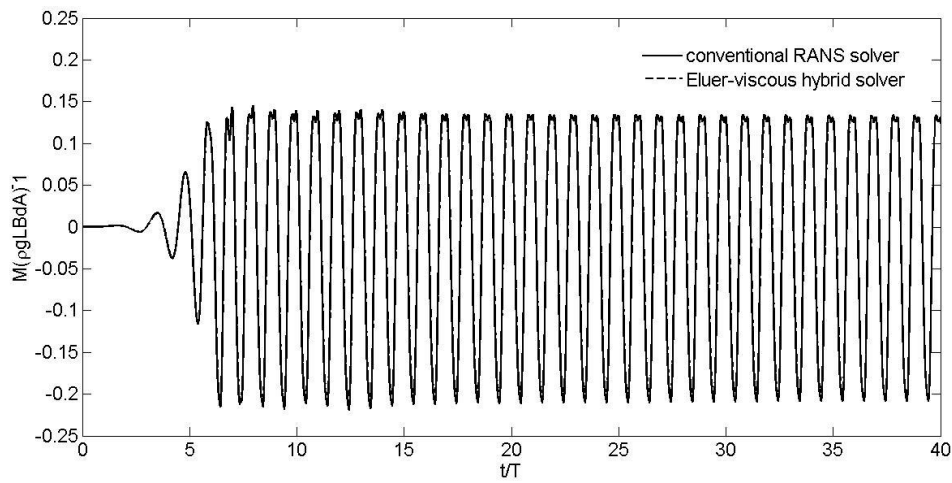
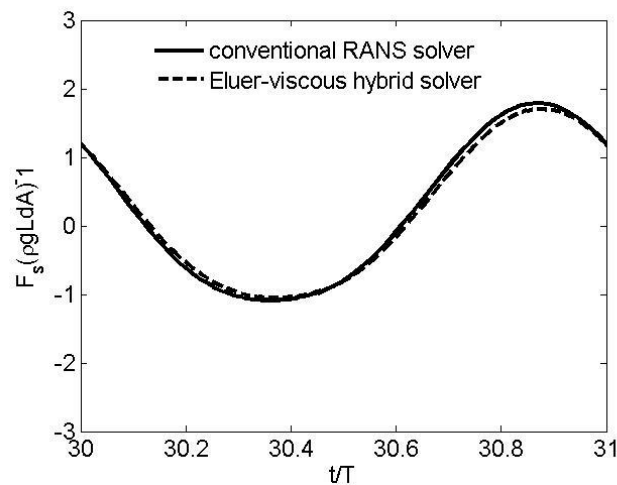
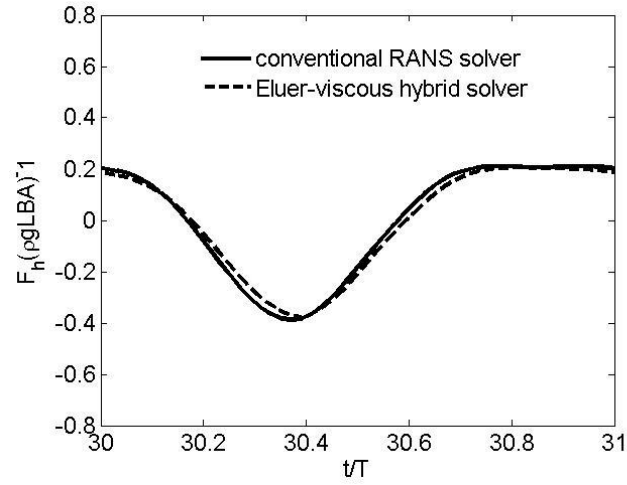


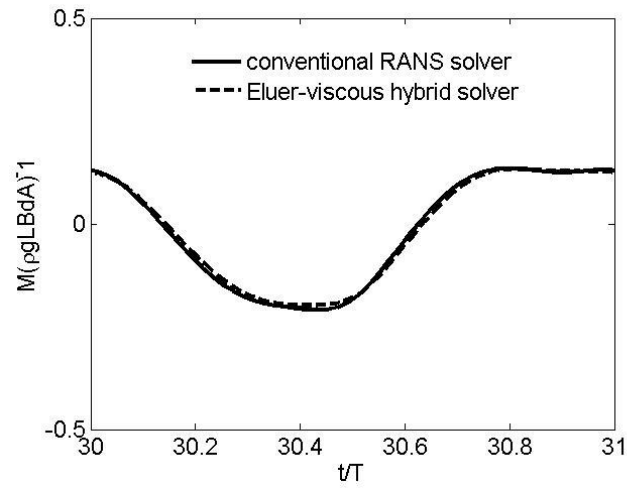
Fig. 5.3.2 Comparison of the time histories of the moment acting on the floating structure subjected to water waves propagating over submerged structure ( $d_2=0.2\lambda$ ,  $\lambda=2.1\text{m}$ ,  $H_w=0.07\text{m}$ )



(a) The horizontal force



(b) The vertical force



(c) The moment

Fig. 5.3.3 The comparison of wave loads in one wave period for wave-structure interaction under the effects of the submerged structure ( $d_2=0.2\lambda$ ,  $\lambda=2.1\text{m}$ ,  $A=0.035\text{m}$ )

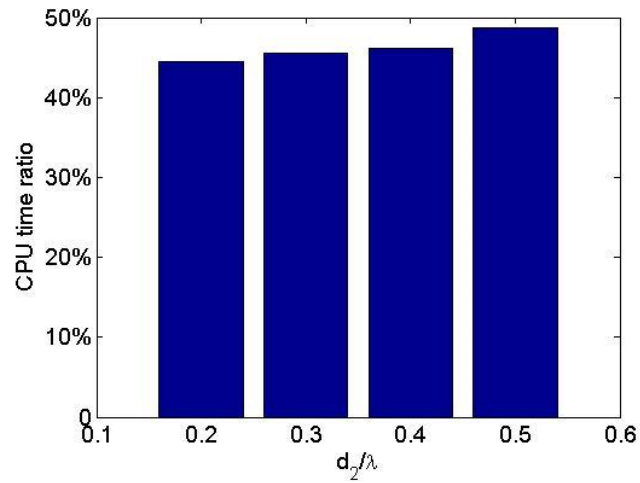


Fig. 5.3.4 The CPU time ratio at different  $d_2$  for wave interactions with the floating structure subject to a submerged structure

### 5.3.3 The CPU time consumed in the simulation

What really interested here is whether the present hybrid model has higher computational efficiency compared to the conventional RANS solver. For this purpose, the comparison of the CPU time spent by both solvers for all cases considered in the validation study is shown in Fig. 5.3.4. For convenience, the ratio of the CPU time spent by the present solver against that by the RANS solver is presented. It is clear that the hybrid model only requires less than 50% of the CPU time that is demanded by the conventional RANS solver. It shall be noted that the mesh resolution used by the conventional RANS solver is the same as that used in the viscous domain of the hybrid solver, which is finer than that used in the Euler domain of the hybrid solve, attributing to the fact that the Euler solver requires coarser mesh resolution than the conventional RANS solver to achieve convergent results. This means that the higher computational efficiency of the present solver attributes to the lower mesh resolution requirement by the Euler solver, compared with the conventional RANS solver.

## 5.4 Results and discussion

In order to investigate effects of the submerged structure on the hydrodynamics associated with the fixed body subjected to incident waves, systematic simulations are carried out under submerged structures with different water depth ( $d_2$ ) and top width ( $B_2$ ). The influence of the submerged structure on wave loads is discussed.

### 5.4.1 The effects of the water depth ( $d_2$ ) on wave loads

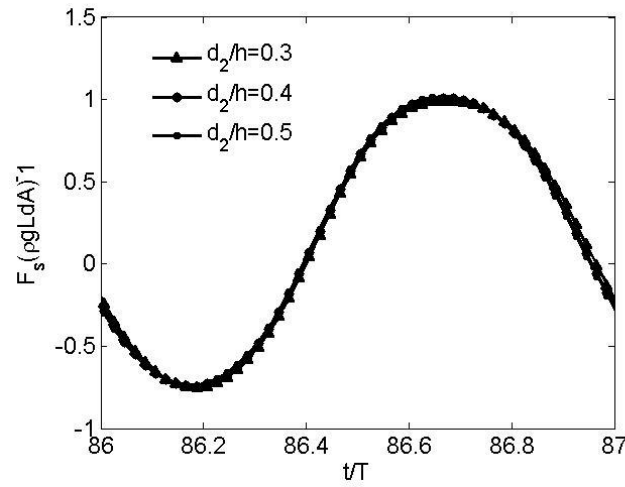
In order to study the effects of  $d_2$  on wave loads, various cases with different value of  $d_2$  are simulated by using the Euler-viscous hybrid solver with  $d_2/h=0.3$ ,  $d_2/h=0.4$ , and  $d_2/h=0.5$ . In numerical simulations, different incident waves with  $f_B=0.25$ ,  $f_B=0.55$ ,  $f_B=0.75$ ,  $f_B=1.0$ , and  $f_B=1.5$  are used as described in Table 5.4.1. In these cases, the same top width  $B_2=B$  is applied.

Table 5.4.1 The incident waves

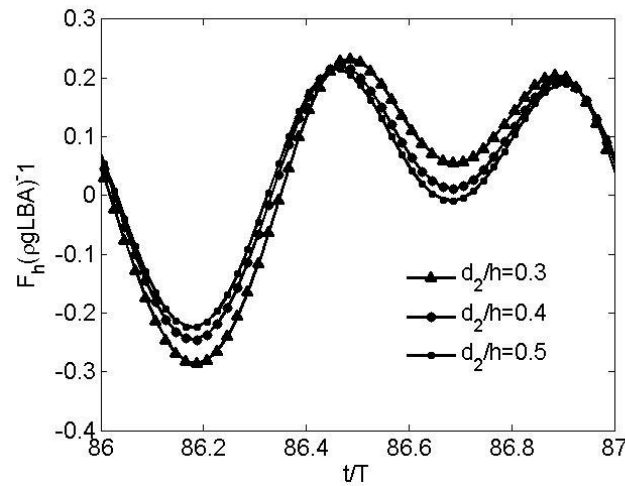
$f_B$	$\lambda$ (m)	$H_w$ (m)	$A$ (m)	$h$ (m)	$\lambda/d$	$H_w/d$	$h/d$
0.25	6.2833	0.07	0.035	6.2833	25.13	0.28	25.13
0.55	2.8560	0.07	0.035	2.8560	11.424	0.28	11.424
0.75	2.1	0.07	0.035	2.0944	8.3776	0.28	8.3776
1.0	1.58	0.07	0.035	1.58	6.32	0.28	6.32
1.5	1.05	0.04	0.02	1.05	4.2	0.16	4.2

Similar to Fig. 5.3.3, the wave loads in the cases with  $f_B=1.5$  over one wave period (from  $t/T=86$  to  $t/T=87$ ) in quasi-steady state are illustrated in Fig. 5.4.1, in which different values of  $d_2$  are used.. It is found that the effects of  $d_2$  on horizontal force are insignificant, whereas

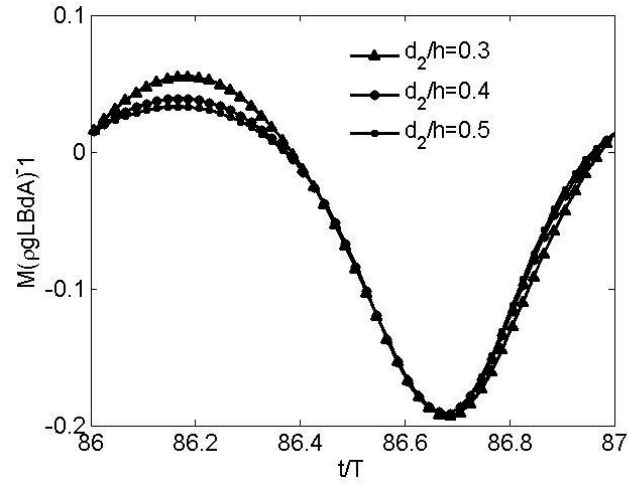
the vertical force and the moment are considerable affected by  $d_2$ , especially when the  $d_2$  is equal or smaller than  $0.3h$ . Specifically, as  $d_2$  reduces, the vertical force and moment seem to increase. For analyzing the effects of  $d_2$  on the amplitude of wave loads under different incident waves, the FFT is conducted for wave loads in the quasi-steady state over 10 continuous wave periods. The comparison of the amplitude of the first harmonic ( $f_a$ ) of the horizontal force, the vertical force, and the moment are shown in Fig. 5.4.2 (a)~(c). It should be noted that if wave length is too small,  $d_2$  may be smaller than the initial draft ( $d$ ) of the floating structure. This is not reasonable for the cases configured here. Hence, at  $d_2=0.2\lambda$ , the case with  $f_B=1.5$  are not considered in the study.



(a) The horizontal force

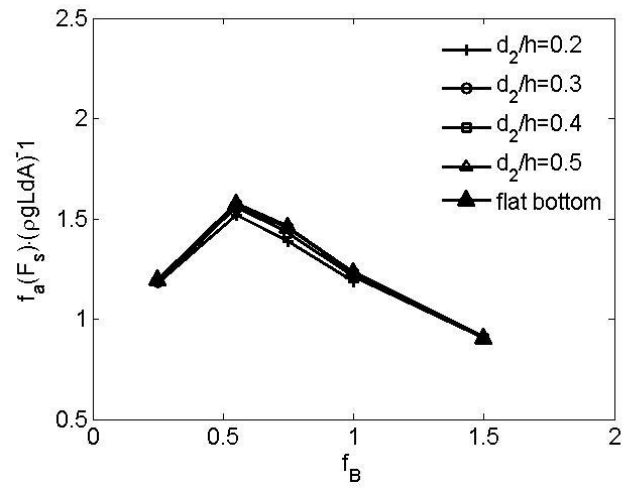


(b) The vertical force

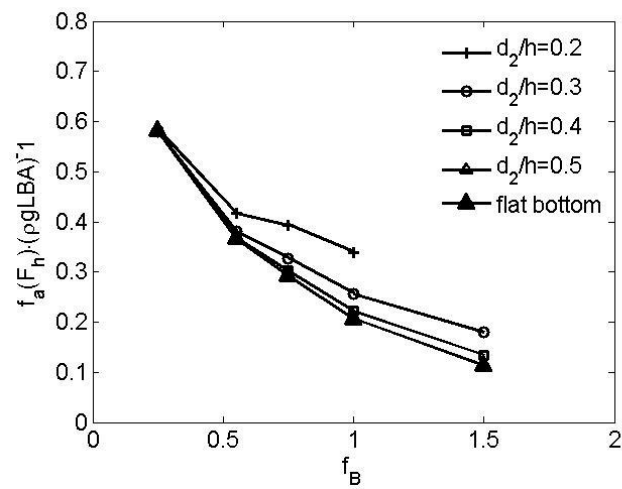


(c) The moment

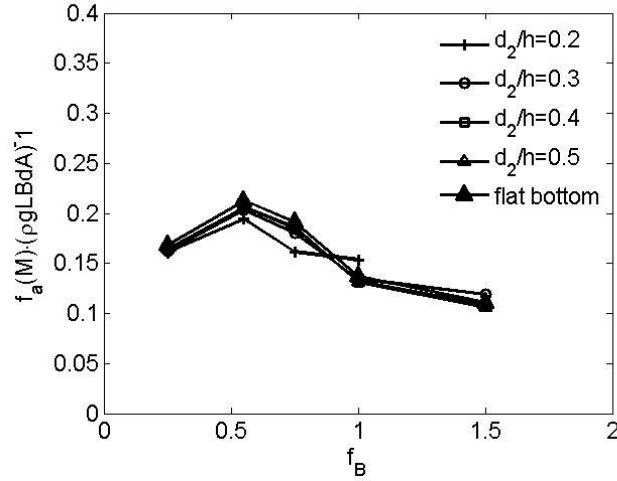
Fig. 5.4.1 The comparison of wave loads under submerged structure with different  $d_2$



(a) 1<sup>st</sup> order horizontal force



(b) 1<sup>st</sup> order vertical force



(c) 1<sup>st</sup> order moment

Fig. 5.4.2 The comparison of 1<sup>st</sup> order wave loads under effects of submerged structures at different  $d_2$

The 1<sup>st</sup> harmonics of the wave loads with different wave length and different  $d_2$  are shown in Fig. 5.4.2. It can be seen that for different wave length, as  $d_2$  decreases from  $d_2=0.5\lambda$  to  $d_2=0.2\lambda$ , the 1<sup>st</sup> order horizontal force decreases slightly. However, the variation is insignificant. The first order moment (Fig. 5.4.2 (c)) seems not to be affected by the water depth  $d_2$  under different wave conditions considered in this study. For specific wave length, the first order vertical force ( Fig. 5.4.2 (b)) increases as  $d_2$  decreases, except the long-wave case with  $\lambda/d=25.13$  ( $f_B=0.25$ ) in which the effect is insignificant.

In order to quantitatively analyse the amplification of the vertical force by the submerged structure, the relative amplification factor of 1<sup>st</sup> order vertical force is defined as followed, the relative amplification factor =  $\frac{f_{h, \text{str}} - f_{h, \text{org}}}{f_{h, \text{org}}}$  (5.4.1)

in which subscribes ‘str’ and ‘org’ stand for the cases with and without submerged structure. Some results are shown in Fig. 5.4.3. It is observed that as  $d_2/d < 3$ , 1<sup>st</sup> order vertical force decreases distinctively, as  $d_2/d$  increases. As  $d_2/d$  increases from  $d_2/d=3$  to  $d_2/d=6$ , 1<sup>st</sup> order vertical force decreases as well. As  $d_2/d$  is larger than  $d_2/d=6.0$ , 1st order vertical force seems not to be affected by  $d_2/d$ . Finally, as  $d_2/d$  arranging from  $d_2/d=1$  to  $d_2/d=6$ , 1<sup>st</sup> order vertical force decreases as a power function by  $2.379 \cdot (d_2/d)^{-3.31}$ . It is also interesting to find that the amplification factor seems to be less dependent on the ratio  $\lambda/d$  when  $d_2/d \approx 3.0$ . Taking  $d_2/d=2.5$  at  $\lambda/d=5$ ,  $d_2/d=2.52$  at  $\lambda/d=6.32$  for instance, the corresponding amplification factor can be obtained as 13.10% and 13.13% respectively. Nevertheless, when  $d_2/d$  is much smaller than 3.0, the ratio  $\lambda/d$  plays an important role on evaluating the amplification factor and small ratio of  $\lambda/d$  leads to more significant amplification for specific  $d_2/d$ . Taking  $d_2/d=1.68$  for

example, the corresponding amplification factor are 46.30% and 38.50% respectively, for  $\lambda/d=4.2$  and  $\lambda/d=8.37$ .

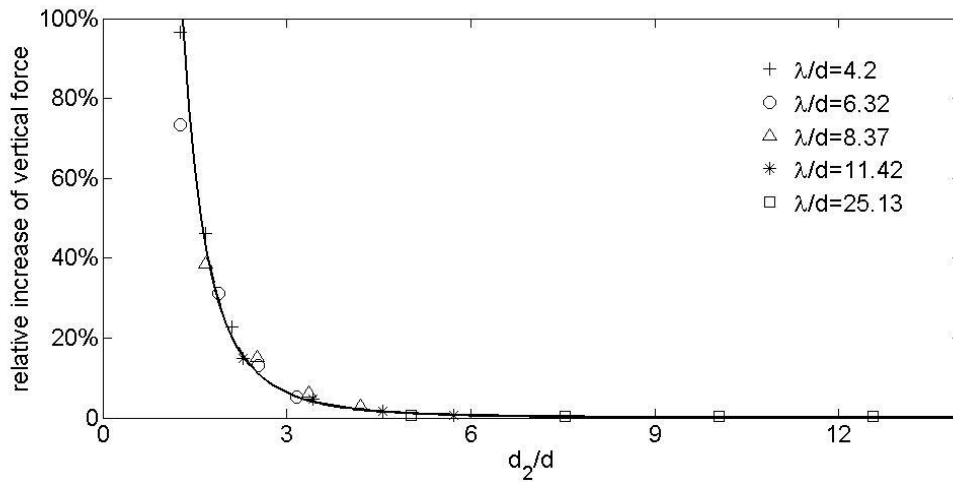
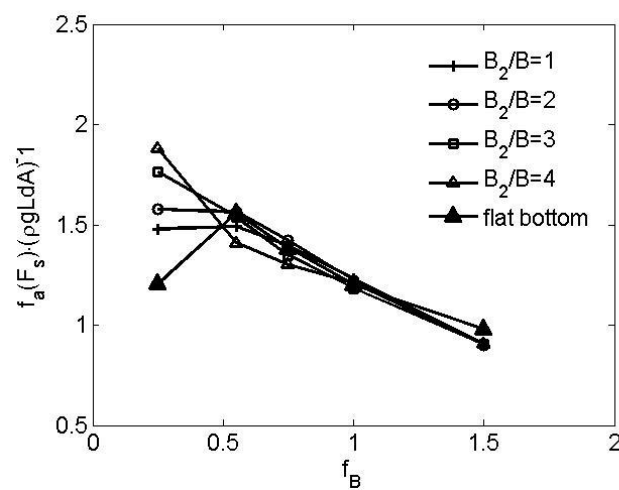


Fig. 5.4.3 the comparison of the amplification factor of linear vertical force component under different incident waves at different  $d_2$

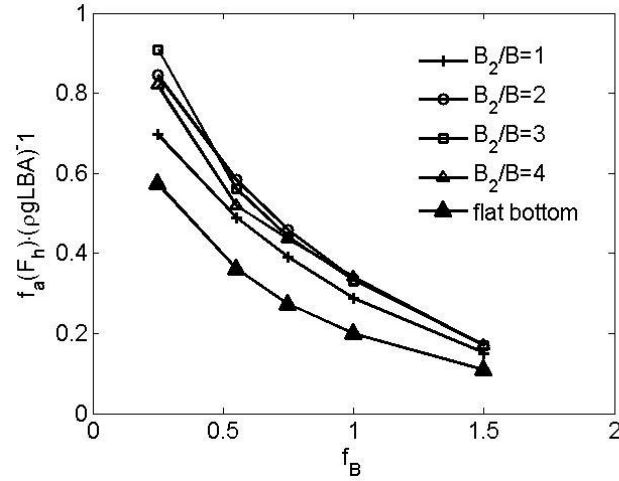
#### 5.4.2 The effects of the top width ( $B_2$ ) on the wave loads

It is understandable that the shape of the submerged structure plays important role in the above investigation. For simplification, only the effects of the width  $B_2$  are taken into account in order to shed some light on this issue. To do so, different widths  $B_2$  ranging from  $1B$  to  $4B$ , are considered, while other parameters associated with the submerged structure remain the same. All wave conditions described in Table 5.4.1 are adopted in this investigation. In these cases, the water depth ( $d_2$ ) of the submerged structure is fixed as  $d_2=1.5d=0.375m$ .

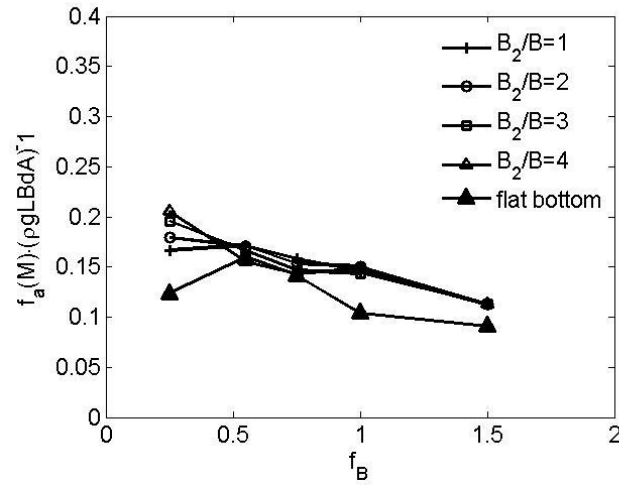


(a) 1<sup>st</sup> order horizontal force





(b) 1<sup>st</sup> order vertical force



(c) 1<sup>st</sup> order moment

Fig. 5.4.4 The comparison of 1<sup>st</sup> order of wave loads under submerged structure at different  $B_2$ . 1<sup>st</sup> order horizontal force components in the cases with different  $B_2$  are shown in the Fig. 5.4.4 (a). It can be seen that the effects of  $B_2$  are not obvious except the case with longest wave, i.e.  $f_B=0.2$ , for which the non-dimensional 1<sup>st</sup> order horizontal force  $f_a(F_s)/(\rho g L d H_w)$  grows continuously from 1.47 to 1.88, as  $B_2/B$  increasing from 1 to 4. It is also interesting to observe that for specific wave condition, e.g.  $f_B \approx 0.5$ , the submerged structures seem not to amplify but to suppress the horizontal force.

The corresponding results of the linear harmonic of moment are shown in Fig. 5.4.4(c). One may find that the linear moment harmonics fluctuates with the increase of  $B_2$ . Similar to the horizontal force, the effects of  $B_2$  are significant at  $\lambda/d=25.13$ . For small and large wave length, i.e.  $\lambda/d=4.2$ ,  $\lambda/d=6.32$  and  $\lambda/d=25.13$ , the linear moment harmonics is amplified by the submerged structure. However, for intermediate wave length, e.g.  $\lambda/d=8.37$  and  $\lambda/d=11.42$ ,

the submerged structures with different width  $B_2$  seem not to influence the moments considerably.

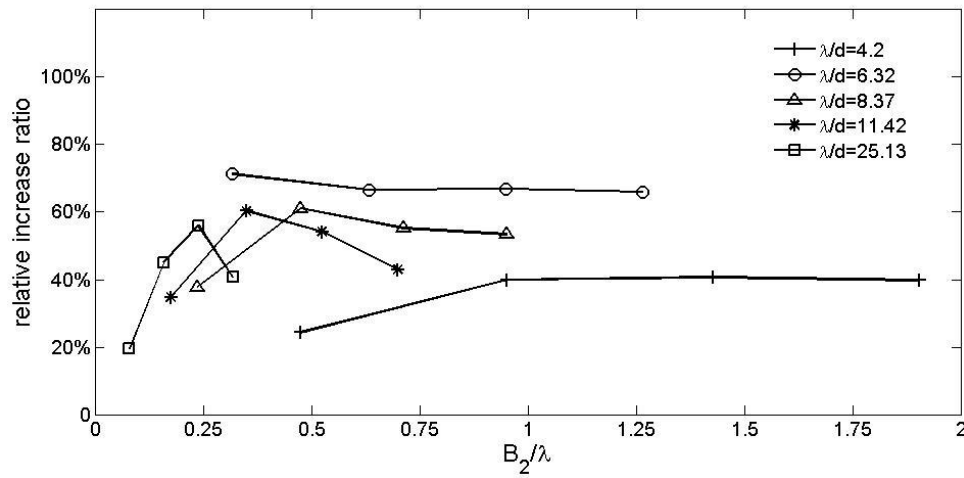


Fig. 5.4.5 The comparison of relative increase ratio under different incident waves at different  $B_2$

In section 5.4.1, it is concluded that effects of water depth  $d_2$  on the vertical force are remarkable. In fact, not only the water depth  $d_2$ , but also the top width  $B_2$  can influence the vertical force significantly. To demonstrate this, some results are shown in Fig. 5.4.4 (b). It is observed that the vertical force can be amplified by the submerged structures regardless the width of  $B_2$  and  $B_2$  may significantly influence the amplification factor. When the incident wave length  $\lambda$  is small such as  $\lambda/d=4.32$ ,  $\lambda/d=6.32$ , and  $\lambda/d=8.37$ , 1<sup>st</sup> order vertical force increases as  $B_2/B$  increases from 1 to 2, and changes slightly when  $B_2/B$  further increases. In fact, at small incident wave length, i.e., including  $\lambda/d=4.32$ ,  $\lambda/d=6.32$ , and  $\lambda/d=8.37$ , the top width  $B_2$  may be larger than the incident wave length  $\lambda$ . Subjected to the condition  $B_2/\lambda > 1$ , 1<sup>st</sup> order vertical force does not change much. For  $\lambda/d=11.42$ , and  $\lambda/d=25.13$ , 1<sup>st</sup> order vertical force increases and then decreases as  $B_2/B$  increases. It is also observed that 1<sup>st</sup> order vertical force is also related with  $B_2/\lambda$ . Hence, the relative increase ratio of 1<sup>st</sup> order vertical force is also affected by the ratio  $B_2/\lambda$ . Hence, the amplification factors of 1<sup>st</sup> order vertical force in the cases with different  $B_2/\lambda$  are analysed and some results are shown in Fig. 5.4.5. It is obviously seen that if  $B_2$  is larger than incident wave length  $\lambda$ , the amplification factor changes slightly ascending  $B_2$ . As  $B_2/\lambda$  is smaller than 1, i.e., the top width is shorter than the wave length, the amplification factor are significantly affected by  $B_2$ .

## 5.5 Summary

The influence of complex seabed topography is investigated by using the Euler-viscous hybrid solver. The effects of the top width  $B_2$  and the water depth  $d_2$  of the submerged

structure on hydrodynamics are discussed. It is found that both the water depth and the top width can affect the vertical force significantly.

1<sup>st</sup> order vertical force increases, as the water depth of the submerged structure increases except the long-wave case. The amplification factor of the 1<sup>st</sup> order vertical force decreases with the increase of  $d_2/d$ , which fulfils a power function relation.

The top width  $B_2$  has significant effects on hydrodynamics acting on the structure. For the influence of the top width on the vertical force, it shows that when the top width is smaller than the incident wave length, the amplification factor can be affected remarkably.

## Chapter 6 Euler-viscous hybrid model for interaction of a surface-piercing moving structure

In Chapter 3, the present Euler-viscous hybrid model for surface-piercing wave-structure interactions is introduced. Nevertheless, this version can only apply to deal with the problem with fixed structures due to the fact that the computational grid in both the Euler and the viscous domains are fixed Eulerian grid. In this Chapter, the function-decomposition method is also used and additional functionalities will be introduced into the present model to deal with the problems with moving structures. Similarly, both the velocity and the pressure are decomposed into two parts including Euler components and complementary components. Correspondingly, a two-phase Euler solver and a two-phase complementary viscous solver exist in the Euler domain and the viscous domain, respectively. Key numerical techniques include the dissipation of viscous effects near the boundary of the viscous domain and the interpolation of data between two computational domains. In this work, the dynamic mesh technique is used for moving the computational mesh in order to conform to the motion of the structure. Thus, the treatment of the dynamic mesh technique is included in the solution procedure of the improved version of the Euler-viscous hybrid model, which is presented in this Chapter. In addition to the dynamic mesh technique, for the simulation of free motion of floating structures under incident waves, the special technique is developed to ensure the consistence of the motions of the structure in two computational domains.

### 6.1 The mathematical model

The two-phase Euler solver with dynamic mesh is introduced firstly. Then, by the function-decomposition method, the two-phase complementary RANS solver with dynamic mesh is proposed. Finally, the corresponding complementary turbulence model under dynamic mesh is also derived by decomposition of velocity.

#### 6.1.1 Governing equations of the two-phase Euler solver with dynamic mesh

A two-phase Euler solver under dynamic mesh is applied in the Euler domain. Comparing with the two-phase Euler solver for fixed Eulerian mesh, the equation is written in term of Arbitrary Lagrangian-Eulerian (ALE) form and the flux induced by the mesh motion must be considered. The ALE form of the Euler equations and the Continuity equation are described below

$$\nabla \cdot (\mathbf{U}^I) = 0 \quad (6.1.1)$$

$$\frac{d(\rho' \mathbf{U}^I)}{dt} + [(\mathbf{U}^I - \mathbf{u}_b^I) \cdot \nabla](\rho' \mathbf{U}^I) = -\nabla(p^I) + \rho' \mathbf{g} \quad (6.1.2)$$

In equation (6.1.2),  $\frac{d(\rho' \mathbf{U}^I)}{dt}$  means the time derivative of momentum in the Euler domain.  $\mathbf{u}_b^I$  is the velocity of the mesh motion. The other variables are the same as those described in section 3.1.1 (Chapter 3). The corresponding volume fraction equation is shown as

$$\frac{d\gamma'}{dt} + \nabla \cdot [\gamma' (\mathbf{U}^I - \mathbf{u}_b^I)] = 0 \quad (6.1.3)$$

In the volume fraction equation,  $\frac{d\gamma'}{dt}$  represents the time derivative of volume fraction.

### 6.1.2 Governing equations of the two-phase complementary RANS solver with dynamic mesh

By the function-decomposition method, a two-phase complementary RANS solver under dynamic mesh is derived from the conventional RANS solver under dynamic mesh. In the viscous solver, the viscous effects are considered including the turbulence model.

By decomposing both the velocity and the pressure into two parts, it can be obtained that

$$\mathbf{U} = \mathbf{U}^I + \mathbf{U}^D \quad (6.1.4)$$

$$p = p^I + p^D \quad (6.1.5)$$

$\mathbf{U}^I$  and  $p^I$  are Euler components, which are explicit from the solution of the two-phase Euler solver described in section 6.1.1. On the other hand,  $\mathbf{U}^D$  and  $p^D$  are viscous components, which are independent unknowns.

Then, by putting  $\mathbf{U} = \mathbf{U}^I + \mathbf{U}^D$  and  $p = p^I + p^D$  into momentum equations

$$\frac{d(\rho \mathbf{U})}{dt} + [(\mathbf{U} - \mathbf{u}_b^D) \cdot \nabla](\rho \mathbf{U}) = -\nabla(p) + \nabla \cdot (\mu_t \nabla \mathbf{U}) + \rho \mathbf{g}$$

It leads to

$$\begin{aligned} & \frac{d(\rho \mathbf{U}^D)}{dt} + \{(\mathbf{U}^I \cdot \nabla) + [(\mathbf{U}^D - \mathbf{u}_b^D) \cdot \nabla]\}(\rho \mathbf{U}^D) - \nabla \cdot (\mu_t \nabla \mathbf{U}^D) + \frac{d(\rho \mathbf{U}^I)}{dt} + \{(\mathbf{U}^I \cdot \nabla) + \\ & [(\mathbf{U}^D - \mathbf{u}_b^D) \cdot \nabla]\}(\rho \mathbf{U}^I) - \nabla \cdot (\mu_t \nabla \mathbf{U}^I) = -\nabla(p^I) - \nabla(p^D) + \rho \mathbf{g} \end{aligned} \quad (6.1.6)$$

In equations (6.1.6),  $\frac{d\rho \mathbf{U}^D}{dt}$  means the time derivative of momentum.  $\mathbf{u}_b^D$  is the velocity of the mesh motion.

Similarly, by the velocity decomposition, the continuity equation  $\nabla \cdot (\mathbf{U}) = 0$  can be changed into

$$\nabla \cdot (\mathbf{U}^I) + \nabla \cdot (\mathbf{U}^D) = 0 \quad (6.1.7)$$

The convective equation of volume fraction is used for tracking the free surface, which is also transformed by the function-decomposition method, from  $\frac{dy}{dt} + \nabla \cdot [\gamma(\mathbf{U} - \mathbf{u}_b^D)] = 0$  to

$$\frac{dy}{dt} + \nabla \cdot [\gamma(\mathbf{U}^I + \mathbf{U}^D - \mathbf{u}_b^D)] = 0 \quad (6.1.8)$$

Finally, the turbulence model is also transformed into the complementary form. Taking the RNG k-epsilon model under dynamic mesh for instance, after decomposition of velocity and pressure, the corresponding complementary RNG k-epsilon equations are changed from

$$\frac{dk}{dt} + \nabla \cdot [(\mathbf{U} - \mathbf{u}_b^D) \cdot \mathbf{k}] = \nabla \cdot \left[ \left( \mu + \frac{\mu_t}{\sigma_k} \right) \nabla \mathbf{k} \right] + G - \varepsilon$$

$$\frac{d\varepsilon}{dt} + \nabla \cdot [(\mathbf{U} - \mathbf{u}_b^D) \cdot \varepsilon] = \nabla \cdot \left[ \left( \mu + \frac{\mu_t}{\sigma_\varepsilon} \right) \nabla \varepsilon \right] + (C_{1\varepsilon} - R) \cdot G \cdot \frac{\varepsilon}{k} - C_{2\varepsilon} \cdot \frac{\varepsilon^2}{k}$$

to

$$\frac{dk}{dt} + \nabla \cdot [(\mathbf{U}^I + \mathbf{U}^D - \mathbf{u}_b^D) \cdot \mathbf{k}] = \nabla \cdot \left[ \left( \mu + \frac{\mu_t}{\sigma_k} \right) \nabla \mathbf{k} \right] + G - \varepsilon \quad (6.1.9)$$

$$\frac{d\varepsilon}{dt} + \nabla \cdot [(\mathbf{U}^I + \mathbf{U}^D - \mathbf{u}_b^D) \cdot \varepsilon] = \nabla \cdot \left[ \left( \mu + \frac{\mu_t}{\sigma_\varepsilon} \right) \nabla \varepsilon \right] + (C_{1\varepsilon} - R) \cdot G \cdot \frac{\varepsilon}{k} - C_{2\varepsilon} \cdot \frac{\varepsilon^2}{k} \quad (6.1.10)$$

$\frac{dk}{dt}$  and  $\frac{d\varepsilon}{dt}$  are the time derivative of the turbulence energy and the turbulence dissipation rate respectively. The constants including  $\sigma_k$ ,  $\sigma_\varepsilon$ ,  $C_{1\varepsilon}$ , and  $C_{2\varepsilon}$  are the same as those in section 3.1.2.  $G$  and  $R$  are defined in 3.1.2 as well.

## 6.2 The numerical methods

The numerical methods used with dynamic mesh are the same as those used in Chapter 3. Finite Volume Method (FVM) is used to discretize governing equations. All parameters are located at the centre of the cell/grid. PISO scheme is applied for decoupling the velocity-pressure relation. The distinguishing difference is that the velocity ( $\mathbf{u}_b$ ) of mesh motion should be determined. This is done by using the existing OpenFOAM functionality. In OpenFOAM, the velocity ( $\mathbf{u}_b$ ) of mesh motion is an independent unknown defined at the cell centre. A diffusion equation of the velocity of mesh motion is applied in the whole computational domain, which is described as

$$\nabla \cdot (\Gamma_b \nabla \mathbf{u}_b) = 0 \quad (6.2.1)$$

In equations (6.2.1), constant  $\Gamma_b$  is the diffusion coefficient. To solve the equation, the velocity of the floating structure is required to specify the boundary condition of Eq. (6.2.1). The velocity of the floating structure may be prescribed or solved by Newton's law. By solving Eq. (6.2.1), the velocity of mesh motion, which is diffusive from the floating structure

(inner boundary) to the outer boundary (the other boundary), can be obtained. Consequently, the position of the computational mesh can be updated. It shall be noted that a smooth function may be used after the velocity of the mesh motion is solved in order to maintain a good mesh quality.

### 6.3 Computational domain configuration for the Euler-viscous hybrid solver with dynamic mesh

The configuration of the computational domain used here is similar to that used for fixed Eulerian grid. The Euler domain and the viscous domain are overlapped as illustrated in Fig. 6.3.1. The viscous domain is smaller than the Euler domain for improving the computational efficiency. The floating structure exists in both the Euler domain and the viscous domain. The motions of the floating structure in both domains are kept the same.

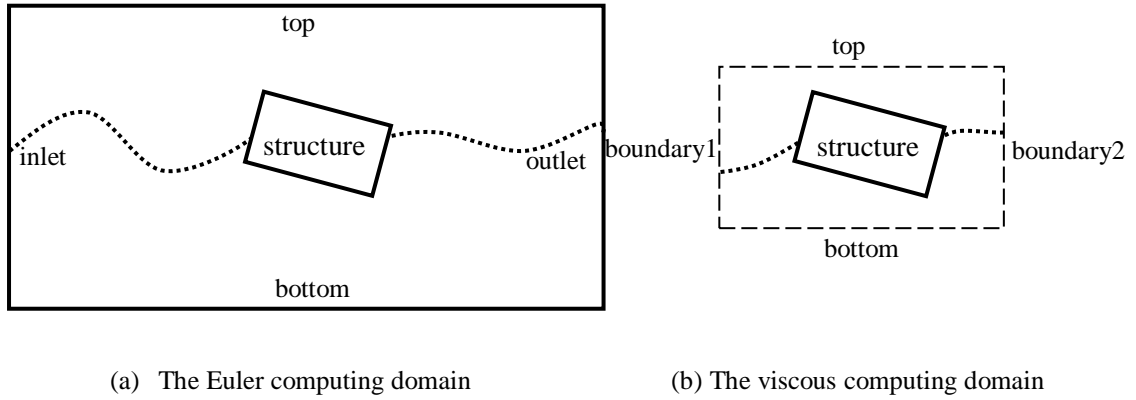


Fig. 6.3.1 the computational domain for the Euler-viscous hybrid model

### 6.4 Boundary conditions

For the problems concerning the interaction between the waves and floating bodies undergoing motions, two types of boundaries are taken into account. One is fixed boundaries, including inlet, outlet, top, bottom as shown in Fig. 6.3.1. The other is structure-surface boundary, which is the surface of the floating structure in contact with fluids. For the former, the boundary conditions are the same as those described in Section 3.4.1. In this section, only the latter is introduced.

#### 6.4.1 Structure-surface boundary condition in the Euler domain

For the structure subjected to motions, the velocity  $\mathbf{U}_{str}^I$  induced by the motion of the structure on the structure-surface can be determined by a prescribed motion for the forced motions or by Newton's 2<sup>nd</sup> law for freely floating structures. In the Euler domain, the slip-wall boundary condition should be fulfilled on the rigid body surface, since the viscosity is ignored. Therefore, the normal component of  $\mathbf{U}^I$  should be equal to the normal component of  $\mathbf{U}_{str}^I$ , i.e.,  $\mathbf{U}^I \cdot \mathbf{n} = \mathbf{U}_{str}^I \cdot \mathbf{n}$ . Meanwhile, the tangential component of  $\mathbf{U}^I$  cannot be

determined by  $\mathbf{U}_{str}^I$ , which may be considered as the tangential component of velocity  $\mathbf{U}_{nbr}^I$  on the neighbour cell of the structure-surface boundary, i.e.,  $\mathbf{U}^I \cdot \mathbf{t} = \mathbf{U}_{nbr}^I \cdot \mathbf{t}$ . Therefore, the velocity on the structure-surface should be described as

$$\mathbf{U}^I = (\mathbf{U}_{nbr}^I \cdot \mathbf{t})\mathbf{t} + (\mathbf{U}_{str}^I \cdot \mathbf{n})\mathbf{n} \text{ on the structure-surface} \quad (6.4.1)$$

In (6.4.1),  $\mathbf{n}$  and  $\mathbf{t}$  is the normal and tangential unit vector on the floating structure, respectively. The volume fraction on the floating structure should fulfil the zero normal gradient condition as well, which is described as

$$\frac{\partial \gamma'}{\partial \mathbf{n}} = 0 \text{ on the structure surface} \quad (6.4.2)$$

#### 6.4.2 Structure surface boundary condition in the viscous domain

In the viscous domain, the no-slip-wall boundary is imposed on the structure-surface. For the total velocity  $\mathbf{U}$  on the structure-surface,  $\mathbf{U} = \mathbf{U}^I + \mathbf{U}^D = \mathbf{U}_{str}^I$  should be satisfied, which means that  $\mathbf{U}^D = \mathbf{U}_{str}^I - \mathbf{U}^I$ . By using (6.4.1), the boundary condition is proposed as

$$\mathbf{U}^D = (\mathbf{U}_{str}^I \cdot \mathbf{t})\mathbf{t} - (\mathbf{U}_{nbr}^I \cdot \mathbf{t})\mathbf{t} \text{ on the structure-surface} \quad (6.4.3)$$

The volume fraction on the structure surface should satisfy the zero normal gradient boundary condition, which is described below

$$\frac{\partial \gamma}{\partial \mathbf{n}} = 0 \text{ on the structure surface} \quad (6.4.4)$$

### 6.5 Numerical techniques in the Euler-viscous hybrid solver with dynamic mesh

In the Euler-viscous hybrid solver with dynamic mesh, specific numerical techniques described in Chapter 3, including the transition zone for dissipating viscous effects in the viscous domain and the numerical interpolation for data transition are also adopted. However, the wave load on the floating structure estimated by the Euler solver in the Euler domain may be considerable different from that predicted by the complementary solver in the viscous domain. Consequently, the motion of the structures and thus the positions of the structure surface boundaries in two computational domains do not match. This causes a problem on data exchanging between two solvers, e.g. some part of the fluid domain in the viscous domain may be occupied by the structure in the Euler domain and thus cannot request  $\mathbf{U}^I$  and  $P^I$  from the Euler solver. A special numerical technique shall be developed for the simulation of the motions of a floating structure subjected to incident waves to make the motion of the structure consistence between two domains. To do so, the total hydrodynamic loading on the



floating structure in the viscous domain is transmitted into the Euler solver and used to evaluate the motion of the floating structure in the Euler domain.

## **6.6 The solution procedure of the Euler-viscous hybrid solver with dynamic mesh**

The solution procedure of the Euler-Viscous hybrid solver with dynamic mesh is different from that without dynamic mesh in Chapter 3. The solution procedures of the Euler-viscous hybrid solver for modelling with the interactions between waves and structures subjected to motions are discussed below.

### **6.6.1 Solution procedure for interaction between waves and a floating structure undergoing forced motion**

For the wave interactions with a floating structure undergoing a forced motion, the motions of the floating structure are prescribed and kept the same in both the Euler domain and the viscous domain. Therefore, the special treatment described in section 6.5 is not taken into account. After the mesh is updated in the Euler domain according to the prescribed motions of the floating structure, the volume fraction equation and Euler equations are solved. Then, the mesh in the viscous domain is also updated following the same motions. By the interpolation process described in section 3.6 (Chapter3), the Euler solution is mapped into the viscous domain. Finally, the free surface in the viscous domain is updated and the complementary RANS equations are solved with the complementary turbulence model. The details are illustrated in Fig. 6.6.1.

Step1 Initialise the unknown variables including  $\mathbf{U}^I$ ,  $p^I$ , and  $\gamma'$  in the Euler domain and establish the projection relationship between the Euler domain and the viscous domain.

Step2 Computational mesh in the Euler domain is updated by using the dynamic mesh technique according to the prescribed motions of the floating structure.

Step3 The volume fraction  $\gamma'$  in the Euler domain is solved by equation (6.1.3). The viscosity and density in the Euler domain is updated by the new volume fraction. After that, the momentum equations and the continuity equation in the Euler domain are solved.  $\mathbf{U}^I$  and  $p^I$  are updated in the new time step.

Step4 Computational mesh in the viscous domain is updated by using the dynamic mesh technique according to the prescribed motions of the floating structure.

Step5 The Euler solutions including  $\mathbf{U}^I$ ,  $p^I$ , and  $\gamma'$  are mapped into the viscous domain, which are regarded as known variables by the complementary solver.

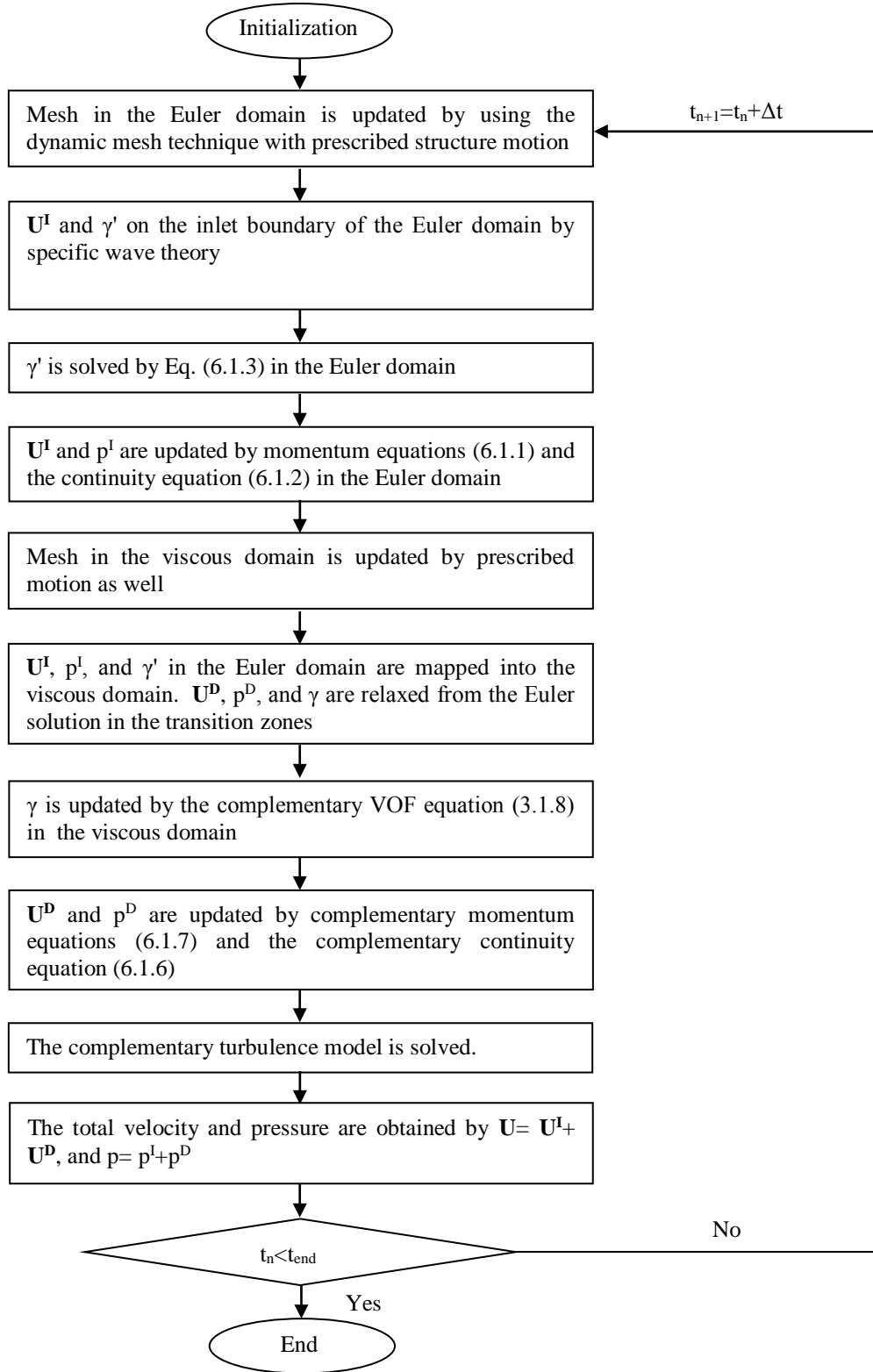


Fig. 6.6.1 The flow chart of the simulation of the floating structure with forced motion by the Euler-viscous hybrid solver under dynamic mesh

Step6 In the viscous domain, the free surface is updated by equation (6.1.8). After that, the viscosity and density in the viscous domain is obtained in the new step. Then, the complementary momentum equations (6.1.6) and the continuity equation are solved by PISO

algorithm, along with the complementary turbulence equations being solved by using  $\mathbf{U}^I$  and  $\mathbf{U}^D$  in the new time step.

Step7 Finally, the total velocity and the total pressure in the new step are calculated by  $\mathbf{U} = \mathbf{U}^I + \mathbf{U}^D$  and  $p = p^I + p^D$  respectively.

The simulation advances into the next time step and the program returns to Step2 until the final time step is reached.

#### 6.6.2 The solution procedure for interaction between waves and floating structure undergoing freely motion

For the simulation involving a freely floating structure subjected to incident waves, special treatment indicated above is conducted to ensure that the motion of floating structures in two domains are the same. In the simulation, the motion of the floating structure is determined by a 6 Degree Of Freedom (6 DOF) model built in OpenFOAM using the hydrodynamic load acting on it.

To illustrate, the forces and moments on the structure are calculated firstly, which are described as below.

$$\begin{cases} \mathbf{F} = \oint_S (\mathbf{F}_{\text{body}} + \mathbf{F}_{\text{fluid}}) ds \\ \mathbf{M} = \oint_S (\mathbf{M}_{\text{body}} + \mathbf{M}_{\text{fluid}}) ds \end{cases} \quad (6.6.1)$$

In equation (6.6.1),  $\mathbf{F}$  and  $\mathbf{M}$  are total forces and moment on the structure by surface integration of  $\mathbf{F}_{\text{body}}$  and  $\mathbf{F}_{\text{fluid}}$ .  $\mathbf{F}_{\text{body}}$  ( $\mathbf{M}_{\text{body}}$ ) are external forces (moments) such as gravity, magnetic forces, and electronic forces etc. In the research, only gravity is considered.  $\mathbf{F}_{\text{fluid}}$  ( $\mathbf{M}_{\text{fluid}}$ ) are fluid forces such as viscous forces and pressures.

After that, the velocity acceleration and angular acceleration can be obtained by the Newton's second law, described as

$$\begin{cases} \mathbf{a} = \frac{\mathbf{F}}{m} \\ \boldsymbol{\alpha} = \frac{\mathbf{M}}{I} \end{cases} \quad (6.6.2)$$

In equation (6.6.2),  $m$  is the mass of the structure, while  $I$  is the moment inertial.

Finally, by a splitting method (Dullweber, Leimkuhler, and McLachlan, 1997), the new position can be obtained, which is described below.

$$\begin{cases} (\mathbf{v})_{n+\frac{1}{2}} = 0.5 \cdot (1 - C_{damp}) \cdot (\Delta t)_n \cdot (\mathbf{a})_n \\ (\mathbf{s})_{n+1} = (\mathbf{s})_n + (\Delta t)_n \cdot (\mathbf{v})_{n+\frac{1}{2}} \end{cases} \quad (6.6.3)$$

In equation (6.6.3),  $(\mathbf{a})_n$  is the velocity acceleration in the time step  $n$ .  $(\Delta t)_n$  is the time step from  $n$  to  $n+1$ .  $(\mathbf{v})_{n+1/2}$  can be regarded as velocity between time step  $n$  and  $n+1$ , which is assumed to be unchanged in  $(\Delta t)_n$ . Finally, the new position  $(\mathbf{s})_{n+1}$  at time step  $n+1$  is obtained from the old position  $(\mathbf{s})_n$ .  $C_{damp}$  is the damping coefficients for avoiding the numerical instability.

Similarly, the new orientation can be obtained by

$$\begin{cases} (\boldsymbol{\omega}I)_{n+\frac{1}{2}} = 0.5 \cdot (1 - C_{damp}) \cdot (\Delta t)_n \cdot (\boldsymbol{\alpha}I)_n \\ (\mathbf{Q})_{n+1} = (\mathbf{Q})_n \cdot \mathbf{R}_1 \cdot \mathbf{R}_2 \cdot \mathbf{R}_3 \cdot \mathbf{R}_4 \cdot \mathbf{R}_5 \end{cases} \quad (6.6.4)$$

In fact, the new orientation  $(\mathbf{Q})_{n+1}$  at time step  $n+1$  is obtained from the old orientation  $(\mathbf{Q})_n$ , by the unchanged angular acceleration  $(\boldsymbol{\omega})_{n+1/2}$  in time step  $(\Delta t)_n$ .  $\mathbf{R}_1$ ,  $\mathbf{R}_2$ ,  $\mathbf{R}_3$ ,  $\mathbf{R}_4$ , and  $\mathbf{R}_5$  are functions with the variable  $(\boldsymbol{\omega})_{n+1/2}$ .

The solution procedure of the Euler-Viscous hybrid solver with dynamic mesh for a freely floating structure is described below in Fig. 6.6.2, in which the most steps are the same except those related to the motion of the freely floating structures.

Step1 Initialise the unknown variables including  $\mathbf{U}^I$ ,  $p^I$ , and  $\gamma'$  in the Euler domain and establish the mapping between the Euler domain and the viscous domain.

Step2 The volume fraction  $\gamma'$  in the Euler domain is solved by equation (6.1.3). The viscosity and density in the Euler domain is updated by the new volume fraction. After that, the momentum equations (6.1.2) and the continuity equation (6.1.1) are solved.  $\mathbf{U}^I$  and  $p^I$  are updated in the new time step.

Step3 The Euler solutions including  $\mathbf{U}^I$ ,  $p^I$ , and  $\gamma'$  are mapped into the viscous domain by interpolation, which are regarded as known variables.

Step4 The volume fraction  $\gamma$  in the viscous domain is solved by equation (6.1.8). Besides that, the viscosity and density in the viscous domain are obtained by the free surface at the new time step. Then, the complementary momentum equations and the corresponding continuity equation are solved by the PISO algorithm.  $\mathbf{U}^D$  and  $p^D$  are updated at the new time step, along with the complementary turbulence equations are solved by using  $\mathbf{U}^I$  and  $\mathbf{U}^D$  in the new time step.

Step5 Finally, the total velocity and the total pressure at the new step are calculated by  $\mathbf{U} = \mathbf{U}^I + \mathbf{U}^D$  and  $p = p^I + p^D$  respectively.

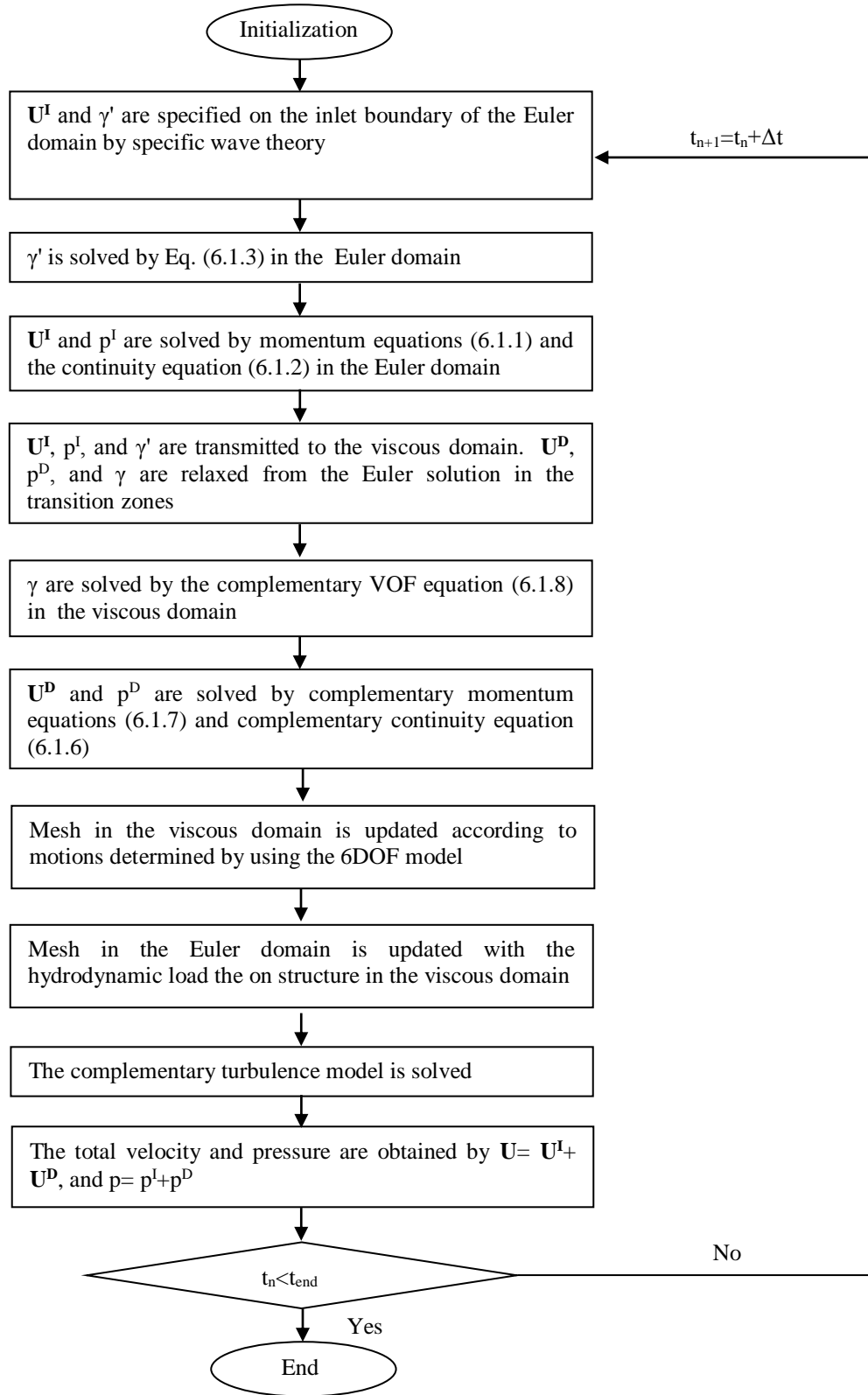


Fig. 6.6.2 The flow chart of the simulation of the floating structure with free motion by Euler-viscous hybrid solver under dynamic mesh

Step6 In the viscous domain, hydrodynamics is calculated on the floating structure, which is used to determine the motion of the floating structure by the 6DOF model. Then, dynamic mesh in the viscous domain is updated.

Step7 In the Euler domain, with the feedback of hydrodynamics on the floating structure in the viscous domain, the motion of the floating structure is determined by the 6DOF model. Then, dynamic mesh is updated.

The simulation continues into the next time step and the solution procedure goes back to Step2 until the final time step is reached.

## Chapter 7 Convergence study of the Euler-viscous hybrid solver for moving surface-piercing structures in waves

In this chapter, the Euler-viscous hybrid solver adopting the dynamic mesh technique is used to simulate the interaction between waves and a moving surface-piercing structure. This chapter mainly focuses on specific numerical tests exploring the convergence property. Two specific cases are taken into account in this chapter to shed light on the feature of the present solver. These include (1) a 2D rectangular floating structure undergoing forced rolling motion; and (2) roll damping of a 2D rectangular floating structure. For the latter, an experimental study has been conducted by Jung et al (2006), this may give good reference for the investigation presented in this chapter. Although incident waves are not considered in both cases, radiation waves are generated by the motion of the structure and interact with the structure.

### 7.1 Description of the physical model

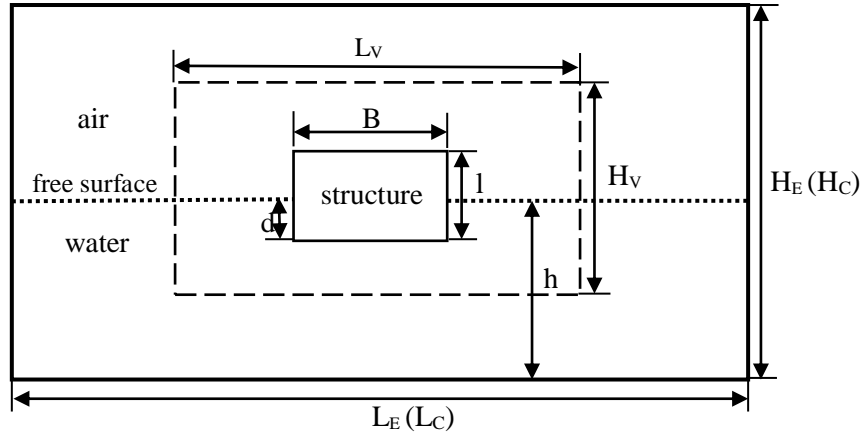


Fig. 7.1.1 the physical model

The physical model to be considered in this chapter is sketched in Fig. 7.1.1. The floating structure is a two-dimensional rectangular barge with width ( $B$ ) of 0.3m and height ( $l$ ) of 0.1m. The initial draft ( $d$ ) of the structure is 0.05m. The water depth  $h$  is 0.9m. The floating structure rolls around a rotating axis across the centre of the gravity centre  $G$  located at the centre of the barge. Using such configuration, it is easy to get that  $B/d=6$ , and  $l/d=2$ .

For the first case, the structure subjected to a forced roll motion, which is specified by a periodic motion with the motion amplitude of  $\alpha_0$ . In this case, the moment acting on the structure due to the water are recorded for comparison. For convenient, the moment  $M$  is nondimensionalised by  $\rho g L B d l$ , where  $L$  is the length of the floating body. The roll angle  $\alpha$  of the floating structure is nondimensionalised by the roll amplitude  $\alpha_0$ . In addition to the present

Euler-viscous hybrid solver with dynamic mesh technique, the conventional RANS solver is also used to simulate the same case for comparison. Both the accuracy and the efficiency of the present solver are discussed.

## 7.2 Convergence study

It is well-known that the mesh plays a crucial role on the accuracy, efficiency and the convergence of any numerical approaches. For both the Euler-viscous hybrid solver and the conventional RANS solver, a mesh with sufficient resolution is required for all cases to ensure the convergence of the solution. In the present Euler-viscous hybrid solver, the requirement of the mesh resolutions in the Euler domain and that in the viscous domain may be different in order to get convergent solution for the Euler equations and the complementary RANS equations, respectively. In the viscous domain, one may agree that adopting the same mesh resolution as the conventional RANS solver is acceptable. Thus, preliminary convergence studies are conducted for the Euler solver of the present solver and the conventional RANS solver, respectively.

### 7.2.1 Computational mesh

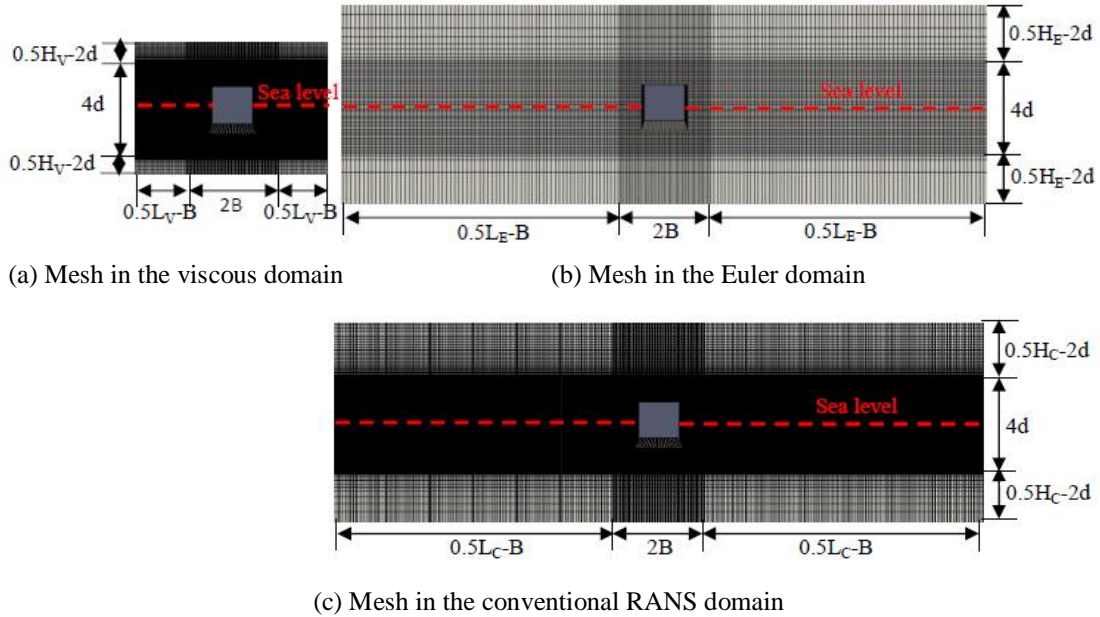


Fig. 7.2.1 mesh with feature parameters

For the conventional RANS solver, the numerical wave tank is rectangular with the length  $L_C$  of 12m ( $L_C/B=40$ ), and the width  $H_C$  of 1.8m ( $H_C/h=2$ ). The floating structure is located at the centre of the tank and the mean sea level is the central horizontal line of the tank. This is sketched in Fig. 7.2.1 (c). The size of the tank and locations of the floating structure and the mean water surface in the Euler domain of the present solver are the same as those used by the conventional RANS solver (see Fig. 7.2.1(b)). The computational mesh is hexahedral and



generated by the OpenFOAM mesh generator blockMesh. Similar to the problem with fixed structures, the mesh near the free surface must be refined for capturing the water waves. In this case, the mesh at a rectangle region with a width of  $4d$  centred at the mean sea level is refined. Furthermore, the mesh around the floating structure may also be refined for capturing small-scale physics, e.g. the turbulence, boundary layer and vortex, which significantly influence the force on the floating structure. Similar to the mesh near the free surface, a rectangle region with length of  $2B$  (in horizontal) are defined. Within such refined regions, the mesh sizes are uniform in both the horizontal and vertical direction. Outside the refined regions, the mesh sizes are uniform in horizontal direction, but gradually increases in vertical direction from the boundary of the refined regions to the outer boundary of the computational domain (the ratio of the maximum mesh size and minimum mesh size in vertical direction is 30). Illustrations of the computational mesh used by the present solver and the conventional RANS solver are given in Fig. 7.2.1. Similar to the cases with fixed structures, the parameters listed in Table 7.2.1 are used to reflect the mesh resolutions in different area

Table 7.2.1 Parameters for features of mesh

$nL_C, nL_E$ and $nL_V$	the numbers of division in the horizontal direction outside the refined regions ( $nL$ ), i.e. four corner areas with lengths of $0.5L_C-B$ , $0.5L_E-B$ and $0.5L_V-B$ , for the conventional RANS solver, the Euler Solver and the complementary RANS solver, respectively.
$nB_C, nB_E$ and $nB_V$	the numbers of division per width of the floating structure in the horizontal direction ( $nB$ ) in the refined region near the floating structure with the length of $2B$ for conventional RANS solver, Euler solver, and complementary RANS solver, respectively
$nH_C, nH_E$ and $nH_V$	the numbers of division per height of the floating structure in the vertical direction ( $nH$ ) in the refined region near the free surface with height of $4d$ for conventional RANS solver, Euler solver, and complementary RANS solver, respectively

## 7.2.2 Convergence properties of the conventional RANS solver and the Euler solver

In the study, simulations of forced rolling of a floating structure in water are carried out using the conventional RANS solver and the Euler solver, respectively. The prescribed roll motion of the structure is described as

$$\alpha = \alpha_0 \sin\left(\frac{2\pi}{T} \cdot t\right) \left\{ \sin\left[\frac{\pi}{2} \cdot \frac{\min(T_0, t)}{T_0}\right] \right\}^3 \quad (7.2.1)$$

In (7.2.1),  $\alpha$  is the roll angle at the time  $t$ ;  $\alpha_0$  is the motion amplitude, which is  $\alpha_0=\pi/36$  (5deg) in the investigation;  $T=0.93s$  is the motion period. . One may notice that a ramping function  $\left\{\sin\left[\frac{\pi}{2}\cdot\frac{\min(T_0,t)}{T_0}\right]\right\}^3$  is applied to duration of  $T_0$  to avoid a sudden increase of the motion speed to improve the stability of the simulation. The moment acting on the forced rolling structure is recorded for comparison due to the fact that the moment induced by the forced roll is used to determine the added-mass coefficient and damping coefficient of the roll motion, which play a crucial role in the design of floating structures. Different time step sizes and mesh resolutions are considered in the convergence investigation. As indicated above, the convergence properties for the Euler solver and the conventional RANS solver are investigated as the preliminary study for the present Euler-viscous coupled solver.

Firstly, the effects of the time step size ( $\Delta t$ ) are investigated. For the conventional RANS solver, the simulations adopting  $\Delta t=T/500$ ,  $\Delta t=T/1000$ , and  $\Delta t=T/2000$  are carried out. The mesh resolution is specified by  $nL_C=460$ ,  $nB_C=50$ , and  $nH_C=46$ . The time history of the moment acting on the floating structure is shown in Fig. 7.2.2. As expected, the moment varies periodically after the initial ramping period. For quantifying the relative error, the time histories of the moment in 5 continuous time periods from  $t/T=5$  to  $t/T=10$  are used for the calculation of relative average error that defined in Section 4.2.2. It is obtained that the REM between the case with  $\Delta t=T/500$  and that with  $\Delta t=T/1000$  is 6.7%, whereas the corresponding value between the case with  $\Delta t=T/2000$  and that with  $\Delta t=T/1000$  is reduced to 0.2%. One may conclude that the time step size of  $\Delta t=T/1000$  is acceptable for the conventional RANS solver. It is well understood that the requirement of the time step by the Euler equation leading to a convergent results shall not be shorter than that by the Navier-Stokes equation. Therefore,  $\Delta t=T/1000$  shall be sufficient for the Euler solver to get convergent results, although we may use a larger time step sizes for the Euler solver.

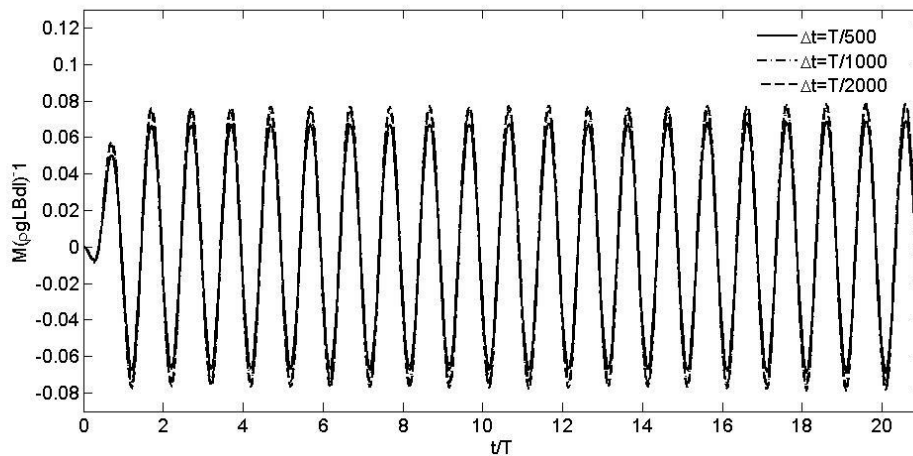
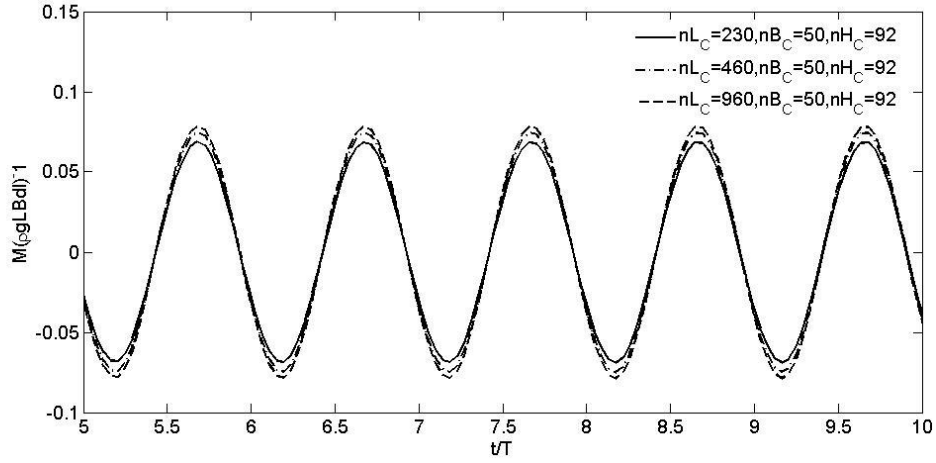
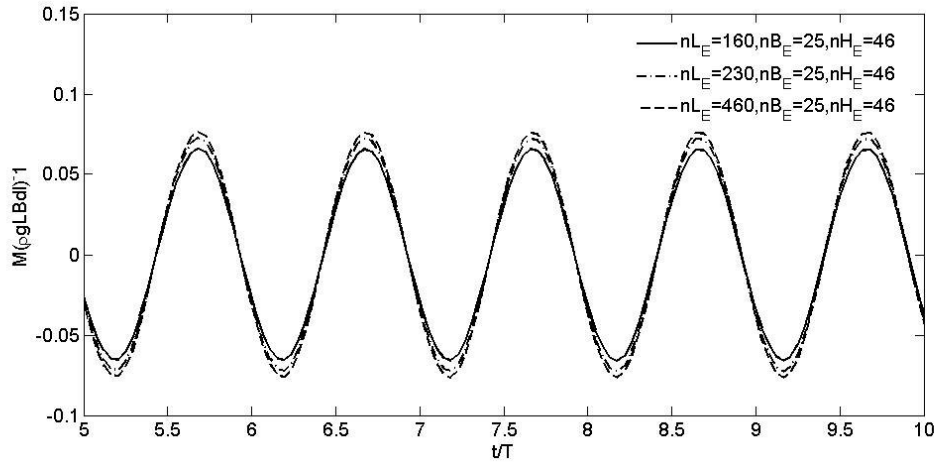


Fig. 7.2.2 The comparison of moment at different time step



(a) The conventional RANS solver



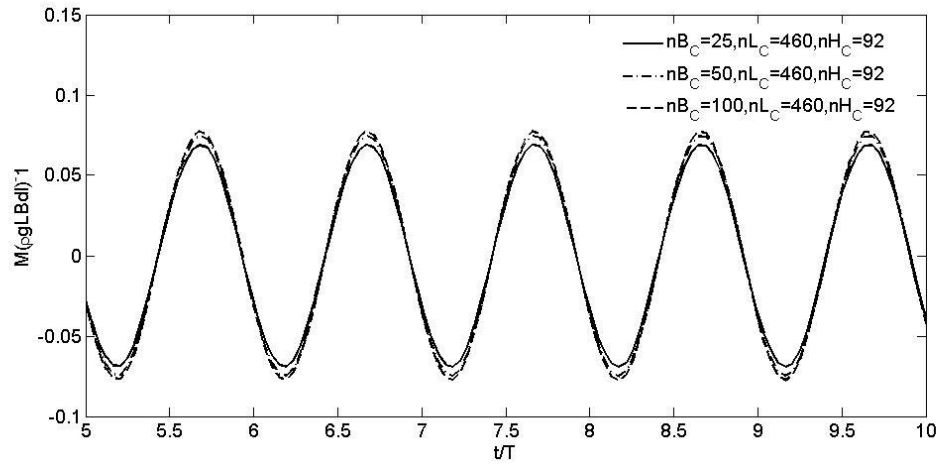
(b) The Euler solver

Fig. 7.2.3 The comparison of moment ( $nL_C$  and  $nL_E$ ) between the conventional RANS solver and the Euler solver

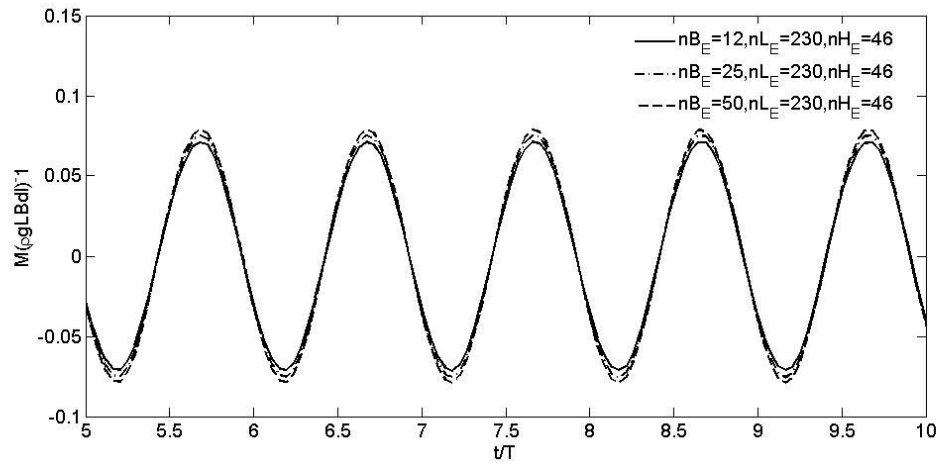
The convergence study in terms of the mesh resolutions are conducted where the time step size is taken as  $\Delta t = T/1000$ . The mesh resolutions are specified by number of divisions defined in Table 7.2.1. The numbers of division per width of the floating structure in horizontal, i.e.  $nB_C$  and  $nB_E$ , ranges from 12 to 100; the numbers of division per height of the floating structure in vertical, i.e.  $nH_C$  and  $nH_E$ , ranges from 23 to 138. The numbers of division in the horizontal direction outside the refined regions, i.e.  $nL_C$  and  $nL_E$ , ranges from 160 to 960.

The effects of numbers of division in the horizontal direction outside the refined regions ( $nL$ ) on numerical results are investigated and some results are shown in Fig. 7.2.3. it shall be noted that the mesh resolutions in the refined regions are the same, i.e.  $nB_C=50$  &  $nH_C=92$  for the conventional RANS solver and  $nB_E=25$  &  $nH_E=46$  for the Euler solver. These are sufficient for achieving convergent results as will be discussed below. As observed from Fig. 7.2.3 (a),  $nL_C=460$  is sufficient for the conventional RANS solver to achieve convergent results.

Evaluation also show that the REM for the cases with  $nL_C=230$  and  $nL_C=460$  is 8.3%, whereas the REM for the cases with  $nL_C=460$  and  $nL_C=920$  is 1.2%. It is also found from Fig. 7.2.3(b) that a coarser mesh resolution outside the refined regions, i.e.  $nL_E=230$  is sufficient for the Euler solver. The corresponding REM is 8.8% for cases with  $nL_E=160$  and  $nL_E=230$ , and reduces to 0.8% for  $nL_E=230$ ,  $nL_E=460$ .



(a) The conventional RANS solver

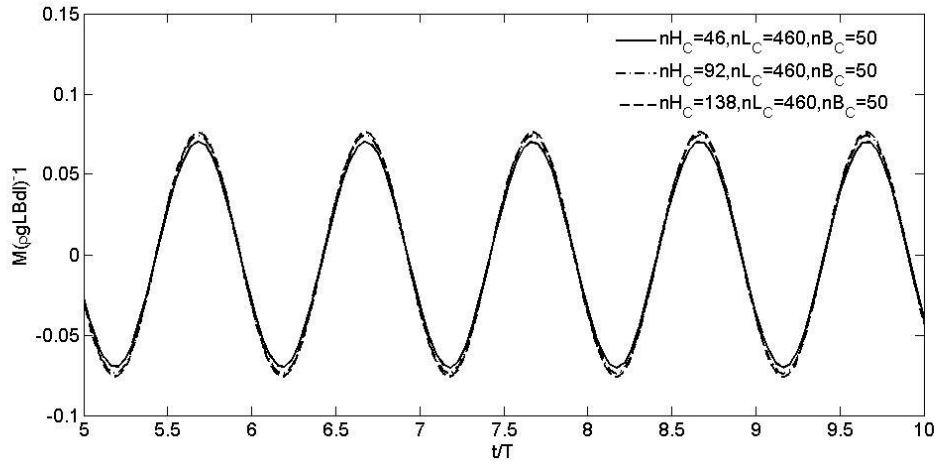


(b) The Euler solver

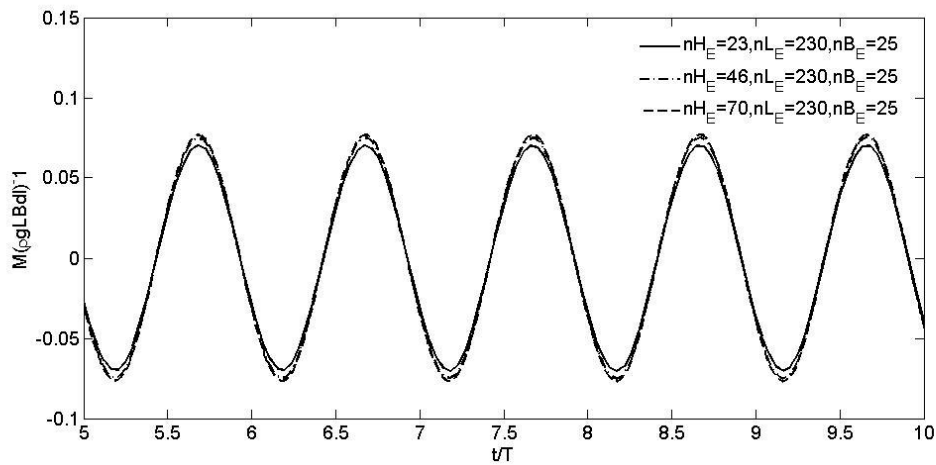
Fig. 7.2.4 The comparison of moment ( $nB_C$  and  $nB_E$ ) between the conventional RANS solver and the Euler solver

The convergence properties in terms of the numbers of division per width of the floating structure in horizontal direction ( $nB$ ) in the refine region are also analysed. Some results are shown in Fig. 7.2.4. Similar to Fig. 7.2.3,  $nL$  and  $nH$  for both solvers are fixed but sufficiently smaller to ensure a convergent solution. For the conventional RANS solver,  $nL_C=460$ ,  $nH_C=92$  and  $nB_C$  ranges from 25 to 100. Obviously,  $nB_C=50$  is sufficient for the conventional RANS solver (REM for the cases with  $nB_C=50$  and  $nB_C=100$  is 1.3%). The comparison of moment in the cases with different  $nB_E$  ( $nB_E=12$ ,  $nB_E=25$ , and  $nB_E=50$ ) by the Euler solver

(Fig. 7.2.4 (b)) suggest that the Euler solver only requires  $nB_E=25$  to achieve convergence results (REM for the cases with  $nB_E=25$  and  $nB_E=50$  is 1.6%), providing sufficiently large value of  $nL_E$  and  $nH_E$ .



(a) The conventional RANS solver



(c) The Euler solver

(a)

Fig. 7.2.5 The comparison of moment ( $nH_C$  and  $nH_E$ ) between the conventional RANS solver and the Euler solver

Finally, the effects of  $nH$ , i.e. the numbers of division per height of the floating structure in the vertical direction, are discussed. Some results are shown in Fig. 7.2.5. For the conventional RANS solver (Fig. 7.2.5(a)), numerical simulations are carried out with different  $nH_C$  including  $nH_C=46$ ,  $nH_C=92$ , and  $nH_C=138$ ; whereas the same  $nL_C$  and  $nB_C$  are used, i.e.  $nL_C=460$  and  $nB_C=50$ , which are sufficient as indicated by Fig. 7.2.3 and Fig. 7.2.4. It can be seen that  $nH_C=92$  is sufficient for the conventional RANS solver to achieve convergent results. The corresponding values of REM are 0.8% for the cases with  $nH_C=92$  &  $nH_C=138$ , which is much smaller than the REM for the cases with  $nH_C=46$  and  $nH_C=92$  (7.2%). For the Euler

solver (Fig. 7.2.5(b)),  $nH_E=46$  should be used. The corresponding values of REM are 0.6% for the cases with  $nH_E=46$  and  $nH_E=70$ , whereas it is 5.2% for the cases with  $nH_E=46$  and  $nH_E=23$ .

In summary, for numerical simulations of forced rolling structure in water, the time step  $\Delta t=T/1000$  is sufficient for the convention RANS solver and the Euler solver. In addition to the time step, sufficient mesh resolution is also found. Specifically, for the conventional RANS solver, the mesh resolution shall be specified by  $nL_C=460$ ,  $nB_C=50$ , and  $nH_C=92$ . On the other hand, for the Euler solver, mesh resolution with  $nL_E=230$ ,  $nB_E=25$ , and  $nH_E=46$  is acceptable. By comparison of mesh resolution, it is indicated that mesh for the conventional RANS solver must be finer than that for the Euler solver. That's because the viscous effects including turbulence are considered in the conventional RANS solver, which requires finer mesh resolution (about half of the mesh size on both horizontal and vertical direction). Therefore, CPU time consumed by the conventional RANS solver is much longer than that by the Euler solver. This builds the basis for the necessity of developing the Euler-viscous hybrid solver, in which the viscosity and the turbulence are only considered in the viscous domain i.e. a smaller region near the floating body.

### 7.2.3 Convergent property of the Euler-viscous hybrid solver

The preliminary study in Section 7.2.2 has found the appropriate mesh resolution for both the Euler and the conventional RANS model for simulating the forced rolling structure in water. The questions to be answered here include (1) are the requirements of the time step size and the mesh resolution by the complementary solver of the present hybrid solver similar to the conventional RANS model? (2) is the hybrid solver convergent to the same results as the conventional RANS solver? These questions have been answered previously for the cases with fixed structures. Systematic results for the convergence investigation for the hybrid solver are not presented in this section to save the space, and only some results are shown to confirm that the conclusion drawn by using the case with fixed structures still stand for the cases with moving structures. For this purpose, the Euler-viscous hybrid solver with dynamic mesh technique is used to model the same case as that presented in Section 7.2.2. The size of computational domain and mesh resolution are described in Table 7.2.2, which are results of convergence study in section 7.2.2. It shall be noted that for the Euler-viscous hybrid solver, the Euler domain is the same as the domain used by the conventional RANS solver in Section 7.2.2. The value of the parameters for specifying the mesh resolutions in the Euler domain of the present solver and those in the corresponding simulation by the conventional RANS solvers are taken according to the convergence investigation shown in Section 7.2.2. The size of the viscous domain for the Euler-viscous hybrid solver are given as  $L_v = 6B$  (about 15% of

the length of the Euler domain) and  $H_v = 2h$  (the same height as the Euler domain). The mesh resolution in the viscous domain is the same as that used in the computational domain for the conventional RANS simulation.

Table 7.2.2 The mesh for the study of convergent property

(a) The mesh for the conventional RANS solver

Conventional RANS domain				
$L_c$	$H_c$	$L_c$	$nB_c$	$nH_c$
40B	2h	460	92	50

(b) The mesh for the Euler-viscous hybrid solver

Euler domain					Viscous domain					
$L_E$	$H_E$	$nL_E$	$nB_E$	$nH_E$	$L_V$	$H_V$	$L_{tr}$	$nL_V$	$nB_V$	$nH_V$
40B	2h	230	46	25	6B	2h	3B	460	92	50

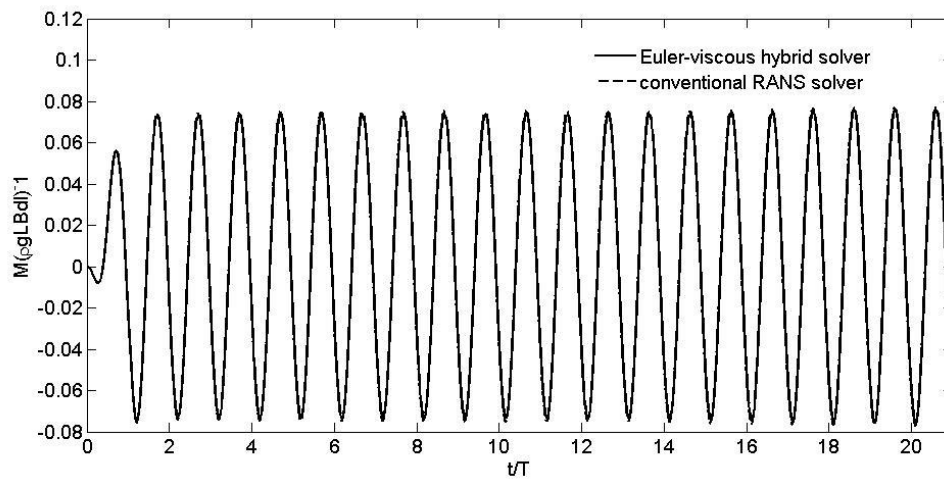


Fig. 7.2.6 The comparison of time history of moment between the Euler-viscous hybrid solver and the conventional RANS solver

The comparison of time history of moment is shown in Fig. 7.2.6. It can be seen that the numerical results based on the Euler-viscous hybrid solver agree well with those by the conventional RANS solver. In order to analyze the relative difference between two sets of results in Fig. 7.2.6, time histories of moment in 5 continuous time periods from  $t/T=5$  to  $t/T=10$  are used by formula (4.2.2). The average difference is 1.05%. This confirms that the requirement for the mesh resolution in the viscous domain to achieve convergent results may be the same as the corresponding values required by the conventional RANS solver. It also confirms that the accuracy of the hybrid solver is at the same level as that of the conventional RANS solver.

It shall be pointed out that the sizes of the viscous domain and the transitional zone play important role on the efficiency and the accuracy of the present Euler-viscous hybrid solver.

This will be explored in the following sections. In these investigations, the mesh resolutions are taken as the same as those used here. Different values of the length ( $L_v$ ) and the width ( $H_v$ ) of the viscous domain, as well as the length of the transitional zone ( $L_{tr}$ ) are focused.

### 7.3 Performance of the Euler-Viscous Hybrid solver a forced rolling floating structure in water

In this section, the forced rolling floating structure in water is simulated by the Euler-Viscous hybrid solver and the conventional RANS solver. The motion of the structure and the size of the entire computational domain are the same as those in the previous section. The mesh resolutions used by both solvers are the same as the case presented in Section 7.2.3.

#### 7.3.1 The effects of the length of the viscous domain ( $L_v$ )

In order to study the effects of  $L_v$ , numerical simulations with different values of  $L_v$ , ranging from 3B to 14B, are carried out by using the Euler-viscous hybrid solver. The width remains the same as  $H_v = 2h$ , the same as the width of the Euler domain. The detail of configuration is described in table 7.3.1.

Table 7.3.1 The mesh for the study of effects of  $L_v$

(a) The mesh resolution for the Euler-viscous hybrid solver

No.	Euler domain					Viscous domain					
	$L_E$	$H_E$	$nL_E$	$nH_E$	$nB_E$	$L_v$	$H_v$	$L_{tr}$	$nL_v$	$nH_v$	$nB_v$
1	40B	2h	230	46	25	3B	2h	3B	460	92	50
2	40B	2h	230	46	25	6B	2h	3B	460	92	50
3	40B	2h	230	46	25	10B	2h	3B	460	92	50
4	40B	2h	230	46	25	14B	2h	3B	460	92	50

(b) The mesh resolution for the conventional RANS solver

Conventional RANS domain				
$L_v$	$H_v$	$nL_v$	$nB_v$	$nH_v$
40B	2h	460	92	50

From Fig. 7.2.6, one may observe that the moment shows a periodic motion in steady state from the second period. For better visualisation, the time histories over one wave period from  $t/T=6$  to  $t/T=7$  in the cases with different  $L_v$ , are shown in Fig. 7.3.1. It can be seen that the results obtained by using  $L_v=3B$  are considerably different from others. When  $L_v \geq 6B$ , the moment predicted by the Euler-viscous hybrid solver agrees well with that estimated by the conventional RANS solver. The relative error compared to the results by the conventional RANS solver in the cases with different  $L_v$  is analysed and some results are shown in Fig. 7.3.2, together with the CPU time spent by the present Euler-Viscous hybrid solver. For convenience, the CPU time shown in Fig. 7.3.2 is presented in form of the ratio against that



spent by the conventional RANS solver. One may easily conclude that the optimised length of the viscous domain  $L_V$  leading to highest computational robustness is  $6B$ , where more than 60% CPU time can be saved compared with the conventional RANS solver and only 1% relative error is observed.

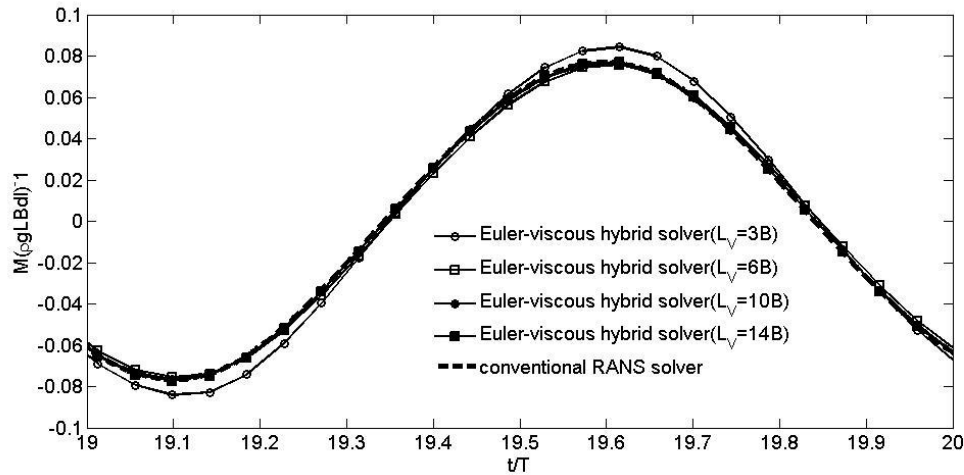


Fig. 7.3.1 The comparison of moment at different  $L_V$  by the Euler-viscous hybrid solver

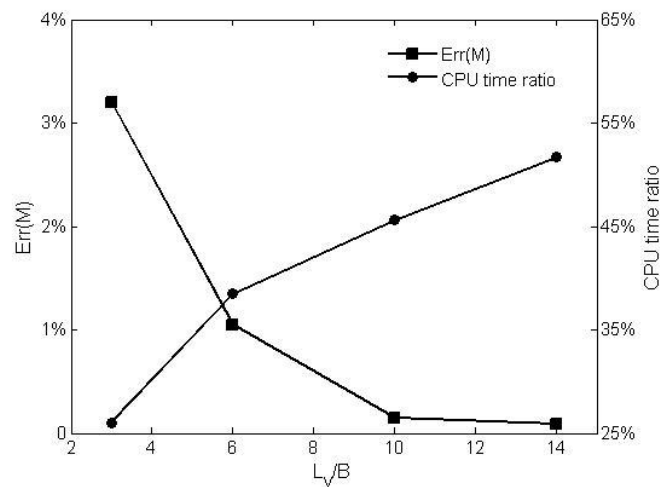


Fig. 7.3.2 The average error and CPU time ratio at different  $L_V$

### 7.3.2 The effects of the width of the viscous domain ( $H_V$ )

Not only the length of the viscous domain ( $L_V$ ), but also the width of the viscous domain ( $H_V$ ) can be optimised to achieve a better computational robustness. Similar to  $L_V$ ,  $H_V$  may also affect both computational accuracy and computational efficiency for the present Euler-Viscous hybrid solver. Hence, it is necessary to study the effects of  $H_V$ . For this purpose, the width of the viscous domain  $H_V$  ranges from  $H_V=2h$  to  $H_V=0.5h$  in the investigation. Details of the configuration can be found in Table 7.3.2.

Table 7.3.2 The mesh for the study of effects of  $H_v$

(a) The mesh for the Euler-viscous hybrid solver

No.	Euler domain					Viscous domain					
	$L_E$	$H_E$	$n_{L_E}$	$n_{H_E}$	$n_{B_E}$	$L_v$	$H_v$	$L_{\pi}$	$n_{L_v}$	$n_{H_v}$	$n_{B_v}$
1	40B	2h	230	46	25	6B	0.5h	3B	460	92	50
2	40B	2h	230	46	25	6B	h	3B	460	92	50
3	40B	2h	230	46	25	6B	1.5h	3B	460	92	50
4	40B	2h	230	46	25	6B	2h	3B	460	92	50

(b) The mesh for the conventional RANS solver

Conventional RANS domain				
$L_v$	$H_v$	$n_{L_v}$	$n_{B_v}$	$n_{H_v}$
40B	2h	460	92	50

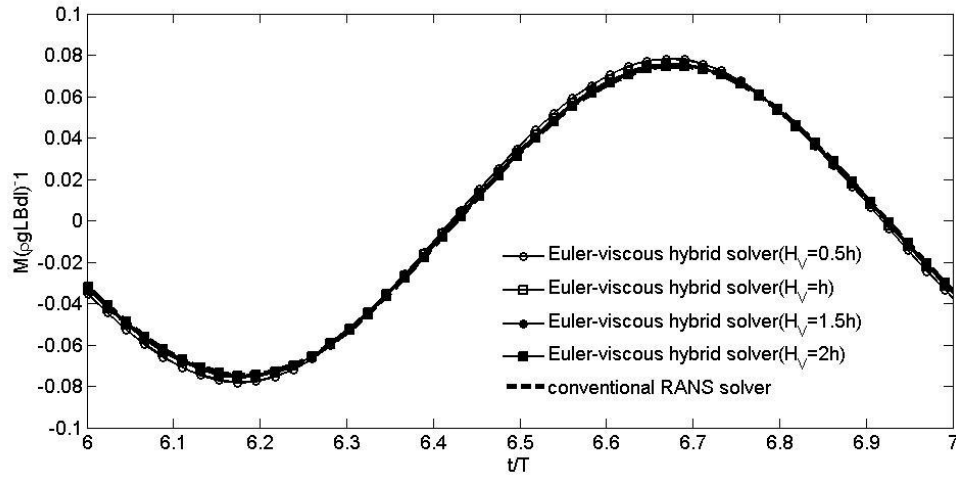


Fig. 7.3.3 The comparison of moment at different  $H_v$  by the Euler-viscous hybrid solver

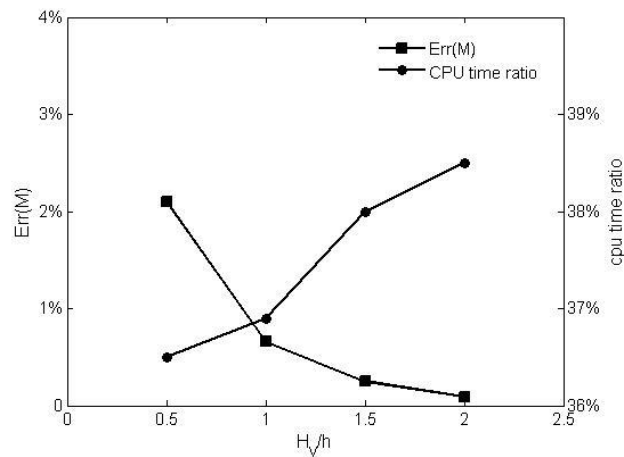


Fig. 7.3.4 The average error and CPU time ratio at different  $H_v$

Similar to Fig. 7.3.1, the comparison of time histories of moment in one period from  $t/T=6$  to  $t/T=7$  is shown in Fig. 7.3.3. It can be seen that the Euler-viscous hybrid solver leads to

results which are all close to the results from the conventional RANS solver, regardless the width of the viscous domain. The relative errors are all smaller than 2% (Fig. 7.3.4). The ratios of the CPU time consumed by the hybrid solver against the conventional RANS solver are also plotted in Fig. 7.3.4 for different value of  $H_v$ . One may conclude that  $H_v=h$  may lead to the highest robustness for the case considered here.

### 7.3.3 The effects of the length of the transition zone ( $L_{tr}$ )

The transition zone is used to dissipate the viscous effects and to ensure a consistent solution on the outer boundary of the viscous domain by both solvers. It also brings benefit on numerical stability and a smooth transmission from the Euler solution outside the viscous domain to the fully RANS solution inside the viscous domain. An appropriate length ( $L_{tr}$ ) of the transition zone may be sought for the Euler-viscous hybrid solver to ensure a good computational robustness. For this purpose, different values of  $L_{tr}$  from  $B$  to  $4B$  are considered in the investigation, where the size of the viscous domain are kept the same, i.e.  $L_v=12B$  and  $H_v=h$ . More details can be found in Table 7.3.3.

Table 7.3.3 The mesh for the study of effects of  $L_{tr}$

(a) The mesh resolution for the conventional RANS solver

Conventional RANS domain				
$L_v$	$H_v$	$nL_v$	$nB_v$	$nH_v$
40B	2h	460	50	92

(b) The mesh resolution for the Euler-viscous hybrid solver

No.	Euler domain					Viscous domain					
	$L_E$	$H_E$	$nL_E$	$nH_E$	$nB_E$	$L_v$	$H_v$	$L_{tr}$	$nL_v$	$nH_v$	$nB_v$
1	40B	2h	230	46	25	12B	h	B	460	92	50
2	40B	2h	230	46	25	12B	h	2B	460	92	50
3	40B	2h	230	46	25	12B	h	3B	460	92	50
4	40B	2h	230	46	25	12B	h	4B	460	92	50

Time history of the moments in the cases with different  $L_{tr}$  are compared with the corresponding results by the conventional RANS solver over the period from  $t/T=6$  to  $t/T=7$ . The results are shown in Fig. 7.3.5. The relative error compared to the results by the conventional RANS solver is shown in Fig. 7.3.6, together with the consumed CPU time. The average error is smaller than 0.5%, regardless the value of the  $L_{tr}$  considered in the investigation. It is also found that the CPU time seems not to be influenced by  $L_{tr}$ .

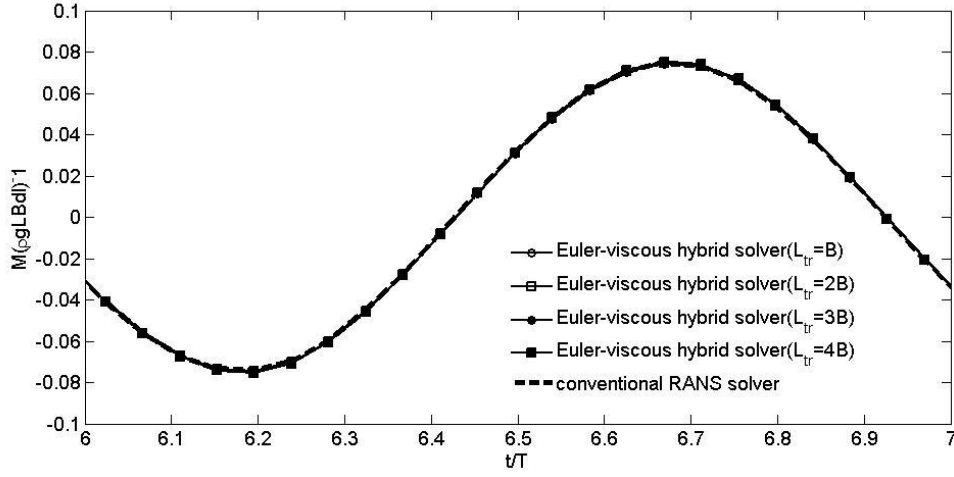


Fig. 7.3.5 The comparison of moment at different  $L_{tr}$  by the Euler-viscous hybrid solver

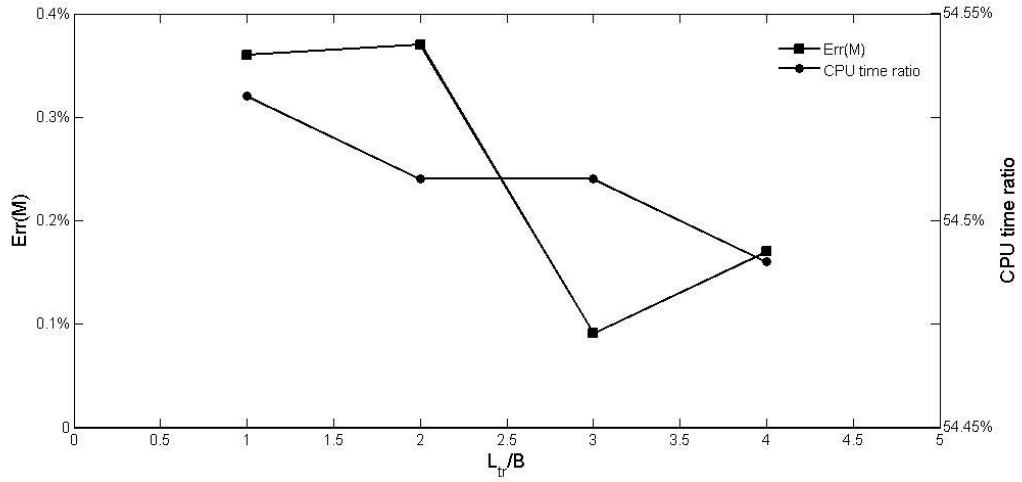


Fig. 7.3.6 The average error and CPU time ratio at different  $L_{tr}$

#### 7.3.4 The effects of the motion frequency

From Section 7.3.1 to Section 7.3.3, the effects of the length ( $L_V$ ) and width ( $H_V$ ) of the viscous domain and length ( $L_{tr}$ ) of the transition zone are studied. However, only one motion frequency, i.e.  $f_0=1.08\text{Hz}$  ( $T=0.93\text{s}$ ) is considered. One may concern that whether the same conclusion stands for different motion frequencies. In this section, the effects of the motion frequency on the Euler-viscous hybrid solver are investigated. Different roll frequencies including  $f=0.67\text{Hz}$  ( $T=1.5\text{s}$ ),  $f=0.83\text{Hz}$  ( $T=1.2\text{s}$ ),  $f=1.08\text{Hz}$  ( $T=0.93\text{s}$ ),  $f=1.25\text{Hz}$  ( $T=0.8\text{s}$ ), and  $f=1.67\text{Hz}$  ( $T=0.6\text{s}$ ) are considered. In these cases, the roll amplitude is kept the same as  $\alpha_0=\pi/36$  (5 deg). For comparison, corresponding results by the conventional RANS solver are also obtained. The mesh resolutions are specified by  $nL_E=230$ ,  $nH_E=46$ , and  $nB_E=25$  in the Euler domain with size of  $L_E=40B$ ,  $H_E=2h$ . Meanwhile,  $nL_V=460$ ,  $nH_V=92$ , and  $nB_V=50$  are used to generate the mesh in the viscous domain with its sizes specified by  $L_V=6B$ ,  $H_V=h$ . The length of the transition zone  $L_{tr}$  is taken as  $0.25L_V$ . The time step size is  $\Delta t=T/1000$  for both

the Euler solver and the complementary RANS solver. For comparison, simulations using the conventional RANS solver are also conducted by using the same size of the computational domain as the Euler domain and the same mesh resolution as the viscous domain, which is specified by using  $n_{LC}=460$ ,  $n_{HC}=92$ , and  $n_{BC}=50$ .

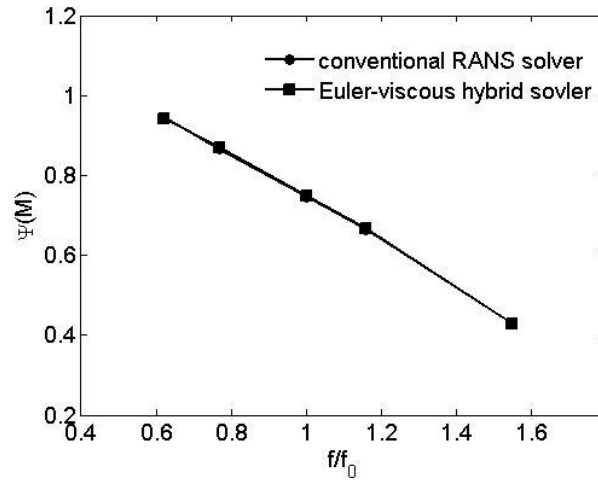


Fig. 7.3.7 The comparison of 1<sup>st</sup> order amplitude of moment between the Euler-viscous hybrid solver and the conventional RANS solver at different motion frequency

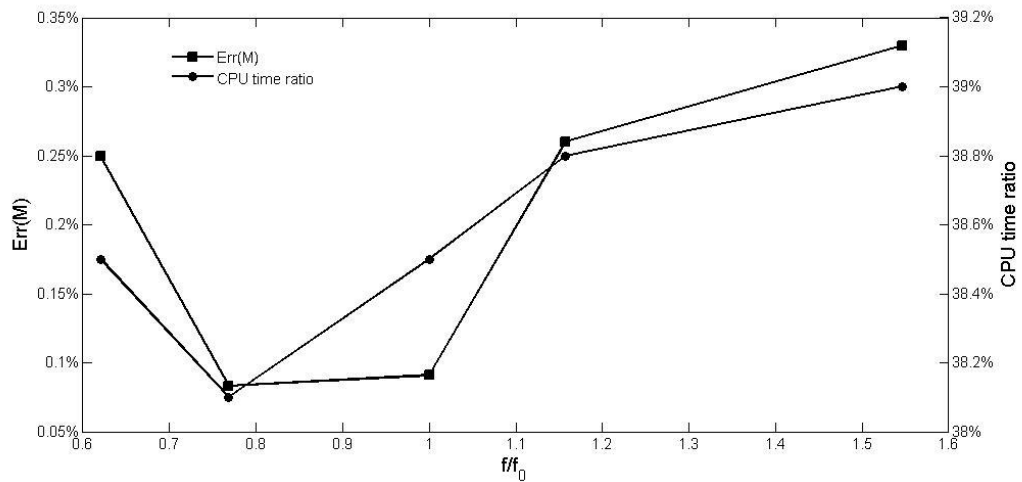


Fig. 7.3.8 The average error and CPU time ratio at motion frequency

In order to compare the numerical results between the Euler-viscous hybrid solver and the conventional RANS solver, 1<sup>st</sup> order moment components ( $\psi(M)$ ) are obtained by FFT using the time histories of the moment over 5 motion periods from  $t/T=5$  to  $t/T=10$ . The comparison of  $\psi(M)$  is shown in Fig. 7.3.7. It can be seen that the results by the Euler-viscous hybrid solver agree well with those by the conventional RANS solver for all motion frequencies considered in this study. Consequently, the present Euler-viscous hybrid solver can have the same computational accuracy as the conventional RANS solver at different motion frequencies. It is clearer in Fig. 7.3.8, which shows the variation of  $Err(M)$  with motion

frequencies. With different motion frequencies, the average errors (Err(M)) are all lower than 1%. Furthermore, more than 50% CPU time can be saved compared with that by using the conventional RANS solver within a wide range of motion frequencies.

## **7.4 Performance of the Euler-viscous hybrid solver for simulating roll damping of a floating structure**

In this section, the performance of the present Euler-viscous hybrid solver is studied for simulating the roll damping of a floating structure. In this investigation, the motion of the floating structure is not prescribed but is determined by using Newton's second law by the hydrodynamic forces acting on the structure. It is distinguishingly different from the simulation of a forced rolling structure. The algorithm in section 6.2.2 is used for this purpose. The simulation of the roll damping of a floating structure is based on the experiment carried out by Jung et al (2006), which is also studied by many researchers (Yang, 2017, 2018). The relevant experimental data is also used for validation purpose.

The physical model is described in section 7.1. The initial roll angle  $\alpha_0$  is  $\pi/12$  (15 deg). The mesh resolution obtained in the convergence study in section 7.2 is applied for current simulations. The size of the Euler domain is specified by  $L_E=40B$  and  $H=2h$ , which is sufficiently large to obtain the results covering 3 natural motion periods. In the viscous domain, the effects of the length ( $L_V$ ) and the width ( $H_V$ ) of the viscous domain and the length ( $L_{tr}$ ) of the transition zone are investigated. The time history of roll angle  $\alpha$  is used for comparison between the Euler-viscous hybrid solver and the conventional RANS solver.

### **7.4.1 The effects of the length of the viscous domain ( $L_V$ )**

Similar to the study in Section 7.3.1, simulations with different  $L_V$  are carried out by the Euler-viscous hybrid solver.  $L_V$  ranges from 14B to 3B. The configuration of mesh is the same as that in Table 7.3.1. The comparison of time histories of the roll angle is shown in Fig. 7.4.1.

From Fig. 7.4.1, it is observed that both the Euler-viscous hybrid solver and the conventional RANS solver can predict the roll damping, which is close to the experimental results. Furthermore, the relative difference between the results by the present hybrid solver with different  $L_V$  and those by the conventional RANS solver are carefully examined. The results are shown in Fig. 7.4.2. It can be seen that with the increase of  $L_V$ , the averaged error of roll angle decreases remarkably. When  $L_V>3B$ ,  $Err(\alpha)$  is below 2%. Correspondingly, the CPU time that consumed by the present solver increases with the increase of the  $L_V$ . Once again,  $L_V=6B$ , where more than 60% CPU time can be saved with  $Err(\alpha)<2\%$  compared to the conventional RANS solver, may be considered as an optimised value of  $L_V$ .

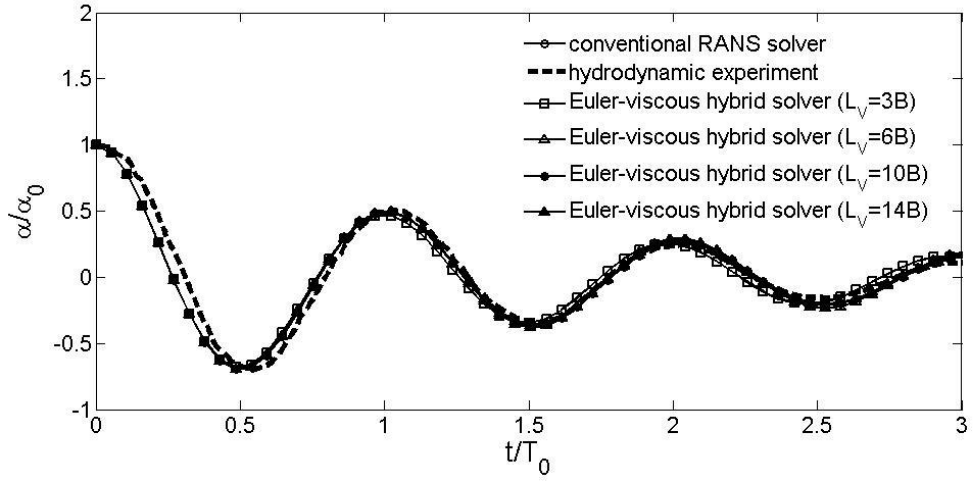


Fig. 7.4.1 The comparison of time history of roll angle at different  $L_v$

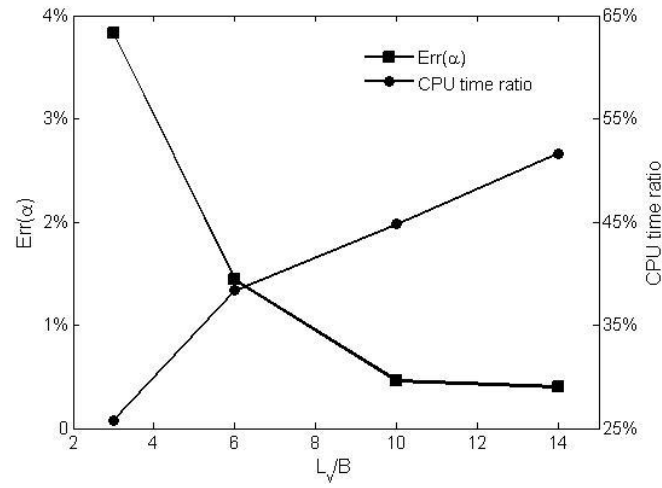


Fig. 7.4.2 The average error and CPU time ratio at different  $L_v$

#### 7.4.2 The effects of the width of the viscous domain ( $H_v$ )

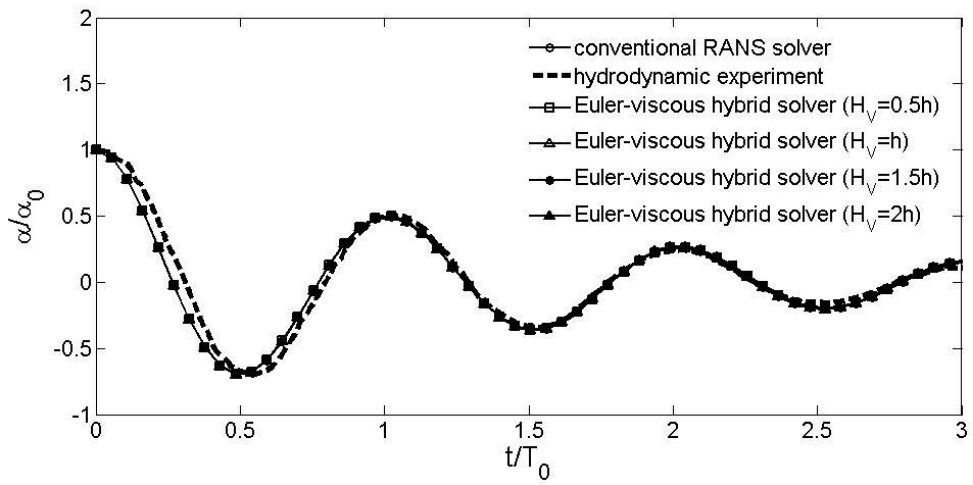


Fig. 7.4.3 The comparison of time history of roll angle at different  $H_v$

The effects of the width ( $H_V$ ) of the viscous domain are also investigated. Cases with different  $H_V$  ranging from  $H_V=2h$  to  $H_V=0.5h$  are simulated by the Euler-viscous hybrid solver. The computational domain and mesh are the same as those described in Table 7.3.2. The comparison of roll angle can be seen in Fig. 7.4.3. It is shown that all numerical results are close to the experimental results.

In order to analyze the relative difference between the results by the Euler-viscous hybrid solver and those by the conventional RANS solver, the average error of roll angle is duplicated and shown in Fig. 7.4.4, which suggests that the relative differences  $\text{Err}(\alpha)$  are all smaller than 0.5%, with different  $H_V$ . From the comparison of CPU time ratio, one can conclude again that 50% CPU time can be saved by the present solver compared with the conventional RANS solver.

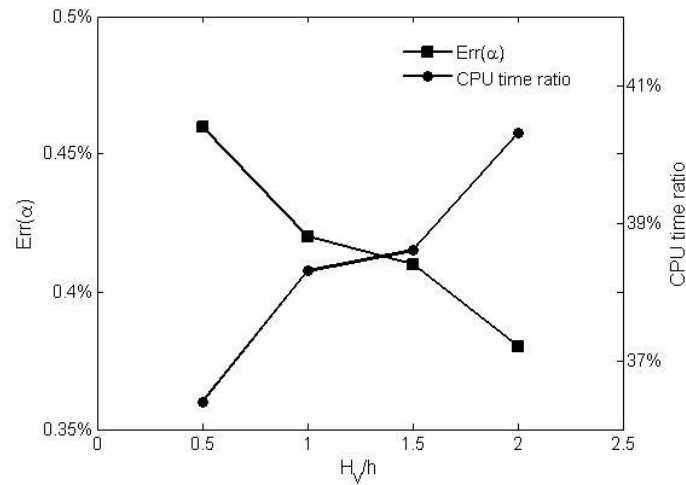


Fig. 7.4.4 The average error and CPU time ratio at different  $H_V$

#### 7.4.3 The effects of the length of the transition zone in the viscous domain ( $L_{tr}$ )

Finally, the influence of the length of the transitional zone ( $L_{tr}$ ) in the simulation of roll damping is discussed. Simulations by the Euler-viscous hybrid solver are carried out with  $L_{tr}$  ranging from  $L_{tr}=B$  to  $L_{tr}=4B$ . The computational domain and mesh are the same as those described in Table 7.3.3.

The comparison of roll angle is shown in Fig. 7.4.5. Once again, the numerical results from the Euler-viscous hybrid solver and from the conventional RANS solver agree well with the experimental data. From the average error between the results by the present hybrid solver and the conventional RANS solver are shown in Fig. 7.4.6, it can be seen that  $\text{Err}(\alpha)$  is smaller than  $\text{Err}(\alpha)=0.5\%$ ; the lowest  $\text{Err}(\alpha)$  exists when  $L_{tr}=2B$ ; whereas the consumed CPU time is quite similar at different  $L_{tr}$ .



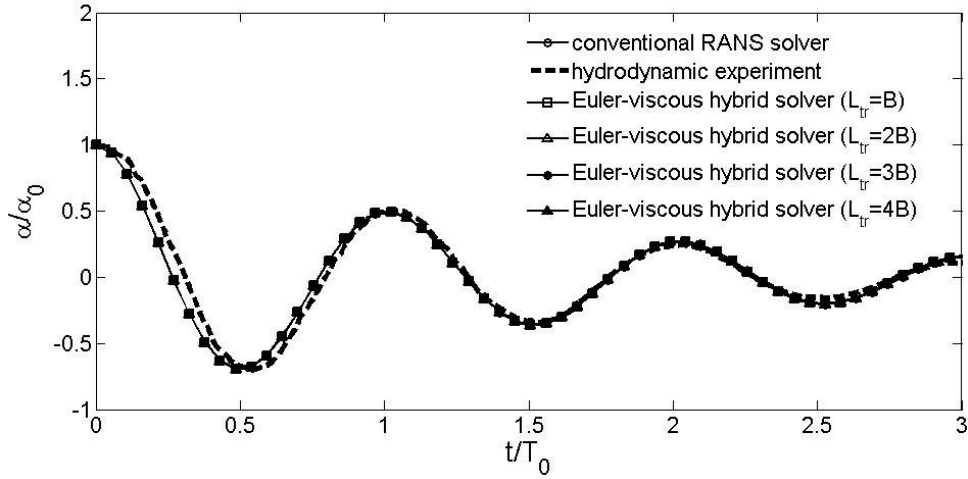


Fig. 7.4.5 The comparison of time history of roll angle at different  $L_{tr}$

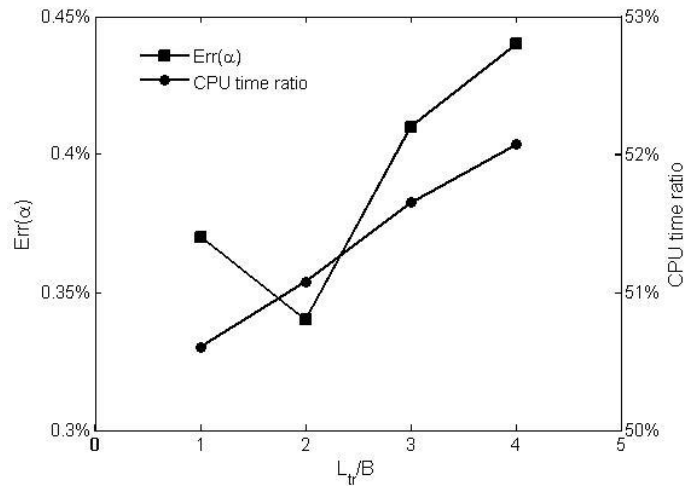


Fig. 7.4.6 average error and CPU time ratio at different  $L_{tr}$

## 7.5 Summary

In this chapter, the convergence study of the Euler-viscous hybrid solver with dynamic mesh is conducted. Numerical simulations for forced rolling and roll damping of a floating structure are applied for different solution procedures described in section 6.6. The effects of the size of the viscous domain, the length of the transition zone on the computational robustness are discussed, respectively. It shows that with the increase of the length of the viscous domain, the computational efficiency decreases while the accuracy increases. With the decrease of the width of the viscous domain, the efficiency increases slightly and the accuracy decreases a little. For the length of the transition zone, a suitable length exists corresponding to the best computational accuracy, while the computational efficiency decreases slightly with the increase of the length of the transition zone.

By the validation of the Euler-viscous hybrid, it shows that the same computational accuracy can be obtained, comparing with the conventional RANS solver. The computational efficiency can be enhanced.

## **Chapter 8 Hybrid Model Incorporating Domain-decomposition and Function-decomposition Methods for Wave-Structure Interaction**

In the previous chapters, the Euler-viscous hybrid models based on the function-decomposition method has been developed and tested for wave interactions with a floating structure. Compared with the conventional RANS solver, the Euler-viscous hybrid model requires much less CPU time (approximate 50% CPU time can be saved) in order to get solution at the same level of computational accuracy. It is admitted that all cases simulated by the Euler-viscous hybrid model and the conventional RANS model are limited to a relatively small computational domain compared to the physical wave basin in the experimental study or real sea state. This may be acceptable for normal sea state modelling where the nonlinearity of the wave is insignificant and simplified wave theories, such as linear and 2<sup>nd</sup> order wave theory, can be used to specify the wave condition in the inlet of the computational domain. Nevertheless, in practices, especially when evaluating the survivability of the structure, one may need to consider extreme waves, which cannot be accurately modelled by the above-mentioned simplified wave theories.

Compared with the two-phase Euler equation adopted by the present Euler-viscous hybrid model, the fully nonlinear potential theory (FNPT) is more robust due to the fact that it is single phase and has simpler governing equation. The FNPT has been proved to be efficient and sufficiently accurate for modelling large-scale long-duration wave propagation. Following the same method and assumption of the Euler-viscous hybrid model, i.e. the viscous effects can be ignored in the region far away from the structures, the FNPT model will be used to govern the motion of the fluid outside of the Euler domain using a domain-decomposition method. Overall, it aims to combine a function-decomposition method and a domain-decomposition method towards a multi-scale multi-model hybrid system. By the combination of two hybrid strategies, wave generation and propagation in large spatial domain are simulated by a FNPT solver and the local wave-structure interactions are modelled by the Euler-viscous hybrid solver. By the domain-decomposition method, the further provides a wave condition at the boundary of the Euler domain of the Euler-viscous hybrid solver.

In this section, the function-decomposition based Euler-viscous hybrid solvers are extended to be coupled with the FNPT solver using the domain-decomposition method. The developed model, which is referred to as an extended Euler-viscous hybrid solver, will be applied to model the interaction between waves and structures which may be fixed or undergo motion.

The performances of the Extended Euler-viscous hybrid solver are studied. Both the computational efficiency and computational accuracy will be discussed..

## 8.1 Extended Euler-viscous hybrid solver

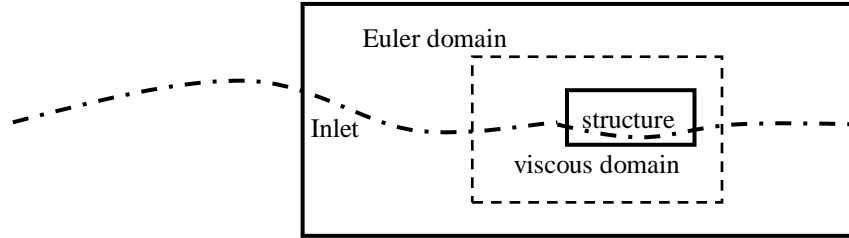


Fig. 8.1.1 The extending of the Euler-viscous hybrid solver with a fully nonlinear potential solver

In the Euler-viscous hybrid solvers, incident waves are prescribed on the inlet boundary of the Euler domain by classic simplified wave theories such as 1<sup>st</sup> order stokes waves and 5<sup>th</sup> order stokes waves assuming the wave condition at the inlet is known. Nevertheless, in practices, one may only obtain the wave forecasting/hindcasting data at a resolution at a scale of ~10s km, as indicated above. This means that one may need to apply the Euler domain at a size of ~10s km. In such a way, the computational demands may be impractical high. More importantly, such classic simplified wave theories may not be able to reproduce highly nonlinear waves, e.g. extreme focusing wave groups, as indicated above. In order to improve the computational efficiency, a fully nonlinear potential solver called OceanWave3D (Engsig-Karup, Bingham, and Lindberg, 2009) is coupled with the present Euler-viscous hybrid solvers. As described in Fig.8.1.1, the potential solver, OceanWave3D, covers the majority of the computational domain and the Euler-viscous hybrid solvers only cover a small area near the floating structures. The wave will be generated and propagates in a long-distance in the domain for the OceanWave3D. The procedure can be described in Fig. 8.1.2.

In the Extended Euler-viscous hybrid solver, the potential solver OceanWave3D is used firstly at a time step, in which the domain of the OceanWave3D covers the water phase of the Euler domain. Then, the fluid velocity and volume fraction at the inlet boundary of the Euler domain can be determined by OceanWave3D using its predicted wave elevation and the gradients of the velocity potential (fluid velocity). Only one-way coupling is considered here. This means that no feedback from the Euler domain to the potential domain will be considered. The solution in the Euler domain is then updated and the Euler solution is mapped into the viscous domain for seeking the solution of the complementary solver. Finally, the final solution is obtained in the viscous domain. For the problems associated with moving structures, the overall hydrodynamic forces on the structures predicted in the viscous domain

will be feedback to the Euler domain for updating the Euler mesh and the body-surface boundary condition.

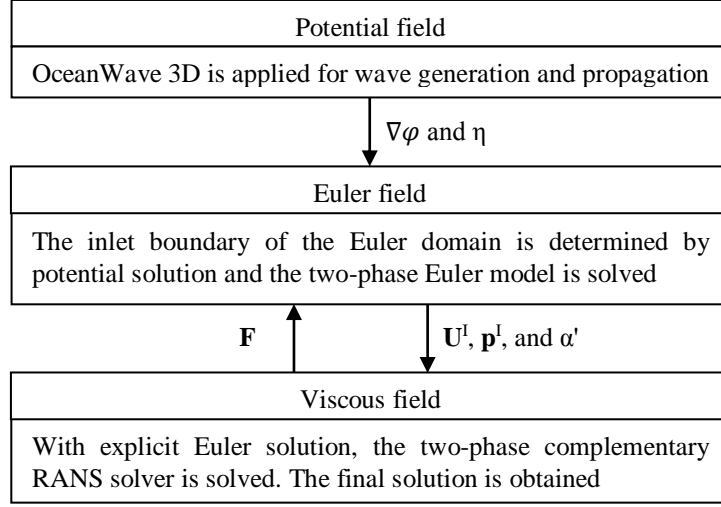


Fig. 8.1.2 Data flow in the extended Euler-viscous hybrid solver

The Extended Euler-viscous hybrid solver can be used for wave-structure interaction, no matter the structure is fixed or subjected to motions. Validations are conducted for the cases with a fixed structure or a free rolling structure subjected to incident waves, respectively. Finally, performance of the developed solver is investigated.

## 8.2 Computational domain

When the extended Euler-viscous hybrid solver is used for the simulations of wave-structure interactions in a large numerical wave basin, the computational domain is complex, due to the combination of the domain-decomposition method and the function-decomposition method. The simulation is carried out in three domains including the one-phase potential domain, the two-phase Euler domain and the two-phase viscous domain, which are illustrated in Fig. 8.2.1. According to Fig. 8.2.1, the features of computing domains can be described by parameters including  $L_P$ ,  $L_{EH}$ , and  $L_{ER}$ . Specifically,  $L_P$  presents one part of the potential domain, which is the distance of the wave propagation until the inlet boundary of the Euler domain.  $L_{EH}$  is the head part of the Euler domain, which is the distance from the inlet boundary to the gravity centre of the structure.  $L_{ER}$  is the rear part of the Euler domain, which is the distance from the gravity centre of the structure to the outlet boundary. In the simulation, the potential domain covers the entire wave basin without considering the floating structure and the OceanWave3D is used to model the water waves. The incident waves are generated in the potential domain and propagate along the distance of  $L_P$  before reaching the inlet boundary of the Euler domain, where the inlet boundary condition is imposed to the Euler equations. The inlet boundary condition of the Euler domain is specified by the solution in the potential solution. The

viscous domain is a small area surrounding the floating structure, which is overlapped with the Euler domain. The floating structure exists both in the Euler domain and the viscous domain.

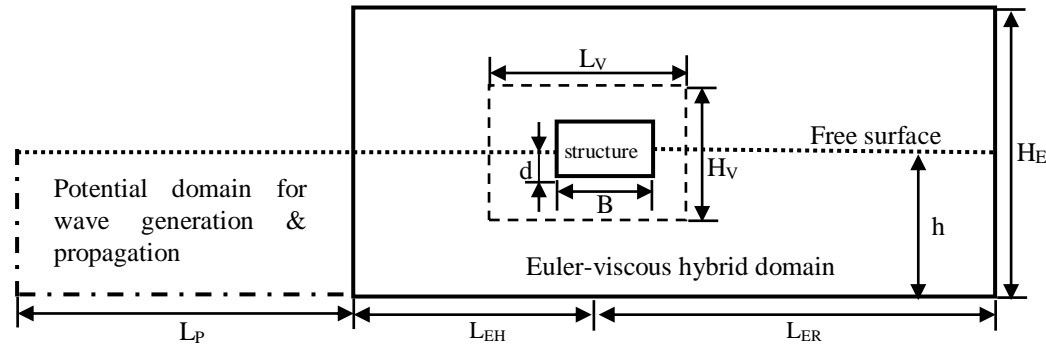


Fig. 8.2.1 Surface-piercing potential-Euler-viscous hybrid domains

Computational accuracy and efficiency of the extended Euler-viscous hybrid solver are mainly affected by two issues. The first one is associated with the coupling of the Euler domain and the viscous domain, including the mesh resolution, the size of viscous domain, and the length of transition zone. This has been discussed in Chapter 4 and Chapter 7. The second one is related to the one-way coupling of the potential solver and the Euler solver, e.g. how to effectively damp the reflection/radiation waves from the floating structure when it reaches the interface between the potential domain and the Euler domain. For the latter, one may terminate the simulation before the reflection/radiation waves reaches the interface. Consequently, the length of the Euler domain or the distance  $L_P$  before reaching the inlet boundary of the Euler domain shall be carefully selected. Detailed investigation on the performance of the extended Euler-viscous hybrid solver for wave-structure interactions are discussed below.

### 8.3 Convergence study of the Extended Euler-viscous hybrid solver for interactions between wave and fixed structures

In order to study the performance of the extended Euler-viscous hybrid solver for modelling the interaction between waves and fixed structures, a fixed structure subjected to incident waves is simulated. In this study, the parameters related to the mesh resolution, the size of the viscous domain, and the length of the transitional zone have been preliminarily tested in previous chapters and similar configurations will be adopted here. Additionally, the effects of the distance  $L_P$  before reaching the inlet boundary of the Euler domain are primarily studied in order to optimise the size of the Euler domain towards the highest computational robustness.

### 8.3.1 Physical model

Table 8.3.1 Parameters related with mesh features

Parameters	definition
$nL_C$ , $nL_E$ and $nL_V$	the numbers of division in the horizontal direction outside the refined regions ( $nL$ ), i.e. four corner areas with lengths of $(L_P+L_{EH}-B)$ & $(L_{ER}-B)$ , $(L_{EH}-B)$ & $(L_{ER}-B)$ , and $0.5L_V-B$ , for the conventional RANS solver, the Euler Solver and the complementary RANS solver, respectively.
$nB_C$ , $nB_E$ and $nB_V$	the numbers of division per width of the floating structure in the horizontal direction ( $nB$ ) in the refined region near the floating structure with the length of $2B$ for conventional RANS solver, Euler solver, and complementary RANS solver, respectively
$nH_C$ , $nH_E$ and $nH_V$	the numbers of division per height of the floating structure in the vertical direction ( $nH$ ) in the refined region near the free surface with height of $4d$ for conventional RANS solver, Euler solver, and complementary RANS solver, respectively

In this test, a real wave tank is simulated. The length of the wave tank is 32m and the mean water depth is 0.8m. According to the specification shown in Fig. 8.3.1,  $L_P+L_{EH}+L_{ER}=32m$ , which is also the same as the length of the conventional RANS domain. The distance between the wave maker and the gravity centre of the floating body is 22m ( $L_P+L_{EH}$ ), whereas the length of the rear part of the wave basin is 10m, i.e. the value of  $L_{ER}$ . The floating structure has a breath,  $B$ , of 0.2m and height,  $l$ , of 0.064m. The initial draft of structure,  $d$ , is 0.032m. The incident wave is a regular wave with wave length  $\lambda$  of 1.56m and wave height  $H_w$  of 0.04m ( $A=0.02m$ ). According to the linear dispersion, the group velocity of the incident wave is 0.795m/s. The experiment was conducted by Jung et al (2006). The wave loading, including the horizontal force ( $F_s$ ), the vertical force ( $F_h$ ) and the moment ( $M$ ) are recorded and used to quantify the accuracy of the model. For convenience, they are non-dimensionalised by  $\rho g L d A$ ,  $\rho g L B A$ , and  $\rho g L B d A$  respectively, where  $L = 0.9m$  is the length of the structure.

### 8.3.2 Mesh resolution

The mesh for the extended Euler-viscous hybrid solver is illustrated in Fig. 8.3.1. As above, two sets of mesh for the Euler domain and the viscous domain, as well as the computational mesh for the conventional RANS solver, are all generated by using the blockMesh function of OpenFOAM. Relative parameters to reflect the mesh resolutions are described in Table 8.3.1

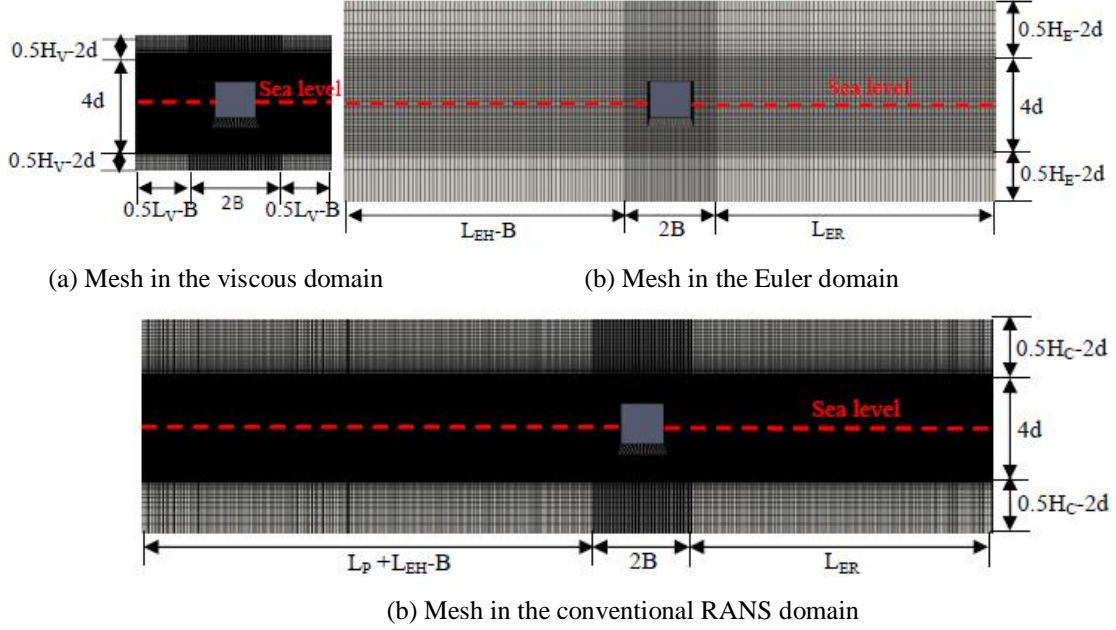


Fig. 8.3.1 Mesh in hybrid domains

Following the convergence test in Chapter 4, those parameters are taken as  $L_t=0.5\lambda$ ,  $L_V=2\lambda$ ,  $H_V=H_E=1.5h$ ,  $nL_V=200$ ,  $nB_V=80$ ,  $nH_V=30$ ,  $nL_E=100$ ,  $nB_E=40$ , and  $nH_E=15$ . These will ensure a sufficient mesh resolution for the Euler and the viscous domains, as well as sufficient size of the transitional zone for suppressing the viscous effects gradually near the boundary of the viscous domain.

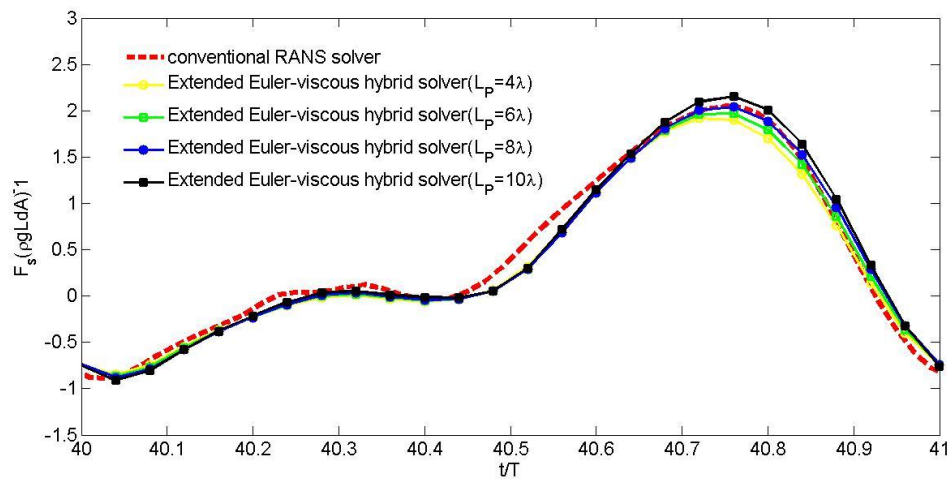
### 8.3.3 The effects of the distance $L_P$ before reaching the inlet boundary of the Euler domain

Because the computational domain of OceanWave3D covers the entire physical domain, i.e. 32m, the distance  $L_P$  before reaching the inlet boundary of the Euler domain does not influence the CPU time used by the OceanWave3D. Furthermore,  $L_P+L_{EH}$  is fixed, i.e. 22m (approximately  $14\lambda$ ). Smaller  $L_P$  means larger  $L_{EH}$ , consequently larger size of the Euler domain and longer CPU time required by the extended Euler-viscous hybrid solver. In order to investigate the effects of  $L_P$ , different values ranging from  $10\lambda$  ( $L_{EH}=4\lambda$ ) to  $4\lambda$  ( $L_{EH}=10\lambda$ ) are considered in the investigation.

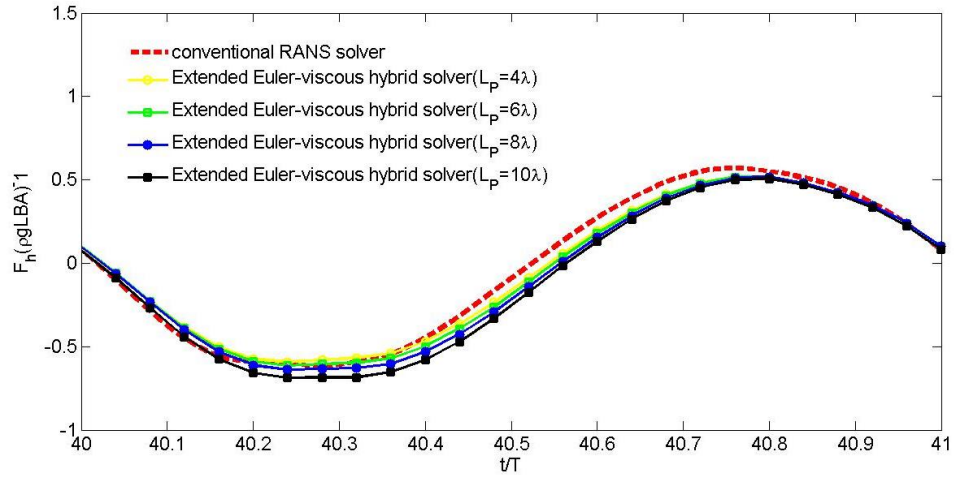


In the physical experiments and the conventional RANS simulation, it takes  $22m/c_g \approx 27.5T$ , where  $c_g$  is the group velocity of the incident waves, for the reflection waves from the floating structure reaching the wave maker, which is installed in the left end of the wave tank. The wave maker will re-reflect the reflected wave. It takes approximately  $27.5T$  for the re-reflected wave from the wave maker reaches the floating body. This means that after  $55T$ , the measurement or the simulation by the conventional RANS model may not be acceptable. On the other hand, for the extended Euler-viscous hybrid solver, the reflection from the floating structure will be re-reflected from the left end of the Euler domain. Taking  $L_P = 4\lambda$  as example, it may take approximately  $39T$  for the re-reflection waves reaches the floating bodies. In order to examine the performance of the Extended Euler-viscous, the wave loading during the period of  $40-55T$  is chosen. During this period, the numerical results by the conventional RANS equations are not affected by the re-reflection waves, whereas those by the extended Euler-viscous hybrid solver do. It shall also be noted that when the re-reflection wave reaches the floating structure, part of them are reflected again by the floating structures. Consequently, for specific value of  $L_P$ , longer the duration of the simulation, more significant the error caused by the reflection by the boundary of the Euler domain might be. In the other words, for specific duration of the simulation, longer value of  $L_P$ , more significant such error might be.

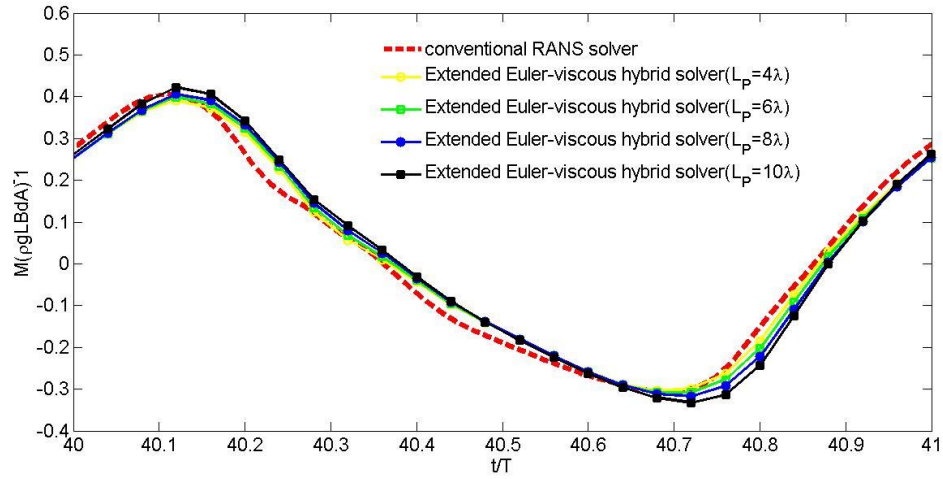
The wave loading on the floating structure in the cases with different  $L_P$  is illustrated in Fig. 8.3.2. For clarity, only the time history at  $40-41T$ , during which all numerical results has shown a quasi-steady state, is plotted. For the purpose of comparison, the corresponding results by the conventional RANS solver are also plotted. It is shown that results from the extended Euler-viscous hybrid solver with different  $L_P$  behave similarly to that from the conventional RANS solver. The relative differences of wave loading obtained by using Eq. (4.2.2) are extracted and plotted in Fig. 8.3.3.



(a) The comparison of the horizontal force ( $F_s$ )



(b) The comparison of the vertical force ( $F_h$ )



(c) The comparison of the moment (M)

Fig. 8.3.2 The comparison of wave loads at different  $L_p$

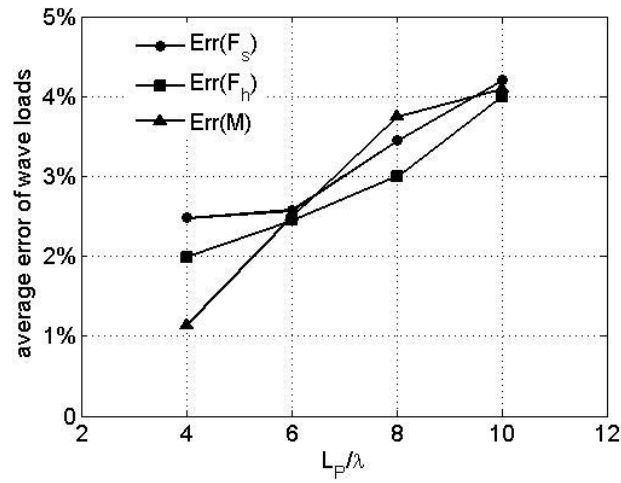


Fig. 8.3.3 average error of wave loads under different  $L_p$

From Fig. 8.3.3, it can be seen that with the increase of  $L_P$ , the average difference increases gradually. It is well understood that the viscosity play insignificant role for non-breaking waves. Therefore, the FNPT or the Euler equation shall be able to accurately model the propagation of the wave away from the structures at the same accuracy level as the conventional RANS solver, providing sufficient mesh resolutions. Therefore, the relative difference shown in these Figures are primarily caused by the reflection from the boundary of the Euler domain.

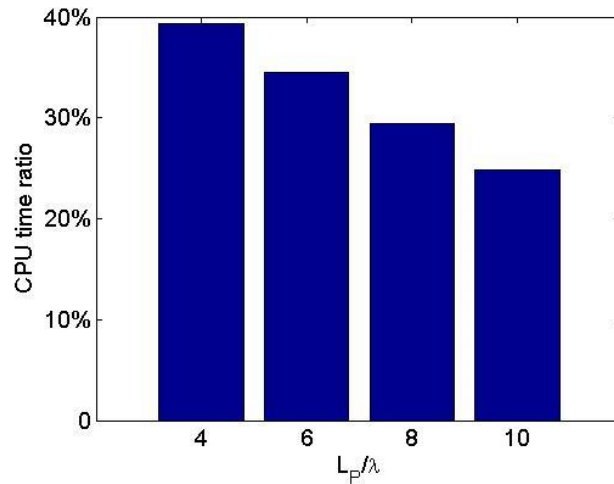


Fig. 8.3.4 CPU time ratio at different  $L_P$

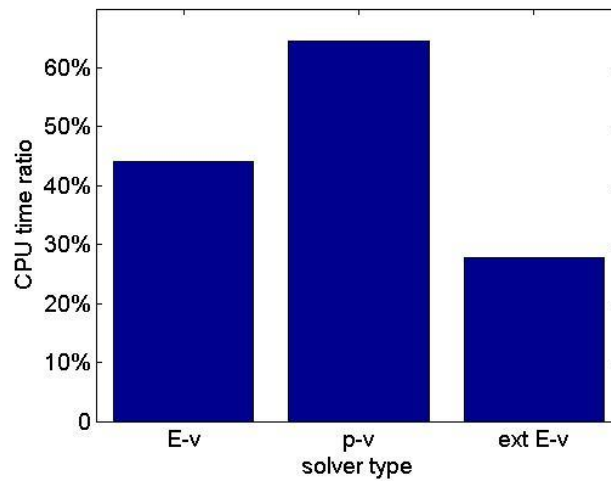


Fig. 8.3.5 CPU time ratio for different solvers

In addition to the computational accuracy, the CPU time consumed by the cases with different  $L_P$  is also concerned and the corresponding results are shown in Fig. 8.3.4. As expected, the CPU time ratio between the extended Euler-viscous hybrid solver and the conventional RANS solver reduces considerably as with the increase of  $L_P$ , attributing the fact that the FNPT solver is more efficient for modelling non-breaking waves. Furthermore, the

computational efficiency of the extended Euler-viscous hybrid solver (ext E-v,  $L_P=10\lambda$ ,  $L_V=2\lambda$ ) is also compared with those of other two solvers. These include (1) the potential-viscous hybrid solver (p-v,  $L_P=10\lambda$ ) which directly couples the OceanWave3D with the conventional RANS solver with  $L_P=10\lambda$ ; and (2) the Euler-viscous hybrid solver (E-v,  $L_V=2\lambda$ ) with  $L_P=0$ . All solvers adopt sufficient mesh resolution towards a convergent solution. The CPU time ratios against the conventional RANS solver is shown in Fig. 8.3.5, which clearly demonstrates the superiority of the extended Euler-viscous hybrid solver over others, which only use either the domain-decomposition method or the function-decomposition method, in terms of computational robustness.

## 8.4 Convergence study of the extended Euler-viscous hybrid solver for modelling rolling structures in waves

In Chapter 7, the Euler-viscous hybrid solver has been used for modelling a moving structure in waves, where no incident waves have been considered. In this section, the incident wave is taken into account and consequently a larger computational domain will be employed by the extended Euler-viscous hybrid solver. For simplification, the structure is subjected free rolling motion excited by the incident waves. All criteria regarding the performance of the present solver, including the mesh resolution, the size of viscous domain, the length of transition zone, and the value of  $L_P$  are discussed in terms of computational robustness.

### 8.4.1 Physical model

The sketch of the physical model is shown in Fig. 8.1.1. The total length of the wave basin is 30m with the mean water depth ( $h$ ) of 0.9m. In the numerical simulation,  $L_P+L_{EH}+L_{ER}=30\text{m}$ . The floating structure is located 20m away from the wave maker, which is installed in the left end of the computational domain, yielding  $L_{ER}=10\text{m}$ . The breath( $B$ ), height( $l$ ) and length ( $L$ , normal to the sketch shown in Fig.8.1.1) of the floating structure are 0.3m, 0.1m and 0.9m, respectively. The initial draft is taken as  $d=0.05\text{m}$ . Regular incident waves are generated in the potential domain with wave length  $\lambda$  and wave height  $H_w$ . The floating structure can only be subjected to roll motion around the centre of gravity, which is located at the centre of the structure. The roll angle  $\alpha$  of the floating structure is recorded and non-dimensionalised by  $kA$ , where  $k=2\pi/\lambda$  is the wave number and  $A$  is the wave amplitude.

### 8.4.2 Convergence study

The structure of the mesh used here is the same as that used in section 8.3. However, the convergence study are conducted to seek appropriate mesh sizes for modelling a free-rolling structure in waves, whose hydrodynamic feature may be different from those presented in Chapter 7 without considering incident waves.

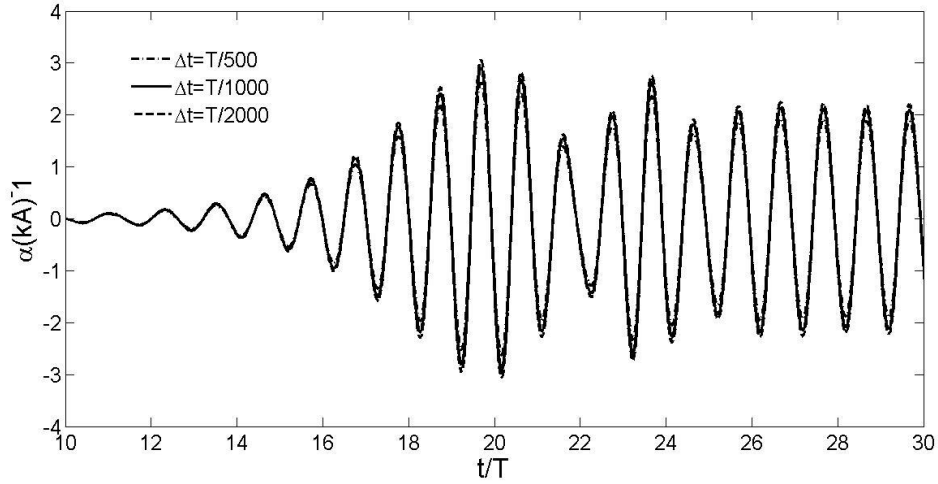


Fig. 8.4.1 The time history of roll angle

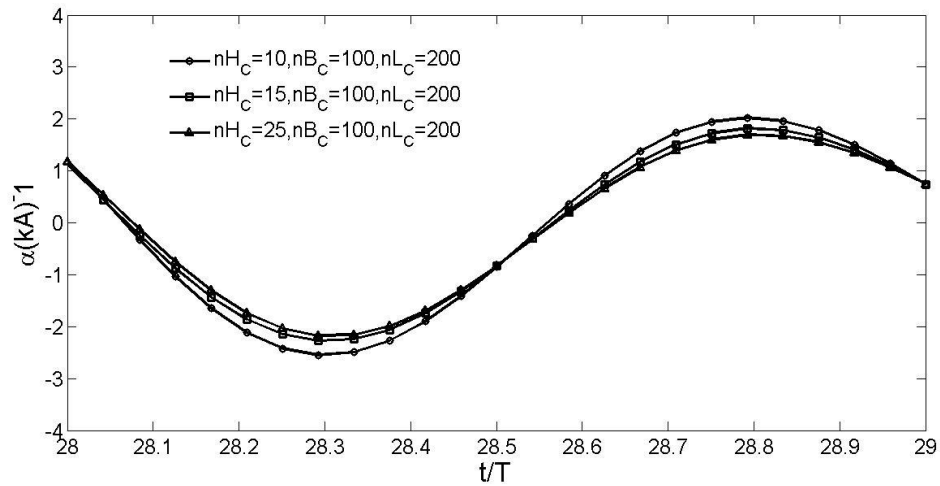
In the convergence study, the incident wave with wave length  $\lambda=2.22\text{m}$  ( $\lambda/h=2.46$ ) and wave height  $H_w=0.032\text{m}$  ( $H_w/h=0.035$ ) is used. Similarly, the convergence property against time step size is investigated firstly. For this purpose,  $\Delta t=T/500$ ,  $\Delta t=T/1000$ , and  $\Delta t=T/2000$  are used. Once again, the convergent results from the conventional RANS solver are regarded as a reference in the convergence test. The time history of roll angle  $\alpha$  from the conventional RANS solver is shown in Fig. 8.4.1, for which the mesh resolution is specified by using  $nH_C=15$ ,  $nL_C=200$ , and  $nB_C=100$ . One can find that after  $t/T=28$ , the roll angle is periodic. Hence, in the convergence study, the relative average error of roll angle is used, defined as

$$\text{REM}(1,2) = \sum_{i=1}^{10} \left[ \frac{\text{Max}(|\alpha_1^i - \alpha_2^i|)}{\text{Max}(\alpha_1^{\text{max}} - \alpha_1^{\text{min}}, \alpha_2^{\text{max}} - \alpha_2^{\text{min}})} \right] / 10 \quad (8.4.1)$$

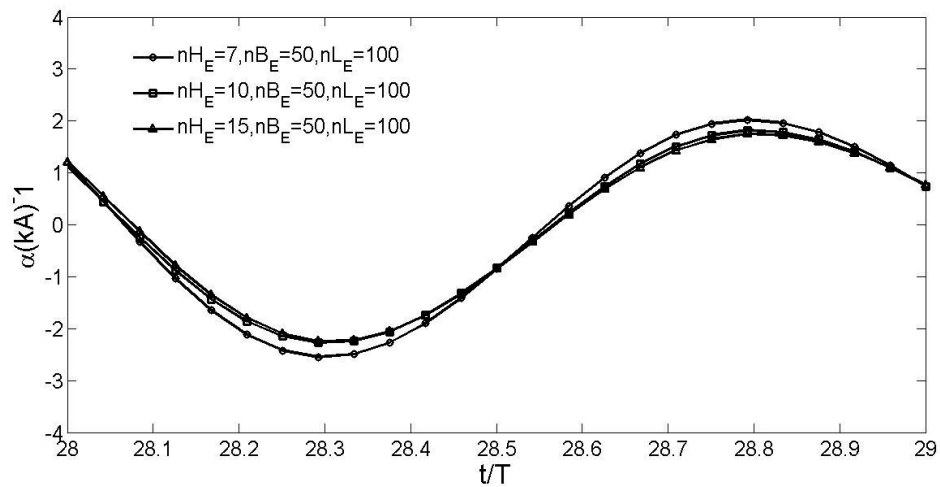
where  $\text{Max}(|\alpha_1^i - \alpha_2^i|)$  is the maximum difference of the roll angle between the results obtained using mesh case 1 and case 2 (represented by the subscripts 1 and 2), in one wave period at quasi-steady state,  $\alpha^{\text{max}}$  and  $\alpha^{\text{min}}$  are the peak and trough values of roll angle in the same wave period. Following the code for engineering practices, 5% error is used as the critical value for evaluating the convergence. For the results shown in Fig. 8.4.1,  $\text{REM}(\Delta t=T/500, \Delta t=T/1000)=9.8\%$  and  $\text{REM}(\Delta t=T/1000, \Delta t=T/2000)=4.2\%$ . One may agree that time step  $\Delta t=T/1000$  is sufficient for the conventional RANS simulation. Similar to the convergent tests presented previously,  $\Delta t=T/1000$  is adopted for the extended Euler-viscous hybrid solver.

Firstly, the convergence study of the number of divisions per wave height is conducted for the conventional RANS solver ( $nH$ ), which is different from the definition in table 8.3.1, due to incident waves. Cases with  $nH_C=10$ ,  $nH_C=15$ , and  $nH_C=25$  are simulated with fixed value of  $nB_C$  and  $nL_C$ , i.e.  $nB_C=100$  and  $nL_C=200$ . The comparison of roll angle in the cases with different  $nH_C$  in one wave period at the quasi-steady state, i.e.  $28-29T$ , is shown in Fig. 8.4.2 (a), which demonstrates that  $nH_C=15$  is sufficient for the conventional RANS solver. The

corresponding values of the relative errors are  $REM(nH_C=15, nH_C=25)=2\%$  and  $REM(nH_C=15, nH_C=10)=10\%$ . Alternatively, Cases with  $nH_E=7$ ,  $nH_E=10$ , and  $nH_E=15$  are simulated by using the Euler solver with  $nB_E=50$  and  $nL_E=100$ . The corresponding results are shown in Fig. 8.4.2(b). One may conclude that  $nH_E=10$  should be taken as the appropriate value. The corresponding REMs are  $REM(nH_E=7, nH_E=10)=7.5\%$  and  $REM(nH_E=10, nH_E=15)=1.2\%$ .



(a) The conventional RANS solver

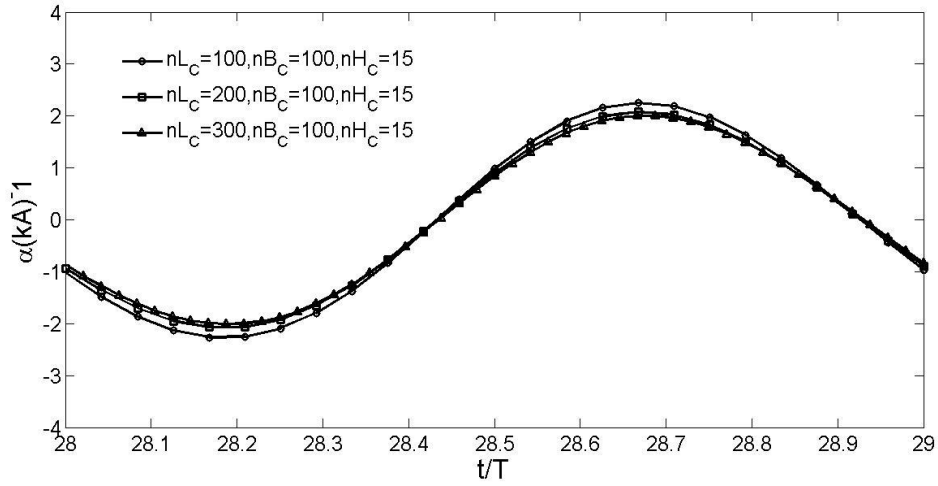


(b) The Euler solver

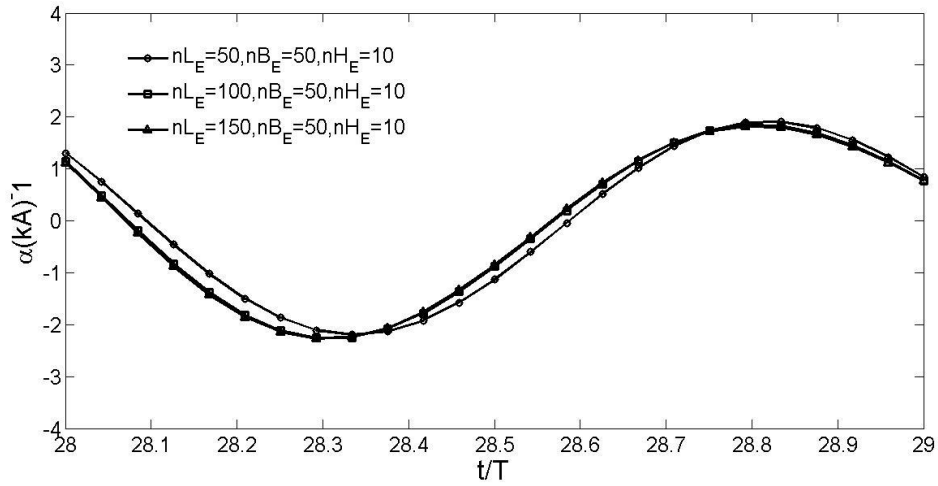
Fig. 8.4.2 The comparison of the roll ( $nH_C$  and  $nH_E$ ) between the conventional RANS solver and the Euler solver

Similar works have been done for the convergence properties against  $nL$  (number of division in horizontal in the region far away from the floating structure) and  $nB$  (number of division in horizontal in the refined area near the floating structure) for the conventional RANS solver and the Euler solver. Some results are shown in Fig. 8.4.3 and Fig. 8.4.4. For the conventional RANS solver,  $nL_C=200$  is sufficient if  $nB_C=100$  and  $nH_C=15$  are applied as demonstrated by Fig. 8.4.3(a)), where  $REM(nL_C=100, nL_C=200)=9.7\%$  and  $REM(nL_C=200,$

$nL_C=300$ )=0.6%;  $nB_C=100$  is sufficient if  $nL_C=200$  and  $nH_C=15$  are employed, as displayed by Fig. 8.4.4(a)), in which  $REM(nB_C=100, nB_C=150)=0.5\%$  and  $REM(nB_C=100, nB_C=50)=8.6\%$ . For the Euler solver,  $nL_E=100$  is sufficient if  $nB_E=50$  and  $nH_E=10$  are used, as shown in Fig. 8.4.3(b), where  $REM(nL_E=50, nL_E=100)=14.2\%$  and  $REM(nH_E=100, nH_E=150)=1.4\%$ ;  $nB_E=100$  shall be used to get convergent results if  $nL_E=100$  and  $nH_E=10$  applied, as illustrated in Fig.8.4.4(b), in which  $REM(nB_E=100, nB_E=50)=0.4\%$  and  $REM(nB_E=50, nB_E=25)=7.3\%$ .

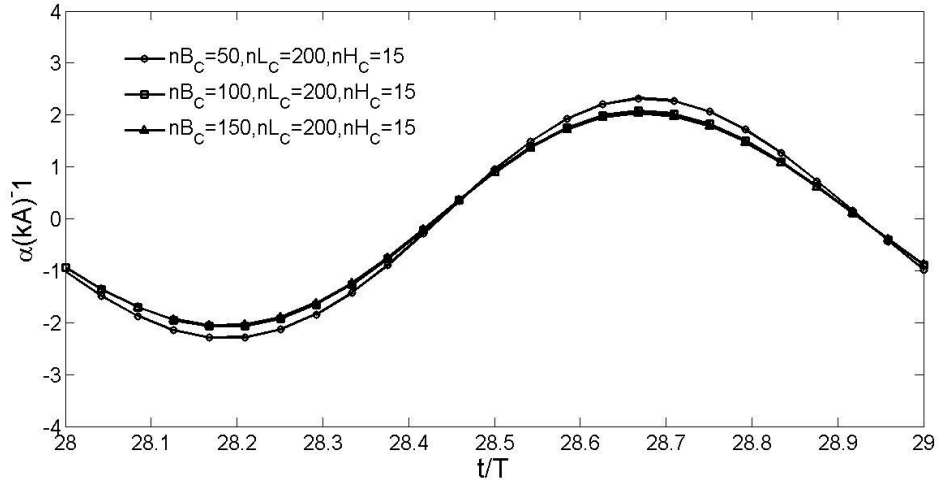


(a) The conventional RANS solver

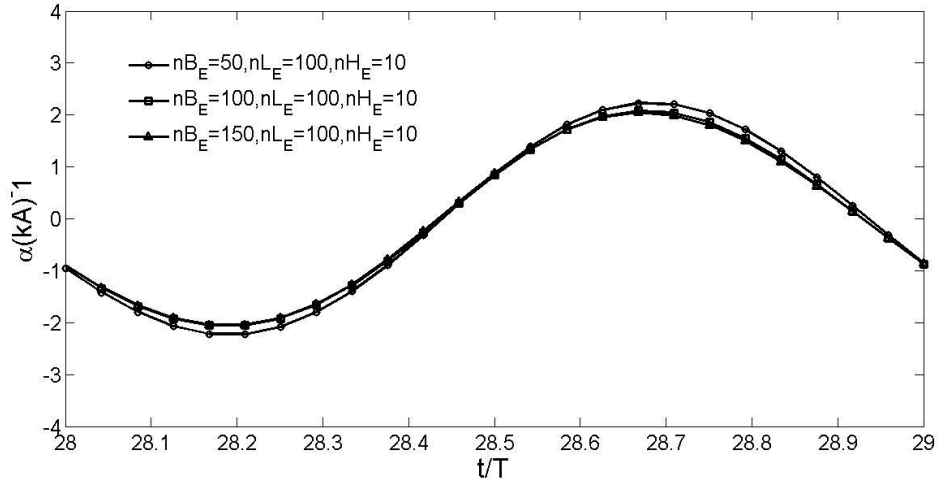


(b) The Euler solver

Fig. 8.4.3 The comparison of the roll ( $nL_C$  and  $nL_E$ ) between the conventional RANS solver and the Euler solver



(a) The conventional RANS solver



(b) The Euler solver

Fig. 8.4.4 Time histories of the roll angles in the cases with different values of  $nB_C$  and  $nB_E$  for the conventional RANS solver and the Euler solver, respectively

In summary, it is found that mesh resolution specified by  $nB_C=100$ ,  $nL_C=200$ , and  $nH_C=15$  are sufficient for the conventional RANS solver to achieve convergent results; whereas the Euler solver requires coarser mesh resolution, which may be specified by  $nB_E=50$ ,  $nL_E=100$ , and  $nH_E=10$ . Once again, this confirms the necessity of the developing the hybrid modelling coupling the Euler solver with the complementary RANS solver. Similar to the investigation in Section 7.2, it is assumed that the same mesh resolution as the conventional RANS solver shall be used in the viscous domain of the hybrid solver and the same mesh resolution as the Euler solver shall be used in the Euler domain in order to achieve convergent results. This is confirmed by the results shown in Fig. 8.4.5, which compares the results from the conventional RANS solver and those from the extended Euler-viscous hybrid solver. For the latter,  $L_P=4\lambda$ ,  $L_{EH}=6\lambda$ ,  $L_{ER}=4.5\lambda$ ,  $H_E=2h$ ,  $L_V=2\lambda$ ,  $H_V=2h$ , and  $L_{tr}=0.5\lambda$  are used to specify the computational domain.  $nB_E=50$ ,  $nL_E=100$ ,  $nH_E=10$ ,  $nB_V=100$ ,  $nL_V=200$ , and  $nH_V=15$  are



used for the mesh generation. From Fig. 8.4.5, one can find that results in the quasi-steady state , i.e. after  $t/T=28$ , obtained by the conventional RANS solver agree well with the corresponding results from the extended Euler-viscous hybrid solver. Noticeable difference is observed at time  $t/T$  ranging from 12 to 18. It seems that the transient effects on the structure motion are damped slower in the modelling by the extended Euler-viscous hybrid solver. This may be due to the fact that the viscous effects are only considered in a small domain near the floating structure by the extended Euler-viscous hybrid solver.

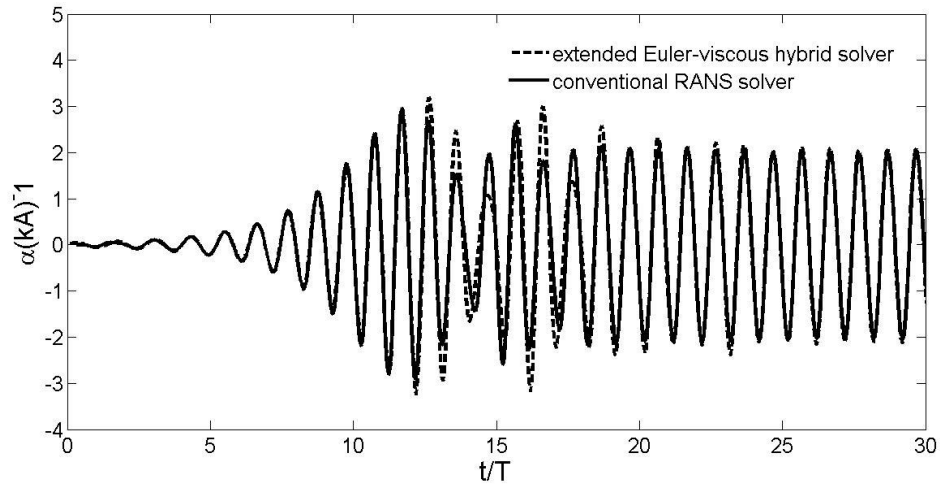


Fig. 8.4.5 The time histories of the roll angle obtained by the conventional RANS solver and the extended Euler-viscous hybrid solver

#### 8.4.3 Effects of the length of the viscous domain ( $L_V$ )

Table 8.4.1 The mesh for the study of effects of length ( $L_V$ ) of the viscous domain

(a) The mesh for the conventional RANS solver

Conventional RANS domain				
$L_C$	$H_C$	$nL_C$	$nB_C$	$nH_C$
$14.5\lambda$	$2h$	200	100	15

(b) The mesh for the extended Euler-viscous hybrid solver

No	Potential domain	Euler domain						Viscous domain					
	$L_P$	$L_{EH}$	$L_{ER}$	$H_E$	$nL_E$	$nH_E$	$nB_E$	$L_V$	$H_V$	$L_{tr}$	$nL_V$	$nH_V$	$nB_V$
1	$4\lambda$	$6\lambda$	$4.5\lambda$	$2h$	100	10	50	$2\lambda$	$2h$	$0.5\lambda$	200	15	100
2	$4\lambda$	$6\lambda$	$4.5\lambda$	$2h$	100	10	50	$3\lambda$	$2h$	$0.5\lambda$	200	15	100
3	$4\lambda$	$6\lambda$	$4.5\lambda$	$2h$	100	10	50	$4\lambda$	$2h$	$0.5\lambda$	200	15	100

In order to study the influence of  $L_V$  used by the extended Euler-viscous hybrid solver in terms of computational robustness, cases with different  $L_V$  ranging from  $2\lambda$  to  $4\lambda$ , are simulated. In these cases, the computational domain and mesh resolution are described in

Table 8.4.1. The wave conditions are the same as that used in section 8.4. The same case is also simulated by the conventional RANS solver for comparison.

Following Fig. 8.4.5, the roll angle over one wave period at quasi-steady state, i.e., from 28T to 29T, is used to evaluate the computational accuracy. Some results are shown in Fig. 8.4.6. It can be seen that the extended Euler-viscous hybrid solver seems not to be disturbed by the value of  $L_V$  considered in the test. All results are slightly different from the corresponding results by the conventional RANS solver. The relative  $\text{Err}(\alpha)$  and the CPU time are examined and shown in Fig. 8.4.7, which suggests that with the increase of  $L_V$ , the relative error decreases whereas the CPU time increases. One may agree that  $L_V=2\lambda$  is suitable for the present solver, at which more than 70% CPU time can be saved and  $\text{Err}(\alpha)$  is smaller than 5% compared to the conventional RANS solver.

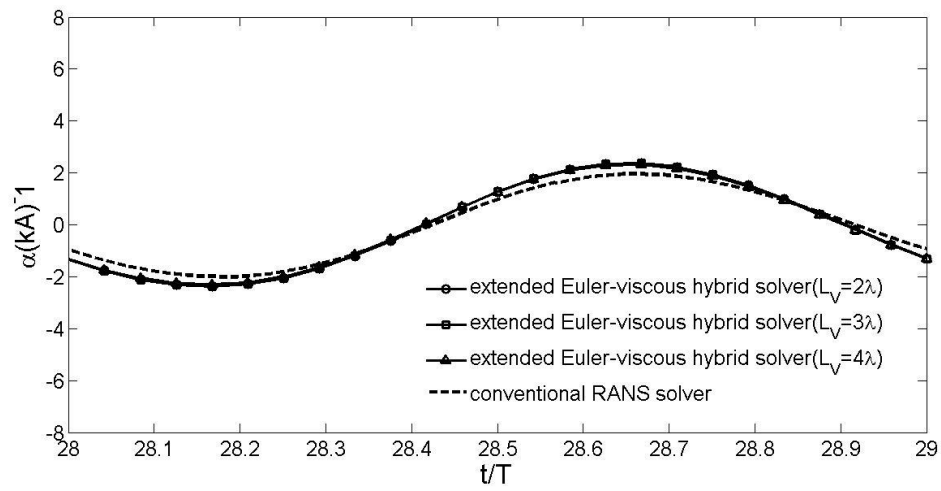


Fig. 8.4.6 The comparison of roll angle at different  $L_V$

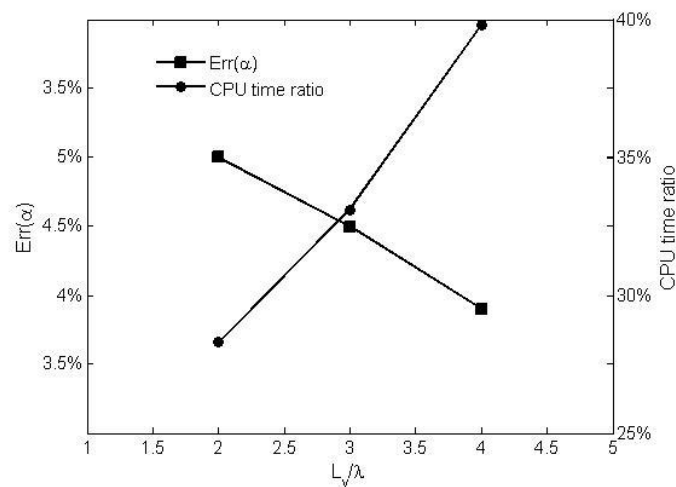


Fig. 8.4.7 Average error and CPU time ratio at different  $L_V$

#### 8.4.4 Effects of the width of the viscous domain ( $H_V$ )

In addition to the length of the viscous domain ( $L_V$ ), the width of the viscous domain ( $H_V$ ) plays an important role. The corresponding effects are also examined. For this purpose, cases with  $H_V=h$ ,  $H_V=1.5h$ , and  $H_V=2h$  are taken into account by the extended Euler-viscous hybrid solver. All other conditions are the same. The configurations of the computational domain and the mesh resolutions in this test are listed in Table 8.4.2.

The comparison of roll motion in the cases with different  $H_V$  is shown in Fig. 8.4.8. Unlike the comparison shown in Chapter 7, for the cases with incident waves, the accuracy of the extended Euler-viscous hybrid solver is sensitive to the value of  $H_V$ . Larger  $H_V$  is closer to the result from the present solver to that from the conventional RANS solver. For  $H_V=2h$ , the relative  $\text{Err}(\alpha)=4.45\%$ , which may be quantified as acceptable. According to the limit investigation in this test, it is therefore recommended to use the same height of the viscous domain as that adopted by the conventional RANS solver.

Table 8.4.2 The mesh for the study of effects of the width ( $H_V$ ) of the viscous domain

(a) The mesh resolution for the conventional RANS solver

Conventional RANS domain				
$L_C$	$H_C$	$nL_C$	$nB_C$	$nH_C$
$14.5\lambda$	$2h$	200	100	15

(b) The mesh for the extended Euler-viscous hybrid solver

No	Potential domain	Euler domain						Viscous domain					
	$L_P$	$L_{EH}$	$L_{ER}$	$H_E$	$nL_E$	$nH_E$	$nB_E$	$L_V$	$H_V$	$L_{tr}$	$nL_V$	$nH_V$	$nB_V$
1	$4\lambda$	$6\lambda$	$4.5\lambda$	$2h$	100	10	50	$2\lambda$	$h$	$0.5\lambda$	200	15	100
2	$4\lambda$	$6\lambda$	$4.5\lambda$	$2h$	100	10	50	$2\lambda$	$1.5h$	$0.5\lambda$	200	15	100
3	$4\lambda$	$6\lambda$	$4.5\lambda$	$2h$	100	10	50	$2\lambda$	$2h$	$0.5\lambda$	200	15	100

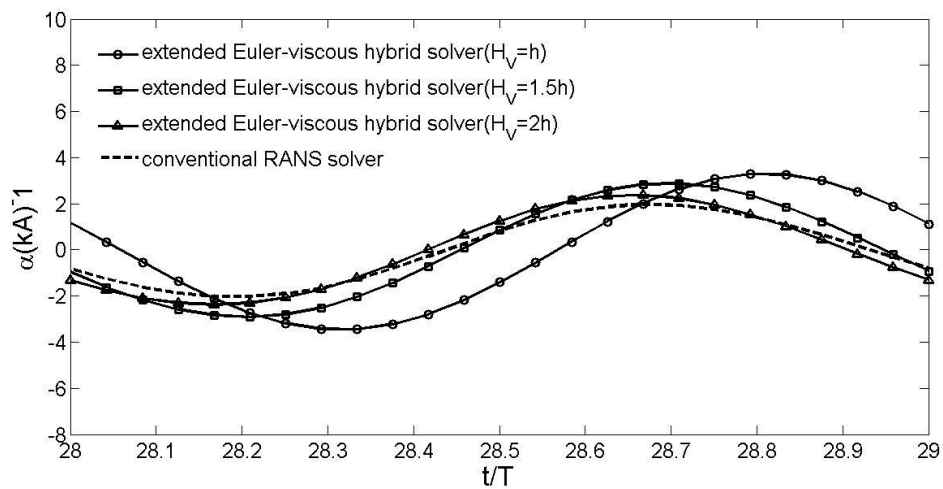


Fig. 8.4.8 The comparison of roll angle at different  $H_V$

#### 8.4.5 Effects of the length of the transition zone ( $L_{tr}$ )

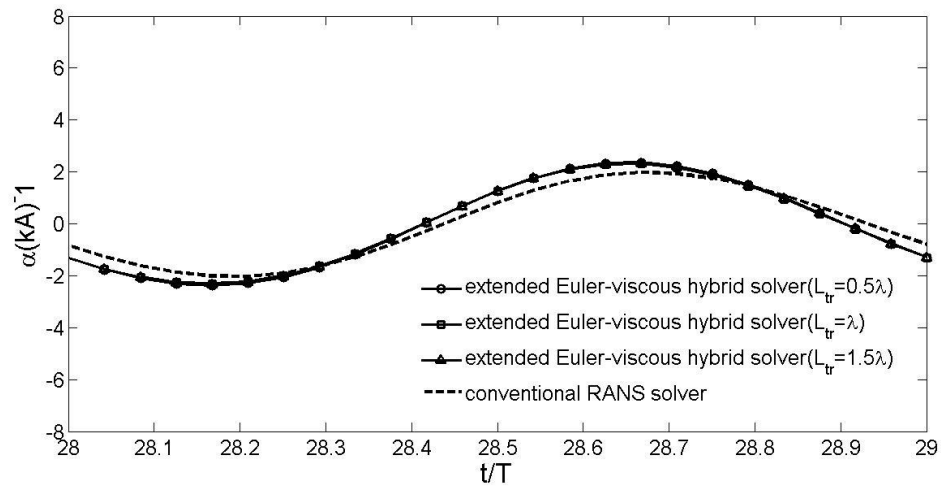


Fig. 8.4.9 The time histories of roll angle in the cases with different  $L_{tr}$

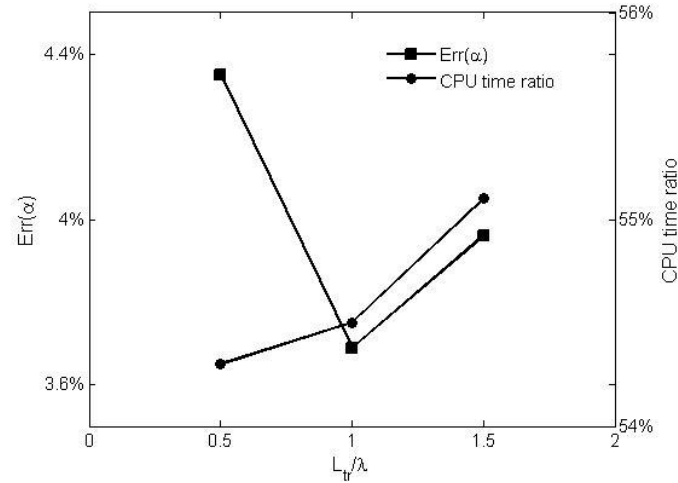


Fig. 8.4.10 Average error and CPU time ratio at different  $L_{tr}$

Table 8.4.3 The mesh for the study of effects of the length ( $L_{tr}$ ) of transition zone

(a) The mesh for the conventional RANS solver

Conventional RANS domain				
$L_C$	$H_C$	$L_C$	$nB_C$	$nH_C$
$14.5\lambda$	$2h$	200	100	15

(b) The mesh for the extended Euler-viscous hybrid solver

No	Potential domain	Euler domain						Viscous domain					
	$L_P$	$L_{EH}$	$L_{ER}$	$H_E$	$nL_E$	$nH_E$	$nB_E$	$L_V$	$H_V$	$L_{tr}$	$nL_V$	$nH_V$	$nB_V$
1	$4\lambda$	$6\lambda$	$4.5\lambda$	$2h$	100	10	50	$4\lambda$	$2h$	$0.5\lambda$	200	15	100
2	$4\lambda$	$6\lambda$	$4.5\lambda$	$2h$	100	10	50	$4\lambda$	$2h$	$\lambda$	200	15	100
3	$4\lambda$	$6\lambda$	$4.5\lambda$	$2h$	100	10	50	$4\lambda$	$2h$	$1.5\lambda$	200	15	100

In order to investigate the effects of the length of the transitional zone ( $L_{tr}$ ), cases with  $L_{tr}=0.5\lambda$ ,  $L_{tr}=\lambda$ , and  $L_{tr}=1.5\lambda$  are simulated by the extended Euler-viscous hybrid solver. Detailed case configuration is described in Table 8.4.3. All other conditions are the same as above.

In these cases, the length  $L_v$  and the weight  $H_v$  of the viscous domain are  $4\lambda$  and  $2h$ , respectively. The time histories of the roll motion are compared in Fig. 8.4.9. It can be seen that the results by the extended Euler-viscous hybrid solver are not sensitive to the size of the transitional zone within the range considered in this test. All results are slightly different from the corresponding result from the conventional RANS solver. The relative error  $Err(\alpha)$  are all lower than 5%, as shown in Fig. 8.4.10, together with the variation of the CPU time against  $L_{tr}$ . One may agree that  $L_{tr}=\lambda$  might be the optimised value for the case considered here.

#### 8.4.6 Effects of distance $L_p$ before reaching the inlet boundary of the Euler domain

The effects of  $L_p$  for the cases with a fixed structure are studied in section 8.3.3, from which one can find that  $L_p$  considerably affect the computational accuracy and efficiency of the extended Euler-viscous hybrid solver. For the case with a free rolling structure, the reflection waves may be more significant and the radiation waves caused by the motion of the structures shall also taken into account. Hence, the effect of  $L_p$  on the robustness of the extended Euler-viscous hybrid solver is investigated again for the case with freely rolling motion. For this purpose, different values of  $L_p$ , i.e.,  $L_p=2\lambda$ ,  $L_p=4\lambda$ , and  $L_p=6\lambda$ , are tested. All other parameters are the same as others in Section 8.4.3~8.4.5 of this chapter. The detailed configurations are described in Table 8.4.4.

Table 8.4.4 The mesh for the study of effects of  $L_p$  of the viscous domain

(a) The mesh for the conventional RANS solver

Conventional RANS domain				
$L_c$	$H_c$	$L_c$	$nB_c$	$nH_c$
$14.5\lambda$	$2h$	200	100	15

(b) The mesh for the extended Euler-viscous hybrid solver

No	Potential domain	Euler domain						Viscous domain					
	$L_p$	$L_{EH}$	$L_{ER}$	$H_E$	$nL_E$	$nH_E$	$nB_E$	$L_v$	$H_v$	$L_{tr}$	$nL_v$	$nH_v$	$nB_v$
1	$2\lambda$	$8\lambda$	$4.5\lambda$	$2h$	100	10	50	$2\lambda$	$2h$	$\lambda$	200	15	100
2	$4\lambda$	$6\lambda$	$4.5\lambda$	$2h$	100	10	50	$2\lambda$	$2h$	$\lambda$	200	15	100
3	$6\lambda$	$4\lambda$	$4.5\lambda$	$2h$	100	10	50	$2\lambda$	$2h$	$\lambda$	200	15	100

The corresponding comparison of the time histories of the roll angle in the cases with different  $L_p$  is shown in Fig. 8.4.11, covering the same wave period as that given in previous Figures. It can be seen that the extended Euler-viscous hybrid results agree well with the

corresponding conventional RANS results. As expected, with the increase of  $L_P$ , the average error  $\text{Err}(\alpha)$  increases, as shown in Fig. 8.4.12. On the other hand, the consumed CPU time increases as  $L_P$  decreases. From Fig. 8.4.12, it is not difficult to conclude that  $L_P=4\lambda$  is suitable for the extended Euler-viscous hybrid solver to achieve the results shown in Fig. 8.4.11. It is important to note that if one wants to acquire results with longer durations, the reflections from the boundary of the Euler domain may become more significant. Thus shorter  $L_P$  may be required.

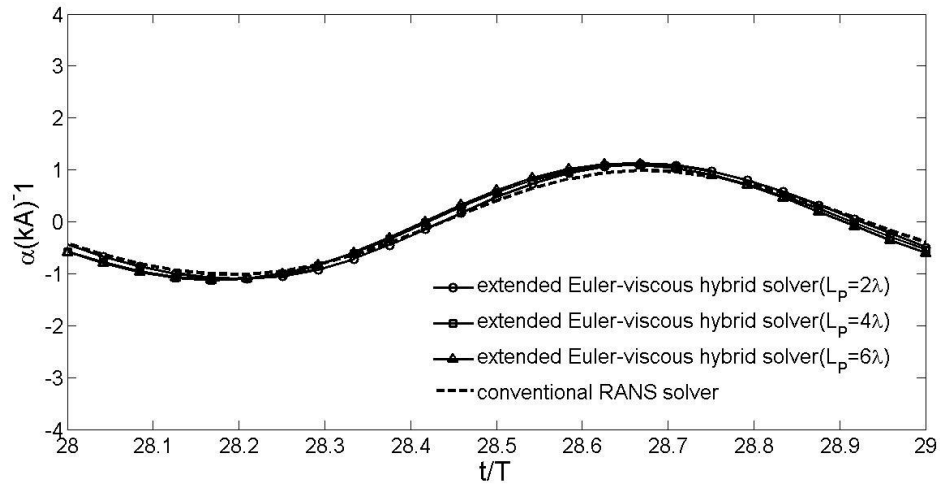


Fig. 8.4.11 The comparison of roll angle at different  $L_P$

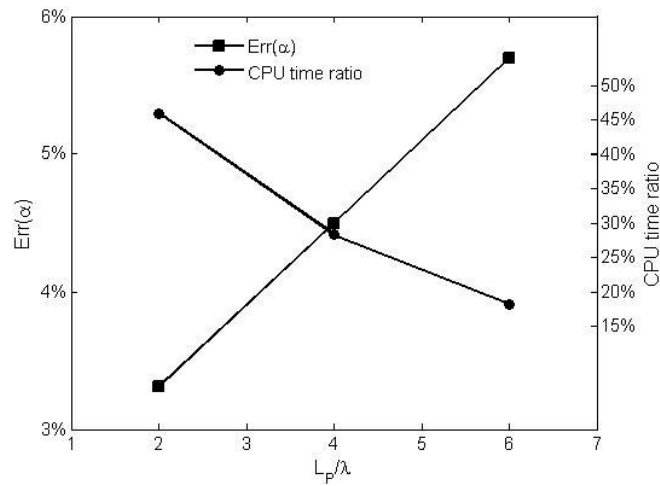


Fig. 8.4.12 Average error and CPU time ratio at different  $L_P$

## 8.5 Validation of the extended Euler-viscous hybrid solver

So far, the extended Euler-viscous hybrid solver is compared with the conventional RANS solver in the performance investigation, through which it is concluded  $\Delta t=T/1000$ ,  $n_{B_E}=50$ ,  $n_{L_E}=100$ ,  $n_{H_E}=10$ ,  $n_{B_V}=100$ ,  $n_{L_V}=200$ ,  $n_{H_V}=15$ ,  $L_V=2\lambda$ ,  $H_V=2h$ ,  $L_{tr}=0.5\lambda$  and  $L_P=4\lambda$  are appropriate for the former to achieve highest robustness against the latter for the case

considered. It is admitted that the conclusion may be problem dependant. Nevertheless, such configurations are used by the extended Euler-viscous hybrid solver for modelling the cases under different wave conditions summarised in Table 8.5.1. Numerical results are compared with the experimental data obtained by Jung et al.(2006). For the comparison, the amplitude of the linear harmonics of the roll angle ( $\psi$ ) is gain by FFT. Considering the fact that a considerable transient effects are observed before  $t=25T$ , the data used for the FFP covers 10 continuous wave periods at the quasi-steady state.

Table 8.5.1 Non-dimensional parameters of incident waves and the computational domain

No.	$f_B/f_N$	$\lambda/h$	$H_w/h$	$L_P/\lambda$	$L_{EH}/\lambda$	$L_{ER}/\lambda$	$H_E/h$	$L_V/\lambda$	$H_V/h$	$L_{tr}/\lambda$
1	1.33	0.86	0.017	19.48052	6	12.98701	2	2	2	0.5
2	1.16	1.11	0.032	14	6	10	2	2	2	0.5
3	1.09	1.26	0.037	11.68142	6	8.849558	2	2	2	0.5
4	1	1.5	0.018	8.814815	6	7.407407	2	2	2	0.5
5	0.77	2.46	0.035	4	6	4.545455	2	2	2	0.5
6	0.71	2.86	0.067	1.789883	6	3.891051	2	2	2	0.5
7	0.62	3.66	0.069	0.303951	6	3.039514	2	2	2	0.5

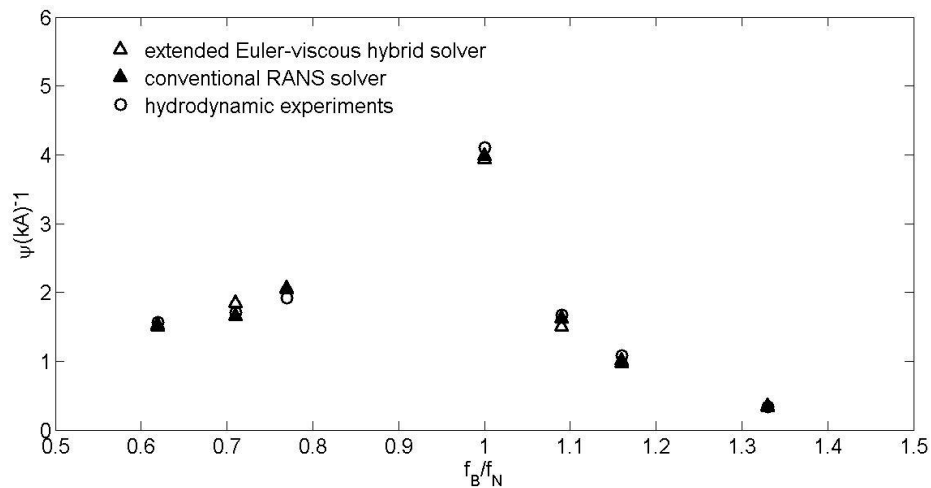


Fig. 8.5.1 The comparison of the first order ( $\psi$ ) of roll angle for incident waves

The comparison of  $\psi$  between the numerical and experimental data is shown in Fig. 8.5.1, in which the numerical results from both the extended Euler-viscous hybrid solver and the conventional RANS solver are included. It is clear that both solvers deliver satisfactory predictions for the roll RAOs within wide range of wave frequency. Nevertheless, the extended Euler-viscous hybrid solver demands less CPU time. This is confirmed by the comparison shown in Fig. 8.5.2, which suggests that the CPU ratio between the CPU consumed by the present solver against that by the conventional RANS solver is always lower than 50%. This means that the present hybrid model can save at least 50% CPU time compared with the conventional RANS solver. It is also interested to observe that the CPU

ratio decreases as the wave frequency increases, up to 85% of the CPU time may be saved by the present solver within all cases considered.

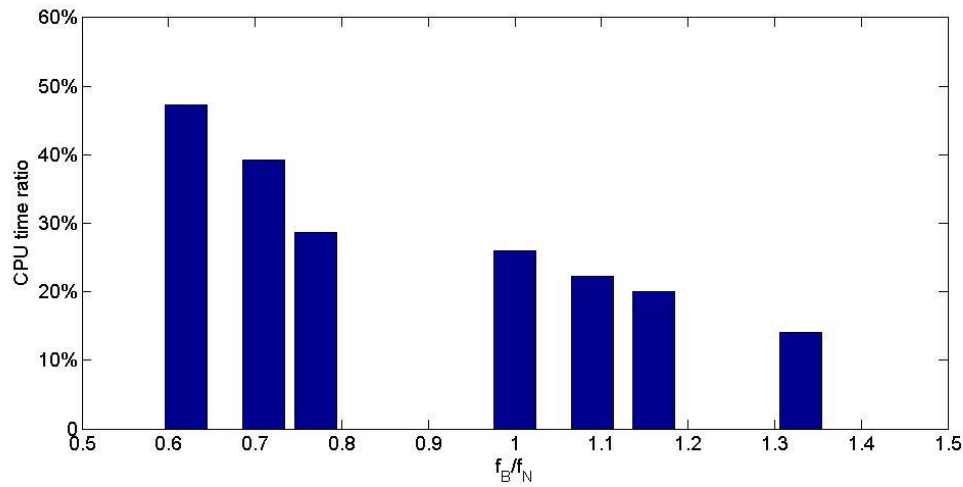


Fig. 8.5.2 The comparison of CPU time ratio for different incident waves

In this chapter, the demonstration of such systematic investigation is given. It is worthy noting that improvement of the computational efficiency by the extended Euler-viscous hybrid solver over the conventional RANS solver may be problem dependent. The conclusion may be applied to similar problems. A systematic investigation following this chapter may be required to achieve the highest computational robustness for modelling other wave-structure interaction problems.

## 8.6 Summary

In this chapter, Euler-viscous hybrid solvers are extended by using domain-decomposition method. The convergence study of the extended Euler-viscous hybrid solver with the static mesh and with the dynamic mesh is conducted for simulating wave-structure interactions in a real wave tank, respectively.

For the extended Euler-viscous hybrid solver with the static mesh, the effects of distance before reaching the inlet boundary of the Euler domain are significant on computational robustness. Specifically, with the increase of the distance, the computational efficiency of the extended Euler-viscous hybrid solver increases significantly, comparing with the original Euler-viscous hybrid solver, the potential-viscous hybrid solver, and the conventional RANS solver.

For the extended Euler-viscous hybrid solver with the dynamic mesh, wave interactions with the free rolling structure are simulated for the convergence study. The sufficient mesh resolution for the Euler domain and the viscous domain is found firstly. Then, the effects of the size of the viscous domain, the length of the transition zone, and the distance before



reaching the inlet boundary of the Euler domain are investigated on the computational robustness. Specifically, with the increase of the length of the viscous domain, the computational efficiency decreases, while the accuracy increases. The computational accuracy decreases significantly with slight decrease of the width of the viscous domain. For the length of the transition zone, a convenient value exists for high accuracy and efficiency. The increase of distance before reaching the inlet boundary of Euler domain leads to the decrease of the CPU time and the increase of the computational efficiency.

From the convergence study, the suitable numerical configuration can be obtained by a series of numerical tests. The validation of the extended Euler-viscous hybrid solver is conducted, by comparing with experiment results and the conventional RANS results. It is found that the extended Euler-viscous hybrid solver owes the same accuracy as the conventional RANS solver. Meanwhile, the computational efficiency is increased significantly.

# **Chapter 9 Investigation of wave interaction with surface-piercing moving structure subjected to complex seabed topography**

## **9.1 Introduction**

As indicated above, the wave interaction with moving structures in the cases with non-flat seabed is a practically important problem. Many researchers have studied the seabed effect on the water waves and their interaction with structures. The linear or weakly non-linear theories (e.g. Liu, Molin, and Kimmoun, 2011; Kim, 2013; Jiang, Cui, and Gao, 2016) are widely used in the design practices for normal and moderate sea state when the motion of the structure is not significant. The fully non-linear potential models have also been developed and applied to investigate the wave-structure interaction with seabed effects. (Yan, and Ma, 2007; Ma, and Yan, 2009) These theories are mainly based on the potential theory, in which the fluid is assumed to be incompressible, inviscid and irrotational. However, it has been confirmed by many researchers (e.g., Carrica, Wilson, and Noack, 2007) that the viscous effects, turbulence and vortex may be significant, in particular for rolling structures with sharp corners. For such cases, the potential theory is not valid (Wilson, Carrica, and Stern, 2006; Seah, and Yeung, 2003).

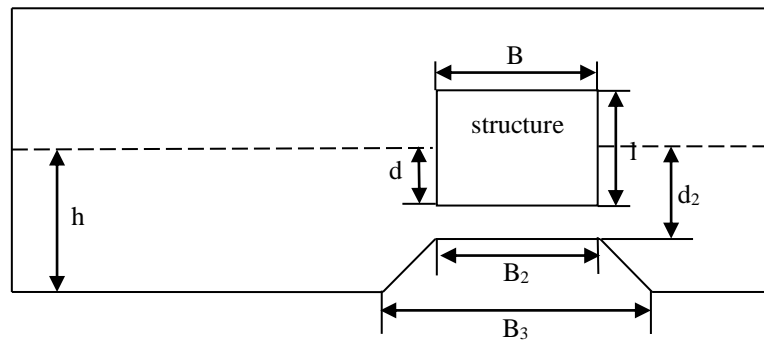
In Chapter 5, the seabed effects on the interaction between wave and fixed surface-piercing floating structures are numerically simulated and discussed by using the Euler-viscous hybrid solver, in which the viscosity and turbulence are taken into account in the area near the floating structure. In that study, the seabed geometry is modified by a bottom-mounted submerged structure. It was found that the wave loads on the fixed structure can be affected considerably by the submerged structure, indicating a significant seabed effect. Such investigation is extended in this chapter to look at the problems with freely floating structures. Similar to the previous study, one only considers the structure subjected to motion of one degree of freedom (DOF), i.e. free rolling. The extended Euler-viscous hybrid solver is applied. To the best of the author's knowledge, such research has not been presented in the public domain.

In order to model the wave induced roll motion subjected to complex topography, some specific numerical issues may be worthy of noting. Firstly, the computational domain must be sufficiently long. This does not only to ensure an accurate modelling of nonlinear wave generation and propagation, but also, perhaps more importantly, this can ensure the re-reflection of the reflection/radiation waves, which are caused by the structure and the seabed, from the wave inlet boundary, where the wave is generated, influence the motion of the floating structure. Secondly, the mesh near the floating structure and the non-flat seabed must

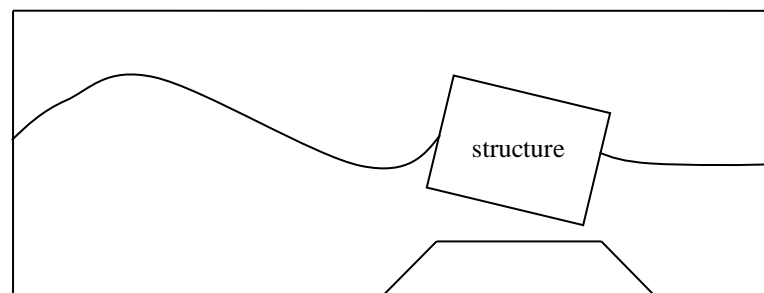
be sufficient fine in order to reveal the complex flow feature, e.g. the turbulence and the vortex shedding.

## 9.2 Physical model

Once again, the hydrodynamic experiments by Jung et al (2006) are used in this chapter. The physical model used in this chapter is similar to that described in section 8.9. The only difference is that a submerged structure is fixed to the seabed and located beneath the floating structure, as shown in the Fig. 9.2.1. Similar to the physical model used in Chapter 5, the submerged structure is a trapezoid with a top width  $B_2$  and a bottom width  $B_3$ . It is located  $d_2$  below the mean water surface; the floating structure has a breadth of  $B$ , depth of  $l$  and initial draft of  $d$ . In this Chapter,  $B=0.2\text{m}$ ,  $l=0.064\text{m}$  height, the length of the structure  $L=0.9\text{m}$  (normal to the paper) and  $d=0.032\text{m}$  are used. The length of the wave tank is 30 m and the mean water depth  $h$  is 0.9m. The details can be found from Jung (2006). The distance between the wave maker and the centre of the gravity of the floating structure, which is the centre of the floating structure, is 20m.



(a) Sketch of the physical model



(b) Interaction of moving structure with waves over complex seabed topography

Fig. 9.2.1 The physical model

## 9.3 The numerical methods

The extended Euler-viscous hybrid solver described in section 8.1 is used here. The computational domain and the mesh configuration are introduced below. Furthermore, the

numerical model is validated by using the experimental data and its computational efficiency is discussed.

### 9.3.1 The computational domain and mesh

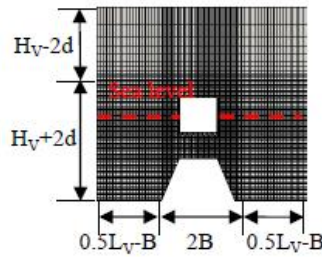
Table 9.3.1 The mesh for conventional RANS solver and Euler-viscous hybrid solver

(a) The mesh for the conventional RANS solver

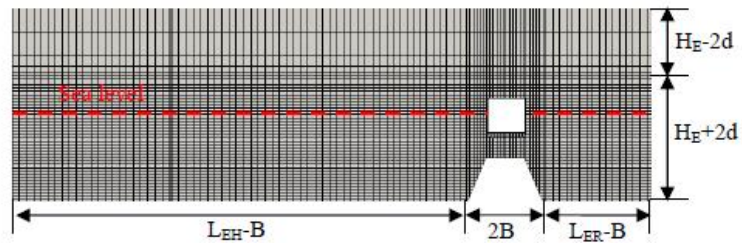
Conventional RANS domain				
$L_C$	$H_C$	$nL_C$	$nB_C$	$nH_C$
$L_T$	$2h$	200	100	15

(b) The mesh for the extended Euler-viscous hybrid solver

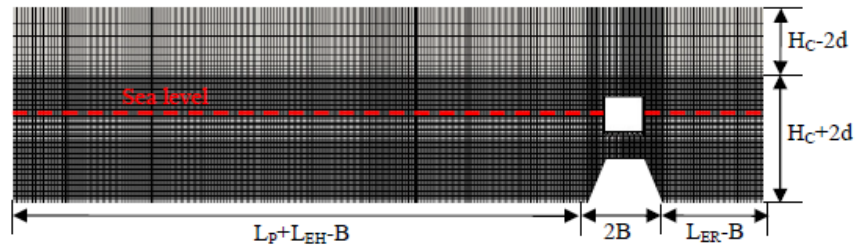
Potential domain	Euler domain					Viscous domain					
$L_P$	$L_{EH}$	$H_E$	$nL_E$	$nH_E$	$nB_E$	$L_V$	$H_V$	$L_{tr}$	$nL_V$	$nH_V$	$nB_V$
$4\lambda$	$L_T - L_P - L_{ER}$	$2h$	100	10	50	$3\lambda$	$2h$	$0.5\lambda$	200	15	100



(a) The viscous domain and mesh



(b) The Euler domain and mesh



(c) The conventional RANS domain and mesh

Fig. 9.3.1 The computational mesh used in the simulation

The computational domain adopted here is similar to that described in section 8.2, i.e.  $L_P + L_{EH} = 20\text{m}$ ,  $L_{ER} = 10\text{m}$ . According to the performance investigation presented in the previous chapter,  $L_P = 4\lambda$  is taken here. Due to the involvement of the submerged structure, the mesh near the submerged structure is also refined in order to well capture the flow features, including the turbulence and vortex. The computational mesh is illustrated in Fig. 9.3.1. The parameters related with the mesh resolution are described in the Table 9.3.1. As usual, the corresponding simulation by using the conventional RANS solver is also carried out for comparison.

### 9.3.2 The validation of the numerical methods

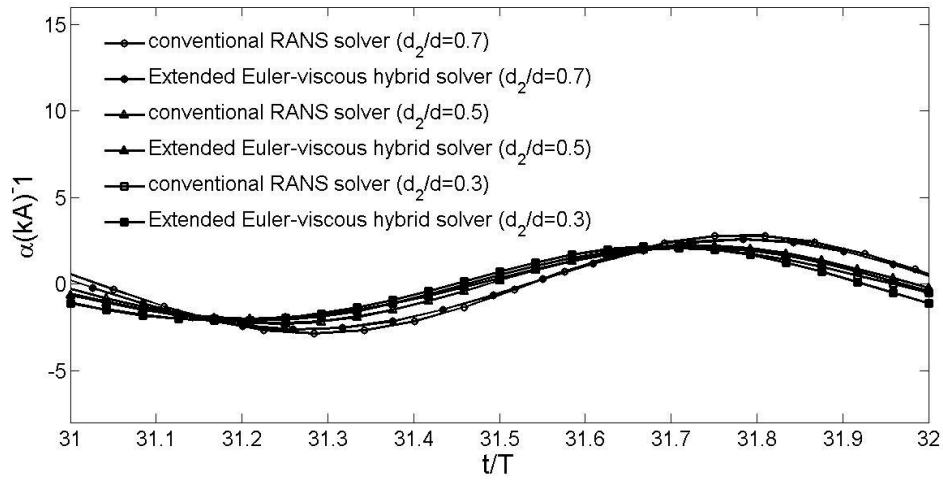


Fig. 9.3.2 The time histories of the roll angle in the cases with different  $d_2$  using different numerical solvers

In the first case considered here, the wave length is taken as  $\lambda=2.22\text{m}$  ( $\lambda/d=44$ ). In order to systematically investigate the seabed effects, the different value of  $d_2$  ranging from  $3d$  to  $7d$  are considered. For simplification, the top width  $B_2$  and the bottom width  $B_3$  and specified as  $B$  and  $2B$ , respectively. The time histories of the roll motion in the cases with different  $d_2$  using different numerical solvers are compared. Some results are shown in Fig. 9.3.2 during one wave period from  $31T$  to  $32T$ , which has been quantified as the quasi-steady state.

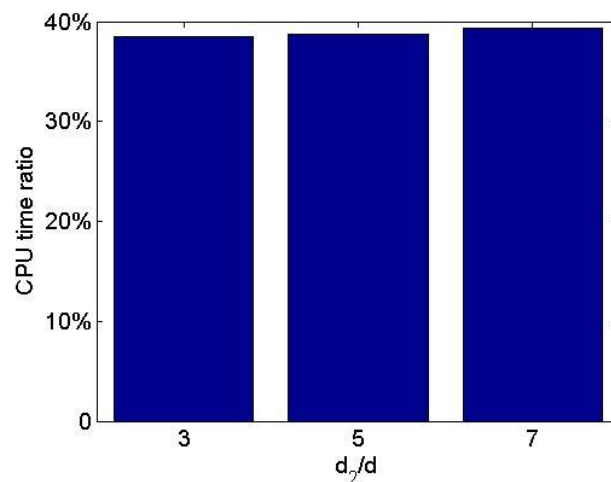


Fig. 9.3.3 CPU time ratio in the cases with different  $d_2$

From Fig. 9.3.2, it can be seen that the roll angles predicted by the extended Euler-viscous hybrid solver are generally close to those from the conventional RANS solver for all  $d_2$  considered in this study. One may agree that the extended Euler-viscous hybrid solver has a similar accuracy as the conventional RANS solver, providing a sufficiently fine mesh

resolution. The comparison of the CPU time ratio between the CPU consumed by the extended Euler-viscous hybrid solver and that by the conventional RANS solver is shown in Fig. 9.3.3. It can be seen that more than 60% CPU time can be saved by the extended Euler-viscous hybrid solver, compared to the conventional RANS solver, for all the cases considered in this investigation.

## 9.4 Systematic Investigation

In the previous section, only one wave condition is considered for validation purpose. Different wave conditions are taken into account in the systematic investigation. The incident waves and the domain sizes are summarised in Table 9.4.1. The effects of  $d_2$  and  $B_2$  on roll motion are examined. The configuration of the computational mesh remains the same as those in section 9.3.1.

Table 9.4.1 The incident waves and domain sizes

No.	$f_B/f_N$	$\lambda/h$	$H_w/h$	$L_P/\lambda$	$L_{EH}/\lambda$	$L_{ER}/\lambda$	$H_E/h$	$L_V/\lambda$	$H_V/h$	$L_{tr}/\lambda$
1	1.33	0.86	0.017	19.48052	6	12.98701	2	2	2	0.5
2	1.16	1.11	0.032	14	6	10	2	2	2	0.5
4	1	1.5	0.018	8.814815	6	7.407407	2	2	2	0.5
5	0.77	2.44	0.036	3.090909	6	4.545455	2	2	2	0.5
6	0.71	2.86	0.067	1.789883	6	3.891051	2	2	2	0.5

### 9.4.1 Effects of $d_2$ on wave-excited roll motions

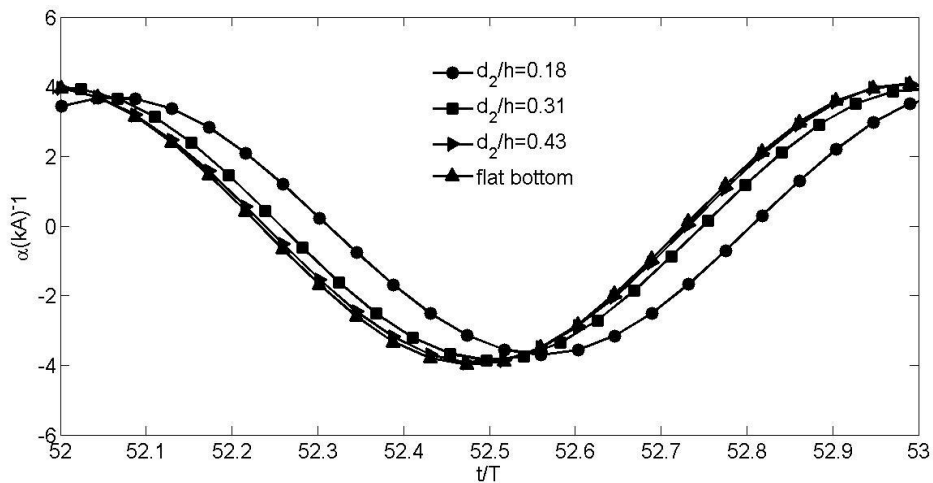


Fig. 9.4.1 The time histories of the roll angle of a free rolling structure subjected to a submerged structure with different  $d_2$

Following the work done for the validation, different  $d_2$  ranging from  $3d$  to  $7d$ , yielding a range of  $d_2/h$  from 0.18 to 0.43, are used for all wave conditions. The time histories of roll motion  $\alpha$  in the cases with different  $d_2$  and the flat seabed (i.e.  $d_2/h = 1$ ) are compared and illustrated in Fig. 9.4.1 for the data over one wave period from  $52T$  to  $53T$ , which is at the

quasi-steady state. In this case, the wave length  $\lambda$  is 1.35m (i.e.  $\lambda/h=1.5$ ). Clearly, the submerged structure influences the motion the floating structure, in particular when  $d_2$  is small, e.g.  $d_2/h=0.18$ . As  $d_2$  increases to be greater than 0.31, the roll motion seems not to be significantly affected by the submerged structure.

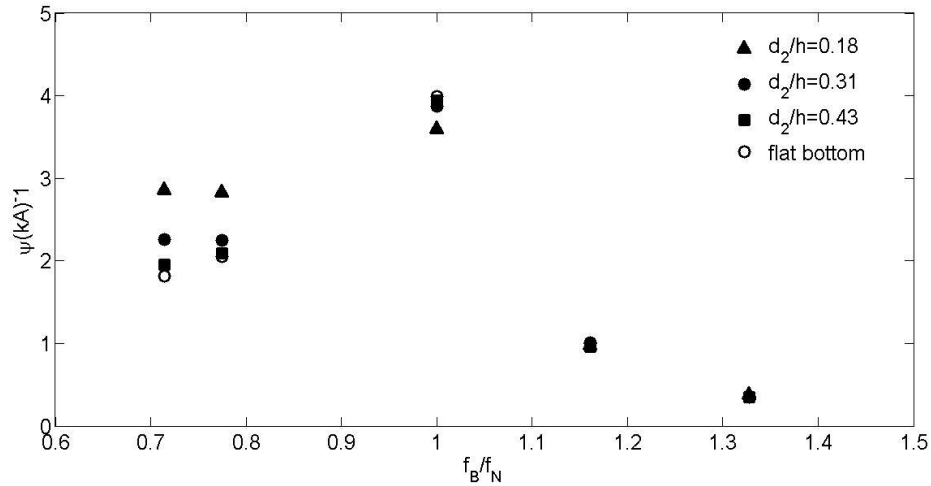


Fig. 9.4.2 First order harmonics of roll motion  $\psi$  at different wave condition and different  $d_2$

In order to study the seabed effects on the roll motion for different wave conditions, the linear harmonics,  $\phi$ , equivalent to the RAO of roll, is duplicated by the FFT using the time history of roll motion in 10 wave periods at the quasi-steady state. The linear roll harmonics  $\phi$  in the cases with different  $d_2$  and wave conditions are compared and illustrated in Fig. 9.4.2. As expected, as the wave length decreases, i.e.  $f_B$  increases, the seabed effects become more insignificant. Especially, when  $f_B$  is larger than  $f_N$ , i.e. the natural frequency, the submerged structure seems not disturb the roll amplitude. Overall, larger wave length ( $\lambda$ ) and/or smaller value of  $d_2$  lead to more significant seabed on the roll motion of the floating structure.

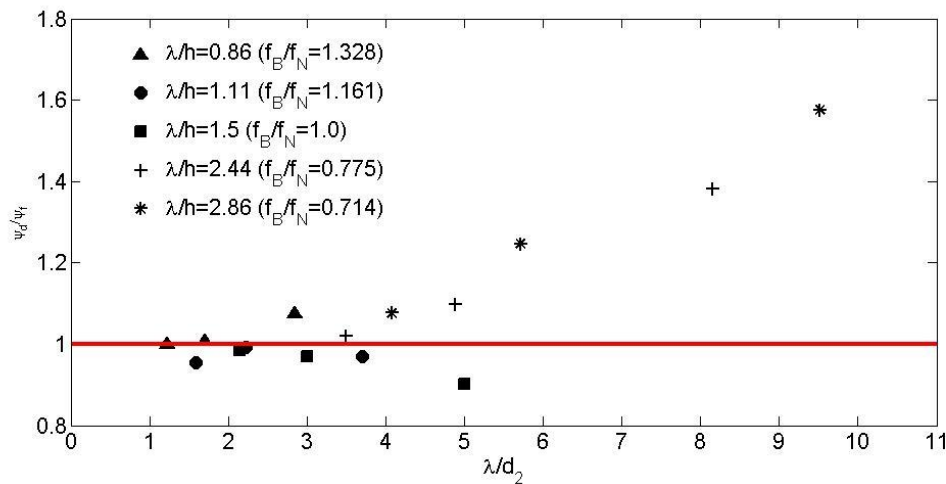


Fig. 9.4.3 The relationship between  $\psi_d/\psi_f$  and  $\lambda/d_2$  in the cases with different  $d_2$

To quantify the significance of the seabed effects on the roll motion of the floating structure, the ratio of  $\psi$  in the case with the submerged structure, referred to as  $\psi_d$ , against the

corresponding value in the case without the submerged structure, i.e.  $\psi_f$ , are defined. The variation of  $\psi_d/\psi_f$  in the cases with different  $\lambda/d_2$  is shown in Fig. 9.4.3. One may find that close to the resonance condition, i.e.  $f_B/f_N=1$  and  $f_B/f_N=1.161$ , the submerged structure trends to suppress the roll motion. If the wave frequency is away from the natural frequency, e.g.  $f_B/f_N=1.328$ ,  $0.775$  and  $0.714$ , the submerged structure amplifies the roll motion and the amplification becomes more significant as  $\lambda/d_2$  increases.

#### 9.4.2 Effects of the top width ( $B_2$ )

The effect of the top width ( $B_2$ ) of the submerged structure on the roll motion is investigated. Submerged structures with  $B_2=2B$ ,  $B_2=B$ , and  $B_2=0.5B$  are used. For all structures  $d_2=0.18h$  and the incident wave with  $\lambda/h=1.5$  ( $\lambda=1.35m$ ) are employed. The time histories of the roll angle during  $t=52T$  and  $53T$  at the quasi-steady state are shown in Fig. 9.4.4 for the cases with or without submerged structures. It is observed that the submerged structure not only influence the amplitude but also influence the phase of the roll motion. It is also noted that different  $B_2$  leads to significant different roll motions.

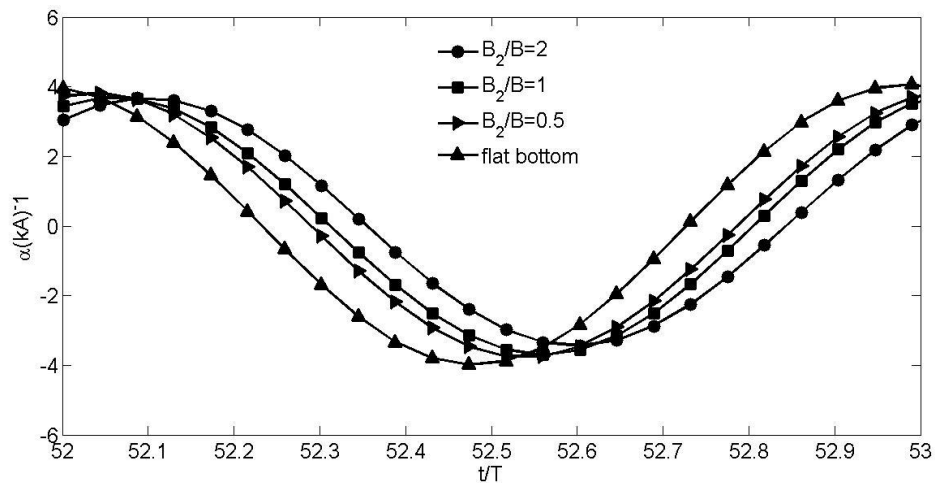


Fig. 9.4.4 The time histories of the roll angle of a free rolling structure subjected to a submerged structures with different  $B_2$

The variations of  $\psi$  at different  $B_2$  and different wave conditions are shown in Fig. 9.4.5. It is clear that, under different incident waves, the effects of  $B_2$  behave differently. Similar to the results shown in Fig. 9.4.2, the submerged structure influence the motion of the structure insignificantly for  $f_B/f_N > 1.0$  (shorter wave), but is significant if the wave length increases, i.e.  $f_B/f_N \leq 1.0$  ( $\lambda/h \geq 1.5$ ). More importantly, different values of  $B_2$  lead to considerably different motion for  $f_B/f_N \leq 1.0$ . The variation of  $\psi_d/\psi_f$  against  $\lambda/d_2 \cdot B_2/B$  are illustrated in Fig. 9.4.6, from which a similar phenomenon to that in Fig. 9.4.3 is observed.



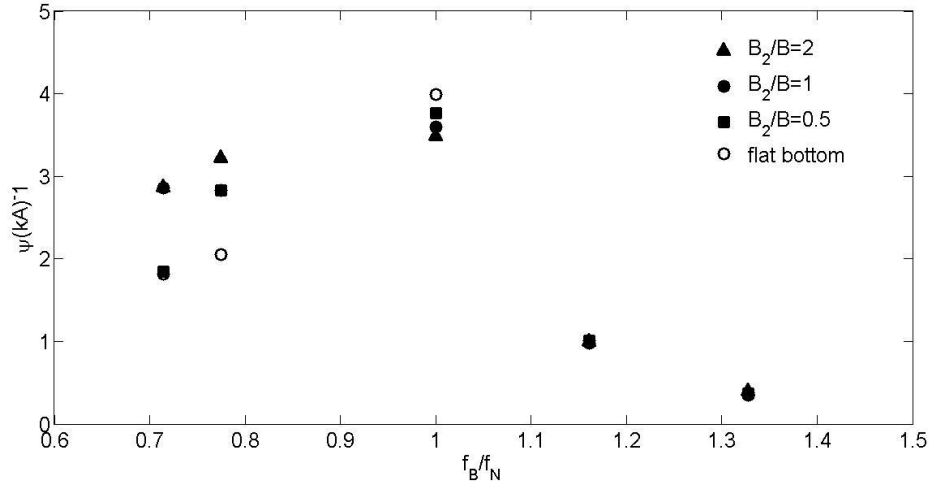


Fig. 9.4.5 The effects of  $B_2$  on 1<sup>st</sup> order roll amplitude under different incident waves at different  $B_2$

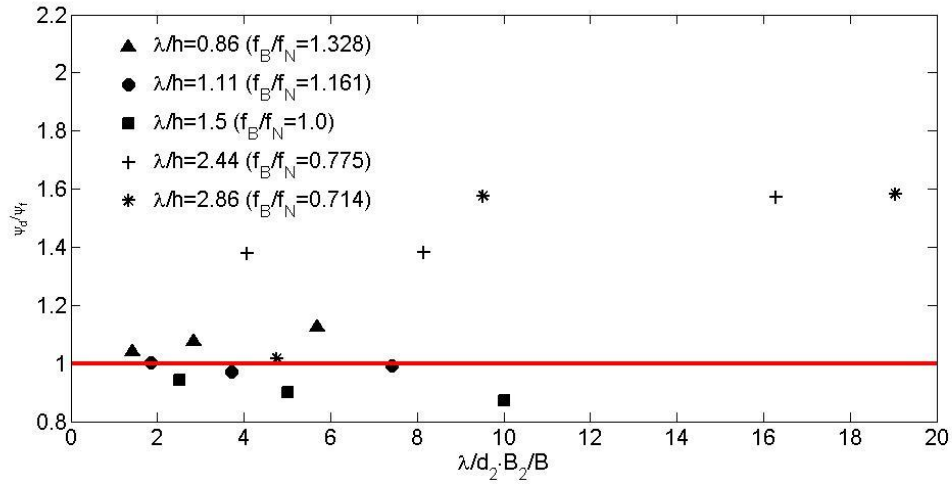


Fig. 9.4.6 The relationship between  $\psi_d/\psi_f$  and  $\lambda/d_2 \cdot B_2/B$

## 9.5 Summary

In this chapter, wave interactions with the floating structure subjected to complex seabed topography are simulated by the extended Euler-viscous hybrid solver. The effects of the water depth and top width of a bottom-mounted submerged structure are investigated. It is found that larger wave length ( $\lambda$ ) and/or smaller value of  $d_2$  lead to more significant seabed on the roll motion of the floating structure. As wave frequency is smaller than the natural frequency, large top width of the submerged structure leads to the amplified roll angle. On the resonance condition, the submerged structure can suppress the roll angle.

## Chapter 10 Conclusions and recommendations

In this thesis, function-decomposition Euler-viscous hybrid models and corresponding extended models are developed for wave-structure interactions, based on OpenFOAM. By decomposing both the velocity and the pressure into the Euler part and the viscous part, complementary RANS equations can be proposed from conventional RANS equations. Corresponding complementary turbulence models can also be derived by function-decomposition method. Finally, the Euler-viscous hybrid solver is extended by coupling function-decomposition method and domain-decomposition method together. Some numerical techniques are used or developed for hybrid models. Specifically, new boundary conditions in the viscous domain are proposed for adapting to the Euler domain. An interpolation algorithm is used for data mapping from the Euler domain to the viscous domain. A relaxation scheme is developed for damping viscous effects and keeping free surface consistent in the transition zone of viscous domain. For the Euler-viscous hybrid model with dynamic mesh, wave loads acting on the structure are transited from the viscous domain to the Euler domain for keeping the same motion of structures in two domains.

Hybrid solvers are validated by experiments and conventional RANS solvers. It is shown that the same computational accuracy can be obtained by hybrid solvers, comparing to conventional RANS solvers. Besides, hybrid solvers own high computational efficiency. For hybrid models, computational accuracy and efficiency are affected by many aspects including the size of the viscous domain, the length of the transition zone, mesh resolution, and distance before reaching the inlet boundary of the Euler domain.

Hybrid solvers can be used in complex computational domains as well. Effects of complex topography on wave-structure interactions are studied based on hybrid solvers. Influence of a submerged bottom-mounted structure is discussed.

### 10.1 Numerical techniques

Some numerical techniques are used for coupling the Euler solver and complementary RANS solver together. In order to map the data from the Euler domain into the viscous domain, an interpolation algorithm is used for data mapping between mesh with different resolution. By the algorithm, the target value in viscous domain can be obtained by interpolation of source values surrounding the target location in the Euler domain. By numerical tests on different mesh resolution in the Euler domain and the viscous domain, it is indicated that the errors induced by the interpolation algorithm are small.

New boundary conditions are proposed for coupling the Euler solver and the complementary RANS solver on the boundary of the floating structure. By the new boundary conditions in the viscous domain, the total values of the velocity and the pressure on the floating structure can be equal to those for the conventional RANS solver.

For coupling the Euler solver and the complementary RANS solver, the viscous effects should be cancelled at two side boundaries far from the floating structure. Besides, free surface should be consistent in the Euler domain and the viscous domain. Hence, a transition zone is used for damping the viscous velocity that is zero at two side boundaries of viscous domain. Similarly, volume fraction in two side boundaries of the viscous domain is kept the same as that in the Euler domain. The variation of volume fraction in transition zone is also smooth by a smooth function. By the comparison of the wave elevation and the velocity near the floating structure, it shows that the numerical technique for relaxation is useful.

To guarantee motions of floating structures the same in both the Euler domain and the viscous domain, a new computing process is designed. In the computing process, the Euler model is solved firstly. However, the mesh in the Euler domain is not updated. Then, after complementary RANS equations are solved and mesh in viscous domain is updated, total forces acting on the structure in the viscous domain are transited on the structure in the Euler domain, by which motions of the structure in the Euler domain is determined. The transiting of total forces can be regarded as a “two-way” treatment from viscous solution to Euler solution.

## **10.2 Computational robustness of hybrid solvers**

For study of computational robustness of Euler-viscous hybrid solvers, some cases are simulated for wave-structure interactions. Effects of the length of the viscous domain, the width of the viscous domain, the length of the transition zone, and mesh resolution are investigated. It is indicated that the length of viscous domain affects computational accuracy and efficiency remarkably. Specifically, with the increase of the length of the viscous domain, computational efficiency is reduced and computational accuracy goes up. As the width of the viscous domain goes down, only a little CPU time can be saved with sharp drop of computational accuracy. The length of transition zone has only small effects on computational efficiency. However, high computational accuracy can only be achieved by suitable length of the transition zone. Different mesh resolution in the Euler and the viscous domain leads to discrepancy of numerical results between the Euler-viscous hybrid solver and the conventional RANS solver. However, the difference of mesh resolution is the main factor that the Euler-viscous hybrid solver is more efficient than the conventional RANS solver. As the Euler-viscous hybrid solver is extended by domain-decomposition method, the distance

before reaching the inlet boundary of the Euler domain also affects computational accuracy and efficiency significantly. With the increase of the distance, the computational accuracy goes down with the enhancing of computational efficiency.

### **10.3 Application to wave interactions with a floating structure subjected to complex seabed topography**

Hybrid solvers are applied to wave interactions with a floating structure subjected to complex seabed topography. On the condition, a computational domain is used for a submerged bottom-mounted structure distributed at the seabed. By the comparison of numerical results between hybrid solvers and conventional RANS solvers, hybrid solvers can be used in complex computational domain. Besides, it is found that the submerged bottom-mounted structure can affect wave-structure interactions remarkably.

### **10.4 Contributions**

There are two originalities in the research including:

- 1 New function-decomposition hybrid methods are developed for surface-piercing wave-structure interactions.
- 2 Multi-model methods including potential, Euler, and viscous models are developed by function-decomposition method and domain-decomposition method together.

The advantage of the numerical model is more efficient comparing with the conventional RANS solver. Specifically, by the Euler-viscous hybrid model, the viscous effects are just considered in the domain close to the floating structure. Outside the viscous domain, simple mathematical model is used for improving the computational efficiency. Furthermore, by the new function-decomposition model that considering the floating structures in both Euler and viscous domains, the reflection waves can be considered in the Euler domain as well, which results in small viscous domain. Besides the new function-decomposition method, by coupling the domain-decomposition method together, the wave propagation can be simulated by potential model, which reduces the CPU time significantly. Finally, comparing with the original RANS solver, the computational efficiency of hybrid solvers can be increased significantly with the same computational precision, which is validated by several cases.

### **10.5 Recommendations**

Although some hybrid solvers are developed for surface-piercing wave-structure interactions, more work for improvement of hybrid solvers is recommended below:

- a) At the current stage, the hybrid solvers can only run in a series mode. In the future, the hybrid solvers will be improved to run in parallel mode. The Euler solver, the viscous

solver and the potential solver can run in different processes separately so that computational efficiency can be improved significantly.

- b) At the current stage, only two dimensional cases are simulated. In the future, three dimensional cases should be simulated by hybrid solvers.
- c) The interpolation algorithm can be improved in the future. By using high order interpolation algorithm, numerical errors induced by the difference of mesh resolution can be reduced.
- d) Many potential models can be hybrid with Euler-viscous hybrid solvers by domain-decomposition method. In the future, more models will be added in the hybrid solvers for solving more kinds of cases.
- e) In the research, only regular waves are considered. In the future, irregular waves and extreme waves should be taken into account in the simulations by hybrid methods.

## References

- Alessandrini, B., & Delhommeau, G., 1999. A fully hybrid Navier–Stokes solver for calculation of turbulent incompressible free surface flow past a ship hull. *International journal for numerical methods in fluids*, 29(2), pp. 125-142.
- Bai, W., and Eatock, T. R., 2009. Fully nonlinear simulation of wave interaction with fixed and floating flared structures. *Ocean engineering*, 36(3), pp. 223-236.
- Biausser, B., Grilli, S. T., and Fraunié, P., 2003. Numerical simulations of three-dimensional wave breaking by coupling of a VOF method and a boundary element method. In: *Proc. 13th Offshore and Polar Engng. Conf*, Hawaii (USA).
- Biausser, B., Grilli, S. T., and Marcer, R., 2004. Numerical analysis of the internal kinematics and dynamics of three-dimensional breaking waves on slopes. In: *Intl. J. Offshore and Polar Engng*, Toulon (France).
- Beji, S., and Battjes, J. A., 1993. Experimental investigation of wave propagation over a bar. *Coastal Engineering*, 19(1-2), pp. 151-162.
- Bhattacharjee, J., and Soares, C. G., 2010. Wave interaction with a floating rectangular box near a vertical wall with step type bottom topography. *Journal of Hydrodynamics, Ser. B*, 22(5), pp. 91-96.
- Bhattacharjee, J., and Soares, C. G., 2011. Oblique wave interaction with a floating structure near a wall with stepped bottom. *Ocean Engineering*, 38(13), pp. 1528-1544.
- Bruinsma, N., Paulsen, B. T., and Jacobsen, N. G., 2018. Validation and application of a fully nonlinear numerical wave tank for simulating floating offshore wind turbines. *Ocean Engineering*, 147, pp. 647-658.
- Chaplin, J. R., Rainey, R. C. T., and Yemm, R. W., 1997. Ringing of a vertical cylinder in waves. *Journal of Fluid Mechanics*, 350, pp.119–147.
- Chen, L. F., Zang, J., Hillis, A. J., Morgan, G. C. J., and Plummer, A. R., 2014. Numerical investigation of wave–structure interaction using OpenFOAM. *Ocean Engineering*, 88, pp.91-109.
- Chen, X. B., and Lu, D. Q., 2009. Time-harmonic ship waves with the effect of surface tension and fluid viscosity. In: *Proceedings of the 24th International Workshop on Water Waves and Floating Bodies*, Zelenogorsk (Russia).

- Chorin, A. J., 1968. Numerical solution of the Navier-Stokes equations. *Mathematics of computation*, 22(104), pp. 745-762.
- Carrica, P. M., Wilson, R. V., Noack, R. W., and Stern, F., 2007. Ship motions using single-phase level set with dynamic overset grids. *Computers & Fluids*, 36(9), pp. 1415-1433.
- Corte, C., and Grilli, S. T., 2006. Numerical modeling of extreme wave slamming on cylindrical offshore support structures. In *Proc. 16th Offshore and Polar Eng. Conf*, San Francisco (USA).
- Campana, E., and Lalli, F., 1992. Viscous-inviscid coupling in shiphydrodynamics. In *Proc. 11th Australian Fluid Mech. Conf*. Hobart (Australia).
- Colicchio, G., Greco, M., and Faltinsen, O. M., 2006. A BEM-level set domain-decomposition strategy for non-linear and fragmented interfacial flows. *International journal for numerical methods in engineering*, 67(10), pp. 1385-1419.
- Colicchio, G., Greco, M., Lugni, C., & Faltinsen, O. M., 2010. Towards a fully 3D domain-decomposition strategy for water-on-deck phenomena. *Journal of Hydrodynamics, Ser. B*, 22(5), pp. 462-467.
- Chang, H. K., and Liu, J. C., 2007. Long wave reflection from submerged trapezoidal breakwaters. *Ocean Engineering*, 34(1), pp. 185-191.
- Carrica, P. M., Wilson, R. V., and Noack, R. W., 2007. Ship motions using single-phase level set with dynamic overset grids. *Computers & fluids*, 36(9), pp. 1415-1433.
- Chen, H., and Christensen, E. D., 2018. Simulating the hydrodynamic response of a floater-net system in current and waves. *Journal of Fluids & Structures*, 79, pp. 50-75.
- Dolling, D. S., 2001. Fifty years of shock-wave/boundary-layer interaction research: what next? *AIAA journal*, 39(8), pp. 1517-1531.
- Davies, A. G., and Heathershaw, A. D., 1984. Surface-wave propagation over sinusoidally varying topography. *Journal of Fluid Mechanics*, 144, pp. 419-443.
- Dullweber A., Leimkuhler B., and McLachlan, R. Symplectic splitting methods for rigid body molecular dynamics. *Journal of Chemistry Physics*, 107(15), pp. 5840-5851.
- Engsig-Karup, A. P., Madsen, M. G., and Glimberg, S. L., 2012. A massively parallel GPU-accelerated model for analysis of fully nonlinear free surface waves. *International Journal for Numerical Methods in Fluids*, 70(1), pp. 20-36.

- Edmund, D. O., Maki, K. J., and Beck, R. F., 2013. A velocity-decomposition formulation for the incompressible Navier–Stokes equations. *Computational Mechanics*, 52(3), pp. 669-680.
- Engsig-Karup, A. P., Bingham, H. B., and Lindberg, O., 2009. An efficient flexible-order model for 3D nonlinear water waves. *Journal of computational physics*, 228(6), pp. 2100-2118.
- Faltinsen, O., 1993. *Sea loads on ships and offshore structures*. Vol. 1. Cambridge university press.
- Fochesato, C., Dias, F., Grilli, S. T., 2003. Numerical Model Using the Fast Multipole Algorithm for Nonlinear Three-dimensional Free Surface Waves over Arbitrary Bottom. In: *Proc. 13<sup>th</sup> International Offshore and Polar Engineering Conference*, Honolulu (USA).
- Ferrant, P., Touzé, D. L., and Pelletier, K., 2003. Non-linear time-domain models for irregular wave diffraction about offshore structures. *International journal for numerical methods in fluids*, 43(10-11), pp. 1257-1277.
- Ferrant, P., Gentaz, L., Monroy, C., Luquet, R., Ducrozet, G., Alessandrini, B., and Drouet, A., 2008. Recent advances towards the viscous flow simulation of ships manoeuvring in waves. In: *Proc. of 23rd International Workshop on Water Waves and Floating Bodies*, Jeju (Korea).
- Grilli, S. T., Guyenne, P., and Dias, F., 2001. A fully non-linear model for three-dimensional overturning waves over an arbitrary bottom. *International Journal for Numerical Methods in Fluids*, 35, pp.829-867.
- Grilli, S. T., Skourup, J., & Svendsen, I. A., 1989. An efficient boundary element method for nonlinear water waves. *Engineering Analysis with Boundary Elements*, 6(2), pp. 97-107.
- Girault, V., Raviart, P. A., 2012. *Finite element methods for Navier-Stokes equations: theory and algorithms*. Springer Science & Business Media.
- Garcia, J., and Oñate, E., 2003. An unstructured finite element solver for ship hydrodynamics problems. *Journal of applied mechanics*, 70(1), pp. 18-26.
- Guignard, S., Grilli, S. T., Marcer, R., and Rey, V., 1999. Computation of shoaling and breaking waves in nearshore areas by the coupling of BEM and VOF methods. In: *Proc. 9<sup>st</sup> Offshore and Polar Engng. Conf*, Brest (France).



- Gilbert, R. W., Zedler, E. A., Grilli, S. T., and Street, R. L., 2007. Progress on nonlinear-wave-forced sediment transport simulation. *IEEE Journal of Oceanic Engineering*, 32(1), pp. 236-248.
- Guo, L. D., Sun, D. P., and Wu, H., 2012. A new numerical wave flume combining the 0–1 type BEM and the VOF method. *Journal of Hydrodynamics, Ser. B*, 24(4), pp. 506-517.
- Greco, M., Faltinsen, O. M., and Landrini, M., 2005. Shipping of water on a two-dimensional structure. *Journal of Fluid Mechanics*, 525, pp. 309-332.
- Grilli, S. T., Harris, J., and Greene, N., 2008. Modeling of wave-induced sediment transport around obstacles. In: *Proc. 31st Intl. Coastal Engng. Conf* (pp. 1-638), Hamburg (Germany).
- Grilli, S. T., 2008. On the development and application of hybrid numerical models in nonlinear free surface hydrodynamics. In: *Proceedings of the 8th International Conference on Hydrodynamics*. Nantes, (France).
- Gentaz, L., Luquet, R., Alessandrini, B., and Ferrant, P., 2004. Numerical simulation of the Harlow, F. H., and Welch, J. E., 1965. Numerical calculation of time-dependent viscous incompressible flow of fluid with free surface. *Physics of fluids*, 8(12), pp. 2182-2189.
- Gatin, I., Vukčević, V., Jasak, H., Seo, J., and Rhee, S. H., 2018. CFD verification and validation of green sea loads. *Ocean Engineering*, 148, pp. 500-515.
- Hirt, Cyril W., and Billy D. Nichols., 1981. Volume of fluid (VOF) method for the dynamics of free boundaries. *Journal of computational physics*, 39(1), pp. 201-225.
- Hafez, M., Shatalov, A., and Nakajima, M., 2007. Improved numerical simulations of incompressible flows based on viscous/inviscid interaction procedures. *Computers & Fluids*, 36(10), pp. 1588-1591.
- Harris, J. C., and Grilli, S. T., 2012. A perturbation approach to large eddy simulation of wave-induced bottom boundary layer flows. *International Journal for Numerical Methods in Fluids*, 68(12), pp. 1574-1604.
- Harris, J. C., and Grilli, S. T., 2010. Coupling of NWT and Large-eddy Simulation for Wave-induced Sediment Transport. In: *Proceedings of the Twentieth International Offshore and Polar Engineering Conference*, Beijing (China).
- Huijsmans, R. H., Graham, M., and Kendon, T., 2005. The Flow Around FPSO's in Steep Regular Beam Waves: Results of PIV Experiments and RANS Computations. In: *ASME 2005*

*24th International Conference on Offshore Mechanics and Arctic Engineering*. Halkidiki (Greece).

Heathershaw, A. D., 1982. Seabed-wave resonance and sand bar growth. *Nature*, 296(5855), pp. 343-345.

Hur, D. S., Lee, K. H., and Choi, D. S., 2011. Effect of the slope gradient of submerged breakwaters on wave energy dissipation. *Engineering Applications of Computational Fluid Mechanics*, 5(1), pp. 83-98

Hu, Z. Z., Greaves, D., and Raby, A., 2016. Numerical wave tank study of extreme waves and wave-structure interaction using OpenFOAM®. *Ocean Engineering*, 126, pp. 329-342.

Higuera, P., Lara, J. L., and Losada, I. J., 2013. Realistic wave generation and active wave absorption for navier–stokes models: application to OpenFOAM®. *Coastal Engineering*, 71, pp. 102-118.

Iafrati, A., and Campana, E., 2003. A domain decomposition approach to compute wave breaking (wave-breaking flows). *International journal for numerical methods in fluids*, 41(4), pp. 419-445.

Iturriz, A., Guanche, R., Lara, J. L., Vidal, C., and Losada, I. J., 2015. Validation of OpenFoam® for oscillating water column three-dimensional modeling. *Ocean Engineering*, 107, pp. 222-236.

Janssen, C. F., Grilli, S. T., and Krafczyk, M., 2010. Modeling of wave breaking and wave-structure interactions by coupling of fully nonlinear potential flow and lattice-Boltzmann models. In: *Proceedings of the Twentieth International Offshore and Polar Engineering Conference*, Beijing, (China).

Jasak, H., Jemcov, A., and Tukovic, Z., 2007. OpenFOAM: A C++ library for complex physics simulations. In: *International workshop on hybrid methods in numerical dynamics*, Dubrovnik (Croatia).

Jung, K. H., Chang, K. A., and Jo, H. J., 2006. Viscous effect on the roll motion of a rectangular structure. *Journal of engineering mechanics*, 132(2), pp. 190-200.

Jiang, Z. Y., Cui, J., and Gao, Y., 2016. Experimental study and numerical simulation on the slow-drift oscillation of a semi-submersible in irregular waves. *Ship Technology Research*, 63(1), pp. 26-37.

- Jiang SC, Bai W, and Tang GQ., 2018. Numerical simulation of wave resonance in the narrow gap between two non-identical boxes. *Ocean Engineering*, 156, pp. 38-60.
- Jose, J., Choi, S. J., Giljarhus, K. E. T., and Gudmestad, O. T., 2017. A comparison of numerical simulations of breaking wave forces on a monopile structure using two different numerical models based on finite difference and finite volume methods. *Ocean Engineering*, 137, pp. 78-88.
- Jacobsen, N. G., Fuhrman, D. R., & Fredsøe, J., 2012. A wave generation toolbox for the open-source CFD library: OpenFOAM®. *International Journal for Numerical Methods in Fluids*, 70(9), pp. 1073–1088.
- Kharif, C., Giovanangeli, J. P., Touboul, J., Grare, L., and Pelinovsky, E., 2008. Influence of wind on extreme wave events: experimental and numerical approaches. *Journal of Fluid Mechanics*, 594, pp. 209-247.
- Kim, S. H., Yamashiro, M., and Yoshida, A., 2010. A simple two-way coupling method of BEM and VOF model for random wave calculations. *Coastal Engineering*, 57(11), pp. 1018-1028.
- Kim, K., Sirviente, A. I., and Beck, R. F., 2005. The complementary RANS equations for the simulation of viscous flows. *International journal for numerical methods in fluids*, 48(2), pp. 199-229.
- Kendon, T., Sherwin, S., and Graham, J., 2003. An irrotational/vortical split-flow approach to viscous free surface flow. In: *Proceedings of the 2nd Workshop MIT*, Cambridge (USA).
- Kärrholm, F. P., 2006. *Rhie-chow interpolation in openfoam*. Chalmers University of Technology.
- Koo, W., Kim, M. H., & Tavassoli, A., 2004. Fully nonlinear wave-body interactions with fully submerged dual cylinders. *International Journal of Offshore and Polar Engineering*, 14(03), pp. 210-217.
- Koo, W. C., and Kim, M. H., 2007. Fully nonlinear wave-body interactions with surface-piercing bodies. *Ocean Engineering*, 34(7), pp. 1000-1012.
- Koo, W., 2004. *Fully nonlinear wave-body interactions by a 2D potential numerical wave tank*, Texas A&m University.
- Kirby, J. T., 1996. *Nonlinear dispersive long waves in water of variable depth*. DELAWARE UNIV NEWARK CENTER FOR APPLIED COASTAL RESEARCH.

- Koley, S., Sarkar, A., and Sahoo, T., 2015. Interaction of gravity waves with bottom-standing submerged structures having perforated outer-layer placed on a sloping bed. *Applied Ocean Research*, 52, pp. 245-260.
- Kim, T., and Kim, Y., 2013. Numerical analysis on floating-body motion responses in arbitrary bathymetry. *Ocean Engineering*, 62, pp. 123-139.
- Longuet-Higgins, M. S., and Cokelet, E. D., 1976. The deformation of steep surface waves on water. I. A numerical method of computation. In: *Proceedings of the Royal Society of London A: Mathematical, Physical and Engineering Sciences*, 350(1660), pp. 1-26.
- Lachaume, C., Biauxser, B., Grilli, S. T., Fraunié, P., and Guignard, S., 2003. Modeling of breaking and post-breaking waves on slopes by coupling of BEM and VOF methods. In *Proc. 13th Offshore and Polar Engng. Conf*, Hawaii (USA).
- Luquet, R., Alessandrini, B., Ferrant, P., and Gentaz, L., 2003. RANSE analysis of 2D flow about a submerged body using explicit incident wave models. In: *Numerical Towing Tank Symposium*. Rome (Italy).
- Luquet, R., Alessandrini, B., Ferrant, P., and Gentaz, L., 2004. Simulation of the viscous flow past a ship in waves using the SWENSE approach. In: *Proc. 24th ONR Symposium on Naval Hydrodynamics*, Newfoundland (Canada).
- Luquet, R., Jacquin, E., Guillerm, P. E., Gentaz, L., Ferrant, P., and Alessandrini, B., 2005. RANSE with free surface computations around fixed and free DTMB 5415 model, in still water and in waves. In: *Proceedings of the CFD Workshop*. Tokyo (Japan).
- Luquest, R., Ferrant, P., Alessandrini, B., Ducrozet, G., and Gentaz, L., 2007. Simulation of a TLP in waves using the SWENSE scheme. In: *The Seventeenth International Offshore and Polar Engineering Conference*. Lisbon (Portugal).
- Li, Y., and Lin, M., 2012. Regular and irregular wave impacts on floating body. *Ocean Engineering*, 42, pp. 93-101.
- Li, Y., and Lin, M., 2010. Wave-body interactions for a surface-piercing body in water of finite depth. *Journal of hydrodynamics, Ser. B*, 22(6), pp. 745-752.
- Liu, Y., and Yue, D. K. P., 1998. On generalized Bragg scattering of surface waves by bottom ripples. *Journal of Fluid Mechanics*, 356, pp. 297-326.

- Liu, Y., and Li, H. J., 2017. Iterative multi-domain BEM solution for water wave reflection by perforated caisson breakwaters. *Engineering Analysis with Boundary Elements*, 77, pp. 70-80.
- Liu, Y. N., Molin, B., and Kimmoun, O., 2011. Experimental and numerical study of the effect of variable bathymetry on the slow-drift wave response of floating bodies. *Applied Ocean Research*, 33(3), pp. 199-207.
- Liu, Y., Xiao, Q., Incecik, A., Peyrard, C., and Wan, D., 2017. Establishing a fully coupled cfd analysis tool for floating offshore wind turbines. *Renewable Energy*, 112, pp. 280-301.
- Lavrov, A., Rodrigues, J. M., Gadelho, J. F. M., and Soares, C. G., 2017. Calculation of hydrodynamic coefficients of ship sections in roll motion using Navier-Stokes equations. *Ocean Engineering*, 133, pp. 36-46.
- Morison, J. R., Johnson, J. W., and Schaaf, S. A., 1950. The force exerted by surface waves on piles. *Journal of Petroleum Technology*, 2(05), pp.149-154.
- MacCamy, R. C., and Fuchs, R.A., 1954. *Wave forces on piles: a diffraction theory*. No. TM-69. Corps Of Engineers Washington DC Beach Erosion Board.
- Markiewicz, M., Ben-Nasr, K., and Mahrenholtz, O., 2003. Numerical simulations of non-linear wave radiation in inviscid fluid with a free surface. *International journal for numerical methods in fluids*, 43(10-11), pp.1279-1300.
- Ma, Q. W., 2005. Meshless local Petrov–Galerkin method for two-dimensional nonlinear water wave problems. *Journal of Computational Physics*, 205(2), pp. 611-625.
- Molteni, D., and Colagrossi, A., 2009. A simple procedure to improve the pressure evaluation in hydrodynamic context using the SPH. *Computer Physics Communications*, 180(6), pp. 861-872.
- Morino, L., Salvatore, F., and Gennaretti, M., 1999. A new velocity decomposition for viscous flows: Lighthill's equivalent-source method revisited. *Computer methods in applied mechanics and engineering*, 173(3), pp. 317-336.
- Monroy, C., Ducrozet, G., de Reilhac, P. R., Gentaz, L., Ferrant, P., & Alessandrini, B., 2009. RANS Simulations of Ship Motions in Regular and Irregular Head Seas using the SWENSE Method. In: *The Nineteenth International Offshore and Polar Engineering Conference*. Osaka, (Japan).

- Monroy, C., Ducrozet, G., Bonnefoy, F., Babarit, A., Gentaz, L., and Ferrant, P., 2011. RANS Simulations of CALM Buoy in Regular and Irregular Seas Using SWENSE Method. *International Journal of Offshore and Polar Engineering*, 21(4), pp. 264-271.
- Morgan, G., Zang, J., 2011. Application of OpenFOAM to coastal and offshore modelling. In: *The 26th IWWFEB*. Athens (Greece).
- Mei, C. C., and Liu, P. L., 1993. Surface waves and coastal dynamics. *Annual review of fluid mechanics*, 25(1), pp. 215-240.
- Mei, C. C., 1985. Resonant reflection of surface water waves by periodic sandbars. *Journal of Fluid Mechanics*, 152, pp. 315-335.
- Ma, Q. W., and Yan, S., 2009. QALE-FEM for numerical modelling of non-linear interaction between 3D moored floating bodies and steep waves. *International Journal for Numerical Methods in Engineering*, 78(6), pp. 713-756.
- Martínez-Ferrer, P. J., Qian, L., Ma, Z., Causon, D. M., and Mingham, C. G., 2018. Improved numerical wave generation for modelling ocean and coastal engineering problems. *Ocean Engineering*, 152, pp. 257-272.
- Moradi, N., Zhou, T., and Cheng, L., 2016. Two-dimensional numerical study on the effect of water depth on resonance behaviour of the fluid trapped between two side-by-side bodies. *Applied Ocean Research*, 58, pp. 218-231.
- Newman, J. N., 1996. The second-order wave force on a vertical cylinder. *Journal of Fluid Mechanics*, 320, pp.417-443.
- Newman, J. N., 1997. *Marine hydrodynamics*, MIT press.
- Na, J. H., Lee, W. C., Shin, H. S., and Park, I. K., 2002. A design of bilge keels for harsh environment FPSOs. In: *Proceedings of the 12th International Offshore and Polar Engineering Conference*, Kitakyushu (Korea).
- Omidvar, P., Stansby, P. K., and Rogers, B. D., 2012. Wave body interaction in 2D using smoothed particle hydrodynamics (SPH) with variable particle mass. *International Journal for Numerical Methods in Fluids*, 68(6), pp. 686-705.
- Patankar, S. V., 1980. *Numerical Heat Transfer and Fluid Flow*. McGraw Hill.

- Park, J. C., Kim, M. H., and Miyata, H., 2001. Three-dimensional numerical wave tank simulations on fully nonlinear wave–current–body interactions. *Journal of Marine Science and Technology*, 6(2), pp. 70-82.
- Panahi, R., Jahanbakhsh, E., and Seif, M. S., 2006. Development of a VoF-fractional step solver for floating body motion simulation. *Applied ocean research*, 28(3), pp. 171-181.
- Porter, R., and Porter, D., 2003. Scattered and free waves over periodic beds. *Journal of Fluid Mechanics*, 483, pp. 129-163.
- Palm, J., Eskilsson, C., Paredes, G. M., and Bergdahl, L. (2016). Coupled mooring analysis for floating wave energy converters using cfd: formulation and validation. *International Journal of Marine Energy*, 16, 83-99.
- Rosemurgy, W., Edmund, D., Maki, K., & Beck, R., 2012. A velocity decomposition approach for steady free-surface flow. In: *29th Symposium on naval hydrodynamics*, Gothenburg (Sweden).
- Rahman, M. A., and Al Womera, S., 2013. Experimental and numerical investigation on wave interaction with submerged breakwater. *Journal of Water Resources and Ocean Science*, 2(6), pp. 155-164.
- Ransley, E. J., Greaves, D. M., Raby, A., Simmonds, D., Jakobsen, M. M., and Kramer, M., 2017. Rans-vof modelling of the wavestar point absorber. *Renewable Energy*, 109, pp. 49-65.
- Ransley, E. J., Greaves, D., Raby, A., Simmonds, D., & Hann, M., 2017. Survivability of wave energy converters using CFD. *Renewable Energy*, 109, pp. 235-247.
- Seah, R. K. M., and Ronald, W. Yeung., 2003. Sway and roll hydrodynamics of cylindrical sections. *International Journal of Offshore and Polar Engineering*, 13(4), pp. 241-248.
- Sussman, M., Smereka, P. and Osher, S., 1994. A level set approach for computing solutions to incompressible two-phase flow. *Journal of Computational physics*, 114(1), pp.146-159.
- Sueyoshi, M., Kashiwagi, M., and Naito, S., 2008. Numerical simulation of wave-induced nonlinear motions of a two-dimensional floating body by the moving particle semi-implicit method. *Journal of Marine science and technology*, 13(2), pp. 85-94.
- Sitanggang, K. I., 2008. *Boussinesq-equation and rans hybrid wave model*. Texas A&M University.
- Schlichting, H., 1968. *Boundary-layer theory*, New York: McGrall-Hill.

- Sriram, V., Ma, Q. W., and Schlurmann, T., 2014. A hybrid method for modelling two dimensional non-breaking and breaking waves. *Journal of Computational Physics*, 272, pp. 429-454.
- Seah, R. K. M., and Yeung, R. W., 2003. Sway and roll hydrodynamics of cylindrical sections[J]. *International Journal of Offshore and Polar Engineering*, 13(04), pp. 104-114.
- Sun, L., Zang, J., Chen, L., Taylor, R. E., and Taylor, P. H., 2016. Regular waves onto a truncated circular column: a comparison of experiments and simulations. *Applied Ocean Research*, 59, pp. 650-662.
- Sjökvist, L., Wu, J., Ransley, E., Engström, J., Eriksson, M., and Göteman, M., 2017. Numerical models for the motion and forces of point-absorbing wave energy converters in extreme waves. *Ocean Engineering*, 145, pp. 1-14.
- Seng, S., Jensen, J. J., and Šime Malenica., 2014. Global hydroelastic model for springing and whipping based on a free-surface cfd code (OpenFOAM). *International Journal of Naval Architecture & Ocean Engineering*, 6(4), pp. 1024-1040.
- Sigmund, S., and Moctar, O. E., 2018. Numerical and experimental investigation of added resistance of different ship types in short and long waves. *Ocean Engineering*, 147, pp. 51-67.
- Schmitt, P., & Elsaesser, B., 2015. On the use of openfoam to model oscillating wave surge converters. *Ocean Engineering*, 108, pp. 98-104.
- Tanizawa, K., and Minami, M., 1998. On the accuracy of NWT for radiation and diffraction problem. In *Proceeding of 6th Symposium on Nonlinear and Free-surface Flow*.
- Teng, T. L., Pizer, D., Simmonds, D., Kyte, A., and Greaves, D., 2018. Simulation and analysis of wave-structure interactions for a semi-immersed horizontal cylinder. *Ocean Engineering*, 147, pp. 676-689.
- Vukčević, V., Jasak, H., & Malenica, Š., 2016. Decomposition model for naval hydrodynamic applications, Part I: Computational method. *Ocean Engineering*, 121, pp. 37-46.
- Van't Veer, R., and Fathi, F., 2011. On the roll damping of an FPSO with riser balcony and bilge keels. *International Journal Of Maritime Engineering*, 153, pp. A125-A135.
- Vuorinen, V., Keskinen, J. P., Duwig, C., 2014. On the implementation of low-dissipative Runge–Kutta projection methods for time dependent flows using OpenFOAM®. *Computers & Fluids*, 93, pp. 153-163.



- Vyzikas, T., Deshoulières, S., Giroux, O., Barton, M., and Greaves, D., 2016. Numerical study of fixed oscillating water column with rans-type two-phase CFD model. *Renewable Energy*, 102, pp. 294-305
- Wu, G. X., Ma, Q. W., and Eatock T. R., 1998. Numerical simulation of sloshing waves in a 3D tank based on a finite element method. *Applied Ocean Research*, 20(6), pp. 337-355.
- Wang, C. Z., Wu, G. X. and Khoo, B. C., 2011. Fully nonlinear simulation of resonant motion of liquid confined between floating structures. *Computers & Fluids*, 44(1), pp. 89-101.
- Widlund, O., and Toselli, A., 2004. Domain decomposition methods-algorithms and theory. In *Computational mathematics*. Springer.
- Weller, H. G., 2002. *Derivation, modelling and solution of the conditionally averaged two-phase flow equations*. Nabla Ltd, Technical Report TR/HGW/02.
- Wilson, R. V., Carrica, P. M., and Stern, F., 2006. Unsteady RANS method for ship motions with application to roll for a surface combatant. *Computers & fluids*, 35(5), pp. 501-524.
- Yan, S., and Ma, Q. W., 2007. Numerical simulation of fully nonlinear interaction between steep waves and 2D floating bodies using the QALE-FEM method. *Journal of Computational physics*, 221(2), pp. 666-692.
- Yan, S., and Ma, Q. W., 2010. Numerical simulation of interaction between wind and 2D freak waves. *European Journal of Mechanics-B/Fluids*, 29(1), pp. 18-31.
- Yi-Hsiang, Y., Kinnas, S. A., Vinayan, V., and Kacham, B. K., 2005. Modeling of flow around FPSO hull sections subject to roll motions: Effect of the separated flow around bilge keels. In: *The Fifteenth International Offshore and Polar Engineering Conference*, ChangSha (China).
- Yang, C., Löhner, R. and Lu, H. D., 2006. An unstructured-grid based volume-of-fluid method for extreme wave and freely-floating structure interactions." *Journal of Hydrodynamics, Ser, B* 18(3), pp. 415-422.
- Yakhot, V., Orszag, S. A., Thangam, S., 1992. Development of turbulence models for shear flows by a double expansion technique. *Physics of Fluids A: Fluid Dynamics*, 4(7), pp. 1510-1520.
- Yan, S., and Ma, Q. W., 2007. Effects of an arbitrary sea bed on responses of moored floating structures to steep waves. In: *The Seventeenth International Offshore and Polar Engineering Conference*.

Yang, L., 2018. One-fluid formulation for fluid–structure interaction with free surface. *Computer Methods in Applied Mechanics & Engineering*, 332, pp. 102-135.

Yang, L, Gil, A.J., Carreno, AA. and Bonet, J., 2018. Unified one-fluid formulation for incompressible flexible solids and multiphase flows: application to hydrodynamics using the Immersed Structural Potential Method (ISPM). *International Journal for Numerical Methods in Fluids*. 86(1), pp.78-106

Zhang, Y., Peszynska, M., and Yim, S., 2013. Coupling of viscous and potential flow models with free surface for near and far field wave propagation. *International Journal of Numerical Analysis and Modeling*, 4(3), pp. 256-282.

Zhang, Y., Yim, S. C., and Pin, F. D., 2015. A non overlapping heterogeneous domain decomposition method for three-dimensional gravity wave impact problems. *Computers & Fluids*, 106, pp. 154-170.

Zhang, Y., Pin, F. D., and Yim, S. C., 2014. A heterogeneous flow model based on DD method for free surface fluid–structure interaction problems. *International Journal for Numerical Methods in Fluids*, 74(4), pp. 292-312.